

UNIVERSITY OF CALIFORNIA

Los Angeles

Ice-Ocean Interactions in the Antarctic Slope Current

by

Yidongfang Si

2023

© Copyright by

Yidongfang Si

2023

ABSTRACT OF THE DISSERTATION

Ice-Ocean Interactions in the Antarctic Slope Current

by

Yidongfang Si

Doctor of Philosophy in Atmospheric and Oceanic Sciences

University of California, Los Angeles, 2023

Professor Andrew L. Stewart, Chair

The Antarctic Slope Current (ASC) is a narrow and westward circulation feature that surrounds the Antarctic continental shelves. It regulates onshore ocean heat transport toward the Antarctic ice shelves and dense water outflow, playing an important role in global meridional overturning circulation, glacier melt, and sea level rise. Despite its significance to Earth's climate system, the circulation and heat transport around the Antarctic margins remain poorly understood due to the difficulties and expense in observation and modeling.

In this work, the dynamics of the ASC and the ice-ocean interactions around the Antarctic margins are investigated using high-resolution process-oriented simulations. The key results are summarized as follows: (i) Due to topographic eddy suppression, almost no wind-input momentum is transferred vertically over the continental slope; as a result, sea ice horizontally redistributes the wind-input momentum away from the continental slope, playing a critical role in the momentum balance of the ASC. (ii) Melt-induced freshening of the coastal waters that are buoyant compared with the open ocean leads to increased eddy-driven shoreward heat flux, which implies a positive feedback in a warming climate that may cause further melt of ice shelves. (iii) The West Antarctic slope undercurrent originates from the cyclonic vorticity input by meltwater upwelling in the cavities of West Antarctic ice shelves, which drives warm Circumpolar Deep Water toward the glaciers; increased basal melt therefore strengthens the slope undercurrent and enhances onshore heat transport, which indicates another positive feedback that may accelerate future melt, potentially further destabilizing the West Antarctic Ice Sheet.

The work in this dissertation advances the understanding of the ice-ocean system near the Antarctic margins and highlights previously unrecognized climate feedbacks that may be key to projecting future changes in Antarctic ice sheets and thus sea level rise. In addition, our results help guide future climate model development and future observations of near-Antarctic ocean heat flux and glacier melt.

Ian Eisenman

James C. McWilliams

Marcelo Chamecki

Andrew L. Stewart, Committee Chair

To fellow physical oceanographers

TABLE OF CONTENTS

1	Introduction	1
1.1	Background	1
1.2	Outline	2
1.2.1	Coupled ice-ocean dynamics of the Antarctic Slope Current	3
1.2.2	Positive feedback of eddy-driven ocean heat transport toward the Antarctic margins	3
1.2.3	Melt-driven undercurrent and the positive circulation-melt feedback in West Antarctica	4
2	Coupled ocean/sea ice dynamics of the Antarctic Slope Current driven by topographic eddy suppression and sea ice momentum redistribution	6
2.1	Introduction	7
2.2	Model configuration	12
2.3	Drivers of ASC ocean and sea ice circulation	20
2.4	Momentum balances for ocean and sea ice in the ASC	26
2.4.1	Zonal momentum balance in the reference simulation	26
2.4.2	Sensitivity of zonal momentum balance to model parameters	30
2.4.3	Vertical momentum transfer over the slope	33
2.5	A reduced-order model of ice-ocean mechanical interactions in the ASC	35
2.5.1	Formulation of the reduced-order model	35
2.5.2	Reduced-order simulations	38
2.6	Discussion and conclusions	42
2.6.1	Key findings	42

2.6.2	Limitations and implications	45
2.7	Appendix	47
2.7.1	Formulation of the reduced-order model	47
2.7.2	Decomposition of the total advection for the 3D MITgcm simulations . . .	53
2.7.3	3D Model bathymetry	55
3	Heat transport across the Antarctic Slope Front controlled by cross-slope salinity gradients	57
3.1	Introduction	58
3.2	Results	62
3.2.1	Shoreward heat transport in the fresh- and dense-shelf regimes	62
3.2.2	Vertical structure of heat flux and overturning circulation	66
3.2.3	Role of small-scale and/or high-frequency variability	69
3.3	Discussion	71
3.4	Materials and methods	74
3.4.1	Model configuration and simulations	74
3.4.2	Model limitations	77
3.4.3	Heat function	79
3.4.4	Operators for temporal decomposition	79
3.4.5	Decomposition of the total meridional heat transport	80
3.4.6	Diffusion and advection by tides and eddies	80
3.4.7	Decomposition of the total kinetic energy	81
3.4.8	Decomposition of the isopycnal overturning streamfunction	82
3.5	Supplementary Materials	83

4 Antarctic slope undercurrent and onshore heat transport driven by meltwater upwelling	105
4.1 Introduction	106
4.2 Simulating West Antarctic slope undercurrent and ice shelf melt	108
4.3 Buoyancy-driven slope undercurrent and onshore CDW heat transport	113
4.4 Implications for future melt of West Antarctic ice shelves	122
4.5 Methods	124
4.5.1 Model configuration	124
4.5.2 Insensitivity of ice-shelf melt rate to wind perturbation and the presence of trough in the idealized model	127
4.5.3 Pseudo-ice shelf	129
4.5.4 Depth-integrated CDW vorticity budget	130
4.5.5 Pressure torques and vertical stretching of the CDW layer	132
4.5.6 Coriolis term and diapycnal upwelling	133
4.5.7 Transport-weighted undercurrent velocity and cross-slope buoyancy gradient	133
4.5.8 Shoreward CDW transport within the trough	135
5 Conclusions and future work	136
5.1 Summary	136
5.2 Looking ahead	137
5.2.1 Circumpolar variability and onshore heat transport	137
5.2.2 West Antarctic slope undercurrent	138
5.2.3 Tidal-mean compensation	139
5.2.4 Seasonality of momentum transfer in the ASC	139

LIST OF FIGURES

2.1 The observed external forcing of the sea ice-ocean system around the Antarctic margin, and the motion of the sea ice and the ocean in the Antarctic winter. (a) The winter (June, July, and August) climatology of zonal wind speed from 2007-2014, using the Antarctic Mesoscale Prediction System (AMPS) products (Powers et al., 2003, 2012). (b) The annual average of tidal current speed including ten major tidal constituents, calculated by the model CATS2008 (Padman et al., 2002, 2008). (c) The winter climatology of zonal ice drift speed from 1979-2015, using the product "Polar Pathfinder Daily 25 km EASE-Grid Sea Ice Motion Vectors, Version 3" (Tschudi et al., 2016). (d) The winter climatology of sea surface elevation using the Dynamic Ocean Topography (DOT) data (Armitage et al., 2018). The gray, white, and orange curved arrows denote the Antarctic Slope Current, the Weddell Gyre, and the Ross Gyre with their directions, respectively. The black dashed curve around the Antarctic continent represents the 1000-m isobath.

2.2 Illustration of the MITgcm Antarctic Slope Front process model (MITgcm ASF) setup. (a) Model bathymetry, snapshot of sea surface salinity (colors), surface ocean currents (arrows), and 0°C isotherms. (b) The steady along- and across-slope wind forcing used in the reference simulation. (c) Time- and zonal-mean sea ice thickness (the gray box, which is exaggerated) and potential temperature (the contour plot, plotted at intervals of 0.13°C) in the reference simulation. The thick dashed and solid black curves show the shallowest and deepest of the bathymetric contours, respectively. At the southern and northern boundaries, temperature and salinity are restored to the reference profiles across sponge layers of 20 km width. (d) The relaxation salinity (orange) and temperature (blue) profiles of the sponge layers. The northern boundary restoring (solid lines) is based on hydrography taken from the sections across the Antarctic Slope Front at Kapp Norvegia (Hattermann, 2018). The southern boundary restoring temperature and salinity are denoted by the dashed lines.	13
2.3 Model evaluation. (a-f) A cross section of ice and ocean properties in the reference simulation using time-mean output, taken along the longitude $x = 0$ km. (g-i) The hydrography taken near East Antarctica during the "BROKE West" survey (Rosenberg and Gorton, 2019) in the Antarctic summer of 2006, along the 60°E line. (a) Sea ice thickness. (b) Sea ice concentration. (c) Sea ice and surface ocean zonal velocities. (d, g) Ocean potential temperature. (e, h) Ocean salinity. (f, i) Ocean zonal velocity. The values on the gray contours denote the neutral densities (kg/m^3).	20

2.4 Time- and zonal-mean zonal velocity for the reference simulation (a, h), simulations with varying tidal current amplitudes (b, c, i, j), thinner sea ice at the southern boundary (d, e, k, l), and varying zonal wind speeds (f, g, m, n). The corresponding upper panels show the time- and zonal-mean zonal ice and surface ocean velocities. The gray contours denote the time- and zonal-mean neutral densities 1027.60, 1028.03, 1028.27, and 1028.35 kg/m ³ . Dashed and solid thick black curves denote the shallowest and deepest of the bathymetric contours, respectively. In these simulations, the southern boundary temperature and salinity are set to be vertically uniform (-1.87 °C, 34.17 psu).	21
2.5 Time- and zonal-mean zonal velocity varying with buoyancy gradients between the continental shelf and the open ocean. Similar to Fig. 2.4, the corresponding upper panels show the time- and zonal-mean zonal ice and the surface ocean velocities. The gray contours denote the time- and zonal-mean neutral densities and the black curves denote the model bathymetry. Other model parameters such as tidal current amplitude, wind speeds, sea ice thickness at the southern boundary, and slope width are the same in these simulations.	22
2.6 The maximum westward ocean speed $ \bar{u}_o _{\max}$, maximum westward ocean bottom speed $ \bar{u}_o^{\text{bot}} _{\max}$, barotropic transport T_{BT} and baroclinic transport T_{BC} per unit width over the continental slope for simulations with varying tidal current amplitude (a), sea ice thickness at the southern boundary (b), maximum westward wind speed (c), maximum northward wind speed (d), continental slope half-width (e), horizontal grid spacing (f), and ocean bottom potential density difference between the northern and the southern boundaries (g). Black dots denote the reference simulation.	24

2.7 Time-mean westward ice speed $ \langle \bar{u}_i \rangle $ and ice thickness $\langle \bar{h}_i \rangle$ over the continental slope, for simulations with varying tidal current amplitude (a), ocean bottom potential density difference between the northern and the southern boundaries (b), maximum westward wind speed (c), maximum northward wind speed (d), continental slope half-width (e), horizontal grid spacing (f), and sea ice thickness at the southern boundary (g). Black dots denote the reference simulation.	25
2.8 Time- and zonal-mean sea ice and ocean zonal force balances for the reference simulation (a, b), the case with zero tidal current amplitude (c, d), the case with a wide and gentle continental slope (e, f), and the very dense shelf case (g, h). Note that the 20-km southern and northern restoring regions have been removed. The y-axis is negative (westward) upward, and the range of y-axis for panel (h) is different from other panels.	28
2.9 Sensitivity analysis: time-mean sea ice and ocean zonal force balances averaged over the continental slope, (a-d) normalized by zonal wind stress, or (e-f) by the sum of zonal wind stress and ocean advection. Simulations with varying (a-b) sea ice thickness at the southern boundary, (c-d) maximum northward wind speed, and (e-f) maximum westward wind speed.	31
2.10 Sensitivity analysis (continued): time-mean sea ice and ocean zonal force balances, averaged over the continental slope and normalized by zonal wind stress. Simulations with varying (a-b) tidal current amplitude, (c-d) continental slope half-width, and (e-f) ocean bottom potential density difference between the northern and the southern boundaries.	32

3.1 Salinity regimes around Antarctica and in our model configuration. **(A)** Climatology (1981-2010) of 500-m depth ocean salinity or seafloor salinity where the ocean is shallower than 500 m with the unit of psu (practical salinity unit). The black dashed curve indicates the 1000-m isobath. The white arrows represent the Antarctic Slope Current (ASC), with white dashed lines in the Bellingshausen (BS), Amundsen (AS), and Ross Seas denoting the uncertain initiation of the ASC ([Thompson et al., 2018](#)). The solid gray arrows represent the Ross Gyre and the Weddell Gyre. The dashed gray arrows represent the Antarctic Circumpolar Current (ACC). **(B)** A cross section of ocean salinity taken in the Ross Sea (73.05° - 69.01° S, 172.13° E), where the shelf is relatively salty, overlaid by gray contours of surface-referenced potential temperature. **(C)** A cross section of ocean salinity taken in East Antarctica (67.75° - 63.71° S, 76.38° E), where the shelf is relatively fresh, overlaid by gray contours of surface-referenced potential temperature. The data used in (A) to (C) come from World Ocean Atlas 2018 ([Zweng et al., 2019](#)). **(D)** Results of the dense-shelf (equivalent to “salty-shelf” in this study) simulation with instantaneous sea surface potential density ($\rho_{\text{dense}}^{\text{surf}}$), 0°C isotherms, and time- and zonal-mean salinity in the background. The white arrows sketch the direction and relative strength of sea surface currents, and the black arrow schematically shows the direction of the ASC. **(E)** As (D), but shows the fresh-shelf simulation. $\rho_{\text{fresh}}^{\text{surf}}$ is the instantaneous sea surface potential density of the fresh-shelf simulation.

59

3.2 Sensitivity of shoreward heat transport. **(A)** Vertically and zonally integrated meridional advective heat flux in the simulations with varied shelf bottom salinity ($S_{\text{shelf}}^{\text{bot}}$) in TW (1 TW = 10^{12} W), as a function of latitude y . The horizontal resolution of these simulations is 2 km. The blue, black, and red lines represent simulations with low, reference, and high shelf salinity, respectively. Light gray denotes the latitudinal band (50 to 75 km) used to calculate the averaged heat transferred onto the shelf, F_{shelf} . The 20-km sponge layer at the northern boundary is not shown. **(B)** Heat transferred onto the continental shelf (F_{shelf}), as a function of shelf bottom salinity prescribed at the southern boundary. The solid, dotted, and dashed lines denote simulations with 2-, 5-, and 10-km resolution, respectively. The green and orange curves denote the fresh- and dense-shelf regimes, respectively. Positive slopes of F_{shelf} in the dense-shelf regime indicate a negative feedback; negative slope of F_{shelf} in the fresh-shelf regime indicates a positive feedback; zero slope corresponds to no feedback. For the fresh-shelf, reference, and dense-shelf cases, the sensitivity of F_{shelf} to other model parameters is indicated by markers with various shapes, with larger marker sizes indicating larger values of the corresponding parameters. $U_{\text{a}0}$ and $V_{\text{a}0}$ are the zonal and meridional wind speed at the southern boundary, respectively. A_{tide} is the prescribed barotropic tidal current amplitude. $h_{\text{i}0}$ is the restoring sea ice thickness at meridional boundaries, which is also the initial sea ice thickness across the domain. W_S is the continental slope width. The inset plot is a zoomed-in view of F_{shelf} in the fresh-shelf regime.

63

- 3.5 Schematic of salinity-controlled shoreward heat transport. **(A)** Fresh-shelf case. **(B)** Reference case. **(C)** Dense-shelf case. The gray dashed curves with arrows denote the zonally averaged meridional overturning circulation. The black circle with a cross shows that the direction of the slope current is westward (into the page), with the size of the circle representing the strength of the slope current. The circular arrows denote the transient baroclinic eddies. In (C), the white curve with an arrow denotes the mean gravity current associated with dense water outflow. . . 73
- 3.6 Time- and zonal-mean zonal (along-slope) velocity (A-C), potential temperature (D-F), and salinity (G-I) of the simulations (2-km resolution), overlaid by neutral density contours. **(A, D, G)** The fresh-shelf case. **(B, E, H)** The reference case. **(C, F, I)** the dense-shelf case. In panels (A-C), blue denotes westward flow (into the page), and red denotes eastward flow (out of the page). The gray contours with numbers show the time- and zonal-mean neutral density (kg/m^3). The black solid and dashed curves denote the deepest and shallowest bathymetry (see Figs. 1D, E), respectively. The 20-km sponge layers at the northern and southern boundaries are not shown. **(J-M)** Cross sections of potential temperature and salinity taken in East Antarctica (fresh shelf, $67.75^\circ\text{-}63.71^\circ\text{S}$, 76.38°E) and the Ross Sea (dense shelf, $73.05^\circ\text{-}69.01^\circ\text{S}$, 172.13°E), respectively. Data comes from World Ocean Atlas 2018. 85

3.9 Temporal decomposition of the zonal-mean southward advective heat flux for simulations with 2-km horizontal resolution. Mean, tidal, and eddy heat fluxes of the fresh-shelf (A, C, E) and dense-shelf (B, D, F) cases. The black solid and dashed curves denote the deepest and shallowest bathymetry at each latitude, respectively. The 20-km sponge layers at the northern and southern boundaries are not shown.	88
3.10 Same as Fig. 3.9, but for the surface 600m of the ocean.	89
3.11 Temporal decomposition of the total kinetic energy for simulations with 2-km horizontal resolution. (A-C) Time-mean total kinetic energy, and its tidal, eddy, and mean components in the fresh-shelf, reference, and dense-shelf cases, averaged over the zonal/vertical plane. (D-F) Time- and zonal-mean eddy kinetic energy in the three cases. The colored and solid white contours show intervals of 1.5×10^{-4} m ² s ⁻² and 10^{-3} m ² s ⁻² , respectively. The black solid and dashed curves denote the deepest and shallowest bathymetry at each latitude, respectively. The 20-km sponge layers at the northern and southern boundaries are not shown. Note the total kinetic energy and mean kinetic energy remain the same order of magnitude across simulations, while the eddy kinetic energy increases by 1~2 orders of magnitude in the fresh- and dense-shelf cases.	90

3.12 Temporal decomposition of the isopycnal overturning streamfunction ($\psi_{\text{isop}} = \psi_{\text{EM}} + \psi_{\text{SW}} + \psi_{\text{eddy}} + \psi_{\text{tide}}$) for the fresh-shelf simulation with 2-km horizontal resolution. Isopycnal overturning streamfunction (ψ_{isop}) with a reference depth of 2 km in potential density (σ_2) space (A) and z space (B). (C) Eulerian-mean overturning streamfunction (ψ_{EM}). (D) Standing-wave overturning streamfunction (ψ_{SW}). (E) Tidal overturning streamfunction (ψ_{tide}). (F) Transient-eddy overturning streamfunction (ψ_{eddy}). The white dashed and solid contours show intervals of 0.05 Sv (1 Sv = $10^6 \text{ m}^3 \text{ s}^{-1}$) and 0.1 Sv, respectively. The black arrows show the direction of the overturning circulation, with positive values (red) corresponding to clockwise circulation, and negative values (blue) corresponding to counter-clockwise circulation. The black solid and dashed curves denote the deepest and shallowest bathymetry at each latitude, respectively. The 20-km sponge layers at the northern and southern boundaries are not shown. Note that the tidal component is largely compensated by the Eulerian-mean component.	91
3.13 Temporal decomposition of the isopycnal overturning streamfunction for the dense-shelf simulation with 2-km horizontal resolution. As Fig. 3.12, but for the dense-shelf case.	92
3.14 Eddy/mean heat decomposition for simulations with no tides and 2-km horizontal resolution.	93
3.15 Temporal decomposition of the total shoreward heat transport. As Fig. 3.4, but for simulations with 5-km horizontal resolution.	94
3.16 Temporal decomposition of the total shoreward heat transport. As Fig. 3.4, but for simulations with 10-km horizontal resolution.	95
3.17 Temporal decomposition of the zonal-mean southward advective heat flux. As Fig. 3.9, but for simulations with 5-km horizontal resolution.	96
3.18 Temporal decomposition of the zonal-mean southward advective heat flux. As Fig. 3.9, but for simulations with 10-km horizontal resolution.	97

3.19 Temporal decomposition of the total kinetic energy. As Fig. 3.11, but for simulations with 5-km horizontal resolution.	98
3.20 Temporal decomposition of the total kinetic energy. As Fig. 3.11, but for simulations with 10-km horizontal resolution.	99
3.21 Temporal decomposition of overturning streamfunction for the fresh-shelf case. As Fig. 3.12, but for simulations with 5-km horizontal resolution.	100
3.22 Temporal decomposition of overturning streamfunction for the fresh-shelf case. As Fig. 3.12, but for simulations with 10-km horizontal resolution.	101
3.23 Temporal decomposition of overturning streamfunction for the dense-shelf case. As Fig. 3.13, but for simulations with 5-km horizontal resolution.	102
3.24 Temporal decomposition of overturning streamfunction for the dense-shelf case. As Fig. 3.13, but for simulations with 10-km horizontal resolution.	103
3.25 EKE power spectra for fresh-shelf simulations with different horizontal resolutions, normalized by the length of the timeseries. (A) EKE spectrum over the continental shelves (latitude $y=20\text{-}125$ km and depth $z=0\text{-}500$ m). (B) Surface 500 m EKE spectrum for all latitudes (latitude $y=20\text{-}430$ km excluding the 20km sponge layers at the southern and northern boundaries, and depth $z=0\text{-}500$ m).	104
3.26 EKE power spectra over the continental shelves (latitude $y=20\text{-}125$ km, depth $z=0\text{-}500$ m), normalized by the length of the timeseries. (A) Fresh-shelf, reference, and dense-shelf simulations in the 2-km model. (B) 5-km model. (C) 10-km model. . .	104

4.3 Area-integrated vorticity budget of the cyclonic circulation in the CDW layer.	112
a , Onshore CDW heat flux (color) and CDW volume flux (arrows) in the reference simulation, with red corresponding to shoreward (southward) heat flux. There is a cyclonic flow (relative vorticity $\zeta < 0$) comprising the slope undercurrent and the CDW circulation in the trough. The black solid line denotes the location of the ice shelf front at $y = 100$ km. The bathymetric contours are denoted by the thin dashed lines with an interval of 1000 m, and thin dotted lines with an interval of 100 m. b , Potential vorticity (PV) of the CDW layer denoted by the gray contours with an interval of $10^{-8} \text{ m}^{-1}\text{s}^{-1}$. The colored PV contours denote the selected region, with the maximum and minimum PV values of $-1.0 \times 10^{-7} \text{ m}^{-1}\text{s}^{-1}$ and $-3.5 \times 10^{-7} \text{ m}^{-1}\text{s}^{-1}$, respectively. Over the shelf break and upper slope ($225 \text{ km} \leq y \leq 240 \text{ km}$), the selected region is cut off at $x = -100 \text{ km}$ and $x = 40 \text{ km}$, respectively. c , The vorticity budget of the CDW layer cumulatively integrated from south to north within the selected region shown in panel b , as a function of latitude.	112
4.4 Cross-sections of potential temperature, salinity, and zonal velocity. a-c , West of the trough at $x = -50 \text{ km}$. d-f , Trough center at $x = 0 \text{ km}$. g-i , East of the trough at $x = 50 \text{ km}$. The shallowest and deepest bathymetric contours are indicated by the thick solid and dashed lines, respectively.	113

4.5 Perturbation experiments. Correlation between the diapycnal upwelling across the 0°C isotherm in the ice-shelf cavity with **a**, ice shelf melt rate, **b**, Coriolis term in the CDW vorticity budget integrated within the cavity, **c**, total pressure torque of the CDW layer integrated over the shelf break west of the trough ($210 \text{ km} \leq y \leq 235 \text{ km}$, $-120 \text{ km} \leq x \leq 0 \text{ km}$, the green box in Fig. 4.9*i*), **d**, cyclonic vorticity integrated over the shelf break west of the trough, and **e**, transport-weighted undercurrent velocity west of the trough (Eq. 4.17). **f**, Correlation between transport-weighted undercurrent velocity and shoreward CDW transport within the trough ($1 \text{ Sv} = 10^6 \text{ m/s}$, Eq. 4.19). The names of the experiments in the figure are consistent with Table 4.1. In each panel, r_1 is the correlation coefficient for simulations with fixed topographic geometry and boundary isopycnal geometry, denoted by the filled markers; r_2 is the correlation coefficient for all simulations, including simulations with varied topographic geometry and boundary isopycnal geometry, denoted by the hollow markers; the thin black line is the linear fit for the filled markers. . . . 114

4.6 **Perturbation experiments.** **a**, Correlation between the cumulative heat transport at the ice-shelf front ($y = 100$ km) with ice shelf melt rate. **b**, Correlation between the diapycnal upwelling across the 0°C isotherm in the ice-shelf cavity with the thermal-wind velocity, which is a quantification of the cross-slope buoyancy gradient (Eq. 4.18b). **c**, Correlation between ice shelf melt rate and zonal-mean undercurrent transport west of the trough ($1 \text{ Sv} = 10^6 \text{ m/s}$; Eq. 4.16). **e,f**, Correlation between the transport-weighted undercurrent velocity (Eq. 4.17) with the pressure torque of the CDW layer integrated over the shelf break west of the trough ($210 \text{ km} \leq y \leq 235 \text{ km}$, $-120 \text{ km} \leq x \leq 0 \text{ km}$, the green box in Fig. 4.8*i*) and thermal-wind velocity (Eq. 4.18b), respectively. The names of the experiments in the figure are consistent with Table 4.1. In each panel, r_1 is the correlation coefficient for simulations with fixed topographic geometry and boundary isopycnal geometry, denoted by the filled markers; r_2 is the correlation coefficient for all simulations, including simulations with varied topographic geometry and boundary isopycnal geometry, denoted by the hollow markers; the thin black line is the linear fit for the filled markers. 115

4.7 Onshore CDW heat transport increases with a larger prescribed meltwater flux. Left column: Vertically integrated heat flux (color) and volume flux (arrows) in the CDW layer, with red corresponding to shoreward (southward) heat flux. The black solid line denotes the location of the ice shelf front at $y = 100$ km. The bathymetric contours are denoted by the thin dashed lines with an interval of 1000 m, and thin dotted lines with an interval of 100 m. Right column: Cumulative CDW heat transport at the ice shelf front as a function of longitude. The CDW heat flux is first integrated vertically and then integrated zonally along the ice shelf front, from $x = 100$ km to $x = -100$ km. a-b , Pseudo-ice shelf with no melt. c-g , The equivalent basal melt rates prescribed at the titled surface of the pseudo-ice shelf (ω_{melt}) are 8, 16, and 24 m/yr, respectively. Configurations of the pseudo-ice shelf simulations are presented in the section “Pseudo-ice shelf” in the Methods and in Table 4.1.	116
4.8 Vorticity budget of the CDW layer. The total advection (b) balances total pressure torque (a) and dissipation (c). The total pressure torque comprises the interfacial pressure torque (d) and bottom pressure torque (e). The total advection comprises the Coriolis term (f), vorticity advection (g), vertical advection (h), and residual term (i). The bathymetric contours are denoted by the thin dashed lines with an interval of 1000 m, and thin dotted lines with an interval of 100 m. The green box in panel i indicates the selected region to calculate the shelf-break-integrated relative vorticity and pressure torque of the CDW layer, presented in Fig. 4.5c, d and Fig. 4.6c, respectively.	118
4.9 Vertical velocities and vertical stretching for the reference simulation. a , Vertical velocity at the ocean bottom (ω_{bot}). b , Vertical velocity at the upper bound of the CDW layer (ω_{up}). c , Vertical stretching of the CDW layer ($\omega_{\text{up}} - \omega_{\text{bot}}$).	119
4.10 CDW vorticity budget for the pseudo ice shelf simulation with no melt. Figure labels are the same as Fig. 4.8.	121

4.11 Schematic illustrating the mechanism of Antarctic Slope Undercurrent formation.

The ice shelf meltwater creates an offshore buoyancy gradient with shoreward deepening of the thermocline, which is maintained by shoreward Ekman transport associated with westward coastal winds. As CDW melts the ice shelf, ice-shelf meltwater transforms the CDW to a lighter water mass and vertically stretches the CDW layer, which injects cyclonic vorticity into the CDW layer. The source of the cyclonic vorticity is then transported offshore by the pressure-torque vorticity flux (Eq. 4.14), provided that there is a trough extending onto the shelf. Over the shelf break, the cyclonic vorticity steers CDW toward the ice shelf, driving an eastward undercurrent west of the trough. Stronger basal melt leads to stronger diapycnal upwelling of meltwater, increasing the strength of the slope undercurrent and therefore enhancing onshore CDW heat transport. The vertical stretching of the CDW layer is illustrated by the orange columns, with black arrows at the top or bottom of the columns denoting the direction of the stretching and circular arrows denoting the resulting cyclonic rotation. As CDW flows towards the ice shelf, it is primarily stretched downward following the topography (Extended Fig. 4.9); within the ice shelf cavity, the CDW layer is stretched upward due to the upwelling of meltwater. 122

4.12 A compensation between heat transport through the trough and by the boundary current. Left column: Vertically integrated heat flux (color) and volume flux (arrows) in the CDW layer, with red corresponding to shoreward (southward) heat flux. The black solid line denotes the location of the ice shelf front at $y = 100$ km. The bathymetric contours are denoted by the thin dashed lines with an interval of 1000 m, and thin dotted lines with an interval of 100 m. Right column: Cumulative shoreward CDW heat transport at the ice shelf front as a function of longitude. The CDW heat flux is first integrated vertically and then integrated zonally along the ice shelf front, from $x = 100$ km to $x = -100$ km. **a-b**, The reference simulation. T_{trough} is the heat carried by the undercurrent through the trough (T_{trough}). $T_{\text{boundary current}}$ is the heat carried by the coastal boundary current. **c-d**, The simulation with no trough. **e-f**, The simulation with weak surface winds ($U_{a0} = -2$ m/s, $V_{a0} = 2$ m/s). **g-h**, The simulation with strong surface winds ($U_{a0} = -8$ m/s, $V_{a0} = 8$ m/s). . . . 128

LIST OF TABLES

2.1 List of parameters used in the experiments.	14
2.2 List of parameters varied among the experiments. The bold fonts denote the values used in the reference simulation. When varying continental slope width W_s , the corresponding meridional slope position Y_s is 150 , 175, 200, 225, and 250 km, respectively. Note that varying $\Delta\sigma_4$ is achieved by varying the restoring salinity profiles at the southern boundary. In those simulations, the salinity difference between the northern and the southern boundaries at depth $z = 500$ m are -1.695, -1.108, -0.578 , -0.315, -0.053, 0.210 psu, respectively (Fig. 2.2d).	18
3.1 List of experiments. Δ_x and Δ_y are the horizontal grid spacings in the zonal and meridional direction, respectively. $\Delta S = 0.23$ psu is the vertical difference in the restoring salinity at the southern boundary between the sea surface ($S_{\text{south}}^{\text{surf}}$) and the seafloor of the continental shelf (500 m depth, $S_{\text{south}}^{\text{bot}}$) of the reference case. $U_{\text{a}0}$ and $V_{\text{a}0}$ are the zonal (along-slope, positive eastward) and meridional (cross-slope, positive northward) wind speed at the southern boundary, respectively. A_{tide} is the prescribed barotropic tidal current amplitude at the northern boundary. $h_{\text{i}0}$ is the restoring sea ice thickness at the southern boundary, which is also the initial sea ice thickness across the domain. W_S is the continental slope width. The boldface shows the three experiments mainly described in this article (the fresh-shelf, reference, and dense-shelf cases), as well as perturbation simulations.	84

4.1 List of experiments. The reference simulation and perturbed parameters are marked in boldface. h_{i0} is the initial ice thickness across the domain, and the restoring ice thickness at the eastern, western, and northern boundaries. U_{a0} and V_{a0} are the zonal and meridional wind extrema at the southern boundary, respectively. The magnitude of the wind speed decreases linearly offshore. A_{tide} is the prescribed tidal current amplitude at the northern boundary. W_{tr} is the half-width of the trough. H_{bed} is the change in bedrock elevation from the shelf break to the southern boundary. H_{tr} is the depth of the trough over the continental shelf. The thermocline depth at the northern boundary, shelf break, and southern boundary are Z_n ($Z_n = 350$ m in all simulations), Z_{sb} , and Z_s , respectively, with larger values corresponding to a deeper thermocline (Fig. 4.1d). κ_{max}^{3D} is the maximum value of the 3D vertical diffusivity. ω_{melt} is the equivalent basal melt rate prescribed at the titled surface the pseudo ice shelf (0, 8, 16, and 24 m/yr, respectively).

$Nt = 3.0672 \times 10^7$ is the number of seconds per year. 110

ACKNOWLEDGMENTS

I would like to thank my advisor Professor Andrew Stewart, who introduced me to the field of Physical Oceanography. I couldn't be luckier to have him as my PhD advisor. I tremendously appreciate all the insightful knowledge, guidance, and support he has provided for me. He is the role model of an incredible scientist, teacher, and advisor to me and many others in the Stewart group. Becoming an independent researcher and a great advisor like him is what I hope to accomplish in the future as I navigate my academic journey.

I would like to express my gratitude to my collaborators for their support and for the insight they have shared throughout the past five years: Ian Eisenman, Carolyn Schmidgall, Sophia Spungin, Alberto Naveira Garabato, Alessandro Silvano, Michael Schodlok, and Madeleine Youngs. I also thank my dissertation committee: James McWilliams and Marcelo Chamecki for their constructive feedback. In addition, I would like to thank Andy Thompson for valuable feedback on my work and Tore Hattermann who reviewed two chapters of my thesis for publication and provided numerous comments. I sincerely thank the U-DOG (UCLA Dynamical Oceanography Group): Yan Wang, Jordyn Moscoso, Ken Zhao, Aviv Solodoch, Garrett Finucane, Sunny Yeh, Kaylie Cohanim, Jennifer Kosty, Luna Bai, Xiaoyang Chi, Julia Hazel, and many others. Finally, I would like to thank my family, my friends, and my cat.

The work in this thesis is supported by the Faculty Early Career Development Program of the National Science Foundation, under award numbers OCE-1751386 and OPP-2023244 (A. L. Stewart), and awards OCE-2048590 and OPP-1643445 (I. Eisenman). The work is partially supported by the China Scholarship Council Fellowship and the UCLA Dissertation Year Fellowship. This work used the Extreme Science and Engineering Discovery Environment (XSEDE, [Towns et al., 2014](#)) supported by National Science Foundation grant number ACI-1548562 (A. L. Stewart) and the Hoffman2 Cluster supported by the IDRE Research Technology Group at UCLA. We thank the MITgcm team for their contribution to numerical modeling, and for making their code available.

VITA

- 2020 M.S. in Atmospheric and Oceanic Sciences. Department of Atmospheric and Oceanic Sciences, UCLA.
- 2018 B.S. in Astronomy. School of Physics, Peking University.

PUBLICATIONS

Y. Si, A. L. Stewart, A. Silvano, and A. Naveira Garabato. Antarctic slope undercurrent and onshore heat transport driven by meltwater upwelling. *In prep.*

S. Spungin[†], **Y. Si**, and A. L. Stewart. Observed seasonality of mixed-layer eddies and vertical heat transport over the Antarctic continental shelf. *In prep.*

C. R. Schmidgall[†], **Y. Si**, A. L. Stewart, A. F. Thompson, and A. McC. Hogg. Dynamical controls on bottom water transport and transformation across the Antarctic Circumpolar Current. *Journal of Physical Oceanography*, 2023.

Y. Si, A. L. Stewart, and I. Eisenman. Heat transport across the Antarctic Slope Front controlled by cross-slope salinity gradients. *Science Advances*, 2023.

A. Silvano, P. Holland, K. Naughten, O. Dragomir, P. Dutrieux, A. Jenkins, **Y. Si**, A. L. Stewart, B. Pena-Molino, G. Janzing, T. Dotto, and A. C. Naveira Garabato. Baroclinic ocean response to

[†]Student Advisees

climate forcing regulates decadal variability of ice-shelf melting in the Amundsen Sea. *Geophysical Research Letters*, 2022.

Y. Si, A. L. Stewart, and I. Eisenman. Coupled ocean/sea ice dynamics of the Antarctic Slope Current driven by topographic eddy suppression and sea ice momentum redistribution. *Journal of Physical Oceanography*, 2022.

Y. Si, J. Yang, and Y. Liu. Planetary climate under extremely high vertical diffusivity. *Astronomy & Astrophysics*, 2022.

CHAPTER 1

Introduction

1.1 Background

The Antarctic Slope Front (ASF) is a strong gradient in ocean temperature and salinity around the Antarctic margins, separating the cold shelf water from the warm Circumpolar Deep Water (CDW). There is a narrow and swift westward ocean current over the Antarctic continental slope, known as the Antarctic Slope Current (ASC). The ASF/ASC system forms a strong barrier to exchanges such as heat, freshwater, and nutrients between the continental shelf and the open ocean (Jacobs, 1991; Whitworth et al., 1998; Heywood et al., 2014). In the region where the ASC is weaker, warm water is able to flood the shelf, leading to enhanced melting of ice shelves in West Antarctica (Thompson et al., 2018), with implications for destabilization of the West Antarctica Ice Sheets and global sea level rise. The dense water export across the ASF drives global overturning circulation (Marshall and Speer, 2012) and is shown to play an important role in driving warm water toward the Antarctic glaciers (Stewart and Thompson, 2016; Morrison et al., 2020). Therefore, understanding the circulation and exchanges near the Antarctic margins is critical for predicting future climate change.

There are various drivers that affect the circulation and variability near the Antarctic margins. Wind and buoyancy forcing have historically been recognized as key drivers of the ASC (e.g., Jacobs, 1991; Whitworth et al., 1998; Nøst et al., 2011; Hattermann, 2018), as they play an important role in the overturning circulation and cross-slope transport. Recently there are mounting studies that emphasize the role of small-scale and/or high-frequency variability in the cross-slope heat and water mass exchanges, such as mesoscale eddies, tides, dense outflows, and shelf waves (e.g.,

[Thompson et al., 2018](#); [Heywood et al., 2014](#)).

Despite the significance to Earth's climate system, the circulation and heat transport around the Antarctic margins remain poorly understood due to the difficulties and expense in observation and modeling. The environmental conditions around Antarctica create difficulties in making measurements, and therefore limit the dynamical insight available directly from observations, especially in the regions covered by sea ice and floating ice shelves ([Thompson et al., 2018](#)). In addition, previous studies indicate that a very high horizontal resolution of 1~2 km is required to fully resolve the small-scale processes over the continental shelf and slope in the polar regions, such as mesoscale eddies and slope waves (e.g., [Hallberg, 2013](#); [St-Laurent et al., 2013](#); [Nakayama et al., 2014c](#); [Stewart and Thompson, 2015](#)), which creates difficulties for modeling. Global models are not available at such a high resolution due to the huge amount of data and computational cost. Therefore, the ocean community tends to develop high-resolution process-oriented models to understand the dynamics of the ASC.

The work in this dissertation seeks to provide a better understanding of the dynamical processes of the ASC/ASF system and ice-ocean interactions around the Antarctic margins. In particular, we are interested in the following science questions: **(i)** How is the momentum input from the winds mediated by sea ice, tidal forcing, and transient eddies in the ASC (Chapter 2)? **(ii)** Will additional meltwater enhance shoreward heat transport, leading to a positive feedback in a warming climate, or further isolate the continental shelves from the open ocean heat, leading to a negative feedback (Chapter 3)? **(iii)** What drives the slope undercurrent and onshore heat transport in West Antarctica (Chapter 4)?

1.2 Outline

In the rest of this section, we provide an overview of the studies in Chapters 2-4. We summarize this dissertation and discuss the open science questions for future work in Chapter 5.

1.2.1 Coupled ice-ocean dynamics of the Antarctic Slope Current

The ASC has historically been understood as a wind-driven circulation. In previous studies, the momentum transfer from the wind to the sea ice and ocean in the ASC was assumed as follows (Nøst et al., 2011; Stewart and Thompson, 2013; Huneke et al., 2019): The wind injects momentum into the sea ice and drives the ice flow westward; then the sea ice accelerates the ocean through ice-ocean stress; the momentum is vertically transferred within the ocean via isopycnal form stress and is finally transferred to the seafloor. This concept is drawn from the literature on the Antarctic Circumpolar Current (e.g., Vallis, 2017). However, Stewart et al. (2019) indicated that this simple assumption may be incorrect. They have found that the westward ice-ocean stress vanishes or is even directed eastward in the core of the ASC, and they attributed the vanishing of ice-ocean momentum transfer to the acceleration of the ASC by strong tidal momentum advection.

In Chapter 2, we investigate the momentum balance of the ice-ocean system in the ASC using a high-resolution process model with coupled ocean and sea ice. Consistent with Stewart et al. (2019), the ocean surface velocity matches the sea ice velocity in the core of the ASC, and the ice-ocean momentum transfer is diminished over the slope. With the aid of a reduced-order model, it is revealed that the fundamental reason for the vanishing of ice-ocean momentum transfer over the slope is the suppression of eddies by the strong topographic vorticity gradient, and therefore almost no momentum is transferred vertically via isopycnal form stress. Over the continental shelf break, tidal acceleration reduces the ice-ocean stress, but the ice-ocean stress does not necessarily approach zero even with the appearance of tides. Sea ice plays a critical role in horizontally redistributing the wind-input momentum away from the slope. The implication of this study is that sea ice can not just be thought of as a forcing for the ocean or vice-versa: The circulations of ocean and sea ice are intrinsically linked and must be understood together.

1.2.2 Positive feedback of eddy-driven ocean heat transport toward the Antarctic margins

Previous studies based on relatively low-resolution models have reported contradictory findings regarding the impact of additional meltwater on heat transport toward the Antarctic continental

shelf. Using coarse-resolution climate models, previous studies suggested that additional meltwater increases ocean stratification, trapping heat in the subsurface and increasing melting at glacial grounding lines (Golledge et al., 2019; Bronselaer et al., 2018; Schloesser et al., 2019; Sadai et al., 2020; Fogwill et al., 2015). Using a 0.1° -resolution global ocean-sea ice model, Moorman et al. (2020) indicated that coastal freshening tends to isolate the continental shelves from heat. Lockwood et al. (2021) found that the representation of the ASC and ASF in different models is the key to explaining the differences between CM2.6 (0.1° resolution) and coarse-resolution CMIP5 models: In high-resolution models, the enhanced meltwater input under global warming is restricted to the shelf region by the ASF; While in low-resolution models, freshwater spreads to the open ocean and increases open-ocean stratification in the absence of the ASF. It remains unclear whether meltwater enhances shoreward heat transport, leading to a positive feedback, or further isolates the continental shelf from the open ocean heat.

In Chapter 3, we investigate the control of heat transport across the ASF using high-resolution process-oriented simulations that are able to resolve eddies and barotropic tides on the shelf and slope. It is found that the heat transferred onto the continental shelf is strongly influenced by the cross-slope salinity gradient. In particular, the key result is that coastal freshening leads to enhanced onshore heat transport driven by mesoscale eddies; previous studies could not resolve these eddies and thus could not represent this mechanism. The findings indicate a positive feedback in a warming climate: Large volumes of meltwater may enhance onshore heat transport, leading to further melt of ice shelves.

1.2.3 Melt-driven undercurrent and the positive circulation-melt feedback in West Antarctica

Due to ocean-driven basal melt, the most rapid Antarctic ice-shelf thinning and iceberg calving are detected in the Amundsen Sea of West Antarctica (Paolo et al., 2015; Liu et al., 2015; Rignot et al., 2013; Pritchard et al., 2012). Observations and numerical models have suggested that the variations in the Amundsen Sea ice shelf melt are linked to the Antarctic slope undercurrent, which is an eastward, subsurface current that opposes the direction of surface winds (e.g., Silvano et al.,

2022; Kimura et al., 2017; Walker et al., 2013; Azaneu et al., 2023). When encountering submarine troughs, the undercurrent transports warm Circumpolar Deep Water (CDW) directly toward ice shelf cavities (Walker et al., 2013), driving strong basal melt and retreat of the grounding line. This reduces the ability of ice shelves to buttress the flow of the ice sheet into the ocean (Gudmundsson et al., 2019), which will potentially cause a complete collapse of the West Antarctic Ice Sheet in the future (Joughin et al., 2021; Joughin and Alley, 2011), leading to sea-level rise (DeConto et al., 2021). To accurately predict the future of the West Antarctic Ice Sheet and global sea-level rise, it is essential to understand the formation mechanisms of the undercurrents and the feedback between undercurrent and ice shelf melt. However, it remains poorly understood what drives the undercurrent and thus what controls the mean heat transport toward West Antarctic glaciers.

In Chapter 4, we investigate the formation mechanisms of the undercurrents and the feedback between undercurrent and ice shelf melt using a process model with coupled ocean, sea ice, and ice shelf components. We close the scientific gap by analyzing the vorticity budget of the CDW layer. It is found that the undercurrent is driven by cyclonic vorticity input from meltwater upwelling in the ice shelf cavity. Increased basal melt therefore strengthens the undercurrent and enhances onshore CDW transport, which indicates another previously unrecognized positive feedback that may accelerate future melt of ice shelves, potentially further destabilizing the West Antarctic Ice Sheet.

CHAPTER 2

Coupled ocean/sea ice dynamics of the Antarctic Slope Current driven by topographic eddy suppression and sea ice momentum redistribution

This chapter contains the manuscript by Y. Si, A. L. Stewart, and I. Eisenman, published in the Journal of Physical Oceanography in 2022 ([Si et al., 2022](#)).

Abstract

The Antarctic Slope Current (ASC) plays a central role in redistributing water masses, sea ice, and tracer properties around the Antarctic margins, and in mediating cross-slope exchanges. While the ASC has historically been understood as a wind-driven circulation, recent studies have highlighted important momentum transfers due to mesoscale eddies and tidal flows. Furthermore, momentum input due to wind stress is transferred through sea ice to the ASC during most of the year, yet previous studies have typically considered the circulations of the ocean and sea ice independently. Thus it remains unclear how the momentum input from the winds is mediated by sea ice, tidal forcing, and transient eddies in the ocean, and how the resulting momentum transfers serve to structure the ASC. In this study the dynamics of the coupled ocean/sea ice ASC circulation are investigated using high-resolution process-oriented simulations, and interpreted with the aid of a reduced-order model. In almost all simulations considered here, sea ice redistributes almost 100% of the wind stress away from the continental slope, resulting in approximately identical sea ice and ocean surface flows in the core of the ASC in a fully spun-up equilibrium state. This ice-ocean coupling results from suppression of vertical momentum transfer by mesoscale eddies over the

continental slope, which allows the sea ice to accelerate the ocean surface flow until the speeds coincide. Tidal acceleration of the along-slope flow exaggerates this effect, and may even result in ocean-to-ice momentum transfer. The implications of these findings for along- and across-slope transport of water masses and sea ice around Antarctica are discussed.

2.1 Introduction

The Antarctic Slope Current (ASC) is a westward narrow and swift circulation that surrounds the Antarctic margins. The ASC is important for the climate system and biogeochemistry, as it forms a barrier for the cross-slope exchanges such as heat, freshwater, nutrients and biota between the Antarctic continental shelf and the open ocean (Jacobs, 1991; Whitworth et al., 1998; Heywood et al., 2014). Fig. 2.1d shows the winter climatology of sea surface elevation, with the ASC sketched by the gray arrow. In the regions where the ASC is weaker (denoted by the dashed gray arrow in Fig. 2.1d), warm deep water is able to intrude onto the continental shelf, causing enhanced melting of Antarctic ice shelves (Thompson et al., 2018). The zonal flow of the ASC is an important conduit for the transport of water masses, tracers, sea ice and icebergs around Antarctica (Heywood et al., 1998; Stern et al., 2016).

The surface winds close to the Antarctic margins are mostly parallel to the coastline and directed westward all year round (Powers et al., 2003, 2012; Hazel and Stewart, 2019), with speeds that decrease offshore and drive shoreward Ekman transport (Gill, 1973; Heywood et al., 2014). These winds play an important role in the overturning circulation and cross-slope transport near the continental shelf and slope (Stewart and Thompson, 2013, 2015; Goddard et al., 2017). As a main source of momentum input to the ice and ocean system, surface wind stress has been suggested as having a leading-order impact on the mean transport and seasonal and interannual variability of the ASC (Mathiot et al., 2011; Armitage et al., 2018; Naveira Garabato et al., 2019). The winter zonal wind speed is shown in Fig. 2.1a. In addition to winds, buoyancy forcing has been regarded as an important driver of the ASC (Hattermann, 2018; Thompson et al., 2020). Using a high-resolution global ocean-sea ice model, Moorman et al. (2020) have shown that the intensity and spatial pattern

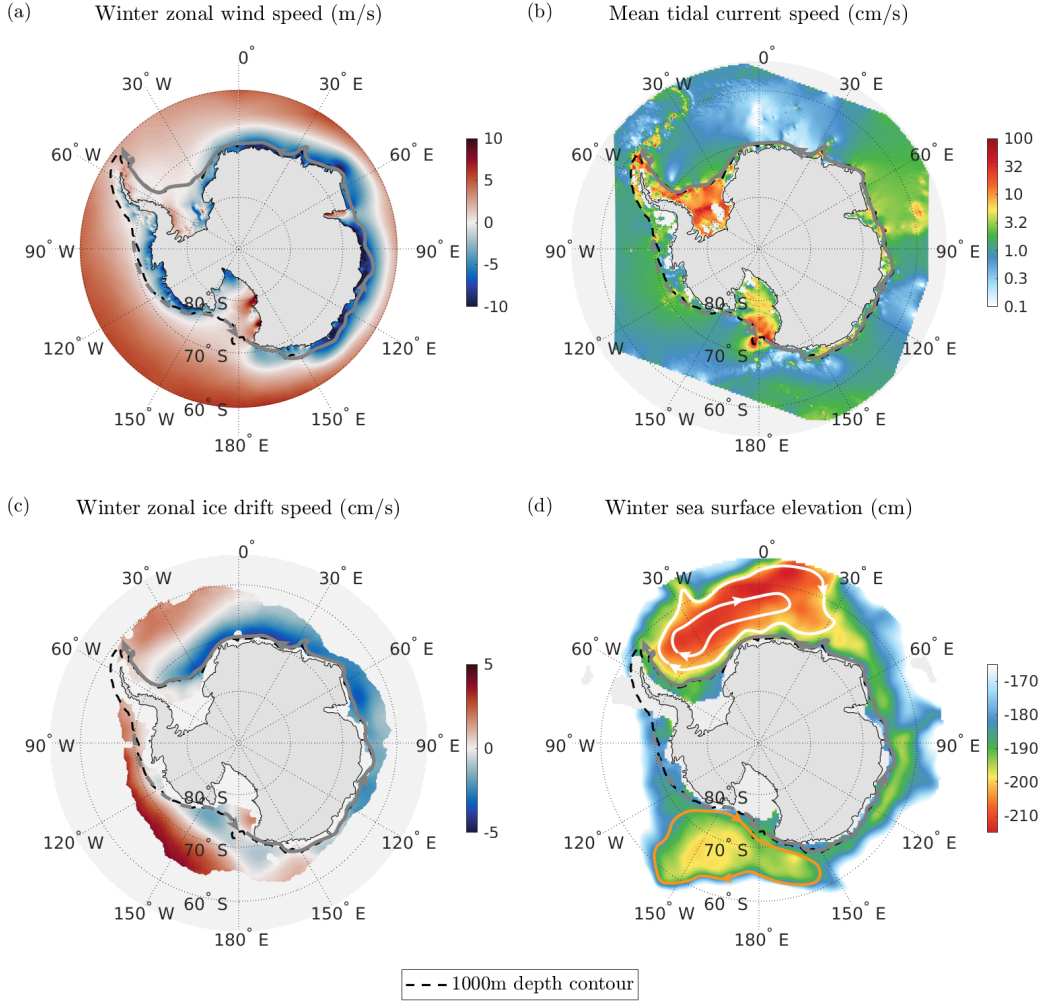


Figure 2.1: The observed external forcing of the sea ice-ocean system around the Antarctic margin, and the motion of the sea ice and the ocean in the Antarctic winter. (a) The winter (June, July, and August) climatology of zonal wind speed from 2007-2014, using the Antarctic Mesoscale Prediction System (AMPS) products ([Powers et al., 2003, 2012](#)). (b) The annual average of tidal current speed including ten major tidal constituents, calculated by the model CATS2008 ([Padman et al., 2002, 2008](#)). (c) The winter climatology of zonal ice drift speed from 1979-2015, using the product "Polar Pathfinder Daily 25 km EASE-Grid Sea Ice Motion Vectors, Version 3" ([Tschudi et al., 2016](#)). (d) The winter climatology of sea surface elevation using the Dynamic Ocean Topography (DOT) data ([Armitage et al., 2018](#)). The gray, white, and orange curved arrows denote the Antarctic Slope Current, the Weddell Gyre, and the Ross Gyre with their directions, respectively. The black dashed curve around the Antarctic continent represents the 1000-m isobath.

of the ASC are substantially modified by coastal freshening, as is projected to occur due to increased ice sheet melt over the coming centuries (Naughten et al., 2018). However, the role of buoyancy forcing in the ASC circulation is less well understood because the observations of buoyancy forcing near the Antarctic margins are spatially and temporally sparse.

Though wind and buoyancy forcings have historically been implicated as key drivers of the ASC (Jacobs, 1991; Whitworth et al., 1998), recent studies have increasingly suggested that high-frequency variability associated with eddies, tides and dense outflows may be critical to the along-slope circulation and cross-slope exchange (Thompson et al., 2018). Eddies are generated by barotropic and baroclinic instabilities of the ASC (Stewart and Thompson, 2016; Stewart et al., 2019), and vorticity conservation of dense outflows (Spall and Price, 1998; Wang et al., 2009). Previous studies have identified mesoscale eddies as a major contributor to the onshore transport of the circumpolar deep water (CDW) (Nøst et al., 2011; Thompson et al., 2014; Stewart and Thompson, 2015) and the offshore export of the Antarctic Bottom Water (AABW) (Wang et al., 2009; Nakayama et al., 2014a; Stewart and Thompson, 2015). Mesoscale eddies are also shown to produce rectified mean along-slope flows (McWilliams, 2008; Wang and Stewart, 2018; Cherian and Brink, 2018). Eddies may play a key role in the momentum balance of major current systems: the isopycnal form stress arising from transient and standing eddies is the primary mechanism of vertical momentum transfer in the Southern Ocean (Tréguier and McWilliams, 1990; Masich et al., 2018). We might expect similar dynamics to take place in the ASC. However, over the continental slope the tracer transport and momentum fluxes carried by mesoscale eddies are greatly reduced, because the baroclinic instability may be suppressed by topographic vorticity gradient (Blumsack and Gierasch, 1972; Isachsen, 2011; Hetland, 2017). The suppression of eddy fluxes over the slope has been invoked to explain the “V-shaped” isopycnals of the Antarctic Slope Front (ASF) in the AABW formation region (Stewart and Thompson, 2013). Yet it is still unclear how eddies mediate momentum input due to wind stress in the ASC under sea ice cover.

In addition to mesoscale eddies, tides are key contributors to the circulation around Antarctic margins (Thompson et al., 2018), and have an impact on water mass exchange and transformation (Muench et al., 2009; Holland et al., 2014; Fer et al., 2016). Fig. 2.1b shows the mean tidal current

speed, highlighting the enhanced tidal current in the Weddell Sea and the Ross Sea, and over the continental shelf break (close to the 1000 m depth contour). There have been many investigations of the mean along-slope circulation generated by non-linear interaction between tides and sloping bathymetry (e.g., [Robinson, 1981](#); [Loder, 1980](#); [Garreau and Maze, 1992](#)), implying that the tidally induced along-slope current increases with stronger stratification ([Chen and Beardsley, 1995](#); [Brink, 2011](#)) and steeper bottom bathymetry ([Loder, 1980](#); [Kowalik and Proshutinsky, 1995](#); [Brink, 2010](#)). [Huthnance \(1973\)](#) suggests that the combination of continuity and the Coriolis effects accumulates along-slope momentum, developing residual along-slope current. The bottom drag associated with this residual along-slope current balances the momentum input from tides. Using the vorticity approach, [Robinson \(1981\)](#) shows that tidal oscillations advect positive and negative vorticity to opposite directions, generating residual along-slope circulation. Other previous studies such as [Garreau and Maze \(1992\)](#) also show that the nonlinear dynamics associated with the fluctuating flow act to redistribute momentum in an inviscid ocean. Increasing evidence shows that tidal rectification may be critical to driving the ASC ([Flexas et al., 2015](#); [Stewart et al., 2019](#)), reproducing the cross-slope structure and time variability of ASF/ASC. [Stewart et al. \(2019\)](#) have highlighted the interaction between tidal flows and sea ice cover for the circulation and overturning of the ASC. They found that the westward ice-ocean stress vanishes or is even directed eastward in the core of the ASC, possibly due to the acceleration of the ASC by strong tidal momentum advection. These studies imply that models without tides are not likely to correctly represent the geometry, state, or the momentum balance of the ASC.

There have been studies of the interactions between the ASC and sea ice melt/formation ([Nicholls et al., 2009](#); [Bull et al., 2021](#)), but the circulation of sea ice within the ASC and the role of sea ice in the ASC momentum budget have received little attention previously. Fig. 2.1c shows the measured winter climatology of zonal sea ice drift speed. Sea ice drifts westward in most of the ASC, which is in consistent with the direction of the zonal wind (Fig. 2.1a). In most sectors Antarctic sea ice drift is largely controlled by local wind forcing ([Holland and Kwok, 2012](#); [Barth et al., 2015](#)). However, close to the coastline or in regions with convergent sea ice motion, where ice internal stresses are large, the correlation between wind and sea ice motion is very low ([Holland and Kwok, 2012](#)).

This suggests that the sea ice drift in the ASC may be affected by other processes, such as tides and buoyancy gradients in the ocean. Note that weak wind/drift correlations may also be expected in regions with nearly static sea ice. Previous studies indicate that the buoyancy gradient in the ocean may play a role in Antarctic sea ice expansion (e.g., [Bintanja et al., 2013](#)). However, how buoyancy gradients directly affect the circulation and momentum balance of the sea ice remains unknown. As the ASC is covered by sea ice throughout most of the year, sea ice can modulate the momentum transfer between the atmosphere and the surface ocean when the ASC lies beneath sea ice ([Thompson et al., 2018](#)). The surface momentum transfer is traditionally parameterized using the quadratic drag laws. Recent studies indicate that the parameterization depends on ice morphology ([Lüpkes et al., 2012](#)) and edge-related turbulence ([Lüpkes and Grynk, 2015](#)), and the magnitude of momentum transfer in model simulations differs depending on the choices of surface stress formulation (e.g., [Le Pail et al., 2020](#)).

Though there have been numerous studies of how the ASC is driven by winds, eddies, tides, and buoyancy gradients, these studies have largely considered the circulations of the ocean and sea ice independently. It remains poorly understood how the strength and structure of the coupled ocean and sea ice ASC circulation is established by its various drivers. In this study we explore the momentum transfer in the wind-sea ice-ASC system by a suite of experiments with a three-dimensional (3D) high-resolution process-oriented model. In Section 2.2, we introduce the 3D model configuration, experimental parameters and model evaluation. In Section 2.3, we use a suite of experiments to identify key controls on the along-slope ice/ocean circulation and transport. The surface ocean and sea ice speeds coincide in the core of the ASC across almost the entire range of experimental parameters, so in Section 2.4 we investigate this phenomenon using the momentum balance. We show that in the core of the ASC, sea ice horizontally redistributes momentum to the continental shelf and open ocean, while downward eddy momentum transfer is suppressed. In Section 2.5 we construct a reduced-order model of the ASC to isolate and identify the contributions of tides and eddies to the momentum balance and the ocean/sea ice circulation. Finally, we summarize the results and discuss the caveats and the implications in section 2.6.

2.2 Model configuration

In this section we describe the process-oriented model, including the choices that we made to configure the model, the rationale for parameter selection and the model evaluation. [Thompson et al. \(2018\)](#) have identified three major ASC regimes with different circulation and frontal structures: (a) fresh shelf and (b) dense shelf based on whether there is water denser than $\gamma^n = 28.0 \text{ kg/m}^3$ on the shelf, and (c) warm shelf where ocean temperature at the seafloor of the continental shelf is 2–3°C warmer than the freezing temperature. Either “fresh shelf” or “dense shelf” has cold shelf water, and γ^n is the neutral density. In this study we focus on the “fresh shelf” and “dense shelf” regimes and use “fresh shelf” as a the reference case to explore parameter dependencies, because fresh shelf occupies the largest fraction of the continental shelf break around Antarctica. In only one experiment with no easterly winds, we touch upon a “warm shelf”-like regime with warm deep water intrusion onto the shelf, though the southernmost of the shelf is restored to the freezing temperature. We use winter-like sea ice conditions for all the simulations because these conditions are representative of more than 8 months of the year (excluding summer and early autumn in Antarctica) in most of the ASC ([Holland, 2014](#); [Stewart et al., 2019](#)).

This model is developed based on the Massachusetts Institute of Technology General Circulation Model (hereafter the MITgcm, [Marshall et al., 1997a,b](#)). We configure the ocean component of this model with the hydrostatic Boussinesq equations and high-order polynomials for the equation of state ([McDougall et al., 2003](#)). The sea ice component of this model includes ridging, formation of frazil ice and leads, and has been described in detail by [Losch et al. \(2010\)](#). The sea ice dynamics and thermodynamics are based on [Hibler \(1979, 1980\)](#) and [Winton \(2000\)](#). We choose viscous-plastic ice rheology ([Hibler, 1979](#)), the Line Successive Relaxation (LSR) sea ice solver ([Losch et al., 2014](#)) and seven thickness categories for ice thermodynamics.

Fig. 2.2 summarizes the configuration of this process-oriented model, and the key parameters used in the simulations are listed in Table 2.1. The MITgcm has been configured into a 450 km (across-slope, meridional) by 400 km (along-slope, zonal) by 4000 m (depth) domain with horizontal grid spacing of 1 km. As revealed by previous modelling studies (e.g., [St-Laurent et al.,](#)

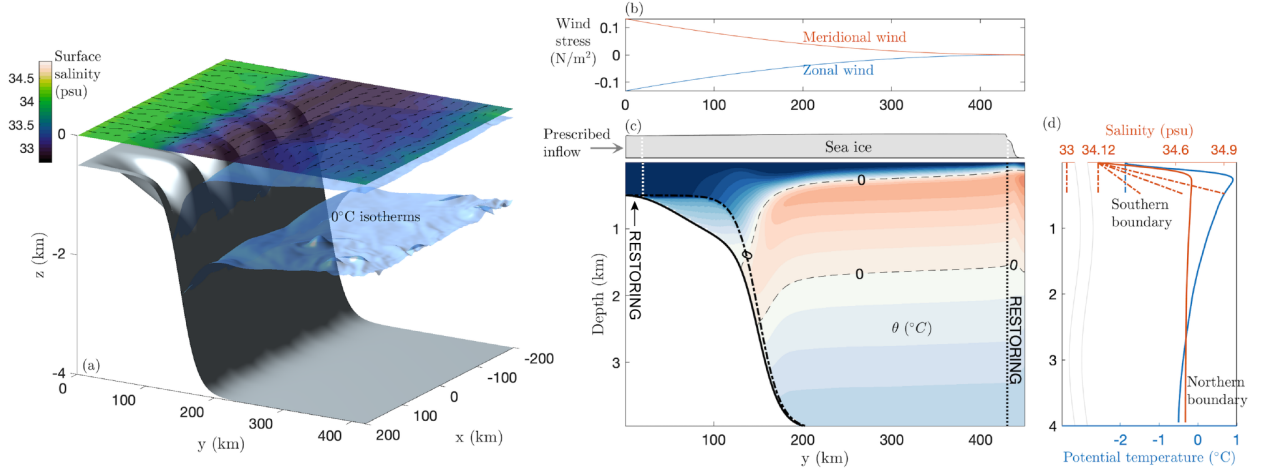


Figure 2.2: Illustration of the MITgcm Antarctic Slope Front process model (MITgcm ASF) setup. (a) Model bathymetry, snapshot of sea surface salinity (colors), surface ocean currents (arrows), and 0°C isotherms. (b) The steady along- and across-slope wind forcing used in the reference simulation. (c) Time- and zonal-mean sea ice thickness (the gray box, which is exaggerated) and potential temperature (the contour plot, plotted at intervals of 0.13°C) in the reference simulation. The thick dashed and solid black curves show the shallowest and deepest of the bathymetric contours, respectively. At the southern and northern boundaries, temperature and salinity are restored to the reference profiles across sponge layers of 20 km width. (d) The relaxation salinity (orange) and temperature (blue) profiles of the sponge layers. The northern boundary restoring (solid lines) is based on hydrography taken from the sections across the Antarctic Slope Front at Kapp Norvegia (Hattermann, 2018). The southern boundary restoring temperature and salinity are denoted by the dashed lines.

Param.	Value	Description
L_x	400 km	Zonal domain size
L_y	450 km	Meridional domain size
H	4000 m	Maximum ocean depth
H_{shelf}	500 m	Continental shelf depth
Y_s	150 km	Meridional slope position
Z_s	2250 m	Vertical slope position
H_{trough}	300 m	Depth of the troughs
W_{trough}	50 km	Width of the troughs
Y_{trough}	0 km	Southern edge of the trough
L_r	20 km	Thickness of sponge layers
T_o^{in}	10 days	Inner relaxation timescale for ocean
T_o^{out}	43200 s	Outer relaxation timescale for ocean
T_i^{in}	86400 s	Inner relaxation timescale for sea ice
T_i^{out}	7200 s	Outer relaxation timescale for sea ice
T_{tide}	43200 s	Tidal period
f_0	$-1.3 \times 10^{-4} \text{ s}^{-1}$	Reference Coriolis parameter
β	$1 \times 10^{-11} (\text{ms})^{-1}$	Rossby parameter
T_{south}	-1.87°C	Ocean temperature at the southern boundary
C_{ao}	1×10^{-3}	Air-ocean drag coefficient
C_{ai}	2×10^{-3}	Air-ice drag coefficient
C_{io}	5.54×10^{-3}	Ice-ocean drag coefficient
C_d	2×10^{-3}	Quadratic bottom-drag coefficient
A_i	1	Sea ice concentration
S_i	6 psu	Sea ice salinity
ϕ_{fr}	0.3	Salinity retention fraction on freezing
ϕ_{fi}	0.01	Frazil to sea ice conversion rate
T_a	-10°C	Surface (2m) air temperature
Q_a	5.7 g kg^{-1}	Surface (2m) specific humidity
F_{w0}	324 W m^{-2}	Reference downward longwave radiation
A_v	$3 \times 10^{-4} \text{ m}^2 \text{s}^{-1}$	Vertical eddy viscosity
$A_{4\text{grid}}$	0.1	Grid dependent biharmonic viscosity
κ_v	$1 \times 10^{-5} \text{ m}^2 \text{s}^{-1}$	Vertical diffusivity
$\kappa_{4\text{grid}}$	0.1	Grid dependent biharmonic diffusivity
Δ_x, Δ_y	1 km	Horizontal grid spacing
Δ_z	10.5-103.8 m	Vertical grid spacing
Δ_t	80-100 s	Time step

Table 2.1: List of parameters used in the experiments.

2013; [Stewart and Thompson, 2015](#)), high horizontal resolution (in the order of 1 km) is required to resolve mesoscale eddies over the continental shelf and slope. The vertical grid of the ocean is comprised of 70 geopotential levels with spacing ranging from 10 m at the surface to 100 m at the seafloor. The model has a re-entrant channel in the along-slope direction, with open boundary conditions applied to the onshore (southern) and offshore (northern) boundaries, which is needed to impose tidal flows with realistic amplitudes in this relatively small model domain. The horizontal dimensions of this domain ensure that the mesoscale eddies generated at the open boundaries and re-entering from the other side of the domain do not have a large impact on the slope current, while limiting the computational cost. Previous studies using eddy-resolving process models of the ASC such as [Stewart and Thompson \(2015, 2016\)](#) have used a comparable domain. We add four 50 km-wide troughs to the hyperbolic tangent-shaped bathymetry (Fig. 2.2a) based on the fact that the Antarctic continental shelf and slope are punctuated by canyons, and that their presence allows topographic form stress to serve as a sink of momentum at the seafloor ([Bai et al., 2021](#)). Without submarine troughs, the large wind-input momentum on the shelf must be balanced by bottom frictional stress, which requires an unrealistically large bottom drag coefficient ([Stewart and Thompson, 2016](#)). The depth and width of the troughs are selected based on observations (e.g., [NOAA National Geophysical Data Center, 2009](#)), and the reference slope steepness is typical of the Antarctic continental slopes ([NOAA National Geophysical Data Center, 2009](#); [Amante and Eakins, 2009](#)). The full formulation of the model bathymetry is given in Appendix C.

In our experimental configuration we aim to approximately control the sea ice thickness, which is set by an inflow at the southern boundary, while permitting the sea ice to evolve freely in response to mechanical interactions with the atmosphere and ocean. To achieve this, we force the model at the surface using a fixed atmospheric state, with air-ice momentum and thermodynamic fluxes computed via standard bulk formulae. The magnitudes of the zonal and meridional wind speeds decrease linearly offshore (northward, Fig. 2.2b), which is consistent with observations (Fig. 2.1a, also [Hazel and Stewart, 2019](#)). The remaining atmospheric properties are configured in such a way as to minimize the net air-ice thermodynamic fluxes, and thereby preserve a relatively uniform, winter-like sea ice cover. Specifically, the downward shortwave radiation is set zero to simulate

winter conditions, and precipitation is set to zero for simplicity. The surface 2m air temperature (-10°C), humidity (5.7 g kg⁻¹), and downward longwave radiative forcing are horizontally uniform. Note that the air temperature and ice surface temperature (described below) are warmer than typical winter conditions, but they have little impact on the results because the sea ice concentration is approximately 100% in all simulations performed in this study, so our results should be insensitive to such choices as long as the net air-ice energy flux remains close to zero. In our simulations, sea ice surface temperature is warmer than the saltwater freezing temperature and doesn't change much in different simulations. Thinner sea ice loses more heat to the ocean via downward conductive heat flux, because the strength of heat conduction is inversely proportional to ice thickness. Therefore, we prescribe a slightly larger downward longwave radiative forcing ($F_{\text{lw}}^{\text{down}}$) in experiments with thinner imposed sea ice to ensure that the sea ice thickness won't change much due to thermodynamic processes. We increase $F_{\text{lw}}^{\text{down}}$ from 324 to 341 Wm⁻² when the imposed ice thickness decreases from 1 to 0.2 m.

The tidal signal propagates westward around Antarctica as coastal-trapped waves (e.g., [Brink, 1991](#)). The associated rise and fall of sea surface elevation induces cross-slope barotropic tidal currents. As the coastal-trapped waves are typically much longer than our model domain (e.g., [Mysak, 1980](#)), tidal flows are generated via imposing a barotropic tidal current on the normal flow through the open northern and southern boundaries, which flow back and forth across the slope. The prescribed tidal currents at the boundaries are ([Loder, 1980](#); [Brink, 2011, 2013](#))

$$v_t \equiv A_{\text{tide}} \sin(\omega t), \text{ at } y = L_y, \quad (2.1a)$$

$$v_t \equiv A_{\text{tide}} \frac{H}{H_{\text{shelf}}} \sin(\omega t), \text{ at } y = 0, \quad (2.1b)$$

where $\omega = 2\pi/43200$ s is the tidal frequency, $L_y = 450$ km is the meridional domain size, $H = 4000$ m is the ocean depth at the northern boundary, and $H_{\text{shelf}} = 500$ m is the depth of the continental shelf at the southern boundary. The tidal period is set to 12 hours for simplicity, which is close to the period of the dominant tidal constituent (M_2 tide) in most locations. [Brink \(2011\)](#) has found that larger tidal frequency is associated with weaker along-slope rectified flow. Changing

tidal frequency also has an impact on the generation of internal tides and mixing (Lamb, 2014), which is not investigated in this study since we do not focus on overturning circulation and water mass formation. The tidal amplitude A_{tide} is selected empirically to produce tidal current speeds comparable to those found around Antarctic margins (Padman et al., 2002, also Fig. 2.1b). In the reference case, $A_{\text{tide}} = 0.05$ m/s at the northern boundary, so the corresponding barotropic tidal current amplitude is 0.4 m/s at the southern boundary (Fig. 2.2).

We use two 20-km-width sponge layers at the southern and northern boundaries to relax ice and ocean velocities, potential temperature, salinity, sea ice thickness and ice concentration towards the boundary values. The sponge layers impose a cross-slope buoyancy gradient, which is one of the control parameters in our simulations. The relaxation timescales decrease linearly with distance from the interior termination of the sponge layers towards the outermost boundaries. The relaxation timescales at the innermost and outermost points of the sponge layers are listed in Table 2.1.

The sea ice concentration near the coastline of East Antarctica is close to 100% in winter (Zwally et al., 2002; Zhang and Rothrock, 2003; Stewart et al., 2019) and the thickness is around 1 m (Worby et al., 2008; Zhang and Rothrock, 2003), so in the reference case we set the southern boundary sea ice thickness and concentration to 1 m, and 100%, respectively. We prescribe inflow of sea ice through the southern boundary based on the free-drift assumption, because this is the simplest possible choice. Under this assumption, the Coriolis force felt by the sea ice balances the air-ice stress and the ice-ocean stress, so we can solve for the sea ice velocities ($U_{\text{i}0}$ and $V_{\text{i}0}$) for given wind speeds ($U_{\text{a}0}$ and $V_{\text{a}0}$) at the southern boundary:

$$-\rho_{\text{i}}H_{\text{i}0}f_0V_{\text{i}0} = \rho_{\text{a}}C_{\text{ai}}\sqrt{U_{\text{a}0}^2 + V_{\text{a}0}^2}U_{\text{a}0} - \rho_{\text{o}}C_{\text{io}}\sqrt{U_{\text{i}0}^2 + V_{\text{i}0}^2}U_{\text{i}0}, \quad (2.2\text{a})$$

$$\rho_{\text{i}}H_{\text{i}0}f_0U_{\text{i}0} = \rho_{\text{a}}C_{\text{ai}}\sqrt{U_{\text{a}0}^2 + V_{\text{a}0}^2}V_{\text{a}0} - \rho_{\text{o}}C_{\text{io}}\sqrt{U_{\text{i}0}^2 + V_{\text{i}0}^2}V_{\text{i}0}, \quad (2.2\text{b})$$

The descriptions and values of the parameters in Eq. 2.2 are listed in Table 2.1 and Table 2.2. At the southern boundary, we fix the sea ice velocities to $U_{\text{i}0}$ and $V_{\text{i}0}$ based on the solutions with different wind speeds and sea ice thickness. Given sea ice thickness at the southern boundary $H_{\text{i}0} = 1$ m, for the reference wind speed $U_{\text{a}0} = -6$ m/s and $V_{\text{a}0} = 6$ m/s, the solutions are $U_{\text{i}0} = -0.14$ m/s and

$V_{i0} = 0.11$ m/s. We impose both zonal and meridional winds instead of imposing zonal wind only because this is more relevant to observations (e.g., Fig. 1 of [Hazel and Stewart, 2019](#)). In addition, if there is no northward meridional wind and thus no northward sea ice inflow, sea ice would drift southward and pile up at the southern boundary due to the Ekman transport associated with the westward zonal wind, resulting in no sea ice cover over the slope and deep ocean. In this case, the slope current would be too strong because of the strong air-ocean stress; deep convection would occur because the ocean surface is directly exposed to the cold atmosphere. Therefore, we impose meridional wind and northward sea ice drift speed associated with the winds to help maintain sea ice cover over the entire domain.

Param.	Value	Description
A_{tide}	0, 0.025, 0.05 , 0.075, 0.1 m s ⁻¹	Tidal current amplitude at the northern boundary
U_{a0}	-8, -6, -4, 0 m s ⁻¹	Eastward wind speed at the southern boundary
V_{a0}	4, 6, 8, 12 m s ⁻¹	Northward wind speed at the southern boundary
h_{i0}	0.2, 0.6, 1.0 , 1.4, 1.8, 2.2 m	Sea ice thickness at the southern boundary
$\Delta\sigma_4$	-1.076, -0.620, -0.207 , 0, 0.204, 0.409 kg m ⁻³	Ocean bottom potential density difference between the northern and the southern boundaries, with a reference pressure of 4000 dbar
W_s	50 , 100, 150, 200, 250 km	Continental slope width
Δ_x, Δ_y	1, 2, 5, 10 km	Horizontal grid spacing

Table 2.2: List of parameters varied among the experiments. The bold fonts denote the values used in the reference simulation. When varying continental slope width W_s , the corresponding meridional slope position Y_s is **150**, 175, 200, 225, and 250 km, respectively. Note that varying $\Delta\sigma_4$ is achieved by varying the restoring salinity profiles at the southern boundary. In those simulations, the salinity difference between the northern and the southern boundaries at depth $z = 500$ m are -1.695, -1.108, **-0.578**, -0.315, -0.053, 0.210 psu, respectively (Fig. 2.2d).

Initially the sea ice and the ocean are stationary, with ocean temperature and salinity in the interior equal the restoring values at the northern boundary. To reduce computational cost, we start each simulation with a 10-year integration at low resolution (2 km horizontal grid spacing and 30 vertical levels) until it has reached a steady state, then initialize the high-resolution simulations from the corresponding low-resolution simulations. Each high-resolution simulation (1 km horizontal grid spacing and 70 vertical levels) is run for a further 10 years, with a 5-year spin-up and a 5-year

analysis period.

Seven model parameters are varied: tidal current amplitude, zonal and horizontal wind speeds, southern boundary sea ice thickness, offshore buoyancy gradient, slope width, and horizontal grid spacing. We independently vary each parameter about the reference values (Table 2.2), and select the range of the parameters based on typical values in the observations. We use $\Delta\sigma_4$, which is the ocean bottom potential density difference between the northern and the southern boundaries with a reference pressure of 4000 dbar, to quantify the offshore buoyancy gradient. Hence the cases with positive $\Delta\sigma_4$ permit bottom water formation. The cases with relatively fresh continental shelves have vertically uniform salinity profiles at the southern boundary (Fig. 2.2d), varying from 33.00 to 34.12 psu ($\Delta\sigma_4$ changes from -1.076 to -0.207 kg m^{-3} in Table 2.2). In the cases named $\Delta\sigma_4 = 0, 0.204, 0.409 \text{ kg m}^{-3}$, the salinity equals 34.17 psu at the sea surface at the southern boundary, and increases linearly with depth (Fig. 2.2d). We need to improve the LSR solver accuracy and increase the number of LSR iterations for the very dense shelf case ($\Delta\sigma_4 = 0.409 \text{ kg m}^{-3}$) to avoid large imbalance in the sea ice momentum budget over the continental shelf. For all simulations considered in this study, the relaxation temperature at the southern boundary is the freezing temperature (Fig. 2.2d, Table 2.1).

We evaluate the model by comparing a cross section of ice and ocean properties in the reference simulation with the hydrography taken in East Antarctica (Fig. 2.3) during the “BROKE West” survey ([Rosenberg and Gorton, 2019](#)). We use a summer measurement to evaluate the model because the winter observations are sparse. Some quantitative differences are expected due to the use of summer observations. In general, this idealized reference simulation captures the key features of hydrography and slope current observed in the East Antarctica, with isopycnals incropping at the surface of the continental slope and a westward slope current. Note that the simulation does not aim to closely match the observations, because the bathymetry, boundary conditions, surface forcing and tidal forcing are idealized. Since the hydrography was taken in the Antarctic summer, a thin layer of surface warm water, and a layer of relatively colder Winter Water underneath are observed (Fig. 2.3g). Compared with the observations, the reference simulation has a colder and fresher southern boundary, thus a larger offshore buoyancy gradient near the continental slope (Fig. 2.3d,

e). The isopycnals connecting to the continental slope are steeper in the model which gives rise to a stronger subsurface-intensified along-slope current (Fig. 2.3f). The model reproduces the key finding of [Stewart et al. \(2019\)](#) with ocean surface velocity approximately matching that of the sea ice (Fig. 2.3c) over the slope, implying that the sea ice and ocean circulations are tightly linked at the core of the ASC. Note that all the conclusions drawn in this study are based on 100% sea ice cover.

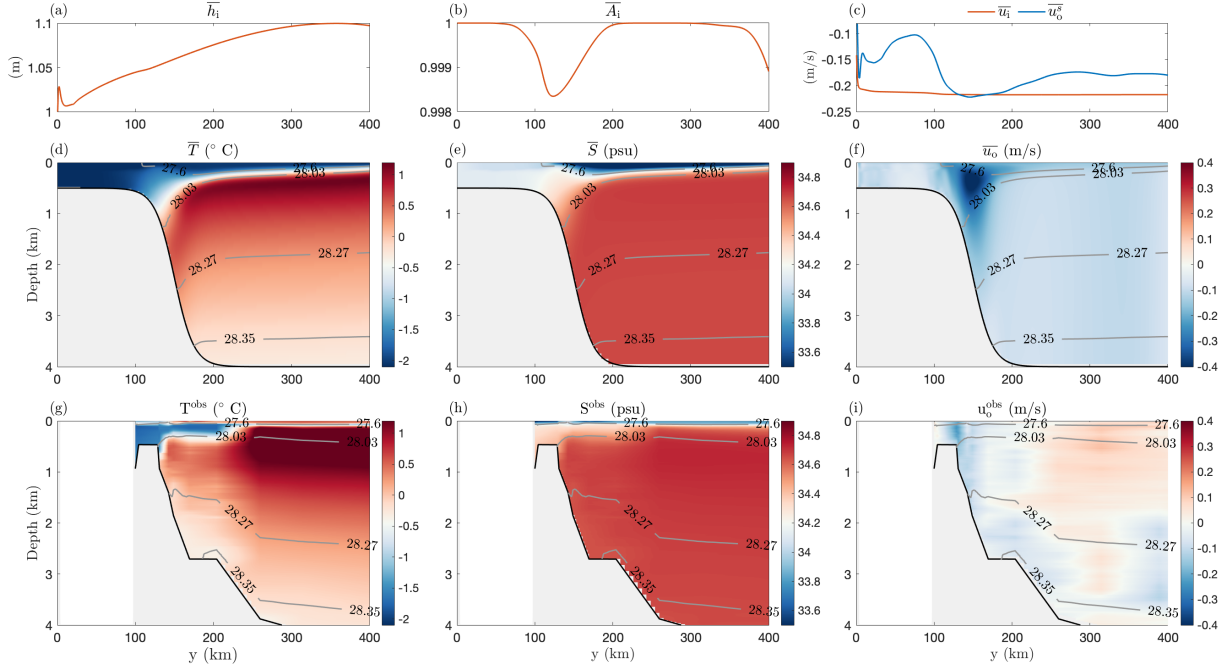


Figure 2.3: Model evaluation. (a-f) A cross section of ice and ocean properties in the reference simulation using time-mean output, taken along the longitude $x = 0$ km. (g-i) The hydrography taken near East Antarctica during the "BROKE West" survey ([Rosenberg and Gorton, 2019](#)) in the Antarctic summer of 2006, along the 60°E line. (a) Sea ice thickness. (b) Sea ice concentration. (c) Sea ice and surface ocean zonal velocities. (d, g) Ocean potential temperature. (e, h) Ocean salinity. (f, i) Ocean zonal velocity. The values on the gray contours denote the neutral densities (kg/m^3).

2.3 Drivers of ASC ocean and sea ice circulation

In section 2.2 we described the selection of experimental parameters and the ice/ocean circulation in the reference simulation. Now we explore what controls the intensity and structure of

the ASC, and quantify the sensitivity of the along-slope ice/ocean circulation and transport to all experimental parameters.

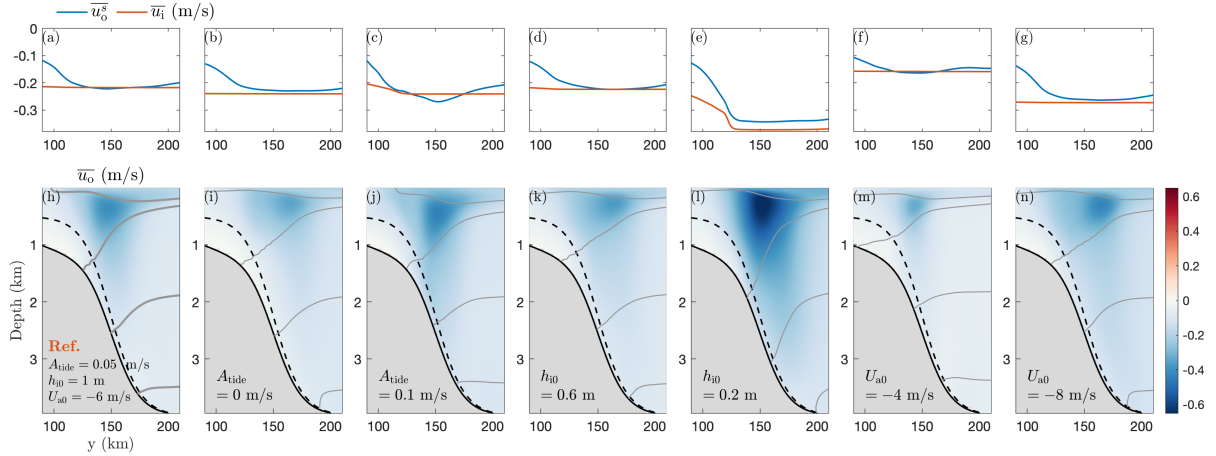


Figure 2.4: Time- and zonal-mean zonal velocity for the reference simulation (a, h), simulations with varying tidal current amplitudes (b, c, i, j), thinner sea ice at the southern boundary (d, e, k, l), and varying zonal wind speeds (f, g, m, n). The corresponding upper panels show the time- and zonal-mean zonal ice and surface ocean velocities. The gray contours denote the time- and zonal-mean neutral densities 1027.60, 1028.03, 1028.27, and 1028.35 kg/m³. Dashed and solid thick black curves denote the shallowest and deepest of the bathymetric contours, respectively. In these simulations, the southern boundary temperature and salinity are set to be vertically uniform (-1.87 °C, 34.17 psu).

The mean zonal ice and ocean velocities over the continental slope are presented in Fig. 2.4 and 2.5. These results agree with previous studies showing that the strength of the ASC increases with stronger zonal wind stress (Fig. 2.4m-n) and stronger tides (Fig. 2.4i-j), since they are the principal sources of the westward momentum put into the ice-ocean system (e.g., [Thompson et al., 2018](#); [Stewart et al., 2019](#)). The intensification of the ASC with tides agrees with previous studies on tidal rectification (e.g., [Huthnance, 1973](#); [Robinson, 1981](#)). The intensity of zonal ocean and sea ice velocities changes dramatically with ice thickness (Fig. 2.4e, l), because the resistance of sea ice chunks to deformation caused by external forcing decreases with reduced ice thickness ([Hibler, 1979](#)). When the sea ice is thin enough ($h_{i0} \lesssim 0.2$ m), the resistance to deformation is sufficiently weak that a strong ice jet forms over the continental slope (Fig. 2.4e). Our results also show that the intensity of slope current increases with steeper topographic slope, the reason for which will be discussed in section 2.4.

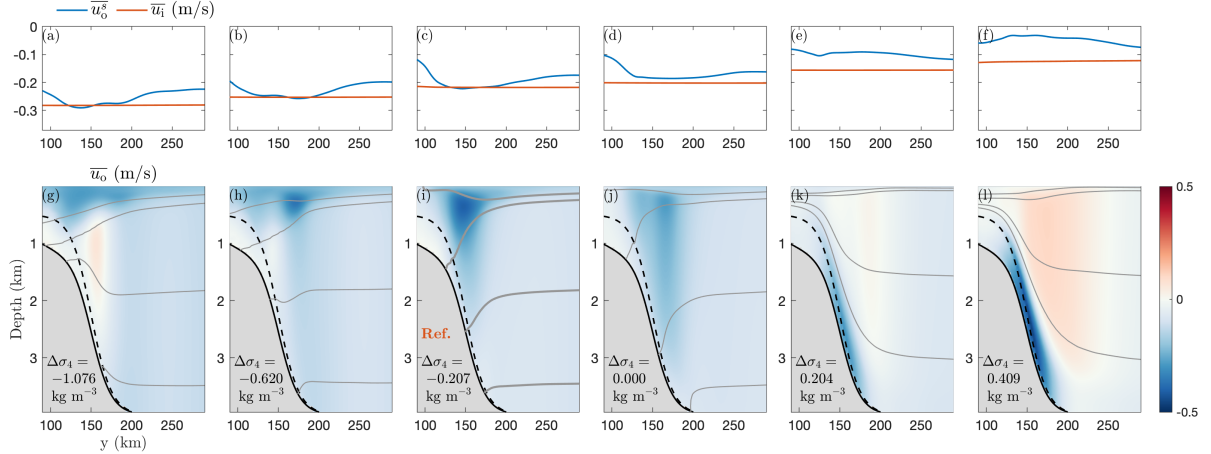


Figure 2.5: Time- and zonal-mean zonal velocity varying with buoyancy gradients between the continental shelf and the open ocean. Similar to Fig. 2.4, the corresponding upper panels show the time- and zonal-mean zonal ice and the surface ocean velocities. The gray contours denote the time- and zonal-mean neutral densities and the black curves denote the model bathymetry. Other model parameters such as tidal current amplitude, wind speeds, sea ice thickness at the southern boundary, and slope width are the same in these simulations.

The structure of the slope current changes dramatically with offshore buoyancy gradient, shifting from a surface-intensified flow, to a barotropic structure, and to a bottom-intensified flow as salinity increases at the southern boundary (Fig. 2.5g-l). This structural change is supported by observational evidence from the Weddell Sea (Le Paih et al., 2020). In the cases with reference restoring salinity, the shelf water below the surface is less dense than the water offshore ($\Delta\sigma_4 = -0.207 \text{ kg m}^{-3}$). Thus the isopycnals in the deep ocean tilt down to the south and incrop on the continental slope (Fig. 2.5i), which gives rise to a slope current that is intensified with elevation above the bathymetry, via the thermal wind relation. When the shelf is very fresh ($\Delta\sigma_4 = -1.076 \text{ kg m}^{-3}$), the shape of the interior density front generates strong vertical velocity shear. The westward velocity weakens with ocean depth, and reverses to the east, causing an undercurrent (opposite the wind direction) over the slope (Fig. 2.5g). When there is bottom water formation ($\Delta\sigma_4 = 0.204, 0.409 \text{ kg m}^{-3}$), the westward slope current is bottom-intensified, with an eastward undercurrent above (Fig. 2.5k-l), because the offshore dense outflow and the onshore return flow are deflected by the Coriolis force.

To quantify the sensitivity of the along-slope circulation to various parameters, we calculate

the following quantities over the continental slope: the maximum westward velocity throughout the water column ($|\overline{u}_o|_{\max}$) and at the seafloor ($\left|\overline{u}_o^{\text{bot}}\right|_{\max}$), the barotropic and baroclinic transports (T_{BT} , T_{BC}), the westward sea ice velocity ($|\langle \overline{u}_i \rangle|$) and the sea ice thickness ($\langle \overline{h}_i \rangle$). Here the overlines denote an average over a 5-year analysis period,

$$\overline{\bullet} = \frac{1}{5 \text{ years}} \int_{t_0}^{t_0 + 5 \text{ years}} \bullet dt, \quad (2.3)$$

and the angle brackets $\langle \bullet \rangle$ denote an average over the continental slope,

$$\langle \bullet \rangle = \frac{1}{L_x W_s} \oint dx \int_{L_0}^{L_0 + W_s} \bullet dy, \quad (2.4)$$

where $L_x = 400$ km is the zonal domain size, W_s is the width of the continental slope, and $L_0 = 125$ km is the starting point of the slope in the meridional direction. The continental slope is defined as the region between the latitudes $y = L_0$ and $y = L_0 + W_s$. The total zonal transport per unit length in the ASC (T_{total}) is the vertically integrated time-mean zonal ocean velocity, averaged over the slope. Its barotropic component (T_{BT}) is the time-mean seafloor zonal velocity ($\overline{u}_o^{\text{bot}}$) times the ocean thickness (h), averaged over the slope. The baroclinic component (T_{BC}) is the difference between the total transport and the barotropic transport. T_{total} , T_{BT} , and T_{BC} are defined to be positive westward,

$$T_{\text{total}} = \left\langle - \int_{-h}^0 \overline{u}_o dz \right\rangle, \quad T_{\text{BT}} = \left\langle - \int_{-h}^0 \overline{u}_o^{\text{bot}} dz \right\rangle, \quad T_{\text{BC}} = T_{\text{total}} - T_{\text{BT}}. \quad (2.5)$$

We find that the barotropic tides change the barotropic transport, while it does not affect the baroclinic transport (Fig. 2.6a). Sea ice thickness, wind stress, slope steepness and horizontal resolution mainly affect the baroclinic transport (Fig. 2.6b-f). Fig. 2.6g highlights the changes in the barotropic and baroclinic transport due to increased offshore buoyancy gradient, which is in agreement with Fig. 2.5. As for the circulation of the sea ice, Fig. 2.7 shows that the trends of $|\langle \overline{u}_i \rangle|$ is approximately consistent with the total transport of the ocean, whereas $|\langle \overline{u}_i \rangle|$ is less sensitive to varying slope width. The along-slope sea ice velocity decreases with increased offshore buoyancy

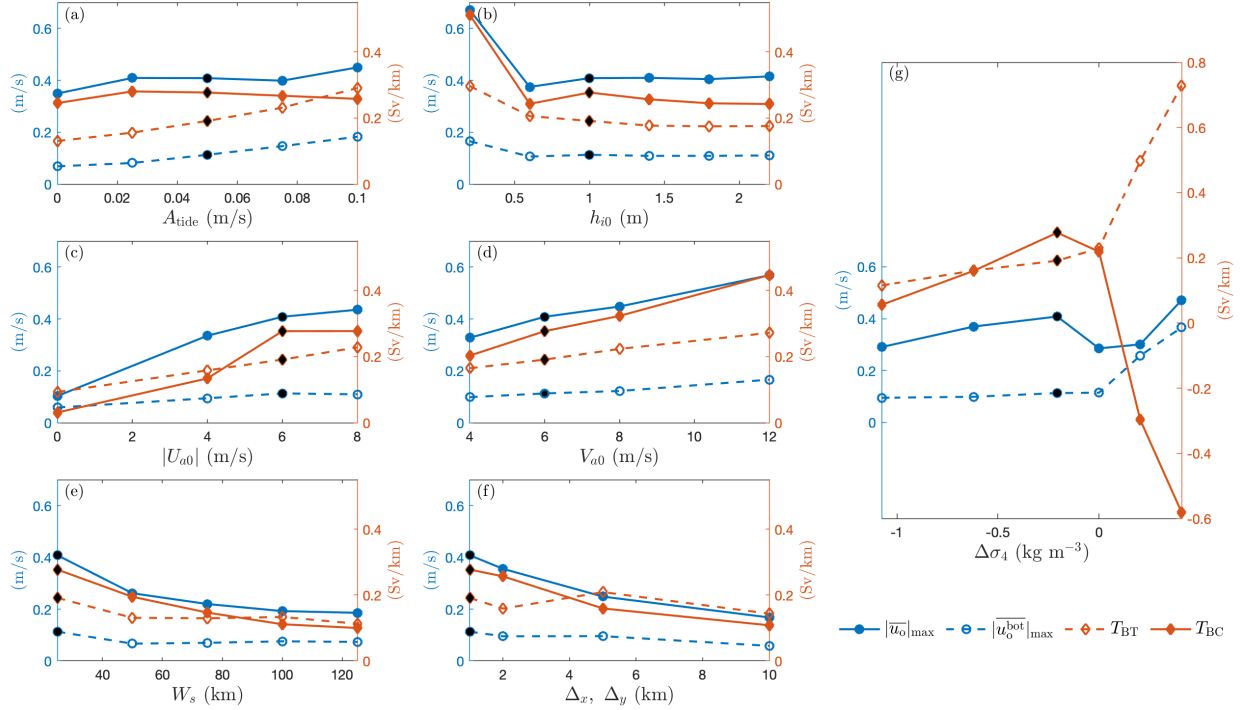


Figure 2.6: The maximum westward ocean speed $|\overline{u}_o|_{\text{max}}$, maximum westward ocean bottom speed $|\overline{u}_o^{\text{bot}}|_{\text{max}}$, barotropic transport T_{BT} and baroclinic transport T_{BC} per unit width over the continental slope for simulations with varying tidal current amplitude (a), sea ice thickness at the southern boundary (b), maximum westward wind speed (c), maximum northward wind speed (d), continental slope half-width (e), horizontal grid spacing (f), and ocean bottom potential density difference between the northern and the southern boundaries (g). Black dots denote the reference simulation.

gradient (Fig. 2.7b), as it is accelerated by the surface-intensified ocean current in fresh-shelf case, and is damped by the eastward undercurrent in the dense-shelf case. The sea ice thickness averaged over the slope is mostly controlled by the prescribed ice thickness at the southern boundary, with an exception in the case $V_{a0} = 12$ m/s, where the sea ice piles up in the middle of the domain due to strong offshore advection imposed by the southern inflow boundary condition, and convergence of meridional ice flow associated with the meridional gradient of the meridional wind stress.

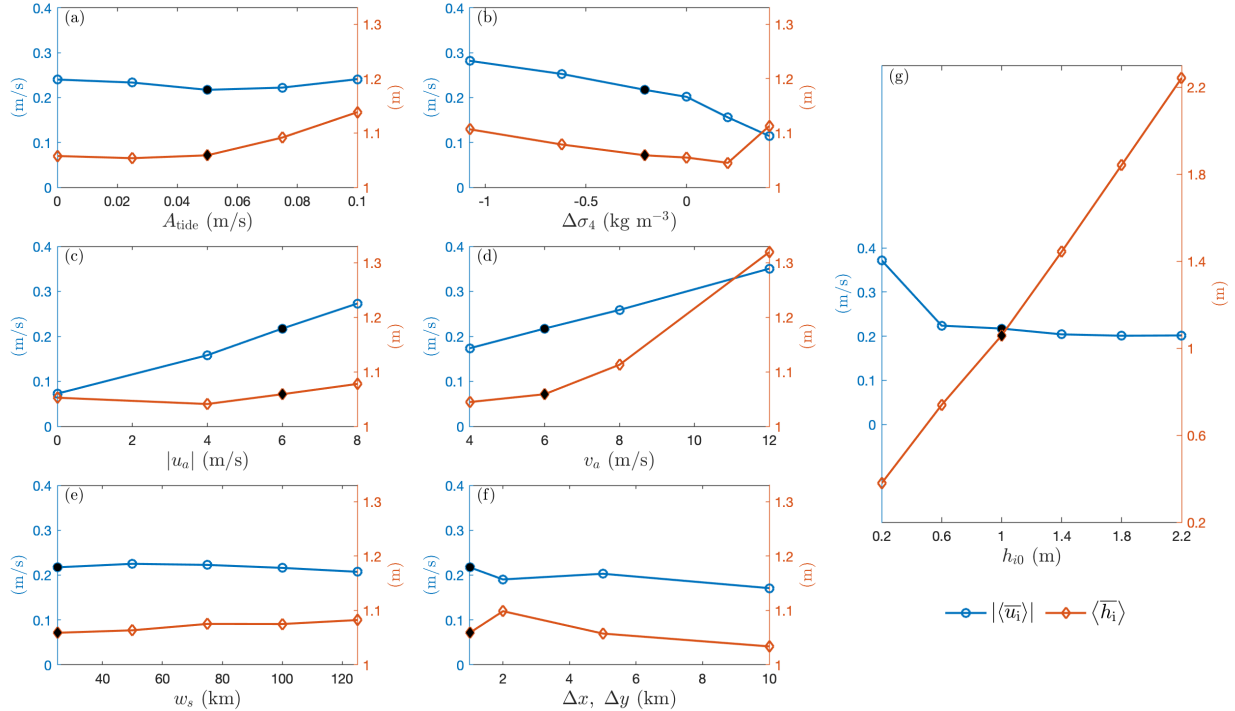


Figure 2.7: Time-mean westward ice speed $|\langle \bar{u}_i \rangle|$ and ice thickness $\langle \bar{h}_i \rangle$ over the continental slope, for simulations with varying tidal current amplitude (a), ocean bottom potential density difference between the northern and the southern boundaries (b), maximum westward wind speed (c), maximum northward wind speed (d), continental slope half-width (e), horizontal grid spacing (f), and sea ice thickness at the southern boundary (g). Black dots denote the reference simulation.

In most simulations, the surface ocean velocity approximately matches the velocity of the sea ice over the continental slope, even in the case with no tides, as shown in the upper panels of Fig. 2.4 and 2.5. Exceptions include cases with very thin sea ice (Fig. 2.4e), a dense southern boundary (Fig. 2.5e-f), and a wide topographic slope (shown later in the next section). To understand the mechanisms that control the ice/ocean circulation, and identify the cause of the ice-ocean velocity match over the slope, we look into the momentum balances of the ice/ocean system in the following

section.

2.4 Momentum balances for ocean and sea ice in the ASC

A simple and intuitive speculation regarding momentum transfer in the wind-sea ice-ocean system is that the wind inputs momentum to the sea ice, and then the sea ice accelerates the ocean by ice-ocean stress. Some previous studies that have worked under this assumption include [Nøst et al. \(2011\)](#), [Stewart and Thompson \(2016\)](#) and [Huneke et al. \(2019\)](#). The momentum is vertically transferred downward through the ocean, primarily via eddy-induced isopycnal form stress, and is finally removed by bottom frictional stress and topographic form stress at the seafloor ([Stewart and Thompson, 2016](#); [Bai et al., 2021](#)). However, in section 2.3 we found that over a large range of model parameters, ocean surface velocity matches the velocity of sea ice over the continental slope; while over the shelf and in the deep ocean, ice and ocean velocities diverge. This is consistent with the results of [Stewart et al. \(2019\)](#). This indicates that some processes occurring over the slope diminish the ice-ocean momentum transfer there, so the speculation discussed above is incomplete. In order to establish the pathways of the wind-input momentum over the slope, and to understand how the wind, sea ice, tidal forcing, offshore buoyancy gradients and bathymetry influence the momentum transfer, we analyze the zonal momentum balances of the ice and ocean system.

2.4.1 Zonal momentum balance in the reference simulation

In the spin-up stage, when the ASC transitions from stationary state to equilibrium state, some combination of the winds, tides and bottom stresses ([Howard et al., 2015](#)) spins up the flow (not shown) until the speeds of sea ice and surface ocean approximately coincide over the slope. We did not distinguish the relative importance of each in the spin-up stage because in nature the ASC already exists, so the steady-state dynamics are more relevant. In this study we focus on the momentum balance in the equilibrium state, when the slope current continues in its state of motion. The current feels almost no drag against the sea ice, so almost no additional momentum source is needed to maintain its motion (Newton's first law).

The vertically and zonally integrated zonal momentum equations for the ocean and the sea ice solved by MITgcm are

$$\oint \rho_o \int_{-h}^0 \frac{\partial \bar{u}_o}{\partial t} dz dx = \oint \left(\underbrace{\tau_{io}^x}_{\text{Tendency}} - \underbrace{\rho_o \int_{-h}^0 \bar{u}_o \cdot \nabla \bar{u}_o dz}_{\text{Ice-ocean stress}} + \underbrace{\rho_o f \int_{-h}^0 \bar{v}_o dz}_{\text{Coriolis}} - \underbrace{p_b \frac{\partial \eta_b}{\partial x}}_{\text{Topog. form stress}} - \underbrace{\tau_b^x}_{\text{Bottom frictional stress}} + \underbrace{\mathcal{V}}_{\text{Viscous diffusion}} \right) dx, \quad (2.6a)$$

$$\oint \rho_i h_i \frac{\partial \bar{u}_i}{\partial t} dx = \oint \left(\underbrace{\tau_{ai}^x}_{\text{Tendency}} + \underbrace{\frac{\partial \bar{\sigma}_{21}}{\partial y}}_{\text{Wind stress}} + \underbrace{\rho_i f \bar{h}_i v_i}_{\text{Ice rheology}} - \underbrace{\tau_{io}^x}_{\text{Coriolis}} \right) dx. \quad (2.6b)$$

Here the subscripts "i" and "o" denote the sea ice and the ocean respectively, p_b is the bottom pressure, and η_b is the seafloor elevation. As the time-averaged mass flux is zero across the northern and the southern boundaries, the Coriolis term is very small in Eq. 2.6a, though in practice it is non-zero due to the spatial discretization in MITgcm. The symbols with σ and indices in the subscription are components of the sea ice internal stress in the standard form, which quantify the resistance of sea ice to deformation (Hibler, 1979). The zonal component of the sea ice internal stress divergence is $\partial_x \sigma_{11} + \partial_y \sigma_{21}$. After taken the zonal integration, $\partial_x \sigma_{11}$ has no contribution to the sea ice momentum budget. The sea surface slope $-\rho_i h_i g \partial \eta / \partial x$ and ice/snow load $-\rho_i h_i g \partial (h_i \rho_i / \rho_o) / \partial x$ also vanish approximately under a zonal integral. Sea ice momentum advection is negligible and is turned off in MITgcm by default.

Fig. 2.8a shows the sea ice zonal force balance of the reference simulation. As assumed by previous studies (Nøst et al., 2011; Stewart and Thompson, 2016; Huneke et al., 2019), the overall momentum balance of the sea ice is primarily between wind stress and ocean-ice stress. This is largely the case over the continental shelf and the open ocean. However, over the slope there is substantial horizontal redistribution of momentum via ice internal stress divergence, and the ocean-ice stress is almost zero. The green arrows in Fig. 2.8a show the momentum fluxes due to sea ice internal stress, which indicate that over the slope the sea ice mainly transfers wind-input momentum onto the continental shelf in the reference case. The Coriolis force felt by the sea ice is negative and approximately uniform, because the time-averaged meridional ice velocity is dominated by the northward ice inflow from the southern boundary.

The ocean zonal force balance of the reference simulation is shown in Fig. 2.8b. For the ocean,

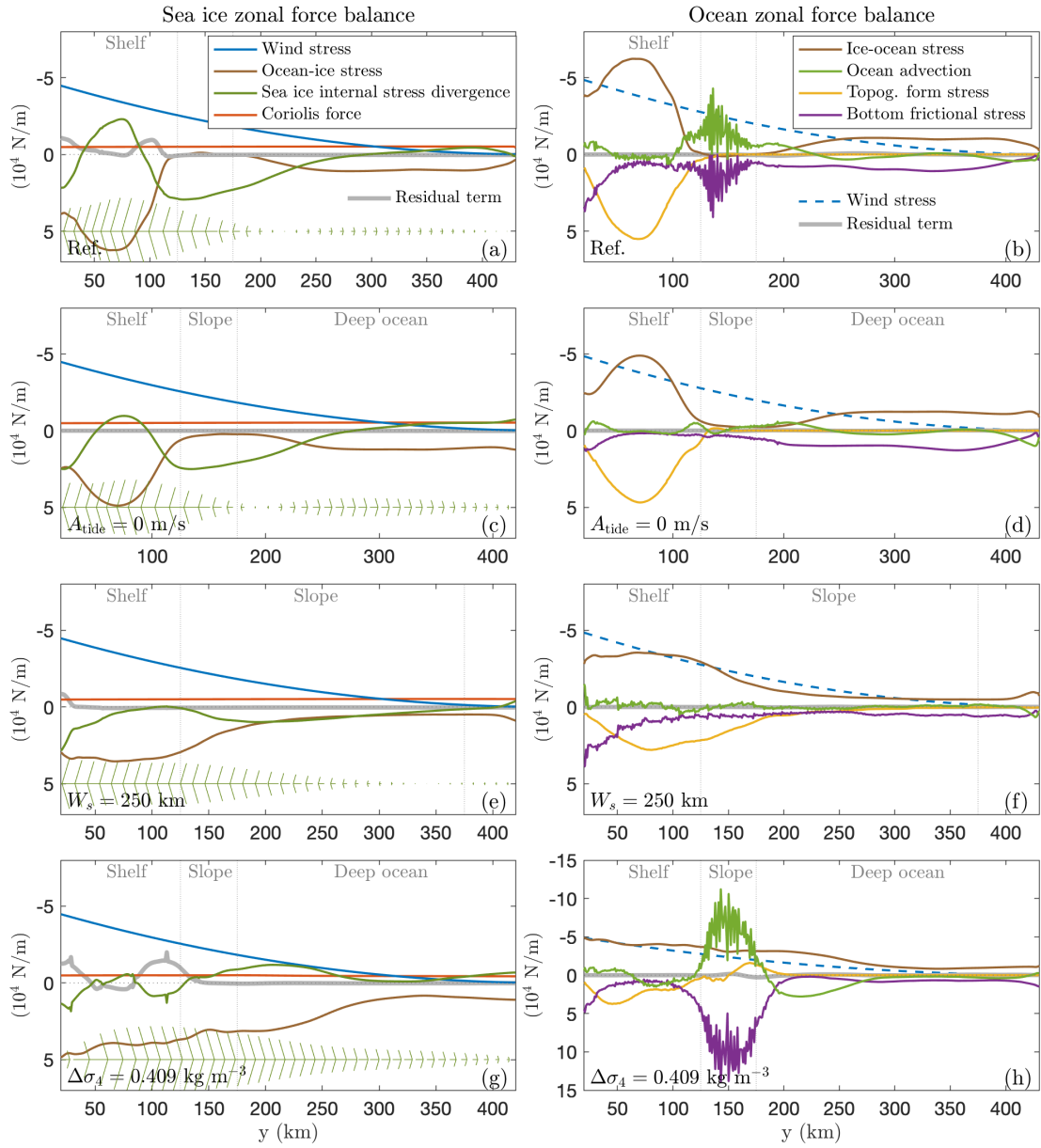


Figure 2.8: Time- and zonal-mean sea ice and ocean zonal force balances for the reference simulation (a, b), the case with zero tidal current amplitude (c, d), the case with a wide and gentle continental slope (e, f), and the very dense shelf case (g, h). Note that the 20-km southern and northern restoring regions have been removed. The y-axis is negative (westward) upward, and the range of y-axis for panel (h) is different from other panels.

the primary momentum input from ice-ocean stress is balanced by topographic form stress (TFS) on the shelf and bottom frictional stress in the open ocean. The secondary momentum input from ocean advection, including the lateral momentum transfer and momentum flux convergence due to tidal rectification, is balanced locally by bottom frictional stress, and thus does not affect the overall picture of the momentum balance. Over the continental shelf, the sea ice flows much faster than the ocean, injecting westward momentum into the ocean via ice-ocean stress. TFS might be expected to be the primary sink of momentum in analogy with the Antarctic Circumpolar Current (ACC, [Munk and Palmén, 1951](#); [Masich et al., 2015](#); [Stewart and Hogg, 2017](#)), but it was unclear previously how important the TFS is in the ASC, since the directions of the ACC and the ASC are opposite relative to topographic Rossby wave propagation ([Bai et al., 2021](#)). In this model with bumps and troughs added to the bathymetry (Fig. 2.2a), TFS is able to extract momentum from the flow on the shelf to balance the momentum input from ice-ocean stress. The inclusion of bumps and troughs is more realistic than the uniform geometries used in previous studies (e.g., [Stewart and Thompson, 2016](#); [Huneke et al., 2019](#); [Stern et al., 2015](#)). Excluding the bumps and troughs would lead to stronger flows along the shelf, and we don't anticipate this changing the findings qualitatively.

The presence of strong advective acceleration also deviates from the speculative momentum balance laid out at the beginning of section 2.4. By temporally decomposing the total ocean advection into mean, eddy, and tidal components, we find that ocean advection is mostly contributed by tidal advection in the reference case (Appendix B), which is strongest over the slope because tidally induced momentum convergence is proportional to topographic slope steepness ([Loder, 1980](#)). The tide-input momentum (tidal advection) is balanced by bottom drag associated with the along-slope tidally rectified flow (Fig. 2.8b), which is consistent with previous studies on the mechanisms of tidal rectification (e.g., [Huthnance, 1973](#)). Additionally, the varying thickness of the staircase-like bottom grid cells generates convergence and divergence in the bottom Ekman transport ([Brink and Lentz, 2010](#)), leading to numerical noise in ocean advection and bottom frictional stress (Fig. 2.8b, h). However, there is no distinguishable noise in the velocity field (Fig. 2.4-2.5), and the residual term is zero in the ocean momentum balance (Fig. 2.8), suggesting

that the overall momentum balance is not contaminated by the numerical noise.

2.4.2 Sensitivity of zonal momentum balance to model parameters

Across a wide range of experimental parameters, the pattern of the zonal force balance is qualitatively similar to the reference case (Fig. 2.9), neither very sensitive to wind speed perturbations (Fig. 2.9c-f) nor sea ice thickness (Fig. 2.9a-b). As the sea ice strength is proportional to ice thickness, thinner sea ice has less resistance to deformation imposed by external forcing (Hibler, 1979), leading to increased ice-ocean shear (Fig. 2.4e, Fig. 2.9a) and decreased ice internal stress divergence (Fig. 2.9a). The results suggest that the characteristics of the momentum balance do not qualitatively depend on meridional gradient in zonal wind stress (Fig. 2.9c-f). When varying wind speeds, we also change the meridional gradient of the wind, as the magnitude of the wind speeds decrease linearly offshore to zero at the northern boundary. In addition, the direction of sea ice momentum transfer (onto the shelf, in many cases, see Fig. 2.9) is against the gradient of wind-input momentum.

In a few cases with wider topographic slope (smaller steepness compared with typical slope steepness around Antarctica, Fig. 2.10c) and dense water outflows (Fig. 2.10e), sea ice internal stress divergence does not redistribute most of the wind-input momentum over the slope. The magnitude of the ice-ocean stress increases substantially with offshore buoyancy gradient $\Delta\sigma_4$ (Fig. 2.10f), consistent with Fig. 2.5l. The strength of ocean bottom velocity increases with $\Delta\sigma_4$ (Fig. 2.6g), leading to a much larger bottom frictional stress over the slope (Fig. 2.8h, 2.10f), which is balanced by enhanced ocean advection and ice-ocean stress. Note that the residual term in the sea ice momentum budget is non-zero in some cases (Fig. 2.8a, 2.8g), but our tests indicate that improving the LSR solver accuracy would reduce those errors, with little impact on the momentum balance.

Stewart et al. (2019) indicate that tides are responsible for the match of ocean and sea ice velocities over the continental slope. Our results show that tidal advection indeed accelerates the ocean and decreases ice-ocean stress over the shelf break. However, tides are not required for the

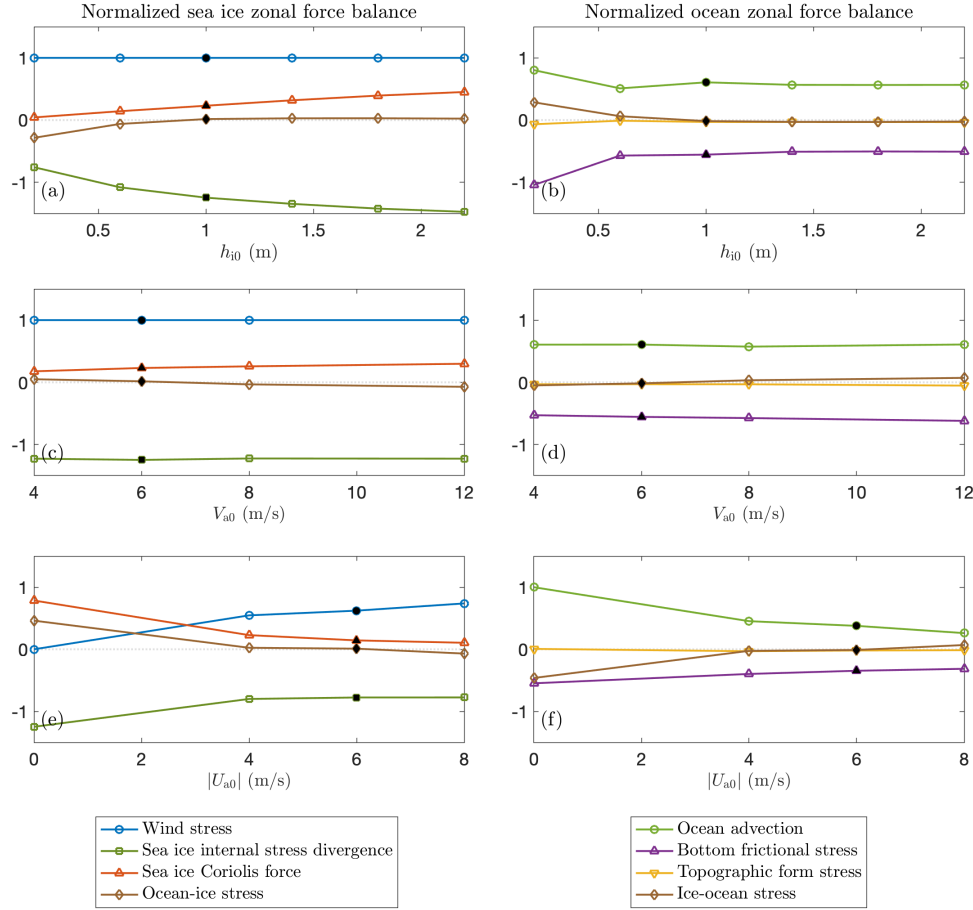


Figure 2.9: Sensitivity analysis: time-mean sea ice and ocean zonal force balances averaged over the continental slope, (a-d) normalized by zonal wind stress, or (e-f) by the sum of zonal wind stress and ocean advection. Simulations with varying (a-b) sea ice thickness at the southern boundary, (c-d) maximum northward wind speed, and (e-f) maximum westward wind speed.

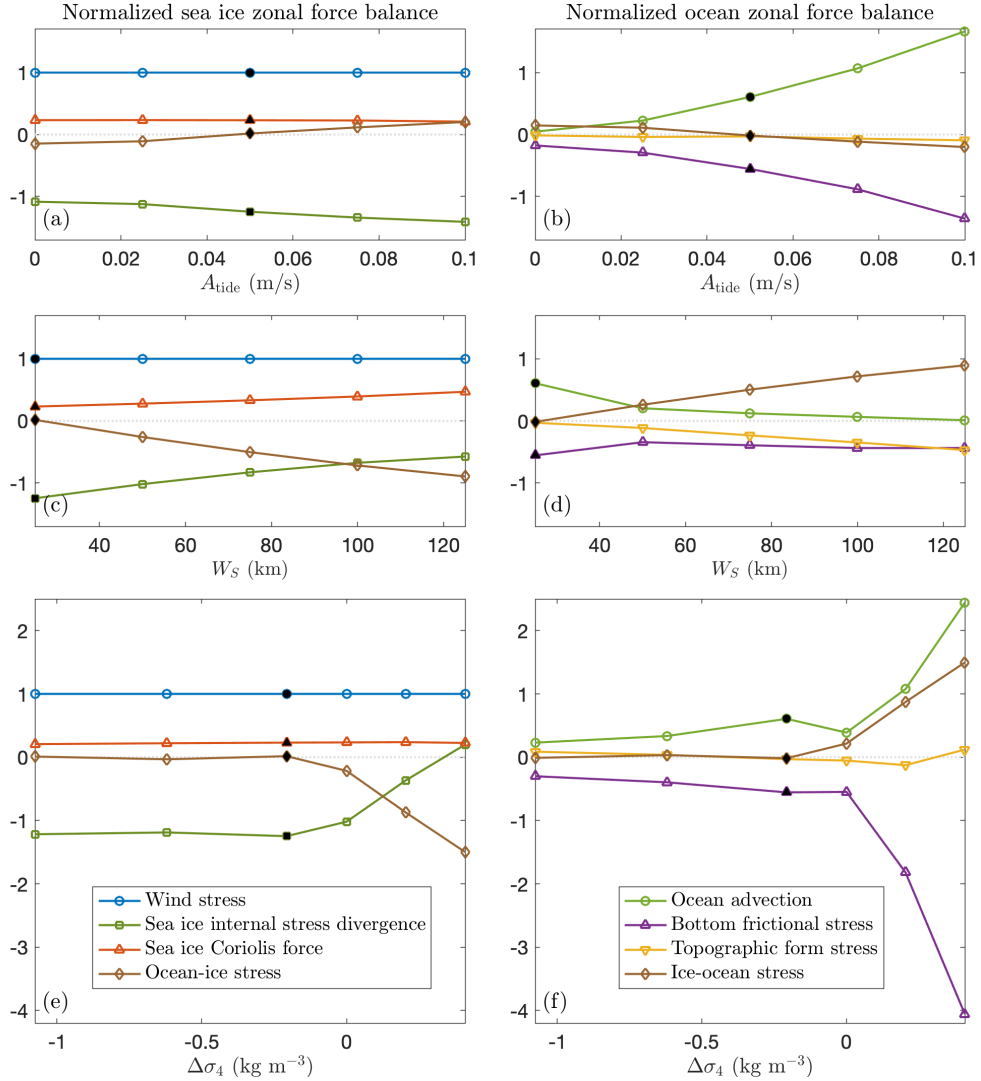


Figure 2.10: Sensitivity analysis (continued): time-mean sea ice and ocean zonal force balances, averaged over the continental slope and normalized by zonal wind stress. Simulations with varying (a-b) tidal current amplitude, (c-d) continental slope half-width, and (e-f) ocean bottom potential density difference between the northern and the southern boundaries.

ice-ocean stress to vanish over the slope. Fig. 2.8c and 2.8d show the sea ice and ocean zonal force balances for a simulation with no tides. In this case, the matching of the ice and surface ocean velocities still occurs. When the tidal current is very strong, the ocean surface velocity exceeds the velocity of sea ice (Fig. 2.4c), causing ocean-to-sea ice westward momentum transfer (Fig. 2.10b).

2.4.3 Vertical momentum transfer over the slope

Fig. 2.11c shows the vertical profiles of zonal velocity in cases with varying topographic slope steepness, averaged over each slope. In the reference case, the vertical velocity shear in the ocean interior is large (the black curve in Fig. 2.11c), suggesting that the vertical momentum transfer is inefficient over the slope. The mesoscale eddies in the ocean transfer momentum downward predominantly by isopycnal form stress (IFS), which is essential to connecting the momentum input from ocean surface, and the momentum sink at seafloor (e.g., [Vallis, 2017](#)). Fig. 2.11a-b show the estimated transient and standing eddy vertical momentum fluxes due to IFS and vertical component of Reynolds stress, normalized by wind stress over the slope. In the reference case, in which the slope steepness is typical of the Antarctic continental slope ([NOAA National Geophysical Data Center, 2009](#); [Amante and Eakins, 2009](#)), the transient and standing eddies are not effective in transferring momentum downward. This is consistent with previous studies that report suppression of baroclinic instability over steep slopes ([Isachsen, 2011](#); [Hetland, 2017](#)).

With decreased topographic slope steepness, the standing and transient eddies are more efficient in transferring momentum downward over the slope (2.11a-b). The resulting ocean velocity shear decreases (2.11c), and the ocean surface velocity falls substantially below the speed of the sea ice. Thus the ice-ocean velocity shear (2.11c) and the ice-ocean stress (Fig. 2.10d) increase with larger slope width. In the case $W_s=250$ km, the ice-ocean stress approximately matches the wind stress (Fig. 2.8f).

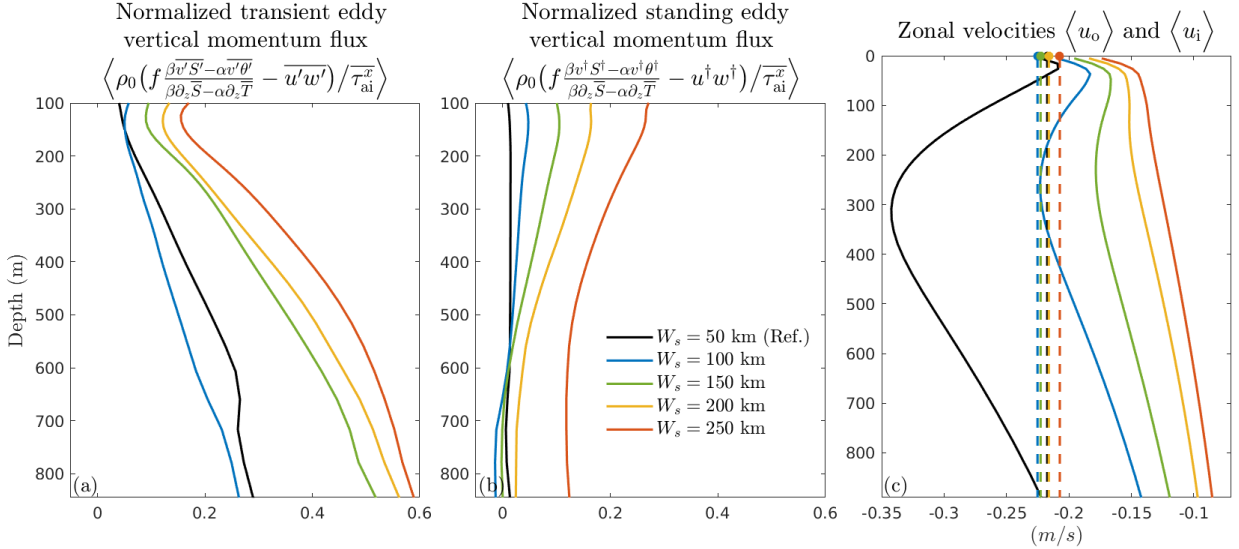


Figure 2.11: (a) The vertical component of the transient eddy momentum flux for cases with varying slope width, normalized by wind stress. The angle brackets denote the averaged values over the continental slope (Eq. 2.4). The overbars denote the time average over a 5-year analysis period (Eq. 2.3), and primes denote departures of state variables from their respective time-averaged values. The first term in the numerator is the estimated isopycnal form stress (IFS) due to transient eddies, and the second term is the vertical component of the Reynolds stress. (b) The vertical component of the standing eddy momentum flux for cases with varying slope width, normalized by wind stress. The daggers denote departures of state variables from their zonally averaged values. The first term in the numerator is the estimated IFS due to standing eddies. (c) Zonal ocean (solid curves) and sea ice (dashed lines) velocities averaged over the continental slope for cases with different slope width. (a)-(c) are plotted from 100 to 800 meters depth to exclude the bottom bathymetry and the surface mixed layer where the ocean is weakly stratified and the estimation of IFS from the density (or equivalently T and S) gradient is invalid.

2.5 A reduced-order model of ice-ocean mechanical interactions in the ASC

As discussed in section 2.4, our results suggest that vertical momentum transfer by standing and transient eddies is inefficient over continental slopes steepnesses typical of Antarctica. However, since we can not explicitly turn off eddy suppression in the 3D models, the mechanism responsible for ice-ocean coupling in the core of the ASC, and to what extent topographic eddy suppression affects the momentum budget, remain unclear. To provide insight into the underlying mechanism, we develop a reduced-order model of ice-ocean mechanical interactions, which is primarily a tool to test the relevance of eddy suppression over the slope. In this model, the ocean is discretized into two vertical levels of equal depth, overlaid by one layer of viscous-plastic sea ice and forced by a specified atmospheric wind stress. We incorporate the effect of eddies via a “residual-mean” formulation of the momentum equations, with an eddy isopycnal form stress that transfers momentum vertically between the two layers, with the rate of momentum transfer being controlled by an eddy diffusivity ([Ferreira and Marshall, 2006](#)). This allows us to optionally suppress vertical eddy momentum transfer over the slope, and thereby isolate the role of eddy suppression from other processes that can reduce ice-ocean shear, such as tidal forcing. In this section we describe the reduced-order model configuration, compare cases with and without eddy suppression over the slope, and compare the results of reduced-order simulations with the 3D MITgcm simulations.

2.5.1 Formulation of the reduced-order model

To simplify the equation of motion, the flow is assumed to be steady ($\partial_t \equiv 0$), invariant in the x -direction ($\partial_x \equiv 0$), and low-Rossby number ($D/Dt \equiv 0$). We consider cases with a weak horizontal buoyancy gradient only, hence the assumption of zero time-averaged meridional (offshore) flow in the ocean. We apply the Boussinesq momentum equations, and fix the densities of the sea ice ($\rho_i = 920 \text{ kg/m}^3$) and the ocean ($\rho_o = 1037 \text{ kg/m}^3$).

The upper level of the ocean is driven by ice-ocean stress and transfers momentum downward to the lower level via isopycnal form stress (IFS). For the lower level, the momentum input by IFS and tidal advection sinks at the seafloor via bottom frictional stress and topographic form stress.

Though the tidal current imposed at the boundaries are barotropic, the tide-induced momentum flux convergence in the ocean, i.e., tidal advection, is bottom intensified. Bottom frictional stress creates a phase lag between the meridional tidal velocity and the transient zonal velocity induced by tides, which regulates the magnitude of the tidal advection (e.g., [Huthnance, 1973](#); [Loder, 1980](#)). Therefore, we only consider the tidal advection term for the lower level where fiction appears. The momentum equations for the ocean are

$$\underbrace{\rho_0 h_o^s \frac{\partial u_o^s}{\partial t}}_{\text{Tendency}} = \underbrace{\tau_{\text{io}}^x}_{\text{Ice-ocean stress}} - \underbrace{F_{\text{ifs}}}_{\text{Isopycnal form stress}}, \quad (2.7a)$$

$$\underbrace{\rho_0 h_o^b \frac{\partial u_o^b}{\partial t}}_{\text{Tendency}} = \underbrace{F_{\text{ifs}}}_{\text{Isopycnal form stress}} + \underbrace{\tau_b^x}_{\text{Bottom frictional stress}} + \underbrace{F_{\text{tide}}}_{\text{Tidal advection}} + \underbrace{F_{\text{tfs}}}_{\text{Topographic form stress}}, \quad (2.7b)$$

$$h_o^s = h_o^b = \frac{h_o}{2}, \quad (2.7c)$$

where the superscripts “s”, “b”, “x”, and “y” denote the upper (surface) and the lower (bottom) levels, and the components in the zonal and the meridional directions, respectively. Note that the interface between the upper and the lower levels should not be interpreted as an isopycnal surface, but rather as a terrain-following coordinate. This formulation can also be derived by considering the evolution of the surface and bottom ocean velocities, and assuming a linear vertical variation between them.

The IFS can be estimated by the product of isopycnal slope and eddy diffusivity (e.g., [Vallis, 2017](#)). We assume that the ocean is in geostrophic balance, which is equivalent to assuming that eddies release available potential energy and relax isopycnal slopes ([Gent and Mcwilliams, 1990](#); [Gent et al., 1995](#)). Then we express the isopycnal slope by the thermal wind relation and assume the horizontal variations in the vertical stratification are very weak. Ultimately we relate IFS to vertical velocity shear, so the isopycnal slope and the IFS can evolve dynamically with time. The

IFS in the reduced-order model is

$$F_{\text{ifs}} = 2\rho_o f^2 K \frac{(u_o^s - u_o^b)}{N^2 h_o}, \quad (2.8)$$

where K is the eddy diffusivity, and $N \approx 8.3 \times 10^{-4} \text{s}^{-1}$ is the mean stratification (buoyancy frequency) between the upper and the lower levels, obtained from the restoring density profile at the northern boundary of the MITgcm simulations (Fig. 2.2d). Note that this eddy diffusivity parameterization only represents the diffusivity due to transient eddies. Since the vertical eddy momentum flux is mostly contributed by transient eddies for the reference slope steepness (Fig. 2.11a-b), this model does not include a standing eddy parameterization for simplicity. Details on the derivation of the IFS are in Appendix A2.7.1.2.

The sea ice follows a standard viscous-plastic rheology given by [Hibler \(1979\)](#) (Appendix A2.7.1.6). Assuming that the ocean is fully covered by the sea ice (the ice concentration is $A_i = 1$), the momentum equations for the sea ice are

$$\underbrace{\rho_i h_i \frac{\partial u_i}{\partial t}}_{\text{Tendency}} = \underbrace{\rho_i h_i f v_i}_{\text{Coriolis}} + \underbrace{\tau_{ai}^x}_{\text{Wind stress}} - \underbrace{\tau_{io}^x}_{\text{Ice-ocean stress}} + \underbrace{\frac{\partial \sigma_{21}}{\partial y}}_{\text{Ice rheology}}, \quad (2.9a)$$

$$\underbrace{\rho_i h_i \frac{\partial v_i}{\partial t}}_{\text{Tendency}} = -\underbrace{\rho_i h_i f u_i}_{\text{Coriolis}} + \underbrace{\tau_{ai}^y}_{\text{Wind stress}} - \underbrace{\tau_{io}^y}_{\text{Ice-ocean stress}} + \underbrace{\frac{\partial \sigma_{22}}{\partial y}}_{\text{Ice rheology}} - \underbrace{\rho_i h_i g \frac{\partial \eta}{\partial y}}_{\text{Sea surface slope}}, \quad (2.9b)$$

where η is the sea surface elevation and g is the gravitational acceleration. The sea surface slope term in Eq. 2.9b can be estimated from the meridional ocean momentum balance

$$g \frac{d\eta}{dy} = \frac{\tau_{io}^y}{\rho_o(h_o/2)} - f u_o^s. \quad (2.9c)$$

We further neglect changes in the sea ice growth rate due to thermodynamic processes (ice formation and melting). So the tendency of ice thickness depends only on the meridional advection of the sea

ice,

$$\frac{\partial h_i}{\partial t} = -\frac{\partial}{\partial y}(h_i v_i). \quad (2.9d)$$

We find that in the 3D MITgcm simulations, tidal advection dominates the total ocean advection (Appendix B). So we substitute the total advection in this reduced-order model by tidal advection, which is derived following Loder (1980) (Appendix A2.7.1.3). In the 3D simulations we also observe that sea ice tends to drift with barotropic tides and diminishes the effect of tides on ice-ocean stress. Therefore we use the standard quadratic drag formulations for air-ice and ice-ocean stress in the reduced-order model, while modifying the ocean bottom stress and the topographic form stress by adding a mean tidal current (Appendix A2.7.1.4-2.7.1.5). Wind distribution and bathymetry of the reduced-order model are identical to those in the 3D simulations. Compared to the 3D model, the reduced-order model has identical wind distribution, and simplified model bathymetry without zonal variations. We integrate the model forward in time until it reaches the steady state, then compare the steady-state solutions with the 3D simulations. Details on the boundary conditions, model initialization, and numerical schemes are presented in Appendix A2.7.1.7-2.7.1.8.

2.5.2 Reduced-order simulations

Fig. 2.12a-b shows the ice and ocean zonal force balance for the reference simulation using the reduced-order model. Compared with MITgcm (Fig. 2.8a-b), this model successfully reproduces the salient features in the momentum budget, i.e., over the slope, sea ice internal stress divergence redistribute wind-input momentum (Fig. 2.12a), ice-ocean stress vanishes, and tidal advection is locally balanced by bottom frictional stress; over the shelf, topographic form stress balances the large momentum input from ice-ocean stress (Fig. 2.12b). There are a few disagreements between the two models with different complexity. The peak of the tidal advection slightly shifts onshore (Fig. 2.12b) in the reduced-order model because the troughs on the shelf modifies the strength of the tidal advection in MITgcm. In addition, the region of ice-ocean stress suppression is narrower in the reduced-order model compared with MITgcm. Overall, the reduced-order model can qualitatively

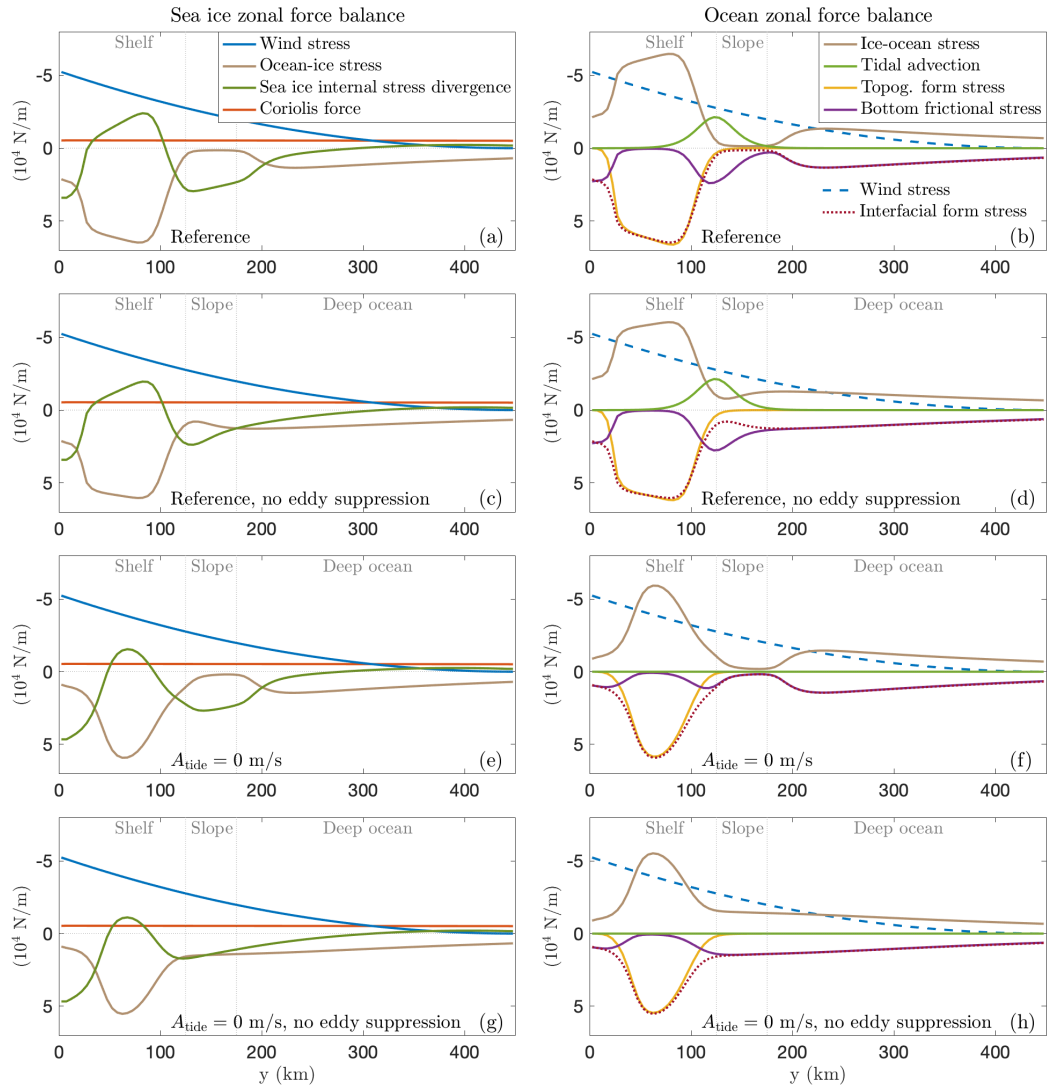


Figure 2.12: Reduced-order model simulation results. Sea ice and ocean zonal force balance for the reference case (a, b), and the no-tide case (e, f) with eddy suppression over the continental slope. Sea ice and ocean zonal force balance for the reference case (c, d), and the no-tide case (g, h) with a uniform eddy diffusivity $K = 300 \text{ m}^2/\text{s}$, i.e., no eddy suppression over the continental slope.

and quantitatively reproduce the ocean and sea ice zonal force balance shown in the 3D MITgcm simulations. For the simulation with no tides, the results of the reduced-order model (Fig. 2.12e-f) are also consistent with that in MITgcm (Fig. 2.8c-d). We will discuss the remaining panels of Fig. 2.12 later in this section.

Fig. 2.13 compares the reduced-order simulations with the corresponding MITgcm simulations. Different colors denote experiments with varying parameters. This model does a fairly good job in predicting the maximum ocean surface and bottom velocities (Fig. 2.13a) and bottom frictional stress (Fig. 2.13d) over the slope. The theory developed by [Bai et al. \(2021\)](#) works very well in predicting the topographic form stress (Fig. 2.13d). The sea ice internal stress divergence and ice-ocean stress over the continental slope, which are the terms in the force balance that this study is most focused on, are accurately captured by the reduced-order model (Fig. 2.13c). Because of the simplified two-layer discretization, which is equivalent to assuming a linear vertical velocity profile in the ocean, this model is not able to represent the complex vertical structure of the slope current. Thus it substantially underestimates the baroclinic transport over the slope (Fig. 2.13b). Since this model has the assumption of zero time-averaged meridional flow in the ocean, it is not suitable for simulating cases with varying offshore buoyancy gradients. Understanding the effects of horizontal buoyancy gradients necessarily requires an understanding of the meridional overturning circulation as well, hence we leave it for further study.

As discussed in sections 2.3 and 2.4, there can be two mechanisms associated with the diminished ice-ocean stress: eddy suppression and tidal acceleration. To separate the effects of eddy suppression and tidal acceleration, we create four control experiments: with and without tides, and with and without eddy suppression. In this model, we can explicitly turn off eddy suppression by setting a horizontally uniform eddy diffusivity $K = 300 \text{ m}^2/\text{s}$. A finite ice-ocean stress appears over the slope when eddies are not suppressed (Fig. 2.12g-h), which proves that eddy suppression is critical for the momentum balance of the ASC. Fig. 2.12c-d shows that tides strongly accelerate the lower level near the shelf break (125km offshore), decreasing the vertical velocity shear ($u_o^s - u_o^b$). Thus the momentum sink of the upper level, i.e., the isopycnal form stress, decreases (Eq. 2.14) near the shelf break, which accelerates the upper level. So the ice-ocean stress decreases near the

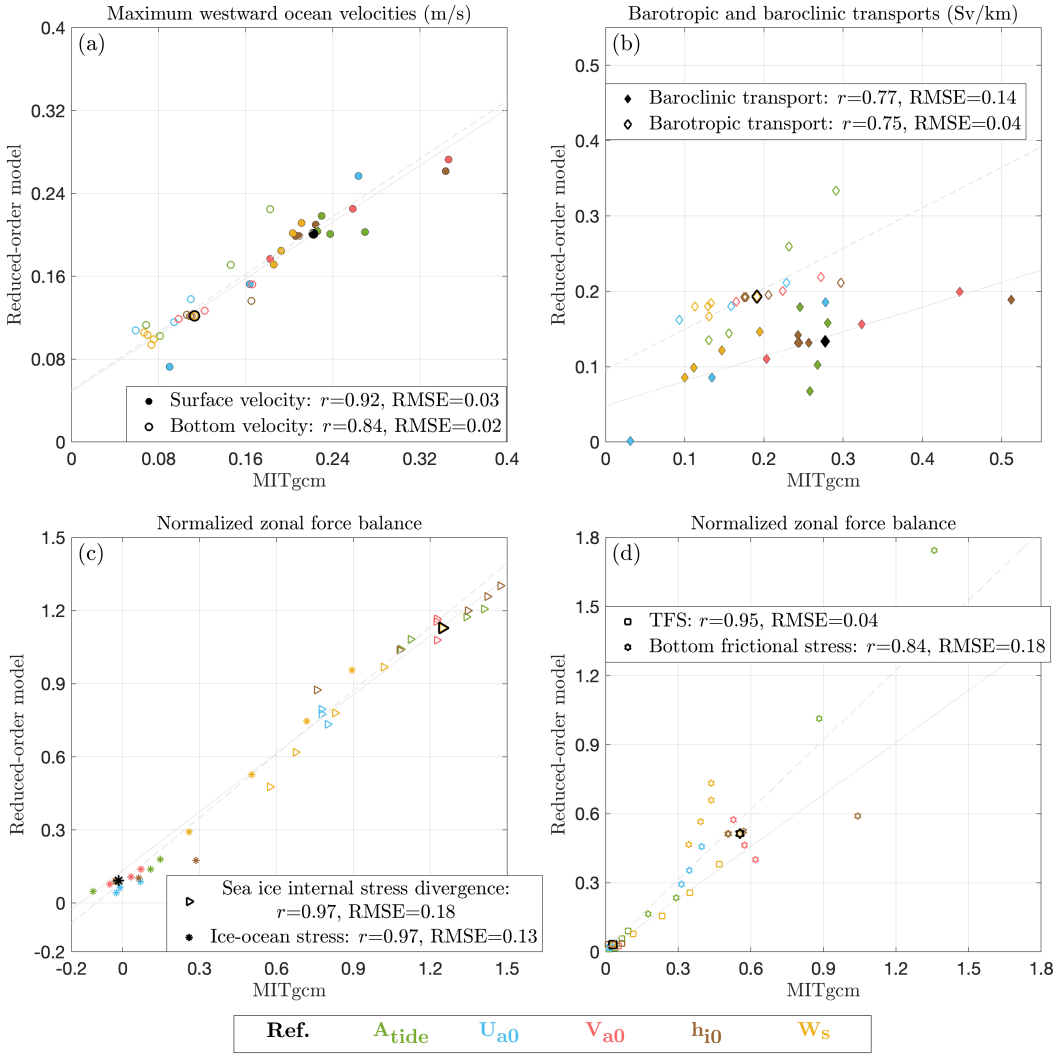


Figure 2.13: The reduced-order simulations compared with the 3D MITgcm simulations, where r is the linear correlation coefficient, and RMSE is the root-mean-square error. (a) Maximum westward ocean surface and bottom velocities in the slope region. (b) Mean westward barotropic and baroclinic transports over the continental slope. The barotropic transport is the ocean bottom velocity times ocean depth, and the baroclinic transport is the difference between the barotropic and the total transports. (c) Mean sea ice internal stress divergence and ice-ocean stress over the slope, normalized by the wind stress in the same region. (d) Mean topographic form stress and bottom frictional stress over the slope, normalized by the wind stress in the same region. The solid reference lines are the linear regression of the maximum westward ocean surface velocity, the baroclinic transport, normalized sea ice internal stress divergence, and normalized topographic form stress. The dashed reference lines are the linear regression of other scattered quantities.

shelf break with tides and no eddy suppression (Fig. 2.12d), though it remains significant over the continental slope. The ice-ocean stress can approach zero over the shelf break driven purely by tides, but this happens only when the tidal amplitude is sufficiently large.

We emphasize that little was done to “tune” this reduced-order model to the 3D simulations, largely because there are very few tunable parameters. Firstly, we choose an empirical constant to set the magnitude of the tidal advection in the reference case of the reduced-order model equivalent to the total ocean advection in the MITgcm reference simulation (Appendix A2.7.1.3). Secondly, the eddy parameterization is also tunable, but we choose to apply the eddy parameterization directly from [Stewart and Thompson \(2016\)](#) without any modification. The last tunable parameter is the minimum deformation rate Δ_0 in sea ice rheology (Appendix A2.7.1.6), which represents the minimum resistance of sea ice to external forcing. We regularize the ice deformation rate with this tunable parameter to prevent the ice internal stress from approaching infinity under the 1D assumption ([Vancoppenolle et al., 2012](#)). Increasing Δ_0 reduces the effective viscosity of sea ice (Appendix A2.7.1.8) and increases the magnitude of ice and ocean zonal velocities, but it does not qualitatively change the ice and ocean momentum budget.

2.6 Discussion and conclusions

In this study we utilized a high-resolution process-oriented model to investigate what controls the ice/ocean circulation and the pathways of momentum transfer in the ASC system with 100% sea ice cover. We also developed a reduced-order model of ice-ocean mechanical interactions to understand the role of eddy suppression over the continental slope. We emphasized the importance of topographic eddy suppression and sea ice momentum redistribution in the wind-ice-ASC system.

2.6.1 Key findings

In section 2.3 we showed the structure and intensity of the ASC in different control experiments, and highlighted the match of ice-ocean velocities over the slope (Fig. 2.4-2.5), indicating that local acceleration of the ocean by sea ice vanishes in this region.

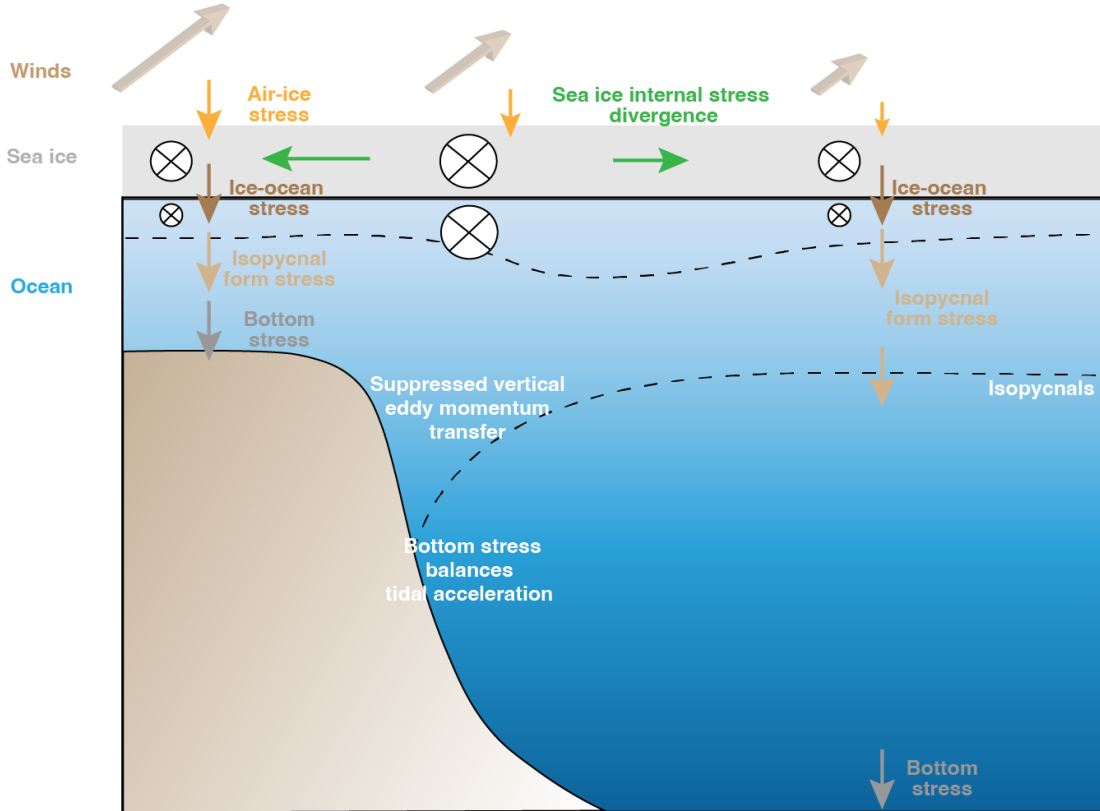


Figure 2.14: Schematic illustrating the momentum transfer in the wind-sea ice-ASC system in an equilibrium state, with exaggerated sea ice thickness. The 3D arrows denote northwestward surface winds, and other arrows denote the direction of zonal momentum transfer. The circles with crosses denote westward (along-slope, into the page) ice and ocean flow. The dashed curves denote isopycnals. Over the continental slope, eddies are suppressed and no momentum is transferred vertically via isopycnal form stress, leading to an equilibrium state in which the surface ocean velocity matches the ice velocity. Consequently, when the winds transfer westward momentum into the sea ice, it is redistributed horizontally away from the slope by sea ice internal stress divergence. Over the continental shelf and open ocean, ocean momentum sourced from ice-ocean stress is transferred downward by isopycnal form stress and finally removed by bottom frictional stress and topographic form stress.

We found that the intensity of the ASC increases with increasing tidal current amplitude, wind stress and slope steepness, and decreasing sea ice thickness (Fig. 2.4). The vertical structure of the ASC is primarily set by the offshore buoyancy gradient, varying from subsurface-intensified flow with a fresh shelf to a deep-reaching barotropic flow with a weak offshore buoyancy gradient, and to a bottom-intensified flow with a dense shelf (Fig. 2.5), in agreement with observations (e.g., [Le Paih et al., 2020](#)). We calculated the barotropic and baroclinic transports, and found that tides mainly change the barotropic transport, while wind forcing, sea ice thickness, slope steepness, and horizontal grid spacing predominantly affect the baroclinic transport (Fig. 2.6). Across a wide range of parameters, the zonal ocean surface velocity matches the velocity of sea ice over the continental slope. The approximate match of ice-ocean velocities occurs regardless of the strength of tidal amplitude, even when there are no tides (Fig. 2.4b). Exceptions occur in cases with very thin sea ice (Fig. 2.4e), dense outflows on the shelf (Fig. 2.5f), and very gentle topographic slope (Fig. 2.11c).

To determine the dynamical mechanisms that control the circulation and transport of the ASC, we analyzed the zonal momentum balance in section 2.4. Fig. 2.14 illustrates the mechanisms and directions of momentum transfer in the ASC in the equilibrium state. Wind transfers momentum to the sea ice via air-ice stress. Then the sea ice horizontally redistributes the wind-input momentum away from the continental slope by internal stress divergence, therefore playing a critical role in the momentum balance of the ASC (Fig. 2.8a). Over the continental slope, the ASC is accelerated during the model spin-up until the speeds of sea ice and surface ocean coincide, and thus there is no ice-ocean momentum transfer. Tidal advection peaks over the slope and is locally balanced by bottom frictional stress (Fig. 2.8b). In the absence of tides, bottom frictional stress is very weak and balanced by a small amount of momentum input from ice-ocean stress and ocean advection (Fig. 2.8d). Over the continental shelf and the deep ocean, wind-input momentum is transferred downward by ice-ocean stress, then by isopycnal form stress, and is eventually dissipated at the sea floor by bottom frictional stress and topographic form stress. Ice-ocean momentum transfer becomes non-negligible for continental slopes that are much wider than is typical around Antarctica (Fig. 2.10c-d), or when dense water production and export occurs (Fig. 2.10e-f).

The reduced-order model verifies the hypothesis that eddy suppression is the key mechanism underlying the vanishing of the ice-ocean momentum transfer over the slope. As discussed in section 2.5, this reduced-order model accurately reproduces the zonal momentum budget in the 3D simulations (Fig. 2.13), and allows us to explicitly compare the cases with and without eddy suppression (Fig. 2.12). Our results show that over the continental shelf break, strong tidal acceleration reduces the ice-ocean stress, but the ice-ocean stress does not necessarily approach zero with the appearance of tides. Note that this contrasts with the suggestions of [Stewart et al. \(2019\)](#) and [Flexas et al. \(2015\)](#): when we turned on vertical momentum transfer over the slope by setting a uniform eddy diffusivity, the matching of sea ice and ocean surface velocities did not take place (Fig. 2.12c-d, g-h). Thus we concluded that the fundamental reason for the ice-ocean velocity match is the suppression of transient and standing eddies over the continental slope.

2.6.2 Limitations and implications

Our idealized model configuration enables efficient exploration of different dynamical mechanisms that control the circulation of the ice-ocean system, but the idealization also carries various limitations. For example, we neglect the baroclinicity of tidal currents, the complexity of varied tidal harmonic constituents, and the spacial variability in the tidal amplitudes, which may lead to underestimation of lateral momentum transfer in the ocean. As discussed by [Howard et al. \(2004\)](#) and [Koentopp et al. \(2005\)](#), the baroclinic tidal currents contribute more to the variability of ice-ocean stress in the northern Weddell Sea and Scotia Sea, compared with barotropic currents. Moreover, the model imitates typical winter conditions around the East Antarctic margins with permanent sea ice coverage, excluding seasonal variations. Though the change of shelf stratification, sea ice concentration and thickness associated with the seasonal cycle can strongly affect the circulation of the ASC, as implied by previous studies as well as our simulation results. Note that our findings are not in dispute with the previously-established understanding that local winds are the primary momentum source for the ASC (e.g., [Núñez-Riboni and Fahrbach, 2009](#)): in the equilibrium state, the vanishing of vertical momentum transfer in the core of the ASC does not imply that local winds are not the primary momentum source to the current as a whole. We expect

the picture of momentum balance drawn in this study to be applicable to the annual-mean state of the real ASC (see [Stewart et al., 2019](#)). Further work will be required to understand the transient adjustment of circulation and momentum balance to changes in sea ice concentration, wind stress, and buoyancy forcing. Another caveat is that we made a simple choice to prescribe sea ice inflow velocity at the southern boundary, and thus ignored the reality that sea ice forms over and interacts with the continental shelf. The influence of the sea ice inflow on the momentum balance remains to be determined. Since our results agree with the findings of [Stewart et al. \(2019\)](#), derived from a realistic ocean/sea ice model, we expect the sea ice inflow to have little impact on the overall momentum balance. In addition, we expect the features of the momentum balance gained here to hold for sea ice concentrations higher than 80% based on [Leppäranta \(2011\)](#). There are also further limitations in the reduced-order model due to the one-dimensional assumption, the oversimplification of vertical discretization, the neglect of sea ice thermodynamics, cross-slope buoyancy forcing, diapycnal mixing, and meridional overturning circulation. Despite the fact that it carries various caveats, the reduced-order model helps us to better understand the continental slope dynamics, especially the role of eddy suppression.

This study has several implications for future research on the ASC, which are potentially relevant to the simulation of Arctic ice-ocean dynamics in the presence of continental slopes. First, a thorough understanding of the feedback between sea ice and ocean transport is required. On the one hand, changes in sea ice properties such as ice thickness, ice concentration, and ice drift speed have an influence on ice internal stress, which is critical to ice and ocean momentum balance, and thus can affect ocean transport. So sea ice will possibly affect the role of ASC as a barrier to prevent warm water intrusion and the melting of ice shelves. Meanwhile some ocean properties such as the lateral buoyancy gradient and tidal amplitude affect the concentration, thickness and transport of sea ice. We therefore emphasize the importance of coupled sea ice-ocean dynamics in future model studies of the ASC. In addition, resolving the eddies or otherwise representing their suppression over the continental slope is important. The large-scale zonal variations in forcing, geometry and state of the ASC should also be addressed in future research. Moreover, this study implies that tides influence the strength of the ASC, but do not qualitatively change the momentum

balance of the ASC, since tidal advection is locally balanced by bottom frictional stress. Lastly, an important step forward from this study is the determination of the role of ASC momentum balance terms and their parameter dependences for the overturning circulation and cross-slope exchange.

2.7 Appendix

2.7.1 Formulation of the reduced-order model

In section 2.5, we included a high-level overview of the reduced-order model. In this appendix we provide more details on the model configuration to better enable reproducibility, including conventional formulations developed by previous studies and our adaptations that make those formulations suitable for this reduced-order model.

2.7.1.1 Model bathymetry

The bathymetry of the reduced-order model is defined as

$$\eta_b(y) = -Z_s - \frac{H - H_{\text{shelf}}}{2} \tanh\left(\frac{y - Y_s}{W_s}\right). \quad (2.10)$$

The description and values of the parameters are in Table 2.1. The ocean thickness in this model is $h_o(y) = -\eta_b(y)$.

2.7.1.2 Isopycnal form stress

The isopycnal form stress (IFS) represents the vertical momentum transfer by transient and standing eddies in the ocean. In this section we describe how to relate the IFS to the vertical velocity shear between the upper and the lower levels ($u_o^s - u_o^b$).

The thermal wind relation indicates that the geostrophic velocity shear $\partial_z u_g \approx (u_o^s - u_o^b)/(\frac{1}{2}h_o)$

is proportional to the latitudinal (offshore) buoyancy gradient,

$$\partial_z u_g = \frac{g}{f\rho_0} \partial_y \bar{\rho} = -\frac{1}{f} \partial_y \bar{b}, \quad (2.11)$$

where $b = -g(\rho/\rho_0 - 1)$ is the buoyancy, and a bar over the symbol represents its time average. The isopycnal slope s_{isop} is

$$s_{\text{isop}} \equiv -\frac{\partial_y \bar{b}}{\partial_z \bar{b}} = \frac{f \partial_z u_g}{\partial_z \bar{b}} \approx \frac{2f(u_o^s - u_o^b)}{N^2 h_o}, \quad (2.12)$$

where $\partial_z \bar{b} = N^2$, and N is the mean stratification between the upper and the lower levels. We assume the horizontal variations in the vertical stratification are very weak, and use a constant stratification in the reduced-order simulations. The topographic parameter δ is

$$\delta \equiv \frac{s_b}{s_{\text{isop}}} \approx -\frac{N^2 h_o}{2f(u_o^s - u_o^b)} \partial_y h_o, \quad (2.13)$$

where $s_b = -\partial_y h_o$ is the topographic slope.

Assuming that the vertical displacement of a given isopycnal η' is small, η' can be estimated as the buoyancy perturbation divided by the vertical buoyancy gradient, $\eta' \approx -b'/\partial_z \bar{b}$ (e.g., [Vallis, 2017](#)). The fluctuation of the pressure gradient is related to the velocity perturbation using the geostrophic balance, $\partial_x p' = \rho_o f v'$. Therefore the IFS is

$$F_{\text{isop}} = -\overline{\eta' p'_x} = \rho_o f \overline{\frac{v' b'}{\partial_z \bar{b}}} = -\rho_o f K \frac{\partial_y \bar{b}}{\partial_z \bar{b}} = \rho_o f K s_{\text{isop}} = 2\rho_o f^2 K \frac{(u_o^s - u_o^b)}{N^2 h_o}, \quad (2.14)$$

where the meridional eddy buoyancy flux is $\overline{v' b'} = -K \partial_y \bar{b}$, and K is the eddy diffusivity. We apply the eddy diffusivity parameterization following [Stewart and Thompson \(2013\)](#),

$$K = K_0 \left[1 + \frac{1}{2} \sqrt{(1 - |\delta|)^2 + 4\gamma^2 |\delta^2|} - \frac{1}{2} \sqrt{(1 + |\delta|)^2 + 4\gamma^2 |\delta^2|} \right], \quad (2.15)$$

where $K_0 = 300$ m²/s and $\gamma = 0.05$. Note that this parameterization doesn't generalize because it is an approximate fit to the diagnosed K in the reference simulation of [Stewart and Thompson](#)

(2013), and can only be applied to simulations with a similar model setup. The key feature of this parameterization is that the eddy diffusivity K is greatly suppressed when $|\delta| \geq 1$.

2.7.1.3 Tidal acceleration

Following Loder (1980), the vertically averaged tidal velocities are

$$v_t = A_{\text{tide}} \frac{H}{h_0} \sin(\omega t). \quad (2.16a)$$

$$u_t \approx A_{\text{tide}} \frac{H}{h_0} \sin(\omega t + \phi_t), \quad (2.16b)$$

where ϕ_t is the phase lag between u_t and v_t . The meridional tidal velocity squared averaged over a tidal cycle is:

$$\overline{v_t^2} = \frac{1}{2} \left(A_{\text{tide}} \frac{H}{h_0} \right)^2. \quad (2.17)$$

Tides enhance ocean bottom frictional stress and topographic form stress, so we add a mean tidal velocity to these terms, described in the following sections. We assume that when averaged over a tidal cycle, the momentum flux convergence in the ocean is mainly contributed by tidal advection (the rationale for this assumption will be described in Appendix B),

$$F_{\text{tide}} = -\rho_o \frac{\partial}{\partial y} \int \overline{u'v'} dz \approx -\rho_o \frac{\partial}{\partial y} \int \overline{u_t v_t} dz = -s_b \rho_o \frac{1}{2} \left(A_{\text{tide}} \frac{H}{h_0} \right)^2 \cos \phi_t = -s_b \rho_o \overline{v_t^2} C \quad (2.18)$$

where $C = \cos \phi_t$ is an empirical constant representing the effect of phase lag ϕ_t between u_t and v_t on the magnitude of tidal advection. $C \approx -0.076$ is selected to set the magnitude of tidal advection in the reduced-order model equivalent to that of the 3D reference simulation.

2.7.1.4 Surface stresses

As discussed in section 2.5, the air-ice stress and ice-ocean stress have standard quadratic formulations, while the ocean bottom stress is modified by tidal oscillations. As in the MITgcm

simulations, the air-ice stress and the ice-ocean stress are

$$\tau_{\text{ai}} = \rho_a C_{\text{ai}} |\mathbf{u}_a| \mathbf{u}_a, \quad (2.19\text{a})$$

$$\tau_{\text{io}} = \rho_o C_{\text{io}} |\mathbf{u}_i - \mathbf{u}_o| (\mathbf{u}_i - \mathbf{u}_o), \quad (2.19\text{b})$$

where $\rho_a = 1.3 \text{ kg/m}^3$ is the air density. The drag coefficients C_{ai} , C_{io} , and the wind speed distribution in the reduced-order model are consistent with the MITgcm simulations. The modified ocean bottom stress averaged over a tidal cycle is

$$\tau_b \approx \rho_o C_b |\mathbf{u}_o^b + \mathbf{u}_t| \mathbf{u}_o^b \approx \rho_o C_d \sqrt{(u_o^b)^2 + \bar{u}_t^2 + \bar{v}_t^2} \mathbf{u}_o^b \approx \rho_o C_d \sqrt{(u_o^b)^2 + 2\bar{v}_t^2} \mathbf{u}_o^b. \quad (2.20)$$

2.7.1.5 Topographic form stress

[Bai et al. \(2021\)](#) have developed a barotropic, quasigeostrophic theory for standing Rossby waves and extended their theory to a bathymetry with a continental shelf and slope. Following [Bai et al. \(2021\)](#), the topographic form stress in the reduced-order model is

$$F_{\text{tfs}} = -\frac{1}{2} \frac{\alpha_b^2}{(h_o^b)^2} \frac{r_b u_o^b f_0^2 / k_0^2}{(u_o^b + c_{k0})^2 + \left(\frac{r_b}{k_0 h_o^b}\right)^2}, \quad (2.21)$$

where $k_0 = 2\pi/100 \text{ km}^{-1}$ is the wavenumber of the zonal bathymetric variation, r_b is the bottom drag coefficient, $c_{k0} = -\beta/k_0^2$ is the barotropic Rossby wave speed, $\beta = \beta_p + \beta_t = \beta_p + fs_b/h_o$ is the sum of the planetary beta parameter and the topographic beta parameter. α_b is the along-slope variation of the bathymetry (the difference in elevation between the bumps and the troughs, Fig. 2.2), obtained from the corresponding 3D MITgcm model bathymetry. Similar to the modified ocean bottom stress (Eq. 2.20), we add the mean tidal velocity to the bottom drag coefficient to simulate the effect of tides on topographic form stress,

$$r_b = C_d \sqrt{(u_o^b)^2 + 2\bar{v}_t^2}. \quad (2.22)$$

In the reduced-order simulations, the first term in the denominator $(u_0^b + c_{k0})^2$ in Eq. 2.21 is about 300 times larger than the second term $(r_b/k_0/h_0^b)^2$.

2.7.1.6 Sea ice rheology

We use a standard viscous-plastic (VP) rheology following [Hibler \(1979\)](#) and [Heorton et al. \(2014\)](#), and derive the sea ice rheology terms in the ice momentum equation under the assumptions (i)-(iii) in section 2.5. The components of the two-dimensional sea ice internal stress tensor σ are expressed as

$$\sigma_{ij} = 2\eta\dot{\epsilon}_{ij} + (\zeta - \eta)\dot{\epsilon}_{kk}\delta_{ij} - \frac{1}{2}p\delta_{ij}, \quad (2.23)$$

where δ_{ij} is the Kronecker delta. $\dot{\epsilon}_{ij} = \frac{1}{2}(\frac{\partial u_i}{\partial x_j} + \frac{\partial u_j}{\partial x_i})$ denote the components of the strain-rate tensor (i and j represent the zonal and the meridional directions), and $\dot{\epsilon}_{kk} = \dot{\epsilon}_{11} + \dot{\epsilon}_{22}$ using the Einstein summation convention. $\zeta = \frac{p}{2\Delta}$ is the bulk viscosity. $\eta = \frac{\zeta}{e^2}$ is the shear viscosity. $e = 2$ is the dimensionless elastic modulus in ice rheology, which defines the elliptical aspect ratio. The ice compressive strength is $p = p^*h_iG(A_i) = p^*h_i\exp[-c(1 - A_i)]$, where $p^* = 4 \times 10^4$ N/m² is the ice pressure constant, and c is an empirical constant ([Hibler, 1979](#)). We assume the sea ice concentration $A_i = 1$ in all of the reduced-order simulations, so $p = p^*h_i$. The sea ice deformation rate is defined as

$$\Delta = \left[(1 + e^{-2})(\dot{\epsilon}_{11}^2 + \dot{\epsilon}_{22}^2) + 4e^{-2}\dot{\epsilon}_{12}^2 + 2(1 - e^{-2})\dot{\epsilon}_{11}^2\dot{\epsilon}_{22}^2 \right]^{1/2}. \quad (2.24)$$

Under the assumptions (i)-(iii) in section 2.5,

$$\dot{\epsilon}_{11} = 0, \quad \dot{\epsilon}_{22} = \frac{\partial v_i}{\partial y}, \quad \dot{\epsilon}_{12} = \dot{\epsilon}_{21} = \frac{1}{2}\frac{\partial u_i}{\partial y}. \quad (2.25)$$

When Δ approaches zero, we regularize σ by setting $\Delta_0 = 10^{-6}s^{-1}$, which is the minimum deformation rate for ice rheology to prevent the viscosity from approaching infinity ([Vancoppenolle et al., 2014](#)).

2012),

$$\Delta = \sqrt{\Delta_0^2 + \left[(1 + e^{-2}) \left(\frac{\partial v_i}{\partial y} \right)^2 + e^{-2} \left(\frac{\partial u_i}{\partial y} \right)^2 \right]}. \quad (2.26)$$

The sea ice internal stress divergence is $\partial_x \sigma_{11} + \partial_y \sigma_{21} = \partial_y \sigma_{21}$ in the zonal ice momentum equation, and $\partial_x \sigma_{12} + \partial_y \sigma_{22} = \partial_y \sigma_{22}$ in the meridional ice momentum equation, where the ice internal stress tensor components are

$$\sigma_{21} = 2\eta \dot{\epsilon}_{21} = \eta \frac{\partial u_i}{\partial y} = \frac{p^* h_i}{2e^2 \Delta} \frac{\partial u_i}{\partial y}, \quad (2.27a)$$

$$\sigma_{22} = 2\eta \dot{\epsilon}_{22} + (\zeta - \eta)(\dot{\epsilon}_{11} + \dot{\epsilon}_{22}) - \frac{p}{2} = (\zeta + \eta) \frac{\partial v_i}{\partial y} - \frac{p}{2} = (1 + e^{-2}) \frac{p^* h_i}{2\Delta} \frac{\partial v_i}{\partial y} - \frac{p^* h_i}{2}. \quad (2.27b)$$

2.7.1.7 Boundary conditions and initialization

Similar to the MITgcm configuration, we assume a free-drift ice boundary for the reduced-order model. We solve Eq. 2.2 for given boundary ice thickness (h_{i0}) and wind speeds to get the sea ice velocities at the southern boundary (U_{i0} , V_{i0}). We linearly extrapolate u_o^s and u_o^b at the southern boundary, and u_i , v_i , h_i , u_o^s and u_o^b at the northern boundary. The reduced-order model is initialized with a uniform ice thickness h_{i0} , a uniform meridional ice velocity V_{i0} , and a stationary ocean.

2.7.1.8 Grid spacing, numerical schemes and time step

The reduced-order model is implemented with Arakawa C-grids (Arakawa and Lamb, 1977) to enforce conservation of mass with a second-order center-in-space scheme for space discretization. The zonal (u-grid) and meridional (v-grid) velocities are staggered in space with u-grid defined at the grid center and v-grid defined at the grid corners. The sea ice thickness is defined on the u-grid. We neglect advection terms in the momentum equations and use the upwind scheme for advection in the sea ice thickness equation.

The time step of the reduced-order model is limited by sea ice internal stress divergence. To estimate the maximum time step, we apply the scale analysis below:

$$\frac{du_i}{dt_{\max}} \sim \frac{1}{h_i} \frac{d\sigma_{21}}{dy} \sim \frac{p^*}{2\rho_i e^2 \Delta_0} \frac{du_i}{dy^2} \sim \nu_{\text{eff}} \frac{du_i}{dy^2}, \quad (2.28)$$

where $\nu_{\text{eff}} = p^{\star}/(2\rho_i e^2 \Delta_0)$ is the effective viscosity, and $dt_{\max} \sim dy^2/\nu_{\text{eff}}$ is the maximum time step. While numerical models are commonly implemented with additional solvers (such as LSR in MITgcm) to deal with the requirement of extremely small time step associated with sea ice rheology, we prefer simple time stepping method because this model is computationally inexpensive. The maximum time step required by the forward Euler method is larger than that of the third-order Adams-Basforth method (AB3) in the experiment, so we implement the forward Euler method for time stepping.

In the reduced-order simulations, the meridional grade spacing is 5 km, and the required time step is 1.8 s ($dt_{\max} \sim 4.7$ s). The spatial convergence of the reduced-order model is examined using 2-km spacing and a 0.25-s time step, and we find that using this higher spatial resolution has little effect on the solution (results not shown). Each simulation reaches its equilibrium state after a 300-day integration, and is run for a total of 500 days to perform analysis.

2.7.2 Decomposition of the total advection for the 3D MITgcm simulations

This appendix includes the methods to temporally decompose the total zonal ocean advection into three components: tidal, eddy and mean, following [Stewart et al. \(2019\)](#), as well as the rationale for representing the total advection by its tidal component in the reduced-order model.

The zonal ocean momentum advection is expressed as

$$-(\mathbf{u} \cdot \nabla)u = -(u\partial_x u + v\partial_y u + w\partial_z u) = \underbrace{v(\partial_x v - \partial_y u)}_{\text{Vorticity Adv.}} \underbrace{-w\partial_z u}_{\text{Vertical Adv.}} \underbrace{-\partial_x(u^2 + v^2)/2}_{\text{Kinetic Energy Gradient}}, \quad (2.29)$$

where *Adv.* is the abbreviation for *Advection*. The following operators are defined for decomposition, representing an average over two tidal periods (1 model day) and an average of *daily averaged* quantities over 5 model years.

$$\overline{\bullet}^T = \frac{1}{1 \text{ day}} \int_{t_0}^{t_0+1 \text{ day}} \bullet dt, \quad (2.30a)$$

$$\overline{\bullet}^E = \frac{1}{5 \text{ years}} \int_{t_0}^{t_0+5 \text{ years}} \overline{\bullet}^T dt. \quad (2.30b)$$

The subscript m , e and t denote time-mean, and the eddy and tidal components of the quantity, respectively (Stewart et al., 2019).

$$\mathbf{u}_m = \overline{\mathbf{u}}^T = \overline{\mathbf{u}}^E, \quad (2.31a)$$

$$\mathbf{u}_e = \overline{\mathbf{u}}^T - \overline{\mathbf{u}}^E, \quad (2.31b)$$

$$\mathbf{u}_t = \mathbf{u} - \mathbf{u}_m - \mathbf{u}_e = \mathbf{u} - \overline{\mathbf{u}}^T. \quad (2.31c)$$

We follow the spacial discretization of the momentum advection implemented in MITgcm, and calculate the mean, eddy, and tidal advection using the 5-year averaged diagnostics u_m , v_m , w_m , Total Adv., and the daily averaged diagnostics \bar{u}^T , \bar{v}^T and \bar{w}^T .

$$\text{Mean Adv.} = v_m(\partial_x v_m - \partial_y u_m) - w_m \partial_z u_m - \partial_x(u_m^2 + v_m^2)/2, \quad (2.32a)$$

$$\begin{aligned} \text{Eddy Adv.} &= \overline{v_e(\partial_x v_e - \partial_y u_e)}^E - \overline{w_e \partial_z u_e}^E - \overline{\partial_x(u_e^2 + v_e^2)/2}^E \\ &= \overline{\bar{v}^T(\partial_x \bar{v}^T - \partial_y \bar{u}^T)}^E - \overline{\bar{w}^T \partial_z \bar{u}^T}^E - \overline{\partial_x(\bar{u}^T)^2 + \bar{v}^T)^2/2}^E - \text{Mean Adv.}, \end{aligned} \quad (2.32b)$$

$$\text{Tidal Adv.} = \text{Total Adv.} - \text{Mean Adv.} - \text{Eddy Adv.} \quad (2.32c)$$

Note that although we endeavored to improve the algorithm, the decomposition is likely somewhat imperfect due to the complexity of reproducing the MITgcm discretization.

Fig. 2.15 shows the zonally and vertically integrated zonal momentum advection for the reference case and the cases with very dense shelf and very fresh shelf. For the simulations with a moderate offshore buoyancy gradient similar to the reference case, the ocean advection is primarily contributed by tidal advection. In the very dense shelf case ($\Delta S = 0.62$ psu), strong vertical stratification intensifies the tidal momentum flux convergence and tidal rectification (Chen and Beardsley, 1995). Baroclinic instabilities arise from the sharp offshore buoyancy gradient and enhance the eddy advection. In the very fresh shelf case ($\Delta S = -1.17$ psu), the mean and eddy components play a role in setting the total advection over the edge of the continental shelf (100-120 km offshore). Except for the cases with extreme offshore buoyancy gradient, total advection is intensified over the continental slope, and is dominated by the tidal component. This supports the interpretation of

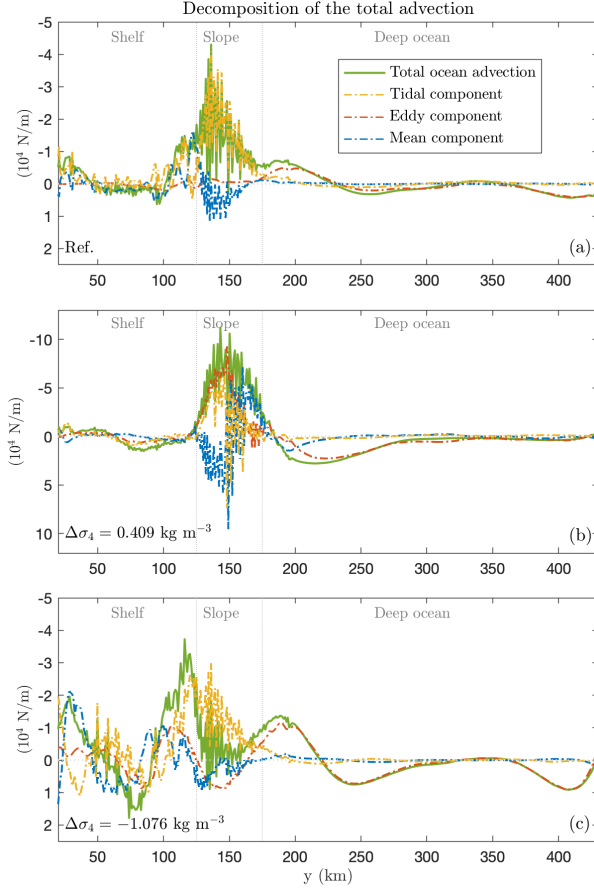


Figure 2.15: Temporal decomposition of the total ocean advection in the reference simulation (a), the very dense shelf case (b), and the very fresh shelf case (c). Note that the y-axis limits are different in the three panels.

the advective forcing as tidal rectification in almost all experiments. Hence we parameterize the tidal advection in the reduced-order model, and neglect other advection components to simplify and stabilize the model.

2.7.3 3D Model bathymetry

In this appendix we describe the formulation of the bathymetry used in the 3D MITgcm simulations. The bathymetry $z = \eta_b(x, y)$ is defined by equation 2.1, where $\mathcal{H}[\cdot]$ denotes the Heaviside step function. The values of the topographic parameters are listed in Table 2.1.

$$\eta_b(x, y) = -Z_s - \frac{H_{\text{trough}}}{2}(N_{\text{trough}} - 1) - h_{\text{trough}}(x, y) - \frac{H - H_{\text{shelf}} - 2h_{\text{trough}}(x, y)}{2} \tanh\left(\frac{y - Y_s}{W_s}\right), \quad (2.1a)$$

$$h_{\text{trough}}(x, y) = \sum_{n=1}^{N_{\text{trough}}} \mathcal{H}[y - Y_{\text{trough}}] H_{\text{trough}} \exp\left(-\left(\frac{x - L_x(2n - 1 - N_{\text{trough}})/2/N_{\text{trough}}}{W_{\text{trough}}}\right)^4\right) \dots \quad (2.1b)$$

$$\times \left(1 - \frac{1}{2} \mathcal{H}[(Y_s - W_s) - y] \left(1 + \cos\left(\pi \frac{y - Y_{\text{trough}}}{Y_s - W_s - Y_{\text{trough}}}\right)\right)\right).$$

CHAPTER 3

Heat transport across the Antarctic Slope Front controlled by cross-slope salinity gradients

This chapter contains the manuscript by Y. Si, A. L. Stewart, and I. Eisenman, published in Science Advances in 2023 ([Si et al., 2023](#)).

Abstract

The Antarctic Slope Front (ASF) is a strong gradient in water mass properties close to the Antarctic margins, separating warm water from the Antarctic ice sheet. Heat transport across the ASF is important to Earth's climate, as it influences melting of ice shelves, the formation of bottom water, and thus the global meridional overturning circulation. Previous studies based on relatively low-resolution global models have reported contradictory findings regarding the impact of additional meltwater on heat transport toward the Antarctic continental shelf: It remains unclear whether meltwater enhances shoreward heat transport, leading to a positive feedback, or further isolates the continental shelf from the open ocean. In this study, heat transport across the ASF is investigated using eddy- and tide-resolving, process-oriented simulations. It is found that freshening of the fresh coastal waters leads to increased shoreward heat flux, which implies a positive feedback in a warming climate: Increased meltwater will increase shoreward heat transport, causing further melt of ice shelves.

3.1 Introduction

Recent studies have shown that the volume loss from Antarctic ice shelves is accelerating (Paolo et al., 2015; Pritchard et al., 2012), which is largely attributed to iceberg calving (Greene et al., 2022; Schloesser et al., 2019; Rackow et al., 2017) and ocean-driven basal melt (Pritchard et al., 2012; Adusumilli, Susheel and Fricker, Helen Amanda and Siegfried, Matthew R and Padman, Laurie and Paolo, Fernando S and Ligtenberg, Stefan RM, 2018). Thinning of the Antarctic ice shelf reduces buttressing, driving acceleration of mass loss from the Antarctic ice sheet (Gudmundsson et al., 2019; Gudmundsson, 2013; Goldberg et al., 2009) and contributing to sea level rise (Pattyn and Morlighem, 2020; DeConto et al., 2021). Observations and model projections have indicated a widespread freshening of the Antarctic margins (Jacobs, 2006; Jacobs and Giulivi, 2010; Schmidtko et al., 2014; De Lavergne et al., 2014) possibly due to increased meltwater discharge (De Lavergne et al., 2014; Silvano et al., 2018; Jullion et al., 2013) and changes in precipitation minus evaporation, combined with wind-driven freshwater advection by sea ice (Haumann et al., 2016; Swart et al., 2018). Coastal freshening can reshape the ocean circulation around the Antarctic margins (Hellmer et al., 2017; Jourdain et al., 2017; Hattermann, 2018; Bronselaer et al., 2018) and potentially modify the shoreward ocean heat transfer. On the other hand, additional on-shelf heat transport will lead to enhanced coastal freshening due to increased melting of ice shelves. Therefore, understanding the interplay between meltwater discharge and ocean heat transport is critical for predicting future climate change, especially for sea level rise (King et al., 2012), dense water formation, and the global overturning circulation (Thompson et al., 2018).

The Antarctic Slope Front (ASF) can be categorized into fresh-, dense-, and warm-shelf regimes (Thompson et al., 2018). Each shelf regime has distinct frontal structure and dynamics. Figure 3.1A shows the climatology of ocean salinity at 500-m depth or at the seafloor where the ocean is shallower than 500 m. In the Ross Sea and the Weddell Sea, where the Antarctic bottom water (AABW) is formed, the coastal salinity is relatively high. Close to the Antarctic Peninsula and in East Antarctica, the continental shelves are fresher than the water masses off-shore. Figure 3.1 (B and C) shows cross sections of ocean salinity, highlighting the “fresh shelves” and “dense shelves”

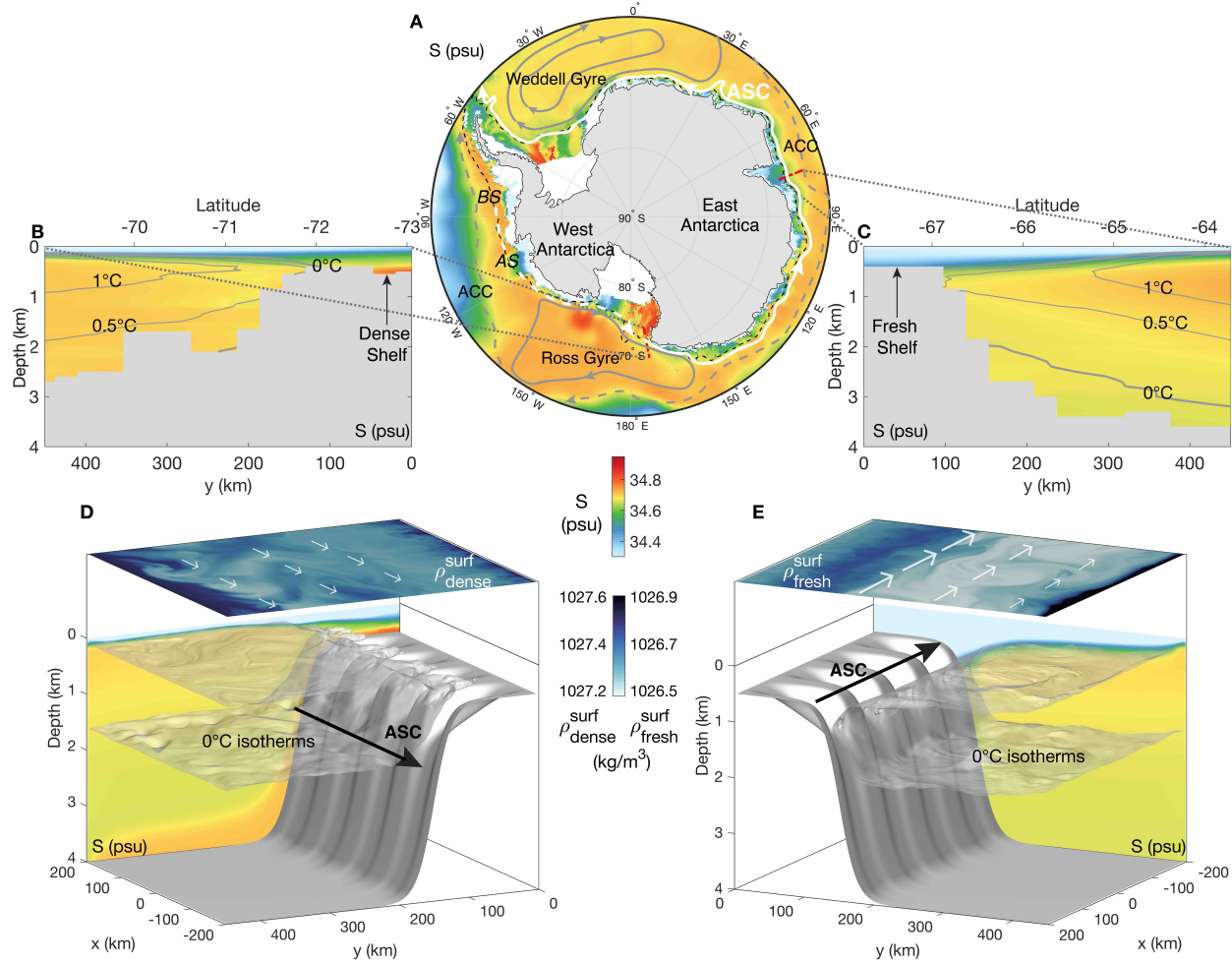


Figure 3.1: Salinity regimes around Antarctica and in our model configuration. **(A)** Climatology (1981–2010) of 500-m depth ocean salinity or seafloor salinity where the ocean is shallower than 500 m with the unit of psu (practical salinity unit). The black dashed curve indicates the 1000-m isobath. The white arrows represent the Antarctic Slope Current (ASC), with white dashed lines in the Bellingshausen (BS), Amundsen (AS), and Ross Seas denoting the uncertain initiation of the ASC (Thompson et al., 2018). The solid gray arrows represent the Ross Gyre and the Weddell Gyre. The dashed gray arrows represent the Antarctic Circumpolar Current (ACC). **(B)** A cross section of ocean salinity taken in the Ross Sea (73.05°–69.01°S, 172.13°E), where the shelf is relatively salty, overlaid by gray contours of surface-referenced potential temperature. **(C)** A cross section of ocean salinity taken in East Antarctica (67.75°–63.71°S, 76.38°E), where the shelf is relatively fresh, overlaid by gray contours of surface-referenced potential temperature. The data used in (A) to (C) come from World Ocean Atlas 2018 (Zweng et al., 2019). **(D)** Results of the dense-shelf (equivalent to “salty-shelf” in this study) simulation with instantaneous sea surface potential density ($\rho_{\text{dense}}^{\text{surf}}$), 0°C isotherms, and time- and zonal-mean salinity in the background. The white arrows sketch the direction and relative strength of sea surface currents, and the black arrow schematically shows the direction of the ASC. **(E)** As (D), but shows the fresh-shelf simulation. $\rho_{\text{fresh}}^{\text{surf}}$ is the instantaneous sea surface potential density of the fresh-shelf simulation.

around Antarctica. The arrows in Fig. 3.1A indicate the major ocean current systems around the Antarctic margins, with the Antarctic Slope Current (ASC) highlighted in white. As a strong gradient in water mass properties between the cold shelf water and the warmer circumpolar deep water (CDW), the ASF is essential in ocean heat transfer toward the Antarctic margins (Thompson et al., 2018). The ASF and the associated westward ASC form a barrier to exchanges such as heat, freshwater, and nutrients between the continental shelf and the open ocean (Jacobs, 1991; Whitworth et al., 1998; Heywood et al., 2014), except along the West Antarctic Peninsula (WAP) and a small sector of East Antarctica (the warm-shelf regime) (Thompson et al., 2018). In the Bellingshausen Sea and the Amundsen Sea, where the ASC is weaker (see Fig. 3.1A), warm water at depth can access ice shelves via submarine troughs (Thompson et al., 2018), leading to the highest ice shelf thinning rates around Antarctica (Paolo et al., 2015; Pritchard et al., 2012; Depoorter et al., 2013) and thereby to coastal freshening.

Previous studies with relatively coarse resolution show that coastal freshening leads to increased shoreward heat transport, which triggers strong subsurface warming around Antarctica (Schloesser et al., 2019; Bronselaer et al., 2018; Menviel et al., 2010; Fogwill et al., 2015; Sadai et al., 2020; Golledge et al., 2019). For example, Golledge et al. (2019) found that meltwater from Antarctica will trap warm water below the sea surface, creating a positive feedback that increases Antarctic ice loss. Some other studies have opposite predictions of ocean heat transport in response to meltwater (Bintanja et al., 2013; Swingedouw et al., 2008). For example, using a global ocean-sea ice model, Moorman et al. (2020) found that coastal freshening tends to isolate the continental shelves from offshore heat. However, these modeling studies did not fully resolve mesoscale eddies in their simulations due to the small Rossby radius of deformation around Antarctica (Stewart and Thompson, 2016; St-Laurent et al., 2013), and thus potentially omitted a key source of onshore ocean heat transfer contributed by eddies. Nakayama et al. (2021) found increased shoreward heat transport associated with coastal freshening in East Antarctica, using a horizontal grid spacing of 3 to 4 km. However, the mechanism underlying the increased onshore heat transport remains unclear.

Though wind and buoyancy forcing have historically been recognized as key drivers of the ASC (Hattermann, 2018; Jacobs, 1991; Whitworth et al., 1998), recent studies have emphasized the role

of small-scale and/or high-frequency variability in the cross-slope heat and water mass exchanges, such as mesoscale eddies (Stewart and Thompson, 2016; Nøst et al., 2011; Thompson et al., 2014; Stewart and Thompson, 2015), tides (Padman et al., 2009; Muench et al., 2009; Holland et al., 2014; Fer et al., 2016), dense outflows (Whitworth and Orsi, 2006), and shelf waves (Kusahara and Ohshima, 2014; Spence et al., 2017). Previous studies have shown that dense AABW export enhances shoreward heat transport by eddies generated at the interface between the AABW and the CDW (Stewart and Thompson, 2016) or by pulses of dense shelf water outflow in canyons (Morrison et al., 2020). For fresh shelves, eddies are shown to be important in advecting warm water into the ice shelf cavities (Hattermann, 2018; Nøst et al., 2011). Using hydrographic observation and high-resolution idealized numerical simulations, Nøst et al. (2011) suggested that overturning circulation induced by baroclinic eddies in the ASF brings warm deep water (WDW) onto the shelf and into the ice shelf cavity. Using hydrographic profiles of the fresh shelf at Kapp Norvegia, Hattermann (2018) showed enhanced baroclinic eddy growth rates in summer with fresher coastal waters compared with that in winter. By incorporating eddy overturning in an idealized two-layer model, Hattermann (2018) revealed that coastal freshening may lead to shoaling of the WDW, which allows more warm water intrusion onto the shelf. However, the tools used in these works are limited to their specific shelf regimes, and there was no comprehensive understanding of the mechanisms from a single consistent model that could be applied to different shelf regimes. Using a high-resolution, eddy- and tide-resolving regional model, Stewart et al. (2018) showed the approximate cancellation between tidal and mean heat fluxes in different Antarctic sectors and emphasized the role of eddies in net onshore heat transport. They suggested that heat transport by eddy stirring along isopycnals (more precisely, “eddy diffusion”) is the principal mechanism of onshore heat transport around the Antarctic margins.

In this study, we investigate the heat transport in the fresh- and dense-shelf regimes using a single consistent model. We show that if the resolution is high enough to resolve mesoscale eddies over the continental shelf and slope, coastal freshening leads to increased shoreward heat transport. In addition, we provide insight into the dynamical mechanisms of shoreward ocean heat transport driven by eddies, tides, and mean flows, as well as its sensitivity to wind forcing, sea ice, and

topography.

3.2 Results

3.2.1 Shoreward heat transport in the fresh- and dense-shelf regimes

We use a high-resolution process-oriented model configuration, MITgcm ASF (see Materials and Methods), which successfully simulates the fresh- and dense-shelf regimes of the ASF ([Si et al., 2022](#)). We varied seven parameters: salinity at the southern boundary, zonal wind speed, meridional wind speed, tidal current amplitude, sea ice thickness, the width of the continental slope, and horizontal grid spacing. We choose these parameters because winds, tides, and buoyancy forcing are the key drivers of the ASC system ([Thompson et al., 2018](#)), sea ice thickness and the geometry of the continental slope are shown to play an important role in redistributing momentum in the ASC ([Si et al., 2022](#)), and the ability of numerical models to resolve mesoscale eddies strongly depends on horizontal grid spacing. The results are compared to a reference simulation that is representative of typical winter conditions of the ASF with stratified shelf water and no dense water formation (see Materials and Methods). Figure 3.1 (D and E) shows the instantaneous 0°C isotherms, surface potential density, and zonal-mean salinity in our simulated “dense-shelf” and “fresh-shelf” cases. The northern boundary temperature and salinity are restored to winter climatology values across the ASF (see Materials and Methods). The southern boundary temperature and salinity are set based on observations: The temperature is restored to freezing temperature throughout the water column for all the simulations, and the salinity profiles are vertically uniform for fresh shelves and increase linearly with depth for dense shelves (see Materials and Methods for details). This is equivalent to adding meltwater throughout the column near the coast. The ASC flows westward along the slope and shifts from a surface-intensified current in the fresh-shelf case (Fig. 3.6A) to a bottom-intensified current in the dense-shelf case (Fig. 3.6C), consistent with observations ([Le Pail et al., 2020](#)).

Figure 3.2 shows that the sensitivity of shoreward heat transport to parameters varied among the simulations. The shoreward heat transport is largely controlled by the magnitude of the cross-slope

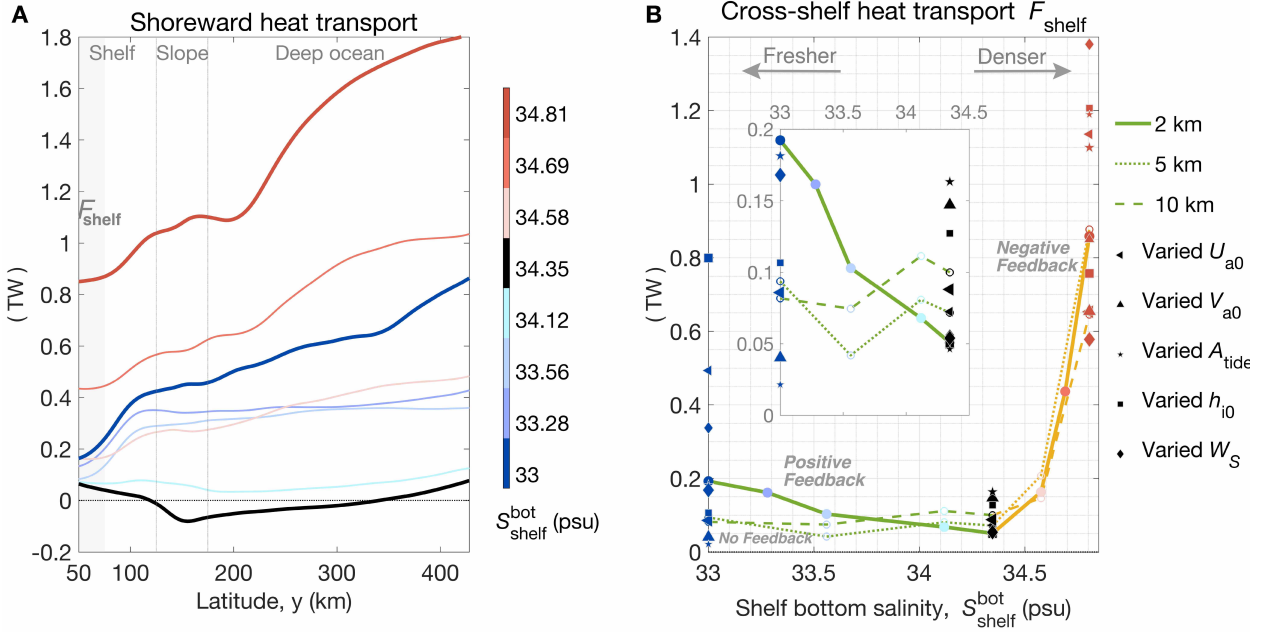


Figure 3.2: Sensitivity of shoreward heat transport. **(A)** Vertically and zonally integrated meridional advective heat flux in the simulations with varied shelf bottom salinity ($S_{\text{bot}}^{\text{shelf}}$) in TW (1 TW = 10^{12} W), as a function of latitude y . The horizontal resolution of these simulations is 2 km. The blue, black, and red lines represent simulations with low, reference, and high shelf salinity, respectively. Light gray denotes the latitudinal band (50 to 75 km) used to calculate the averaged heat transferred onto the shelf, F_{shelf} . The 20-km sponge layer at the northern boundary is not shown. **(B)** Heat transferred onto the continental shelf (F_{shelf}), as a function of shelf bottom salinity prescribed at the southern boundary. The solid, dotted, and dashed lines denote simulations with 2-, 5-, and 10-km resolution, respectively. The green and orange curves denote the fresh- and dense-shelf regimes, respectively. Positive slopes of F_{shelf} in the dense-shelf regime indicate a negative feedback; negative slope of F_{shelf} in the fresh-shelf regime indicates a positive feedback; zero slope corresponds to no feedback. For the fresh-shelf, reference, and dense-shelf cases, the sensitivity of F_{shelf} to other model parameters is indicated by markers with various shapes, with larger marker sizes indicating larger values of the corresponding parameters. U_{a0} and V_{a0} are the zonal and meridional wind speed at the southern boundary, respectively. A_{tide} is the prescribed barotropic tidal current amplitude. h_{i0} is the restoring sea ice thickness at meridional boundaries, which is also the initial sea ice thickness across the domain. W_S is the continental slope width. The inset plot is a zoomed-in view of F_{shelf} in the fresh-shelf regime.

salinity gradient (equivalently offshore buoyancy gradient), with some other parameters such as sea ice thickness and slope width greatly enhancing shoreward heat transport in the fresh-shelf and dense-shelf cases (Fig. 3.2B and Fig. 3.5). The shoreward heat flux is very close to zero in the reference case, in which there is almost no offshore buoyancy gradient. Both freshening and salinification of the shelf waters relative to the offshore waters lead to increased heat flux onto the continental shelf (Fig. 3.2A). The heat convergence over the continental shelf is locally balanced by ocean-sea ice heat flux due to sea ice melting (Fig. 3.8), which is sensitive to tidal amplitude. For continental shelves with large volumes of meltwater (fresh shelves), increased heat transport with freshening indicates further melt of the ice shelves, and thus, we expect a positive feedback based on the conceptual and high-resolution eddy-resolving process models of Hattermann (2018) and previous studies (Schloesser et al., 2019; Menviel et al., 2010; Golledge et al., 2019). In contrast, for dense shelves, since the shoreward heat trans-port increases with salinification, leading to further melt and freshening, we expect a negative feedback. The cross-shelf heat flux increases more rapidly per unit shelf buoyancy change in the dense-shelf regime than in the fresh-shelf regime.

Building on the salinity gradient experiments, we covaried the following additional parameters for three groups of experiments (fresh-shelf, reference shelf salinity, and dense-shelf) (Table 3.1): wind speeds, tidal amplitude, sea ice thickness, and continental slope width. For each group, we compared the perturbation experiments with the reference state of typical wind speeds, tides, winter sea ice thickness, and slope steepness. We additionally run simulations using coarser horizontal grid spacings (5 and 10 km) for comparison with our high-resolution (2 km) runs. To validate whether the standard eddy parameterization scheme can represent the shoreward heat transport accurately in climate models, we run these coarse simulations with and without the standard Gent-McWilliams/Redi (GM-Redi) parameterization schemes for mesoscale eddies (Gent and Mcwilliams, 1990; Gent et al., 1995; Redi, 1982). The perturbation experiments show that the sensitivity of shoreward heat transport to different parameters diverges for the fresh and dense shelf regimes. For fresh shelves, the shoreward heat transport increases greatly with thicker sea ice, weaker meridional or zonal winds, or steeper continental slope (Fig. 3.5 C to H). For dense shelves, the shoreward heat transport increases with steeper continental slope, thinner sea ice, and

weaker zonal wind and exhibits a non-monotonic response to tidal amplitude (Fig. 3.5 C to H).

The lines in Fig. 3.2B show the sensitivity of shoreward heat transport to horizontal grid spacing, with green and yellow lines corresponding to the fresh-shelf and dense-shelf regimes, respectively. For the cross-shelf heat transport (F_{shelf} , shoreward heat transport averaged over the latitudinal band $y = 50$ to 75 km), the simulations with coarser resolution (5 or 10 km) are able to capture the increase of shoreward heat transport in the dense-shelf regime. Since shore-ward heat transport in the dense-shelf regime is driven by dense water export through canyons (Morrison et al., 2020) (Fig. 3.3 B and F), this suggests that models can capture the heat transport as long as they resolve the canyons on the shelf. However, the coarse-resolution simulations perform poorly in the fresh shelf regime because, although they can resolve deep-water eddies, they do not adequately resolve baroclinic eddies over the continental shelf (referred to as “shelf eddies” hereafter). This is because the first baroclinic Rossby radius of deformation (Chelton et al., 1998) (close to 2.3 km over the continental shelf and 6.8 km in the deep ocean) is relatively small over the shelf. In contrast, repeating a subset of our experiments using a model resolution higher than 2 km (e.g., 1 km) does not qualitatively make any difference in reproducing the increased cross-shelf heat transport with coastal freshening in the fresh-shelf regime. It remains unclear at what horizontal resolution will the solution converge, which requires further study.

As for the cross-slope heat transport (F_{slope} , shoreward heat transport averaged over $y = 125$ to 150 km) in the fresh-shelf regime, the 5- and 10-km simulations can capture the trend of F_{slope} with varied shelf bottom salinity (Fig. 3.5B), but the magnitude of the change in F_{slope} is about two times smaller than that in the 2-km simulations. Note that the positive feedback in the fresh-shelf regime is related to the heat delivered onto the continental shelf (i.e., the cross-shelf heat transport) rather than the heat delivered onto the continental slope (i.e., the cross-slope heat transport). The 5- and 10-km models can partially reproduce the cross-slope heat transport, but not the cross-shelf heat transport, because the cross-slope heat transport largely depends on the tidal and mean components; since eddies are suppressed over the slope, the cross-slope heat transport does not rely on the model’s ability to resolve mesoscale eddies. In addition, the Rossby radius of deformation is larger over the slope than the shelf; thus, compared to shelf eddies, the slope eddies can be better

resolved by the 5- and 10-km models. Moreover, the standard GM-Redi eddy parameterization scheme is not enough to reproduce the positive feedback, leading to even worse performance in shoreward heat transport (Fig. 3.5 A and B), although it is possible that sophisticated “slope-aware” eddy parameterization schemes would perform better ([Wei and Wang, 2021](#); [Wei et al., 2022](#); [Wang and Stewart, 2018, 2020](#)).

3.2.2 Vertical structure of heat flux and overturning circulation

To provide mechanistic insight into the shoreward heat transport in different cases, we show the vertical structure of the southward advective heat fluxes in Fig. 3.3 (A and B) and heat function in Fig. 3.3 (C and D), for our high-resolution (2-km grid spacing) simulations. The heat function was first introduced by [Boccaletti et al. \(2005\)](#) to trace the oceanic pathways of heat (see Materials and Methods for details). For both cases, the advective heat flux is offshore directly at the surface due to wind-driven Ekman transport (Fig. 3.10 A and B). For fresh shelves, the shoreward heat transport increases in the ocean subsurface (Fig. 3.3 A and C). For dense shelves, the shoreward heat transport increases near the seafloor (Fig. 3.3 B and D).

In either case, the shoreward heat transport is associated with the overturning circulation. By vertically integrating meridional trans-port within potential density layers, we compute the isopycnal over-turning streamfunction ([Döös and Webb, 1994](#))

$$\bar{\psi}_{\text{isop}}(y, \sigma_2) = \overline{\left\langle \int_{z=\eta_b}^{z=0} v \mathcal{H}[\sigma_2 - \sigma'_2(x, y, z, t)] dz \right\rangle}^E, \quad (3.1)$$

where σ_2 is the potential density with a reference depth of 2 km, $\sigma'_2(x, y, z, t)$ is the simulated σ_2 field, $z = 0$ is the sea surface, $z = \eta_b$ is the sea floor elevation, v is the meridional velocity, $\mathcal{H}[\cdot]$ is the Heaviside function, the overbar denotes a 7-year time average (Eq. 3), and the angle brackets denote zonal integral. For fresh shelves, there is a shallow overturning associated with an export of fresh surface waters (Fig. 3.3E) that drives warm water inflow at the subsurface. The existence of such a shallow overturning due to shelf water freshening was first proposed by [Hattermann \(2018\)](#) based on observations. The deep overturning circulation in the fresh-shelf case is not connected

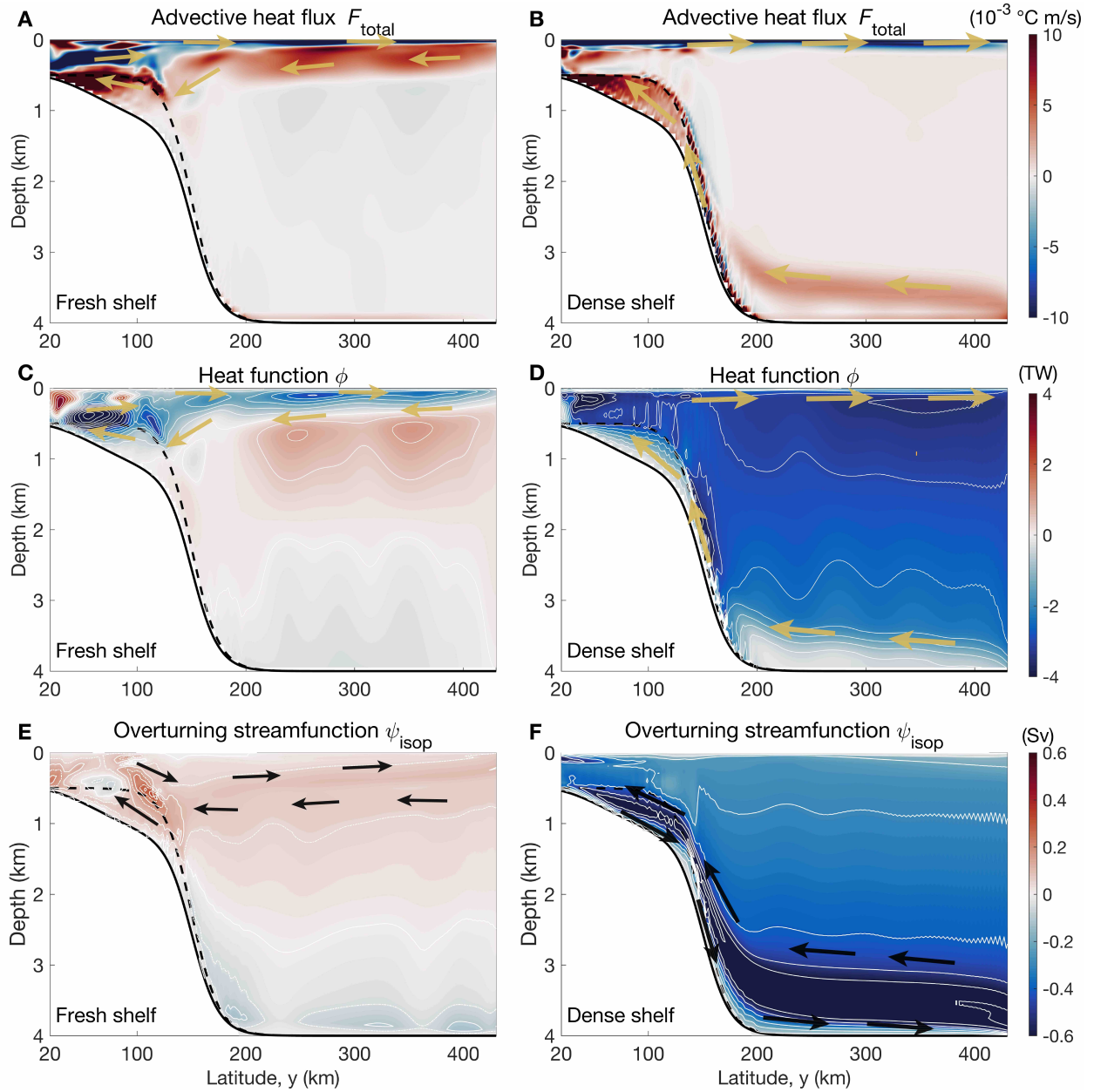


Figure 3.3: Pathways of heat and overturning circulation in the fresh-shelf and dense-shelf cases. (A and B) Time- and zonal-mean meridional advective heat flux. (C and D) Time-mean heat function in TW (1 TW = 10^{12} W). (E and F) Time-mean overturning streamfunction in Sv (1 Sv = $10^6 \text{ m}^3/\text{s}$). Yellow arrows denote the pathways of heat, and black arrows denote the direction of the overturning circulation. (A, C, and E) The fresh-shelf case. (B, D, and F) The dense-shelf case. The spacings of the color contours in all panels are 1/40 of the corresponding colorbar range. The black solid and dashed curves denote the deepest (bottom of the troughs) and shallowest (top of the troughs) bathymetry at each latitude (see Fig. 1, D and E), respectively. The 20-km sponge layers at the northern and southern boundaries are not shown.

to the continental shelf and thus does not affect the heat transport onto the shelf (Fig. 3.3E). For dense shelves, the overturning consists of an export of dense water near the seafloor (Fig. 3.3F) that drives a warmer return flow in the deep ocean.

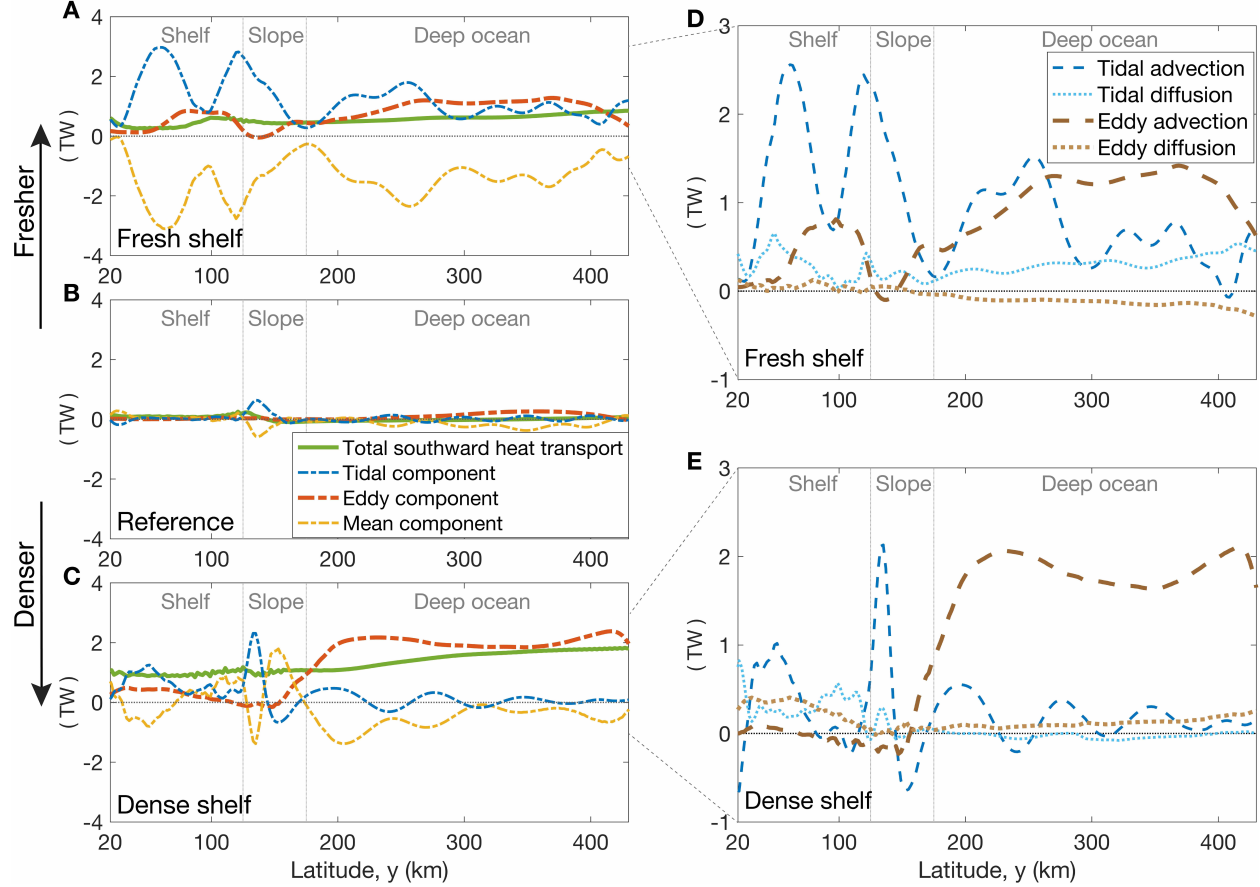


Figure 3.4: Temporal decomposition of the total shoreward heat transport. (A to C) Total shoreward heat transport, and its tidal, eddy, and mean components in the fresh-shelf, reference, and dense-shelf cases, integrated over the zonal/vertical (x/z) plane. (D and E) Tidal advection, tidal diffusion, eddy advection, and eddy diffusion in the fresh-shelf and dense-shelf cases, integrated over the zonal/vertical (x/σ_2) plane. In all panels, positive values correspond to southward (shoreward) heat transport. The 20-km sponge layers at the northern and southern boundaries are not shown. Note that the tidal heat transport is largely compensated by the mean component, except for the shelf break where eddies are suppressed by a strong topographic vorticity gradient. Because of this cancellation, the tidal and mean components contribute less to the total heat transport (especially for the fresh shelves), compared with eddies.

3.2.3 Role of small-scale and/or high-frequency variability

To understand the relative contribution of tides, transient eddies, and mean flows to shoreward heat transport, we temporally decompose the total heat transport into tidal, eddy, and mean components [building on [Stewart et al. \(2018, 2019\)](#); see Materials and Methods]. The vertical-integrated mean heat flux is negative in most regions (northward; Fig. 3.4, A and C) because the shoreward Ekman transport drives strong negative advective heat flux in the very surface of the ocean (Fig. 3.10, A and B). The shoreward heat flux carried by transient eddies substantially increases over the shelf and deep ocean for both fresh and dense shelves (Fig. 3.4, A and C). Near the continental shelf break, the eddy heat transport is weaker (Fig. 3.4, A to C, and Fig. 3.9, E and F) because the baroclinic eddies are suppressed there by strong topographic vorticity gradients ([Blumsack and Gierasch, 1972](#); [Isachsen, 2011](#); [Hetland, 2017](#)). Although the tidal and mean components of the heat transport are stronger than the eddy component over the shelf and slope, their vertical integral largely compensates one another in the reference tidal regime and thus contribute less to the total heat transport (Fig. 3.4 A and C). For fresh shelves, the cancellation between tidal and mean components is pronounced (Fig. 3.4A); for dense shelves, about half of the mean component is balanced by the tidal component (Fig. 3.4C). The residual of this cancellation supports the heat transport across the shelf break where eddies are suppressed. [Stewart et al. \(2018, 2019\)](#) have shown that this cancellation exists in a wide range of realistic tidal regimes around Antarctica. When tides are absent, the eddy component compensates for the mean component completely for fresh shelves (Fig. 3.14A), leading to near-zero total onshore heat transport, while for dense shelves, there is still a large heat flux with no tides (Fig. 3.14C and small stars in Fig. 3.2B and Fig. 3.5E). Note that eddies are not the sole contributor to the increased onshore heat transport with coastal freshening, but they dominate the cross-shelf heat transport for fresh shelves and therefore need to be carefully modeled.

We further quantify the eddy and tidal heat transport due to the net volume fluxes of water across the slope associated with advective overturning (namely, eddy advection and tidal advection) and due to the mixing of heat along isopycnals (eddy diffusion and tidal diffusion). Figure 3.4 (D and E) shows eddy/tidal diffusion and advection in the fresh-shelf and dense-shelf cases. For

dense shelves, the eddy advection dominates the heat transport in the deep ocean, while over the continental shelf, the eddy heat transport is due to eddy diffusion (Fig. 3.4E). For fresh shelves, tidal advection and eddy advection are much larger than the diffusive terms (Fig. 3.4D), indicating that, for fresh shelves, the heat transport is due to net freshwater export. For fresh shelves, coastal freshening enhances onshore heat transfer because it increases eddy heat advection.

Inspired by the finding that eddy heat transport is essential over the shelf, we investigate the sensitivity of shelf eddies and slope eddies to the increased offshore buoyancy gradient using the energy budget. We temporally decompose the total kinetic energy into eddy, tidal, and mean components (see Materials and Methods). Although the eddies are subdominant in the total kinetic energy, the eddy kinetic energy (EKE) increases substantially when the continental shelves are very salty or very fresh, while the magnitudes of the mean kinetic energy and tidal kinetic energy do not change much across the simulations with varying shelf salinity (Fig. 3.11 A to C). Compared to the simulation with reference shelf salinity, the zonally integrated EKE is enhanced over the shelf, upper slope, and near the surface for fresh shelves (Fig. 3.11D), and it is enhanced over the slope and in the deep ocean for dense shelves (Fig. 3.11F).

Since the eddy and tidal advective overturning circulations are strongly related to the advective heat transport, we also temporally decompose the isopycnal overturning streamfunction into tidal, transient-eddy, Eulerian-mean, and standing-wave components (see Materials and Methods). This is the first time that the tidal overturning streamfunction is explicitly computed. The transient-eddy component quantifies the isopycnal transport associated with transient baroclinic eddies, i.e., the deviations of the flow that have a typical time scale of the baroclinic eddies from the time-mean flow. The Eulerian-mean component quantifies the isopycnal transport associated with the time- and zonal-mean flow. The standing-wave component quantifies the isopycnal transport associated with standing eddies or standing waves, which is defined as the deviations of the time-mean flow from the time- and zonal-mean flow. It is shown that for fresh shelves, the overturning circulation is dominated by transient baroclinic eddies (Fig. 3.12F), with the residual of mean and tidal components accounting for the overturning across the slope (Fig. 3.12 C and E). For dense shelves, the overturning circulation is contributed by baroclinic eddies in the open ocean (Fig. 3.13F) and a

mean gravity current over the slope (Fig. 3.13C); the bottom-intensified nature of the dense outflow makes the standing-wave component notable in the troughs of the continental shelf (Fig. 3.13D).

With an inadequate ability to resolve small-scale variability, low-resolution simulations cannot accurately reproduce eddy and tidal heat advection (figs. 3.15 and 3.16) and thus cannot capture the positive feedback in the fresh-shelf regime. For the fresh-shelf regime, tidal advection decreases with coarser horizontal resolution, while the eddy advection exhibits a nonmonotonic response to resolution (figs. 3.15D and 3.16D), which may be due to the spurious mixing in the low-resolution model and the resulting enhancement of eddy overturning over the continental shelf (figs. 3.21F and 3.22F). [Stewart \(2021\)](#) has reported a similar enhancement of eddy overturning circulation with decreased model resolution in a regional model of the Weddell Sea, albeit in a dense shelf regime.

3.3 Discussion

In conclusion, both freshening of the fresh shelves and salinification of the dense shelves lead to enhanced heat flux toward the Antarctic margins. Figure 3.5 schematically summarizes the processes responsible for enhanced shoreward heat transport for fresh shelves and dense shelves. Freshening the shelf leads to baroclinic instabilities of the slope front that drive a shallow overturning, bringing warm waters onto the shelf and exporting fresh surface waters offshore (Fig. 3.5A), while salinifying the shelf leads to dense outflows in canyons that drive a warm return flow at mid-depth (Fig. 3.5C). For fresh shelves, tides are important to transfer heat across the shelf break where eddies are strongly suppressed. The increased onshore heat transfer with coastal freshening in the fresh-shelf regime happens only when the horizontal resolution is high enough, and thus the model is capable of resolving mesoscale eddies over the shelf and slope (Fig. 3.2). These mechanisms of shoreward mass/heat transfer are consistent with the findings of [Stewart and Thompson \(2016\)](#) and [Morrison et al. \(2020\)](#) for dense shelves, [Nøst et al. \(2011\)](#) and [Hattermann \(2018\)](#) for fresh shelves, and previous studies on buoyancy-driven coastal currents in other parts of the ocean [Bryden et al. \(1980\)](#); [Whitney et al. \(2005\)](#). Consistent with [Stewart et al. \(2018\)](#), in our model,

there is a notable cancellation between mean heat transport and tidal heat transport over the shelf and deep ocean; in contrast to their findings, we show that it is the eddy advection rather than eddy diffusion that dominates the cross-shelf heat transport in the fresh-shelf regime.

Our results imply a positive feedback for future climate change: In a warming climate, large volumes of meltwater may increase shoreward heat transport, causing further melt of ice shelves. The enhanced heat transport with weaker zonal winds in the fresh-shelf and dense shelf cases further implies an increased shoreward heat transport in the future, as weakening easterlies may be expected in the future due to warming over Antarctica and southward shift of the westerlies ([Spence et al., 2014](#)). Our results imply that the potential tipping point of the Filchner-Ronne Ice shelf may be affected not only by cavity circulation [e.g., [Hellmer et al. \(2017\)](#)] but also by the response of dense shelves to reduced dense water export in the central and western Weddell Sea, as well as the response of fresh shelves to increased meltwater export in the eastern Weddell Sea. Furthermore, our results imply that models with coarse horizontal resolution tend not to capture the enhanced shoreward heat flux under Antarctic margin freshening, because they do not resolve shelf eddies and therefore cannot accurately represent the response of eddy advection to the increased density gradient across the ASF in the fresh-shelf regime. Therefore, coarse-resolution climate model projections of future Antarctic ice shelf melt and Antarctic coastal ocean changes should be interpreted with caution. For future research on ocean heat transport and ice shelf melting, it is essential to use high-resolution eddy-resolving models and/or improve parameterization schemes for eddy heat flux over the continental shelf and slope. Note that other physical mechanisms may contribute to the positive or negative feedback simultaneously, such as trapping of warm water in the ocean subsurface due to increased shelf stratification under coastal freshening [e.g., [Golledge et al. \(2019\)](#)] and the enhancement of shelf circulation due to additional meltwater fluxes in the warm-shelf regime ([Jourdain et al., 2017](#)), which cannot be ruled out by the findings of this study.

There are some caveats due to the heavy idealization of the model (see Materials and Methods). In particular, models with periodic zonal boundaries may overemphasize eddy- and tidal-driven onshore transport because, in reality, meltwater can flow away along the coast without crossing the shelf break by eddy-driven and tidally driven overturning circulation. Moreover, our conclusions

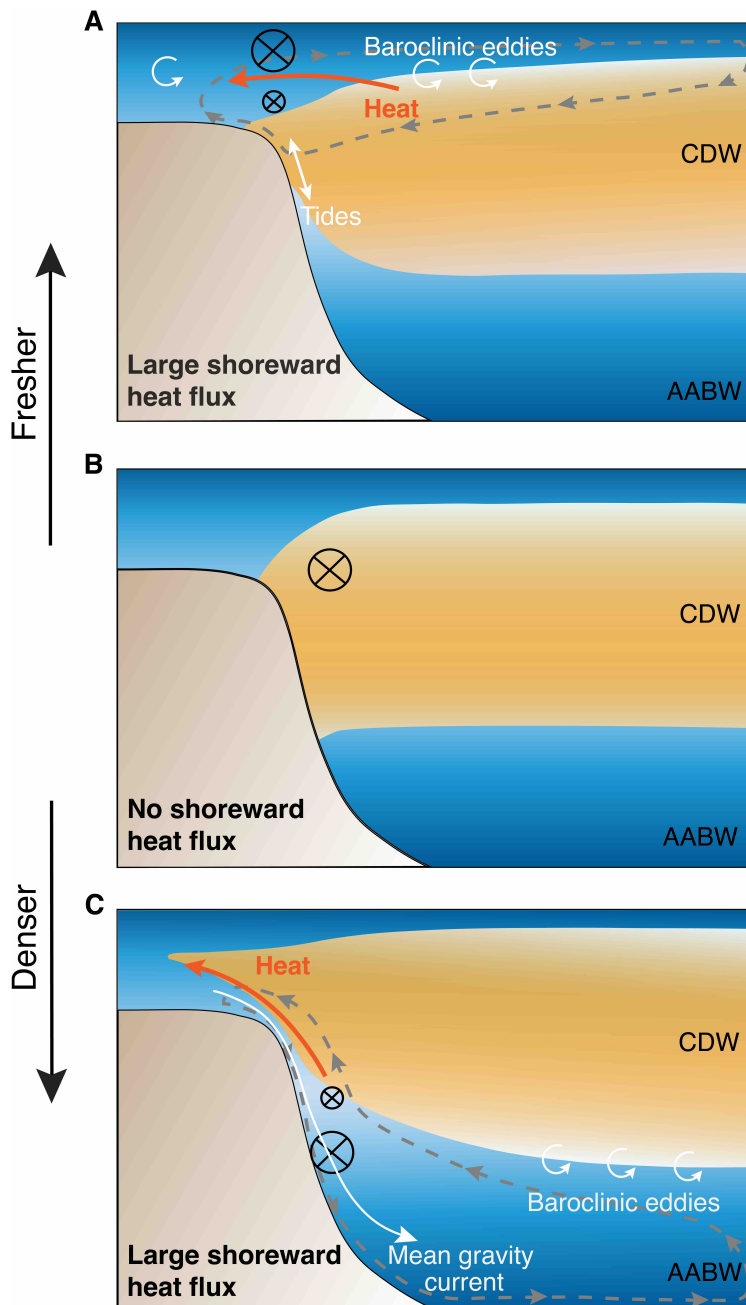


Figure 3.5: Schematic of salinity-controlled shoreward heat transport. (A) Fresh-shelf case. (B) Reference case. (C) Dense-shelf case. The gray dashed curves with arrows denote the zonally averaged meridional overturning circulation. The black circle with a cross shows that the direction of the slope current is westward (into the page), with the size of the circle representing the strength of the slope current. The circular arrows denote the transient baroclinic eddies. In (C), the white curve with an arrow denotes the mean gravity current associated with dense water outflow.

cannot be directly applied to the warm-shelf regime. Although it carries various caveats, the eddy- and tidal-resolving process model successfully reproduces the salient features of the fresh and dense shelves around Antarctica (Si et al., 2022). It helps us disentangle the contributions from eddies, tides, standing waves, and Eulerian mean flows and allows us to explore wide parameter regimes. The idealized model confirms an important climate feedback proposed by Hattermann (2018) that may be key to projecting future changes of Antarctic ice sheets and thus sea level rise. The results of this study help to refine predictions of future changes in different salinity regimes of the Antarctic margins and have implications on eddy heat transport across fronts in other parts of the ocean.

3.4 Materials and methods

3.4.1 Model configuration and simulations

In this study, we use a high-resolution process-oriented model (MITgcm_ASF) developed by Si et al. (2022), based on the Massachusetts Institute of Technology General Circulation Model (MITgcm) Marshall et al. (1997a,b). We use an ocean/sea ice model because the ocean-sea ice interaction exerts an important dynamical influence on the ASF/ASC (Thompson et al., 2018; Si et al., 2022). The model solves the hydrostatic Boussinesq equations with a high-order polynomial approximation to the equation of state (McDougall et al., 2003). The model simulates sea ice dynamics (Losch et al., 2010) using a viscous plastic ice rheology (Hibler, 1979) and thermodynamics with seven sea ice thickness categories (Winton, 2000). We need to use high resolution to resolve mesoscale eddies over the shelf and slope (St-Laurent et al., 2013; Stewart and Thompson, 2015), and hence, we adopt a small domain (450 km by 400 km by 4 km) and fine horizontal grid spacing (2 km). The vertical grid spacing ranges from 10 m at the surface to 100 m at the bottom with 70 vertical levels. We add troughs to the model bathymetry, with the depths and widths of the troughs selected on the basis of observations (NOAA National Geophysical Data Center, 2009), to (i) better represent the geometry of the Antarctic continental shelf and slope, (ii) allow topographic form stress to remove momentum at the seafloor (Si et al., 2022; Bai et al., 2021), and (iii) allow dense water export through these submarine canyons (Morrison et al., 2020). Note that we run

highly idealized simulations and do not seek to accurately recreate the ocean geometry or synoptic forcing.

The model represents typical annual-mean conditions of the fresh- and dense-shelf regimes of the ASF. We exclude seasonal variations from our simulations and set the atmospheric properties to minimize the net air-ice thermodynamic fluxes and thus preserve a relatively uniform sea ice cover, because this is the representative of the typical conditions in Antarctica (Si et al., 2022). Idealized wind forcing and tidal currents are imposed based on typical conditions observed near the Antarctic margins (Powers et al., 2003; Hazel and Stewart, 2019; Padman et al., 2008, 2002). The model has periodic zonal boundaries and open boundary conditions for the meridional boundaries that enable the implementation of tidal currents. We impose the bulk meridional density gradient as a control parameter via two 20-km-wide sponge layers at the northern and southern boundaries. The relaxation time scales are 10 and 0.5 days for the inner and outer boundaries of the sponge layers, respectively.

At the northern boundary, we restore the ocean temperature and salinity to the winter climatology of hydrography across the ASF, taken at Kapp Norvegia (71°S , 17°W) (Hattermann and Rohardt, 2018). At the southern boundary, the potential temperature is vertically uniform and equal to the freezing temperature, as typically observed (Locarnini et al., 2018), and we impose a linear vertical profile of salinity. We control the offshore density gradient by varying the maximum salinity and salinity gradient at the southern boundary (Table 3.1):

- 1) For the reference simulation, the surface salinity of the southern boundary is set to be the same as the surface salinity of the northern boundary [34.12 practical salinity units (psu)]; the bottom salinity of the southern boundary (shelf bottom salinity) is selected to make sure that there is no dense water formation over the shelf; i.e., the potential density with a reference pressure of 4 km (σ_4) at the bottom of the continental shelf ($y = 0 \text{ km}$, $z = -500 \text{ m}$) is identical to that at the seafloor of the northern boundary ($y = 450 \text{ km}$, $z = -4000 \text{ m}$).
- 2) For simulations with shelf salinity fresher than the reference case (“fresh-shelf regime”), we use a vertically uniform salinity profile at the southern boundary.

3) For simulations with shelf salinity saltier than the reference case (“dense-shelf regime”), we set the surface salinity to be 34.12 psu and then increase salinity linearly with depth. Under our model configuration, the shelf bottom salinity (or, equivalently, the maximum meridional salinity gradient at mid-depth) is the key, while the vertical gradient of salinity at the southern boundary makes a smaller impact.

We set the restoring salinity in this way according to the climatology (Fig. 3.1 B and C), i.e., large vertical variation of shelf salinity in the dense-shelf regime and much smaller vertical variation of shelf salinity in the fresh-shelf regime. For the dense shelf, the average and maximum squared buoyancy frequency N^2 are 1.7×10^{-6} and $7.4 \times 10^{-5} \text{ s}^{-2}$ (2.1×10^{-6} and $4.4 \times 10^{-5} \text{ s}^{-2}$) in the steady state of the simulation (the cross section of WOA 2018), respectively. For the fresh shelf, the average and maximum N^2 are 2.7×10^{-6} and $1.1 \times 10^{-4} \text{ s}^{-2}$ (2.1×10^{-6} and $1.4 \times 10^{-4} \text{ s}^{-2}$) in the simulation (the cross-section of WOA 2018), respectively. In all cases, the change of the Rossby radius of deformation is dominated by the change of bathymetry: The first baroclinic Rossby radius of deformation is about 2 to 3 km over the shelf, 3 to 10 km over the slope, and 8 km in the deep ocean.

The model is forced by a fixed atmospheric state. Both the zonal and meridional winds are strongest at the southern boundary ($y = 0 \text{ km}$), decreasing linearly offshore with zero wind speeds at the northern boundary ($y = 450 \text{ km}$). In addition, we prescribe a barotropic tidal current in the meridional direction normal to the northern and southern boundaries, with an idealized tidal period of 12 hours. Because of mass conservation, the tidal current amplitude over the shelf is about eight times larger than that in the deep ocean (Loder, 1980). For a detailed description of model bathymetry, atmospheric state, tides, sea ice, initial and boundary conditions, viscosity, and diffusivity, see Si et al. (2022).

In contrast to Si et al. (2022), we use the Smagorinsky viscosity (Smagorinsky, 1963, 1993) in all the simulations of this study. The Smagorinsky viscosity is based on Kolmogorov’s theory of 3D homogeneous turbulence (Kolmogorov, 1941) and is effective in maintaining numerical stability without suppressing the energy of resolved scales (Griffies and Hallberg, 2000). We turn off the grid-dependent biharmonic viscosities and set the nondimensional Smagorinsky biharmonic

viscosity factor to 4. In addition, we apply standard GM-Redi eddy parameterization ([Gent and Mcwilliams, 1990](#); [Gent et al., 1995](#); [Redi, 1982](#)) for simulations with a horizontal grid spacing of 5 or 10 km. The isopycnal diffusivity and thickness diffusivity are set to $100 \text{ m}^2/\text{s}$. The maximum isopycnal slope is 0.025. The [Danabasoglu and Mc Williams \(1995\)](#) (DM95) tapering scheme is activated for these simulations, with a DM95 critical slope of 0.025 and a DM95 tapering width of 0.0025. The gray lines in Fig. 3.5 (A and B) show that the straightforward application of the GM-Redi parameterization cannot correctly capture the onshore heat transport. We experimented with additional combinations of GM-Redi parameters, not reported here, but were unable to obtain an improved representation of the onshore heat transport.

Table S1 shows the list of experiments. Seven model parameters are varied: (i) shelf salinity profile, including the restoring salinity at the sea surface ($S_{\text{south}}^{\text{surf}}$) and the seafloor ($S_{\text{south}}^{\text{bot}}$) of the continental shelf at the southern boundary; (ii) zonal wind speed at the southern boundary (U_{a0}); (iii) meridional wind speed at the southern boundary (V_{a0}); (iv) barotropic tidal current amplitude (A_{tide}) at the northern boundary; (v) restoring sea ice thickness (h_{i0}) at the southern boundary; (vi) continental slope width (W_S); and (vii) horizontal grid spacing (Δ_x, Δ_y). Each simulation is run for 20 years to spin up from a stationary state, followed by a 7-year analysis period. All the results shown in this manuscript are based on data from the 7-year analysis period.

Figure 3.6 shows the time- and zonal-mean zonal circulation, potential temperature, and salinity in the fresh-shelf, reference, and dense-shelf cases, overlaid by neutral density contours. As reported by previous studies ([Si et al., 2022](#); [Le Paih et al., 2020](#)), the slope current is surface-intensified in the fresh-shelf case (Fig. 3.6A), nearly barotropic in the reference case (Fig. 3.6B), and bottom-intensified in the dense-shelf case (Fig. 3.6C). Undercurrents appear for large salinity gradients, flowing eastward in the fresh-shelf and dense-shelf cases (Fig. 3.6 A and C).

3.4.2 Model limitations

There are several limitations of this work due to the heavy idealization of the model, which was required to allow adequate resolution of eddies.

- 1) The model simulates typical annual-mean conditions of the Antarctic margins with permanent sea ice cover, with the assumption that most of the freezing happens south of the model domain and most of the melt happens to the north. It does not include atmospheric feedbacks and seasonal melting/freezing of sea ice, which strongly influence ocean stratification, and thus may modulate shoreward ocean heat transport ([Hattermann, 2018](#); [Zhou et al., 2014](#)).
- 2) The model does not simulate the dynamics and thermodynamics of ice shelves and thus also lacks ice shelf-ocean interactions.
- 3) When meltwater is injected under ice shelves, it increases both the vertical stratification and the lateral density gradient. Ice shelf meltwater in previous global-scale models is usually injected only on the ocean surface ([Bronsemaer et al., 2018](#); [Sadai et al., 2020](#); [Moorman et al., 2020](#)), while observations and idealized modeling studies have suggested that the injection of meltwater occurs at depth ([Dutrieux et al., 2014](#); [Garabato et al., 2017](#); [Arnscheidt et al., 2021](#)). In this study, we focus primarily on the change of lateral density gradient in response to additional meltwater. We did not investigate how ocean heat transport responds to the depth at which meltwater is injected and defer this question to a future study.
- 4) There is a limitation associated with the re-entrant channel: The periodic boundaries efficiently remove zonal pressure gradients and meltwater/heat advection from upstream; thus, the model may overemphasize eddy- and tidal-driven transport. In reality, meltwater can flow away to the west as a coastal current, without crossing the shelf break by eddy-driven and tidally-driven overturning circulation, and, as a result, the feedback may occur differently. A high-resolution circumpolar regional model is needed to understand the effect of meltwater advection along the coast ([Graham et al., 2013](#); [Nakayama et al., 2014b](#)).
- 5) The parameter regime spanned by the model experiments is not representative of the warm-shelf regime along the WAP, where the ice shelves are melting rapidly ([Paolo et al., 2015](#); [Pritchard et al., 2012](#)), because the model's shelf forcing imposes a strong temperature gradient at the southern boundary that differs from conditions along the WAP. Therefore, our results cannot be directly applied to the warm-shelf regime, where previous studies such as [Nakayama et al. \(2019\)](#) highlight heat transport carried by mean ocean currents. An idealized model that represents the

warm-shelf regime with coupled ocean, sea ice, and ice shelves is needed to better understand the mechanisms and feedbacks.

6) The model bathymetry is also highly idealized. The width and depth of the troughs are selected on the basis of the typical values in observations ([NOAA National Geophysical Data Center, 2009](#)), but we did not test the sensitivity of heat transport to the geometry of the troughs.

3.4.3 Heat function

The heat function ([Boccaletti et al., 2005](#)) is defined as

$$\phi(y, z) = c_p \rho_0 \int_{z'=\eta_b}^z \left\langle \bar{v} \theta^E - \bar{v}^E \theta_{\text{ref}} \right\rangle dz', \quad (3.2)$$

where c_p is the specific heat capacity, ρ_0 is the reference density, η_b is the seafloor elevation, v is the meridional velocity, θ is the potential temperature, θ_{ref} is the reference potential temperature, $\bar{\bullet}^E$ denotes an 8-year time average, and the angle brackets denotes zonal integral. The interpretation of the heat function is very similar for different choices of the reference temperature ([Boccaletti et al., 2005](#)), so we use $\theta_{\text{ref}} = 0^\circ\text{C}$ in this study for simplicity.

3.4.4 Operators for temporal decomposition

To calculate temporal decomposition of shoreward heat transport, overturning streamfunction, and kinetic energy, we define two time-averages over a single day ($\bar{\bullet}^T$) and over the analysis period ($\bar{\bullet}^E$) ([Stewart et al., 2018, 2019](#)),

$$\bar{\bullet}^T = \frac{1}{1 \text{ day}} \int_{t_0}^{t_0+1 \text{ day}} \bullet dt, \quad \bar{\bullet}^E = \frac{1}{8 \text{ years}} \int_{t_0}^{t_0+8 \text{ years}} \bar{\bullet}^T dt. \quad (3.3)$$

These operators allow us to decompose any simulation variable into mean (ξ_m), eddy (ξ_e), and tidal (ξ_t) components:

$$\xi_m = \bar{\xi}^E = \bar{\xi}^E, \quad \xi_e = \bar{\xi}^T - \bar{\xi}^E, \quad \xi_t = \xi - \xi_m - \xi_e = \xi - \bar{\xi}^T, \quad (3.4)$$

where ξ represents velocity $\mathbf{u} = (u, v, w)$, potential temperature θ , or potential density σ_2 with a reference depth of 2 km.

3.4.5 Decomposition of the total meridional heat transport

The total meridional heat transport in the ocean is almost entirely contributed by the advective heat transport. Following [Stewart et al. \(2018\)](#), we temporally decompose the total meridional advective heat flux (F_{total}) into mean (F_{mean}), eddy (F_{eddy}), and tidal (F_{tide}) components, i.e., $F_{\text{total}} = F_{\text{mean}} + F_{\text{eddy}} + F_{\text{tide}}$.

$$F_{\text{total}} = -\overline{v\theta}^E, \quad (3.5a)$$

$$F_{\text{mean}} = -v_m\theta_m, \quad (3.5b)$$

$$F_{\text{eddy}} = -\overline{v_e\theta_e}^E = -\overline{\bar{v}^T\bar{\theta}}^T - F_{\text{mean}}, \quad (3.5c)$$

$$F_{\text{tide}} = -\overline{v_t\theta_t}^E = F_{\text{total}} + \overline{\bar{v}^T\bar{\theta}}^T. \quad (3.5d)$$

Figure 3.4 (A to C) shows the zonally and vertically integrated southward advective heat fluxes. In all cases, the southward tidal heat transport is largely compensated by the offshore mean component, which is consistent with [Stewart et al. \(2018\)](#). The residual of the mean and tidal components comprises the heat transport near the shelf break. Relative to the reference case, the eddy heat transport is enhanced over the shelf and in the deep ocean in both the fresh-shelf and dense-shelf cases (Fig. 3.4 A to C, and Fig. 3.9 E and F).

3.4.6 Diffusion and advection by tides and eddies

We further decompose the isopycnal thickness flux (T_{total} , integrated meridional transport in each isopycnal layer) into mean (T_{mean}), eddy (T_{eddy}), and tidal (T_{tide}) components, i.e., $T_{\text{total}} = T_{\text{mean}} + T_{\text{eddy}} + T_{\text{tide}}$.

$$T_{\text{total}}(x, y, \sigma_2) = \overline{vh^{\text{isop}}}^E \quad (3.6a)$$

$$T_{\text{mean}}(x, y, \sigma_2) = v_m h_m^{\text{isop}} \quad (3.6b)$$

$$\overline{T}_{\text{eddy}}(x, y, \sigma_2) = \overline{v_e h_e^{\text{isop}}}^E = \overline{v^T h^{\text{isop}}}^T - T_{\text{mean}} \quad (3.6c)$$

$$\overline{T}_{\text{tidal}}(x, y, \sigma_2) = \overline{v_t h_t^{\text{isop}}}^E = T_{\text{total}} - \overline{v^T h^{\text{isop}}}^T \quad (3.6d)$$

Here, $h^{\text{isop}}(x, y, \sigma_2, t)$ is the isopycnal layer thickness. We remap the time-mean potential temperature to the potential density coordinates, $\overline{\hat{\theta}}(x, y, \sigma_2)^E$ and then calculate tidal advection, tidal diffusion, eddy advection, and eddy diffusion, following [Stewart and Thompson \(2016\)](#):

$$F_{\text{eddy}}^{\text{adv}} = -T_{\text{eddy}} \overline{\hat{\theta}}^E, \quad F_{\text{tide}}^{\text{adv}} = -T_{\text{tide}} \overline{\hat{\theta}}^E \quad (3.7a)$$

$$F_{\text{eddy}}^{\text{diffusion}} = F_{\text{eddy}} - F_{\text{eddy}}^{\text{adv}}, \quad F_{\text{tide}}^{\text{diffusion}} = F_{\text{tide}} - F_{\text{tide}}^{\text{adv}}, \quad (3.7b)$$

Eddy advection and tidal advection quantify the cross-slope heat transport associated with the net volume fluxes. The eddy and tidal diffusion quantify the mixing of heat along isopycnals ([Stewart and Thompson, 2016](#)). Positive values correspond to southward heat transport.

3.4.7 Decomposition of the total kinetic energy

The total kinetic energy (KE) is decomposed into mean (MKE), eddy (EKE), and tidal (TKE) components, i.e., $\text{KE} = \text{MKE} + \text{EKE} + \text{TKE}$.

$$\text{KE} = \frac{1}{2} \overline{\mathbf{u}^2}^E, \quad (3.8a)$$

$$\text{MKE} = \frac{1}{2} \overline{\mathbf{u}_m^2}^E, \quad (3.8b)$$

$$\text{EKE} = \frac{1}{2} \overline{\mathbf{u}_e^2}^E = \frac{1}{2} \overline{(\bar{\mathbf{u}}^T)^2}^E - \text{MKE}, \quad (3.8c)$$

$$\text{TKE} = \frac{1}{2} \overline{\mathbf{u}_t^2}^E = \text{KE} - \frac{1}{2} \overline{(\bar{\mathbf{u}}^T)^2}^E. \quad (3.8d)$$

3.4.8 Decomposition of the isopycnal overturning streamfunction

As noted in the section “Vertical structure of heat flux and overturning circulation”, the shoreward heat transport is closely related to the meridional overturning circulation. We investigate to what extent different components of the flow contribute to the overturning circulation by decomposing the isopycnal overturning streamfunction (ψ_{isop}) into mean (ψ_{mean}), transient-eddy (ψ_{eddy}) and tidal (ψ_{tide}) components, i.e., $\psi_{\text{isop}} = \psi_{\text{mean}} + \psi_{\text{eddy}} + \psi_{\text{tide}}$. We calculate the overturning streamfunction in potential density (σ_2) coordinate, and then remap it to z coordinate following the standard approach (Nurser and Lee, 2004).

$$\psi_{\text{isop}}(y, \sigma_2) = \left\langle \overline{\int_{z=\eta_b}^{z=0} v \mathcal{H} [\sigma_2 - \sigma'_2(x, y, z, t)] dz}^E \right\rangle, \quad (3.9a)$$

$$\psi_{\text{mean}}(y, \sigma_2) = \left\langle \int_{z=\eta_b}^{z=0} v_m \mathcal{H} [\sigma_2 - \sigma'_{2m}(x, y, z)] dz \right\rangle, \quad (3.9b)$$

$$\begin{aligned} \psi_{\text{eddy}}(y, \sigma_2) &= \left\langle \overline{\int_{z=\eta_b}^{z=0} v_e \mathcal{H} [\sigma_2 - \sigma'_{2e}(x, y, z, t)] dz}^E \right\rangle \\ &= \left\langle \overline{\int_{z=\eta_b}^{z=0} \bar{v}^T \mathcal{H} [\sigma_2 - \overline{\sigma'_2(x, y, z, t)}^T] dz}^E \right\rangle - \psi_{\text{mean}}(y, \sigma_2), \end{aligned} \quad (3.9c)$$

$$\begin{aligned} \psi_{\text{tide}}(y, \sigma_2) &= \left\langle \overline{\int_{z=\eta_b}^{z=0} v_t \mathcal{H} [\sigma_2 - \sigma'_{2t}(x, y, z, t)] dz}^E \right\rangle \\ &= \psi_{\text{isop}}(y, \sigma_2) - \left\langle \overline{\int_{z=\eta_b}^{z=0} \bar{v}^T \mathcal{H} [\sigma_2 - \overline{\sigma'_2(x, y, z, t)}^T] dz}^E \right\rangle. \end{aligned} \quad (3.9d)$$

Here, primes ($'$) denote the simulated field, $\mathcal{H}[\cdot]$ is the Heaviside function, and the angle brackets denote the zonal integral. We further decompose the mean overturning streamfunction into Eulerian-mean (ψ_{EM}) and standing-wave (ψ_{SW} , also referred to as “standing-eddy”) components, i.e., $\psi_{\text{mean}} = \psi_{\text{SW}} + \psi_{\text{EM}}$.

$$\psi_{\text{EM}}(y, \sigma_2) = \int_{z=\eta_b}^{z=0} \langle v_m \rangle \mathcal{H} [\sigma_2 - \langle \sigma_{2m}(x, y, z) \rangle] dz, \quad (3.10a)$$

$$\psi_{\text{SW}}(y, \sigma_2) = \psi_{\text{mean}}(y, \sigma_2) - \psi_{\text{EM}}(y, \sigma_2). \quad (3.10b)$$

Figures 3.12 and 3.13 show the temporal decomposition of the isopycnal overturning streamfunction for fresh and dense shelves with 2-km resolution. For fresh shelves, there is a subsurface, baroclinic, eddy-driven overturning over the continental shelf and in the open ocean (Fig. 3.12F); the tidal overturning is approximately compensated by the Eulerian-mean overturning, with the residual supporting the overturning across the continental slope (Fig. 3.12 C and E). For dense shelves, the transient eddies dominate the overturning in the deep ocean (Fig. 3.13F); gravity currents comprise the Eulerian-mean component over the slope (Fig. 3.13C) where eddies are suppressed; the standing eddy component dominates the isopycnal transport in the troughs on the continental shelf (Fig. 3.13D).

3.5 Supplementary Materials

Δ_x, Δ_y (km)	$S_{\text{south}}^{\text{surf}}$ (psu)	$S_{\text{south}}^{\text{bot}}$ (psu)		U_{a0} (m/s)	V_{a0} (m/s)	A_{tide} (m/s)	h_{i0} (m)	W_S (km)
2, 5, 10	33	33		-6	6	0.05	1.0	50
2	33.28	33.28		-6	6	0.05	1.0	50
2, 5, 10	33.56	33.56		-6	6	0.05	1.0	50
2, 5, 10	34.12	34.12		-6	6	0.05	1.0	50
2, 5, 10	34.12	34.12 + ΔS		-6	6	0.05	1.0	50
2, 5, 10	34.12	34.12 + $2\Delta S$		-6	6	0.05	1.0	50
2	34.12	34.12 + $2.5\Delta S$		-6	6	0.05	1.0	50
2, 5, 10	34.12	34.12 + $3\Delta S$		-6	6	0.05	1.0	50
2	33, 34.12	33, 34.12 + ΔS , 34.12 + $3\Delta S$		-4	6	0.05	1.0	50
2	33, 34.12	33, 34.12 + ΔS , 34.12 + $3\Delta S$		-8	6	0.05	1.0	50
2	33, 34.12	33, 34.12 + ΔS , 34.12 + $3\Delta S$		-6	4	0.05	1.0	50
2	33, 34.12	33, 34.12 + ΔS , 34.12 + $3\Delta S$		-6	12	0.05	1.0	50
2	33, 34.12	33, 34.12 + ΔS , 34.12 + $3\Delta S$		-6	6	0.00	1.0	50
2	33, 34.12	33, 34.12 + ΔS , 34.12 + $3\Delta S$		-6	6	0.10	1.0	50
2	33, 34.12	33, 34.12 + ΔS , 34.12 + $3\Delta S$		-6	6	0.05	0.2	50
2	33, 34.12	33, 34.12 + ΔS , 34.12 + $3\Delta S$		-6	6	0.05	1.8	50
2	33, 34.12	33, 34.12 + ΔS , 34.12 + $3\Delta S$		-6	6	0.05	1.0	25
2	33, 34.12	33, 34.12 + ΔS , 34.12 + $3\Delta S$		-6	6	0.05	1.0	100

Table 3.1: List of experiments. Δ_x and Δ_y are the horizontal grid spacings in the zonal and meridional direction, respectively. $\Delta S = 0.23$ psu is the vertical difference in the restoring salinity at the southern boundary between the sea surface ($S_{\text{south}}^{\text{surf}}$) and the seafloor of the continental shelf (500 m depth, $S_{\text{south}}^{\text{bot}}$) of the reference case. U_{a0} and V_{a0} are the zonal (along-slope, positive eastward) and meridional (cross-slope, positive northward) wind speed at the southern boundary, respectively. A_{tide} is the prescribed barotropic tidal current amplitude at the northern boundary. h_{i0} is the restoring sea ice thickness at the southern boundary, which is also the initial sea ice thickness across the domain. W_S is the continental slope width. The boldface shows the three experiments mainly described in this article (the fresh-shelf, reference, and dense-shelf cases), as well as perturbation simulations.

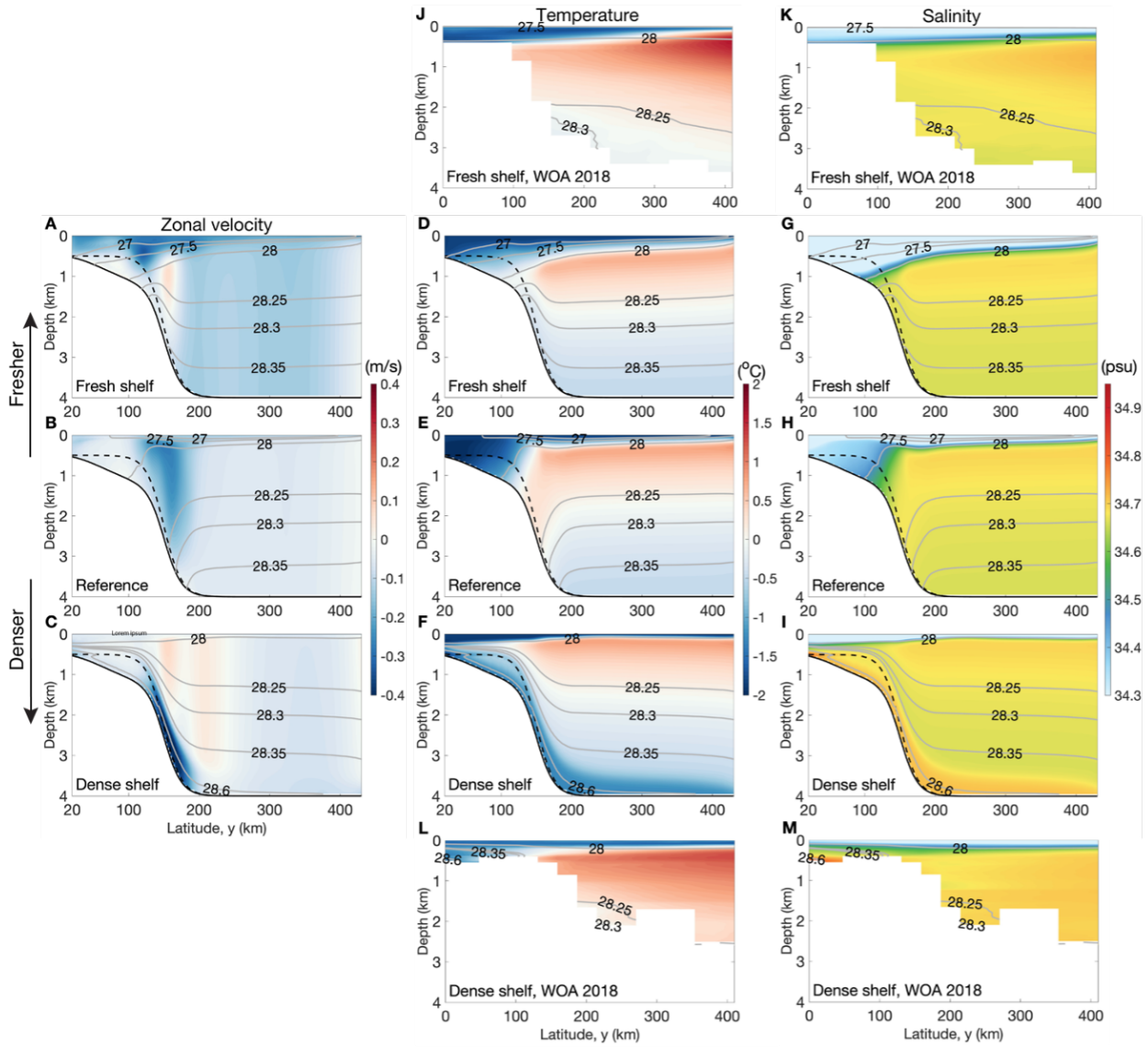


Figure 3.6: Time- and zonal-mean zonal (along-slope) velocity (A-C), potential temperature (D-F), and salinity (G-I) of the simulations (2-km resolution), overlaid by neutral density contours. (A, D, G) The fresh-shelf case. (B, E, H) The reference case. (C, F, I) the dense-shelf case. In panels (A-C), blue denotes westward flow (into the page), and red denotes eastward flow (out of the page). The gray contours with numbers show the time- and zonal-mean neutral density (kg/m³). The black solid and dashed curves denote the deepest and shallowest bathymetry (see Figs. 1D, E), respectively. The 20-km sponge layers at the northern and southern boundaries are not shown. (J-M) Cross sections of potential temperature and salinity taken in East Antarctica (fresh shelf, 67.75° - 63.71°S , 76.38°E) and the Ross Sea (dense shelf, 73.05° - 69.01°S , 172.13°E), respectively. Data comes from World Ocean Atlas 2018.

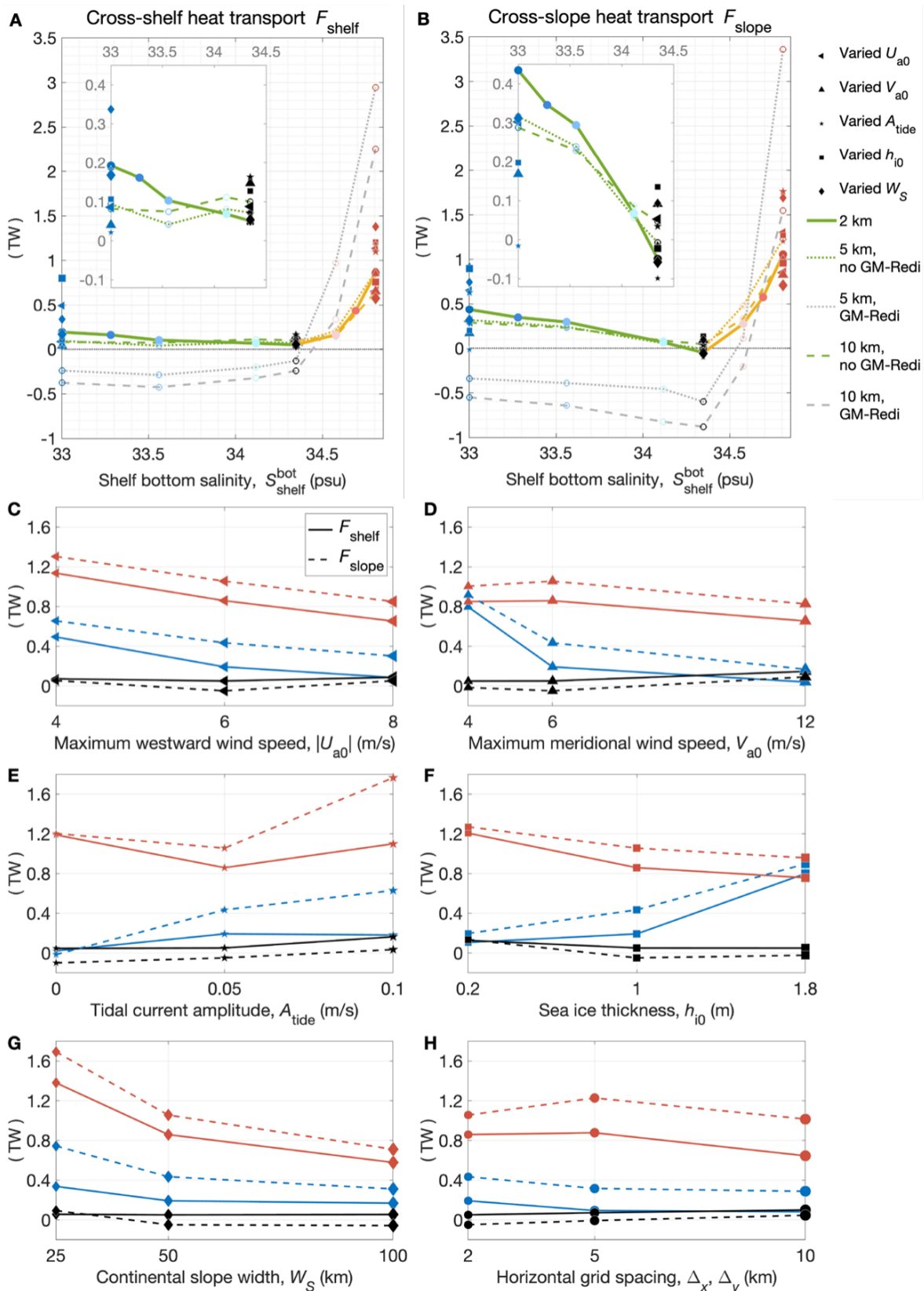


Figure 3.7: Sensitivity of heat transferred onto the continental shelf (F_{shelf}) and to the upper part of the continental slope (F_{slope}). (A) vertically and zonally integrated meridional advective heat flux averaged over the shelf region ($y = 50 \text{ km}-75 \text{ km}$), in unit TW (1 TW = 10^{12} W), as a function of shelf bottom salinity. The solid, dotted, and dashed lines denote simulations with 2-, 5-, and 10-km resolution, respectively. The colored (green for the fresh-shelf regime and orange for the dense-shelf regime) and gray lines denote simulations with no GM-Redi eddy parameterization, and with GM-Redi, respectively. The inset plot is a zoom in of F_{shelf} in the fresh-shelf regime. For the fresh-shelf, reference, and dense-shelf cases, the sensitivity of F_{shelf} to other model parameters is indicated by markers with various shapes, with larger marker sizes indicating larger values of the corresponding parameters. (B) Similar to panel (A) but for the upper part of the continental slope ($y = 125 \text{ km}-150 \text{ km}$). (C-H) Sensitivity of F_{shelf} (solid lines) and F_{slope} (dashed lines) to model parameters. Blue, black, and red represent the fresh-shelf, reference, and dense-shelf cases, respectively. The simulations with 5-km or 10-km resolution in panel (H) are run without the GM-Redi eddy parameterization.

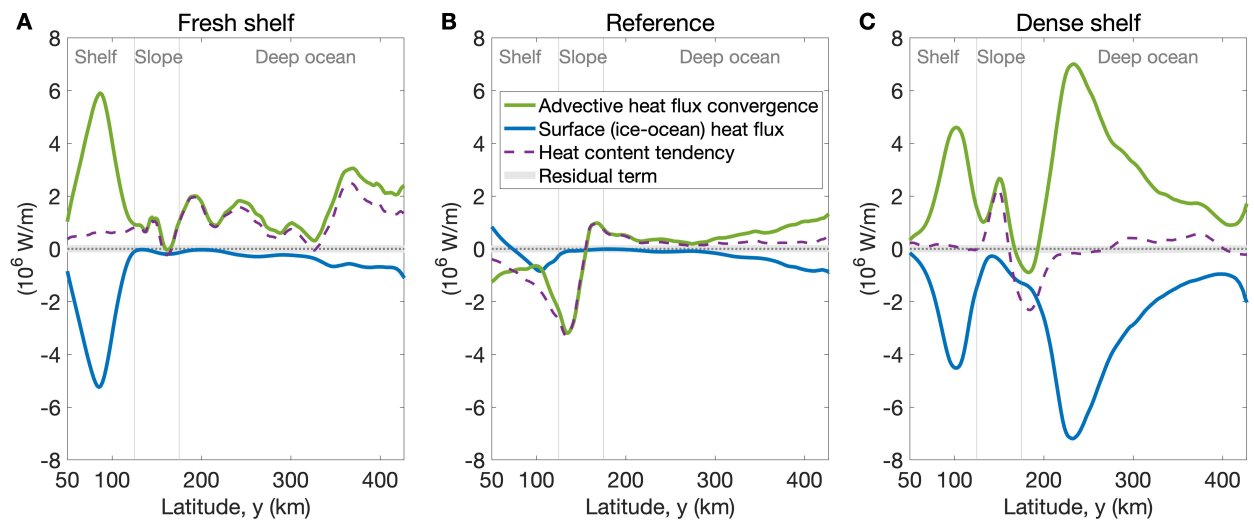


Figure 3.8: Zonally and vertically integrated heat budget for simulations with 2-km horizontal resolution. (A) The fresh-shelf case. (B) The reference case. (C) The dense-shelf case. The residual term = (advectional heat flux convergence) + (ice-ocean heat flux) - (heat content tendency). The heat content tendency is defined as $c_p \rho_0 \int_{z=\eta_b}^{z=0} (\partial T / \partial t) dz dx$, where c_p is the specific heat capacity, ρ_0 is the reference density, η_b is the seafloor elevation, and T is the potential temperature. Positive values are associated with an increase in ocean temperature. Note that for the fresh- and dense-shelf cases, the advective heat flux convergence is balanced by ocean-to-sea ice heat flux over the continental shelf.

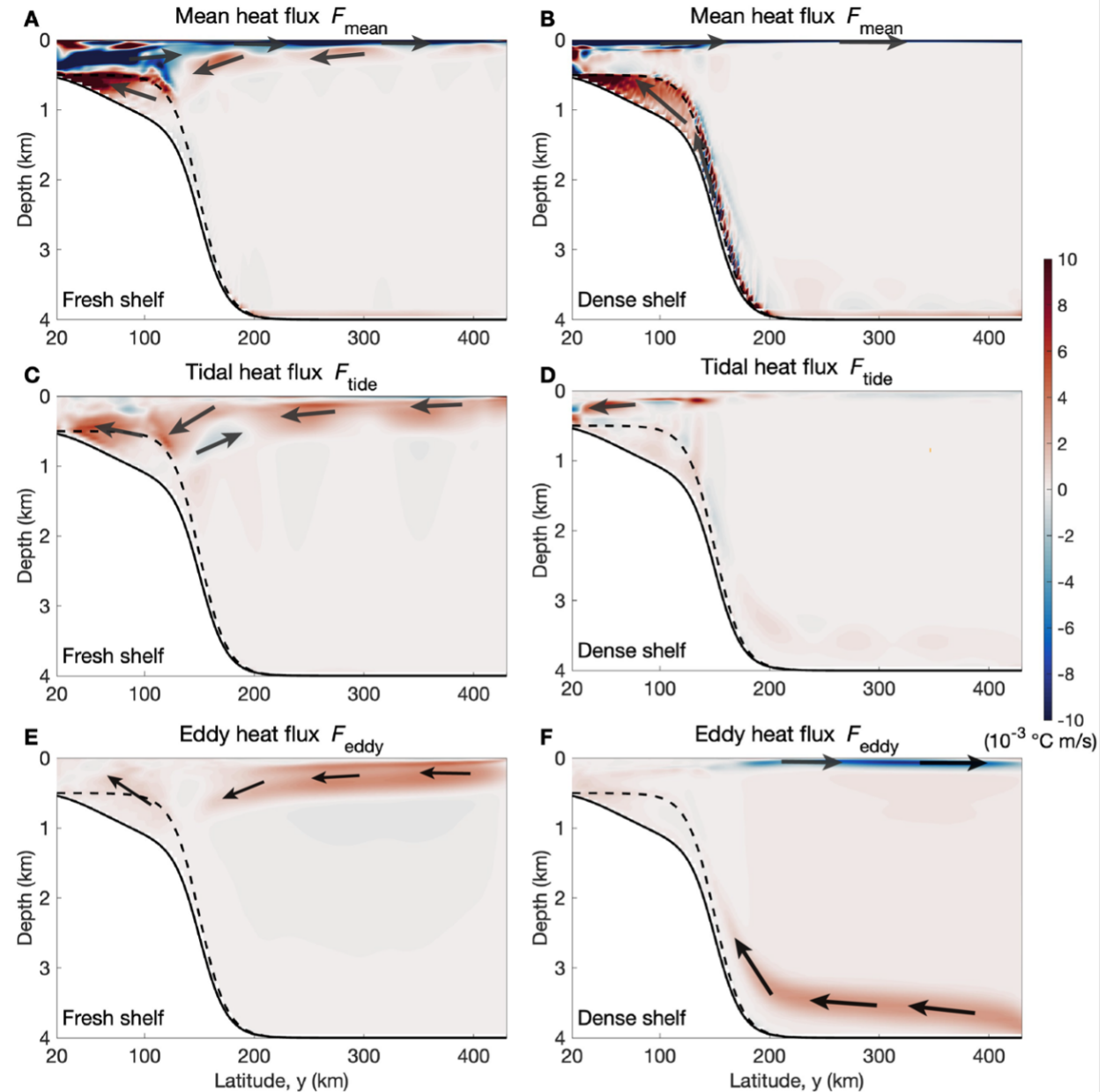


Figure 3.9: Temporal decomposition of the zonal-mean southward advective heat flux for simulations with 2-km horizontal resolution. Mean, tidal, and eddy heat fluxes of the fresh-shelf (A, C, E) and dense-shelf (B, D, F) cases. The black solid and dashed curves denote the deepest and shallowest bathymetry at each latitude, respectively. The 20-km sponge layers at the northern and southern boundaries are not shown.

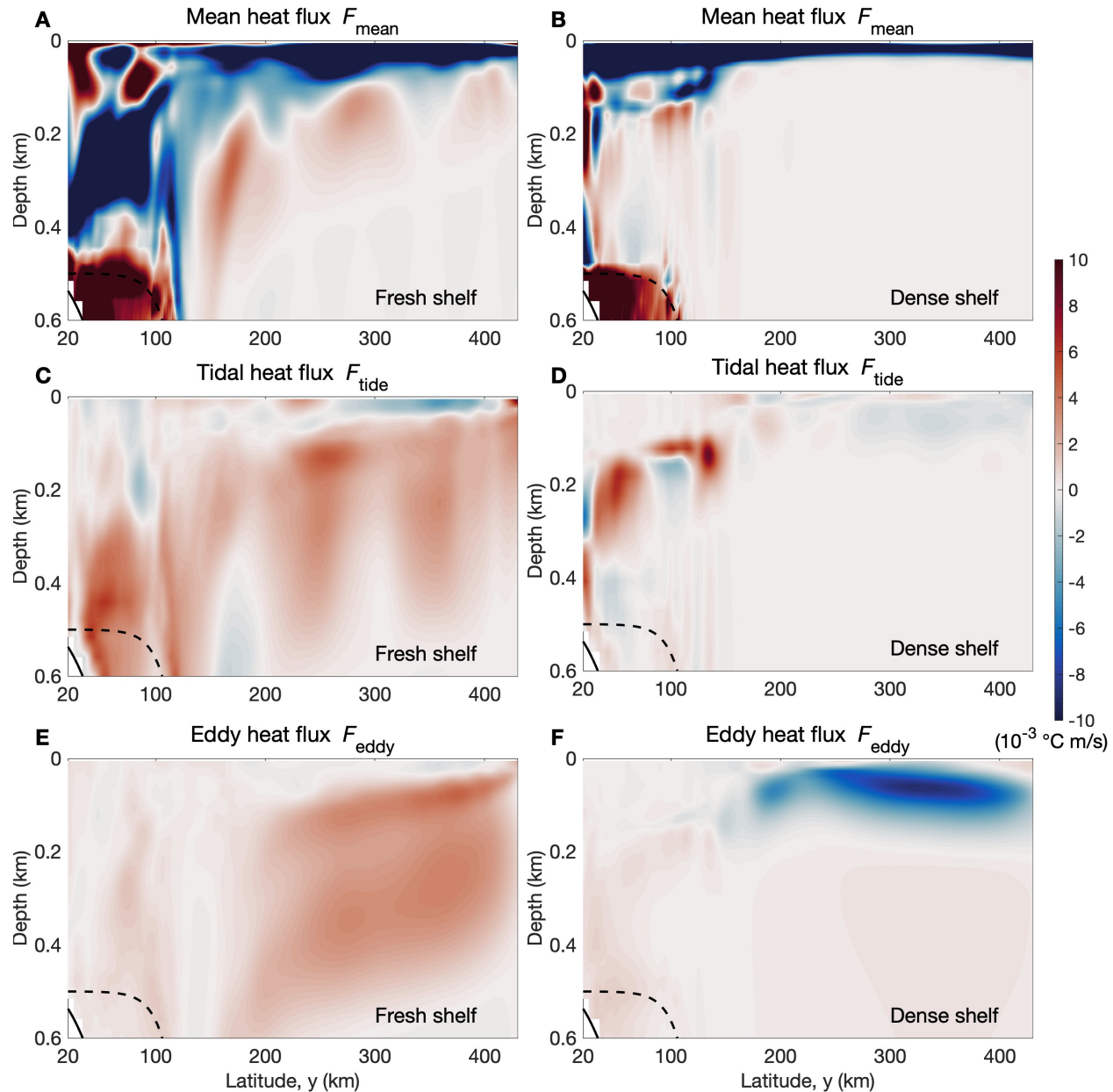


Figure 3.10: Same as Fig. 3.9, but for the surface 600m of the ocean.

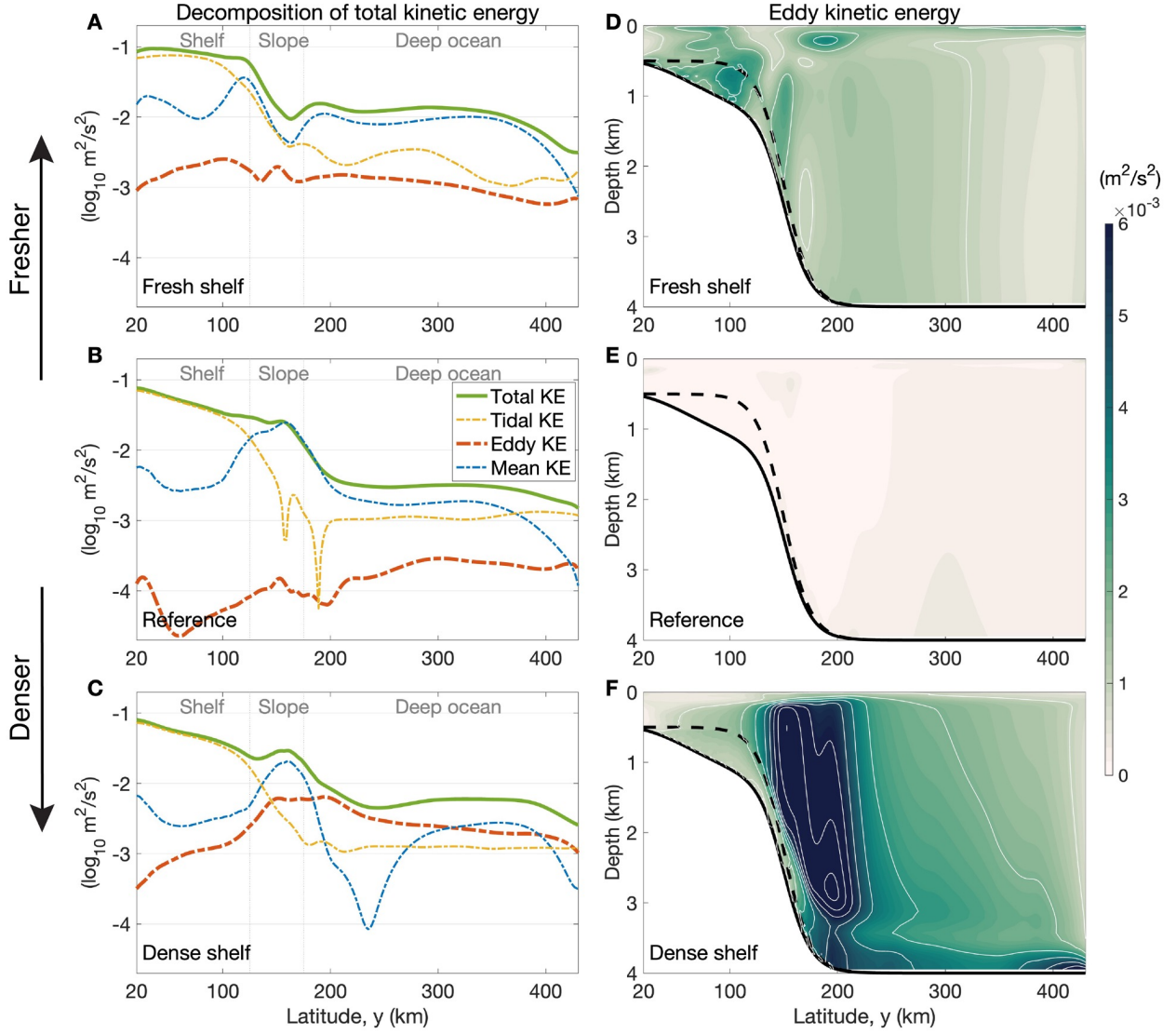


Figure 3.11: Temporal decomposition of the total kinetic energy for simulations with 2-km horizontal resolution. (A-C) Time-mean total kinetic energy, and its tidal, eddy, and mean components in the fresh-shelf, reference, and dense-shelf cases, averaged over the zonal/vertical plane. (D-F) Time- and zonal-mean eddy kinetic energy in the three cases. The colored and solid white contours show intervals of $1.5 \times 10^{-4} m^2 s^{-2}$ and $10^{-3} m^2 s^{-2}$, respectively. The black solid and dashed curves denote the deepest and shallowest bathymetry at each latitude, respectively. The 20-km sponge layers at the northern and southern boundaries are not shown. Note the total kinetic energy and mean kinetic energy remain the same order of magnitude across simulations, while the eddy kinetic energy increases by 1~2 orders of magnitude in the fresh- and dense-shelf cases.

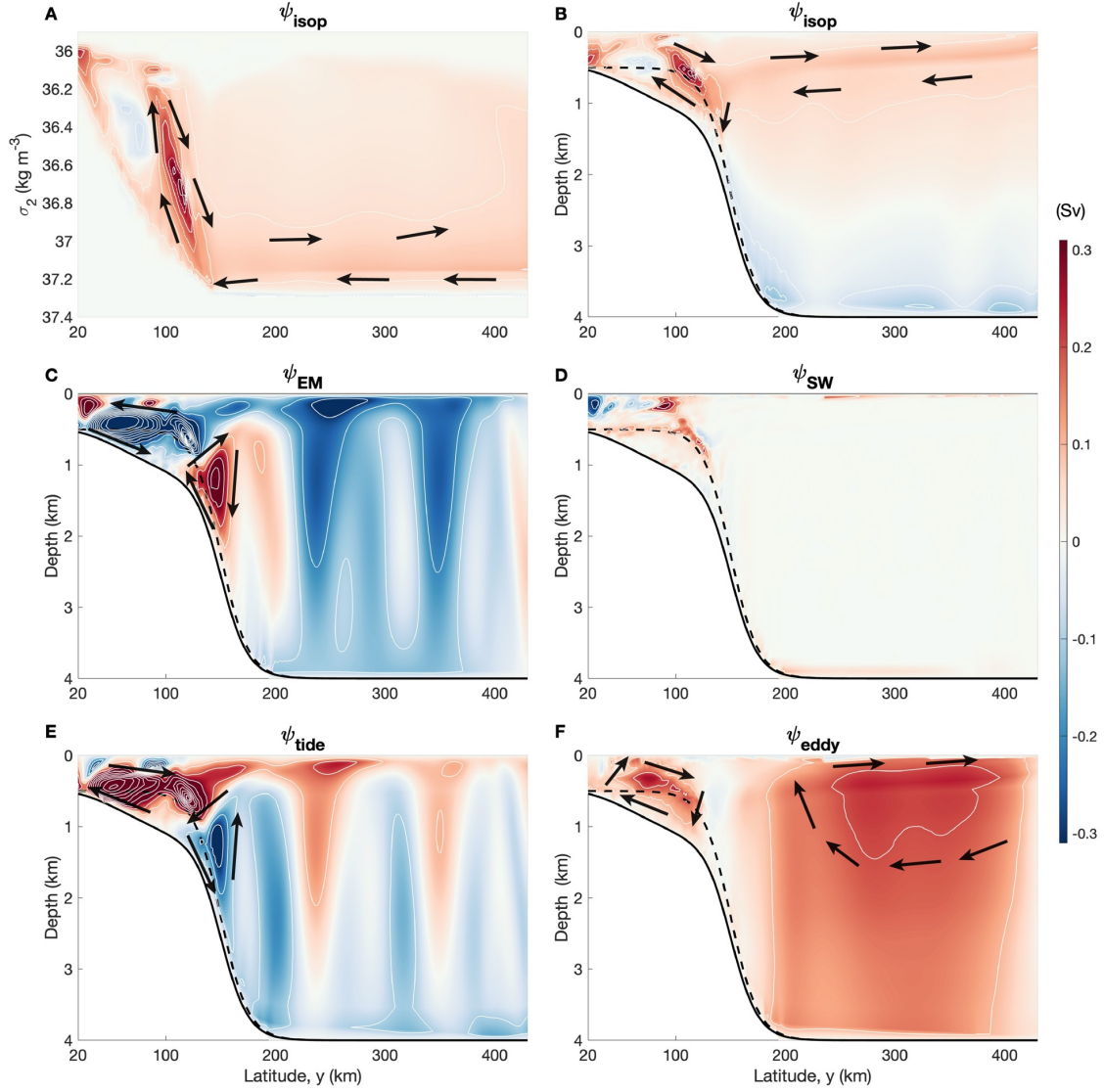


Figure 3.12: Temporal decomposition of the isopycnal overturning streamfunction ($\psi_{\text{isop}} = \psi_{\text{EM}} + \psi_{\text{SW}} + \psi_{\text{eddy}} + \psi_{\text{tide}}$) for the fresh-shelf simulation with 2-km horizontal resolution. Isopycnal overturning streamfunction (ψ_{isop}) with a reference depth of 2 km in potential density (σ_2) space (A) and z space (B). (C) Eulerian-mean overturning streamfunction (ψ_{EM}). (D) Standing-wave overturning streamfunction (ψ_{SW}). (E) Tidal overturning streamfunction (ψ_{tide}). (F) Transient-eddy overturning streamfunction (ψ_{eddy}). The white dashed and solid contours show intervals of 0.05 Sv (1 Sv = $10^6 \text{ m}^3 \text{ s}^{-1}$) and 0.1 Sv, respectively. The black arrows show the direction of the overturning circulation, with positive values (red) corresponding to clockwise circulation, and negative values (blue) corresponding to counter-clockwise circulation. The black solid and dashed curves denote the deepest and shallowest bathymetry at each latitude, respectively. The 20-km sponge layers at the northern and southern boundaries are not shown. Note that the tidal component is largely compensated by the Eulerian-mean component.

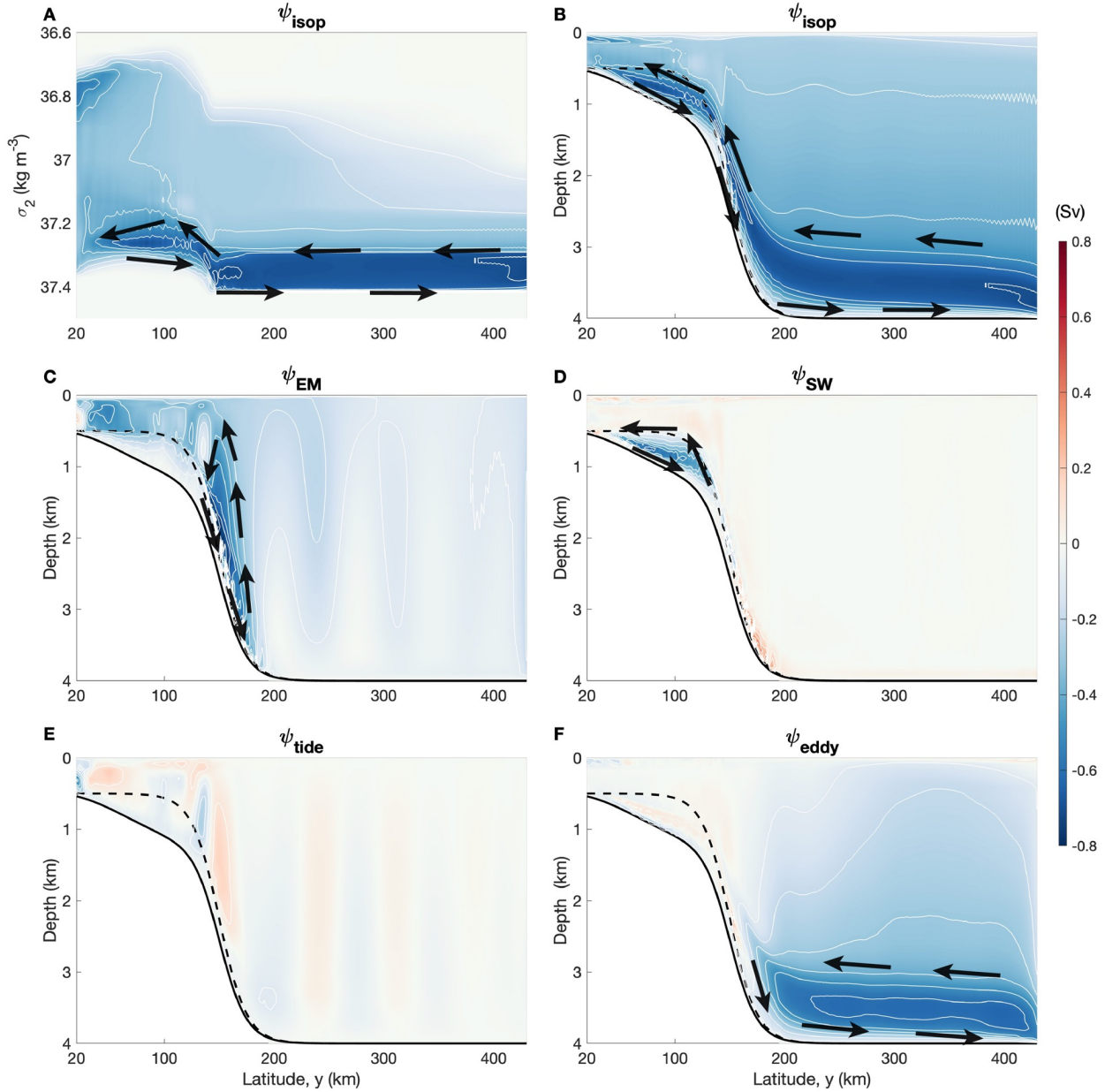


Figure 3.13: Temporal decomposition of the isopycnal overturning streamfunction for the dense-shelf simulation with 2-km horizontal resolution. As Fig. 3.12, but for the dense-shelf case.

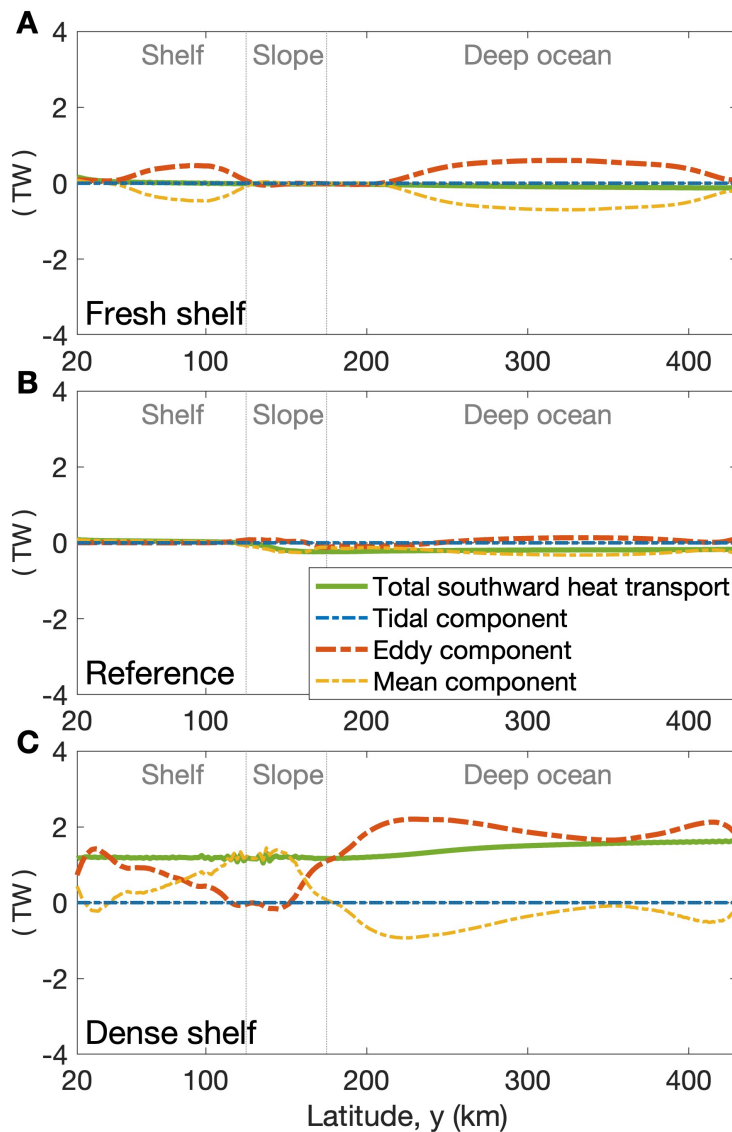


Figure 3.14: Eddy/mean heat decomposition for simulations with no tides and 2-km horizontal resolution.

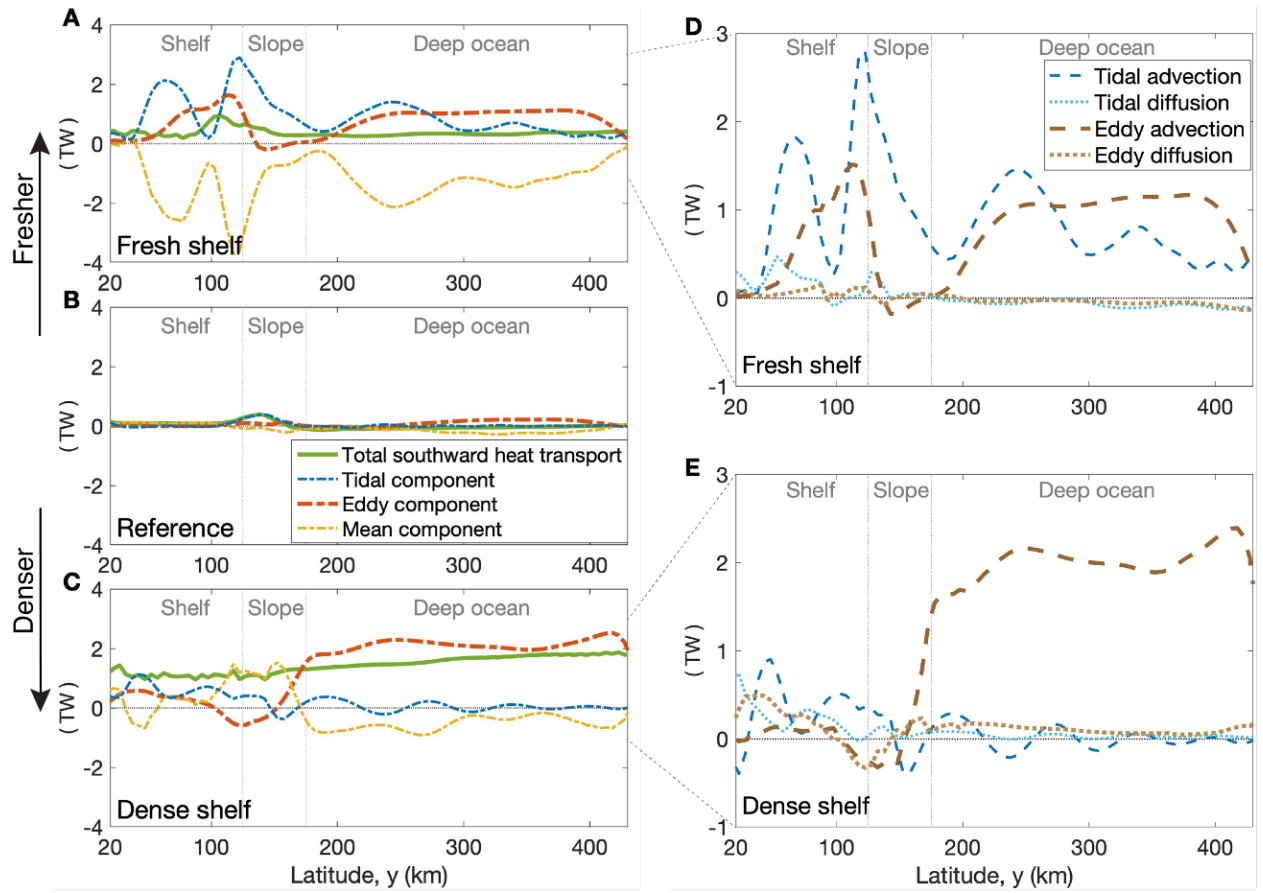


Figure 3.15: Temporal decomposition of the total shoreward heat transport. As Fig. 3.4, but for simulations with 5-km horizontal resolution.

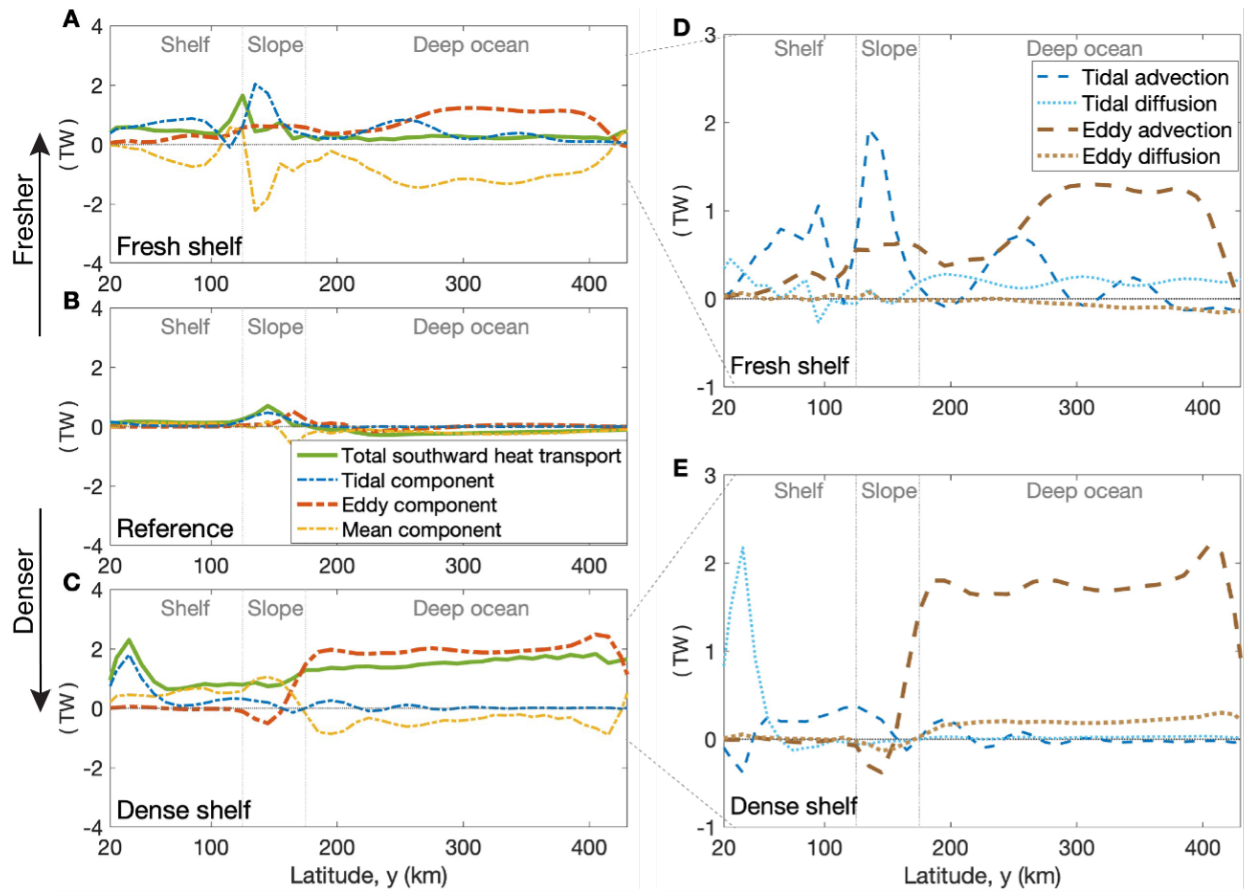


Figure 3.16: Temporal decomposition of the total shoreward heat transport. As Fig. 3.4, but for simulations with 10-km horizontal resolution.

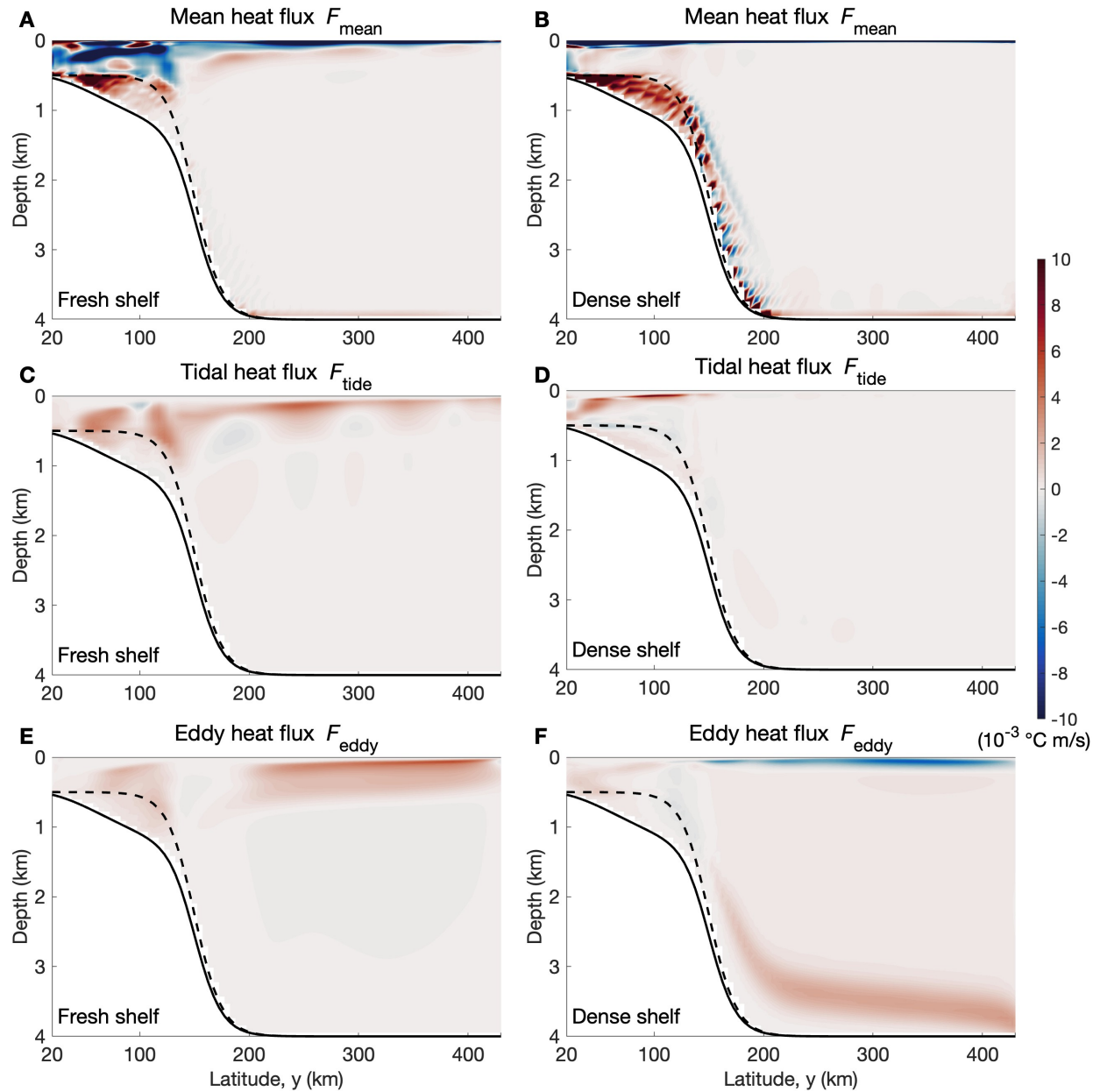


Figure 3.17: Temporal decomposition of the zonal-mean southward advective heat flux. As Fig. 3.9, but for simulations with 5-km horizontal resolution.

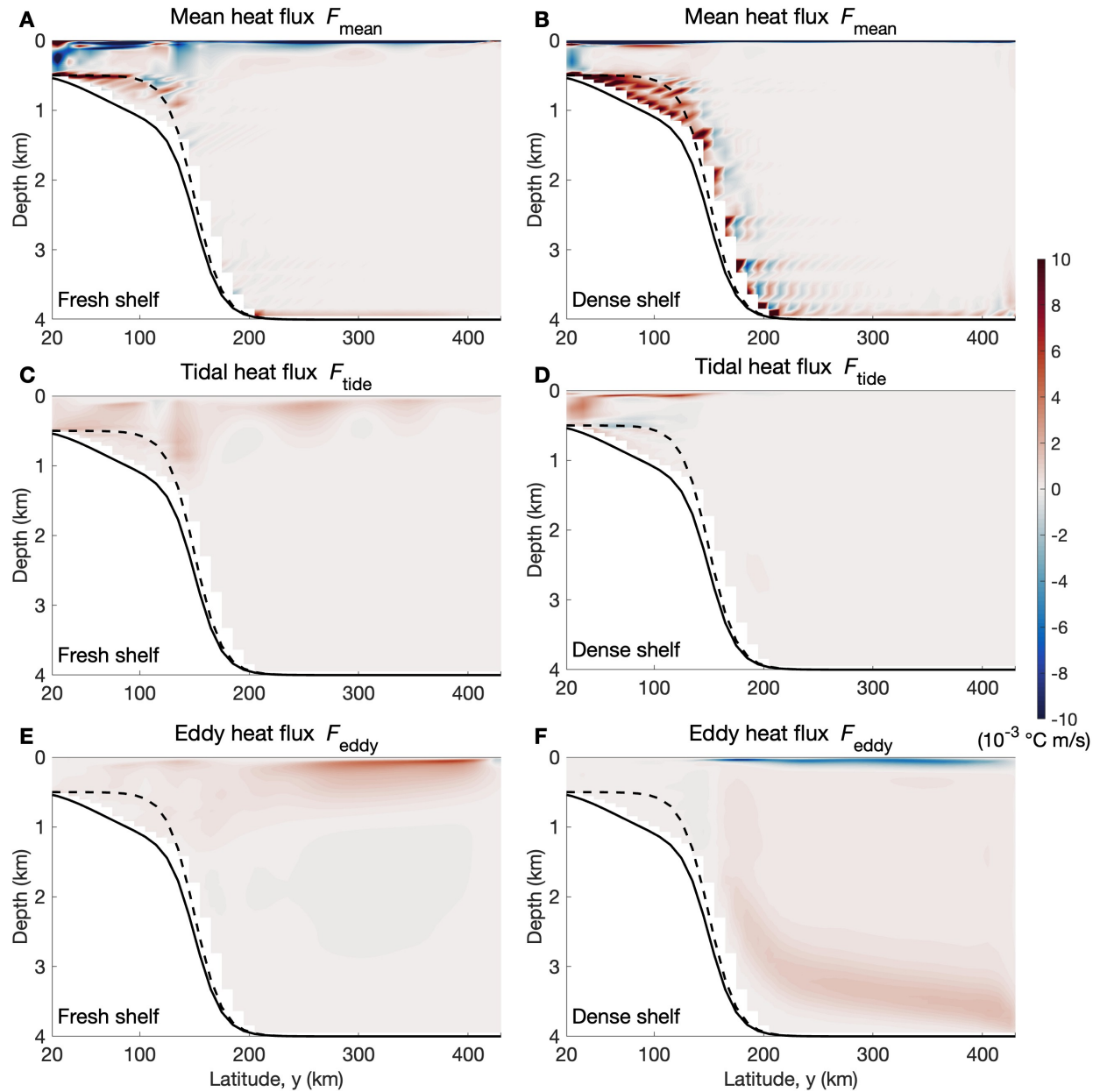


Figure 3.18: Temporal decomposition of the zonal-mean southward advective heat flux. As Fig. 3.9, but for simulations with 10-km horizontal resolution.

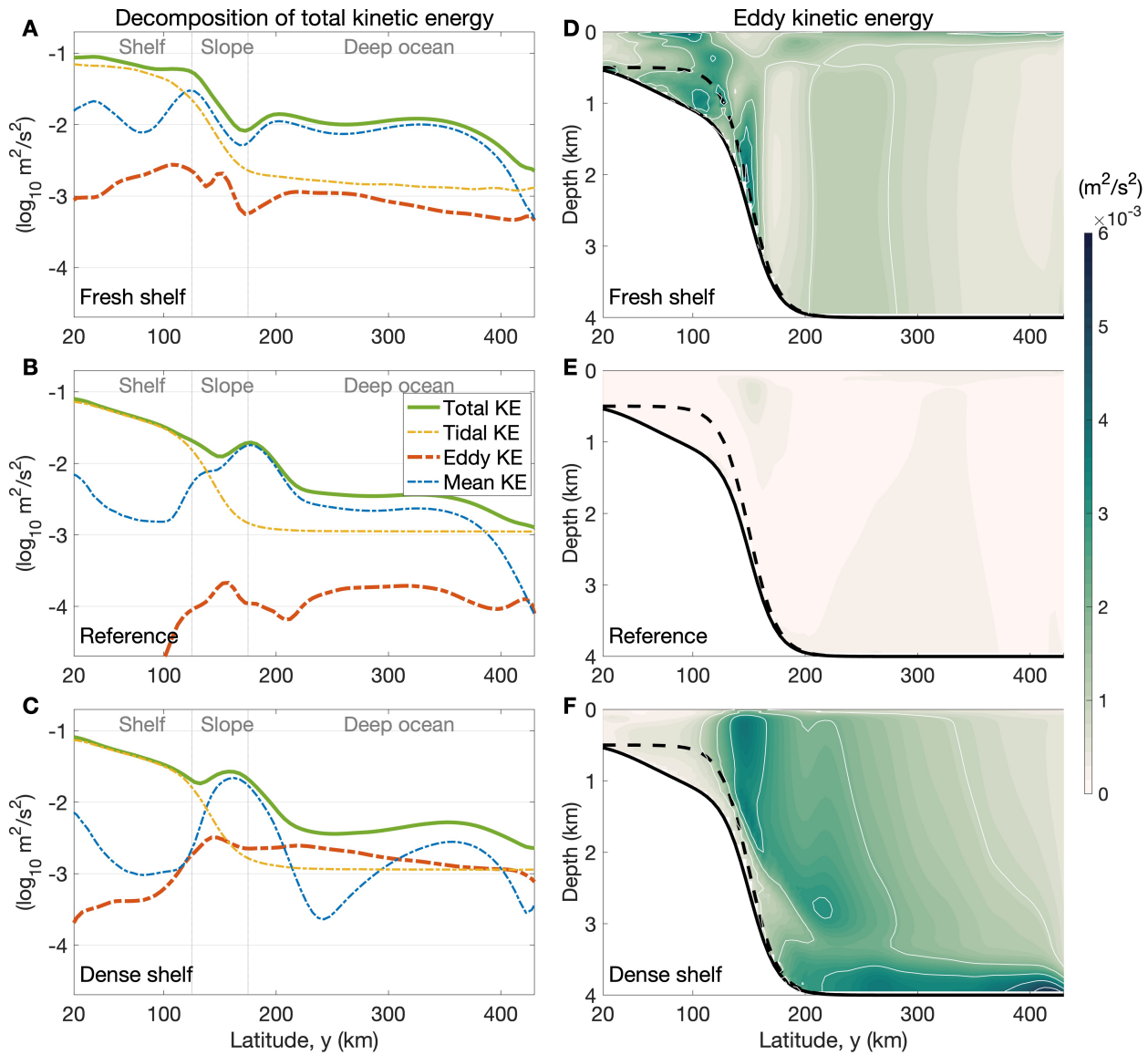


Figure 3.19: Temporal decomposition of the total kinetic energy. As Fig. 3.11, but for simulations with 5-km horizontal resolution.

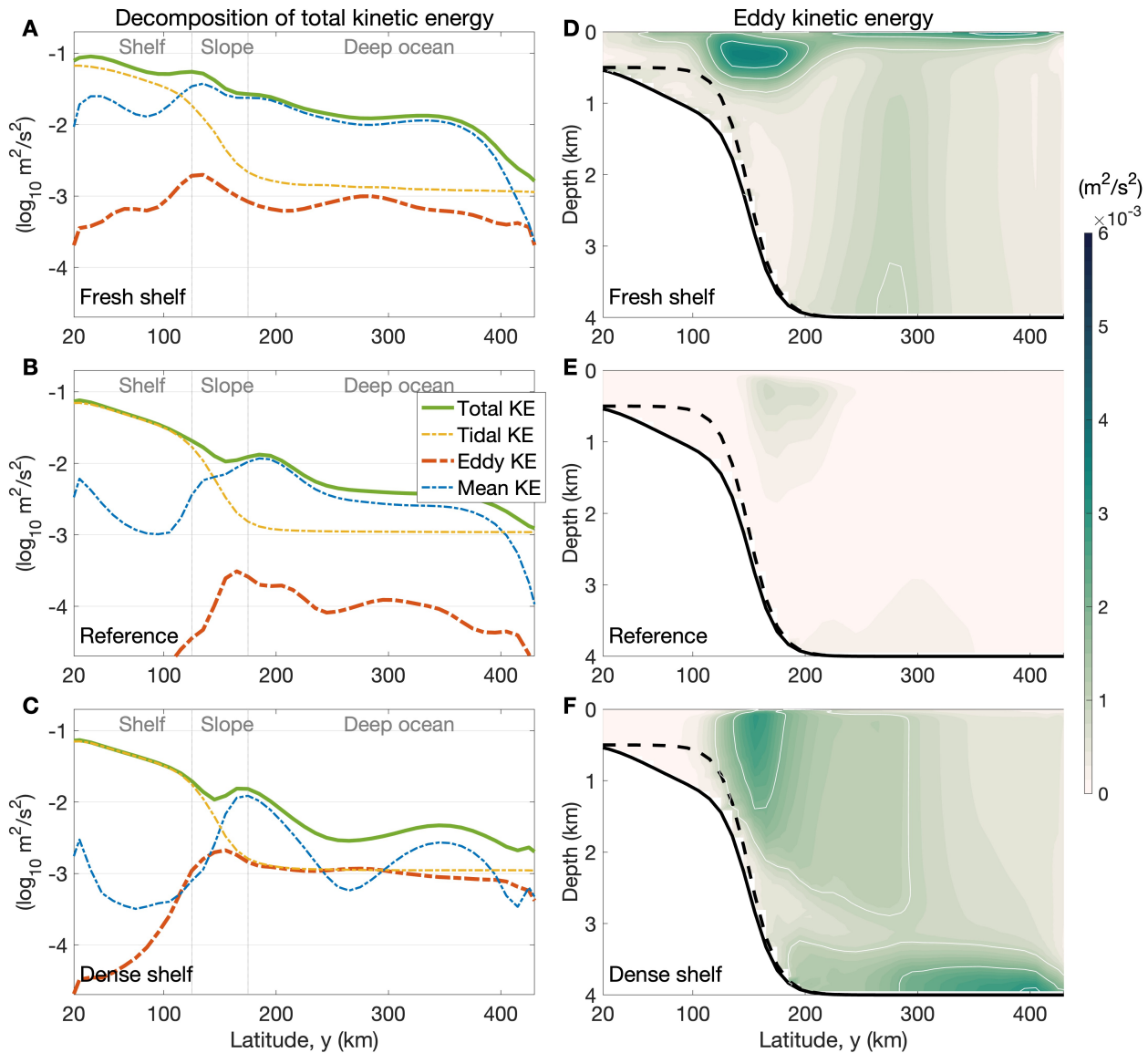


Figure 3.20: Temporal decomposition of the total kinetic energy. As Fig. 3.11, but for simulations with 10-km horizontal resolution.

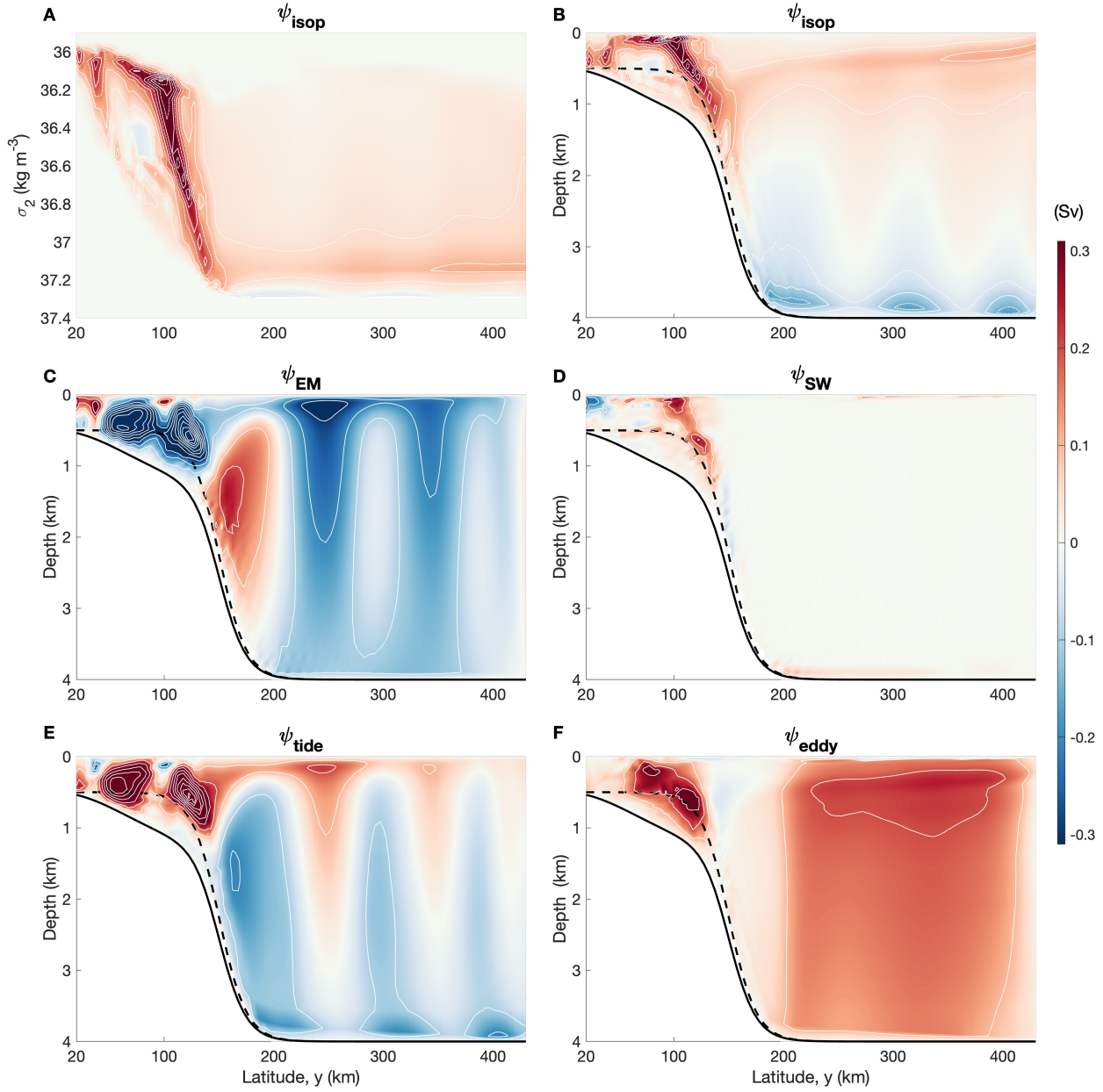


Figure 3.21: Temporal decomposition of overturning streamfunction for the fresh-shelf case. As Fig. 3.12, but for simulations with 5-km horizontal resolution.

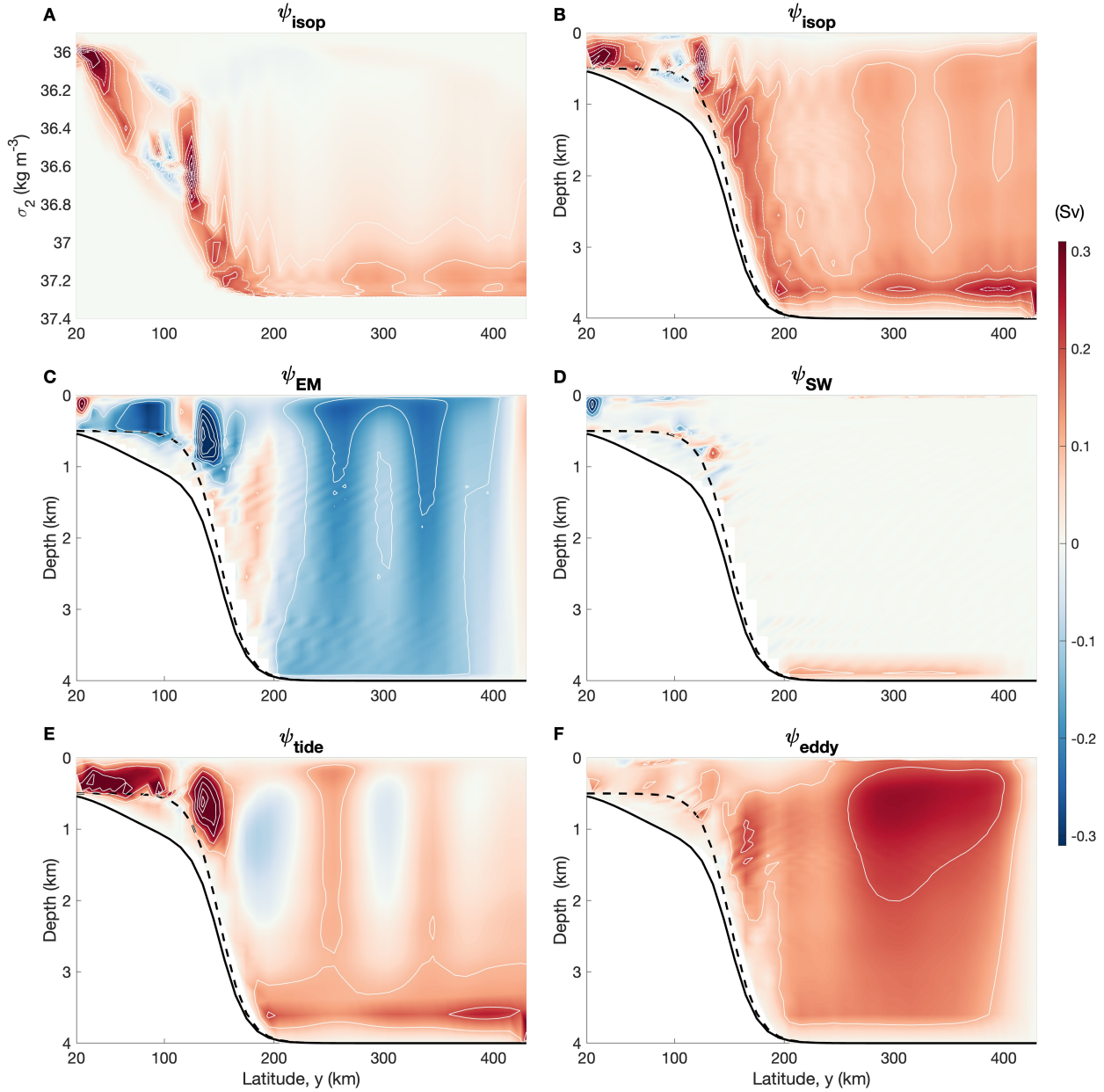


Figure 3.22: Temporal decomposition of overturning streamfunction for the fresh-shelf case. As Fig. 3.12, but for simulations with 10-km horizontal resolution.

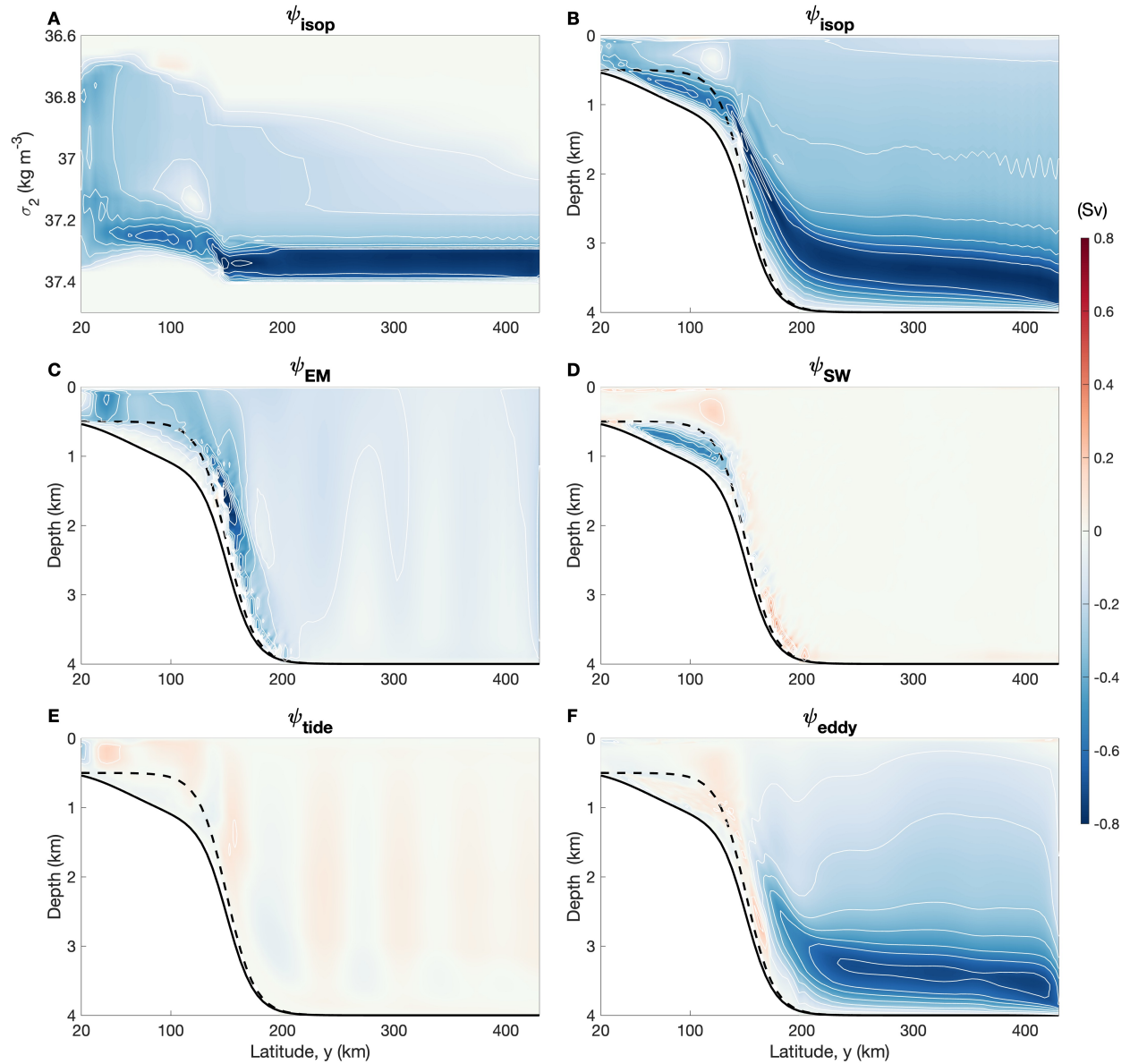


Figure 3.23: Temporal decomposition of overturning streamfunction for the dense-shelf case. As Fig. 3.13, but for simulations with 5-km horizontal resolution.

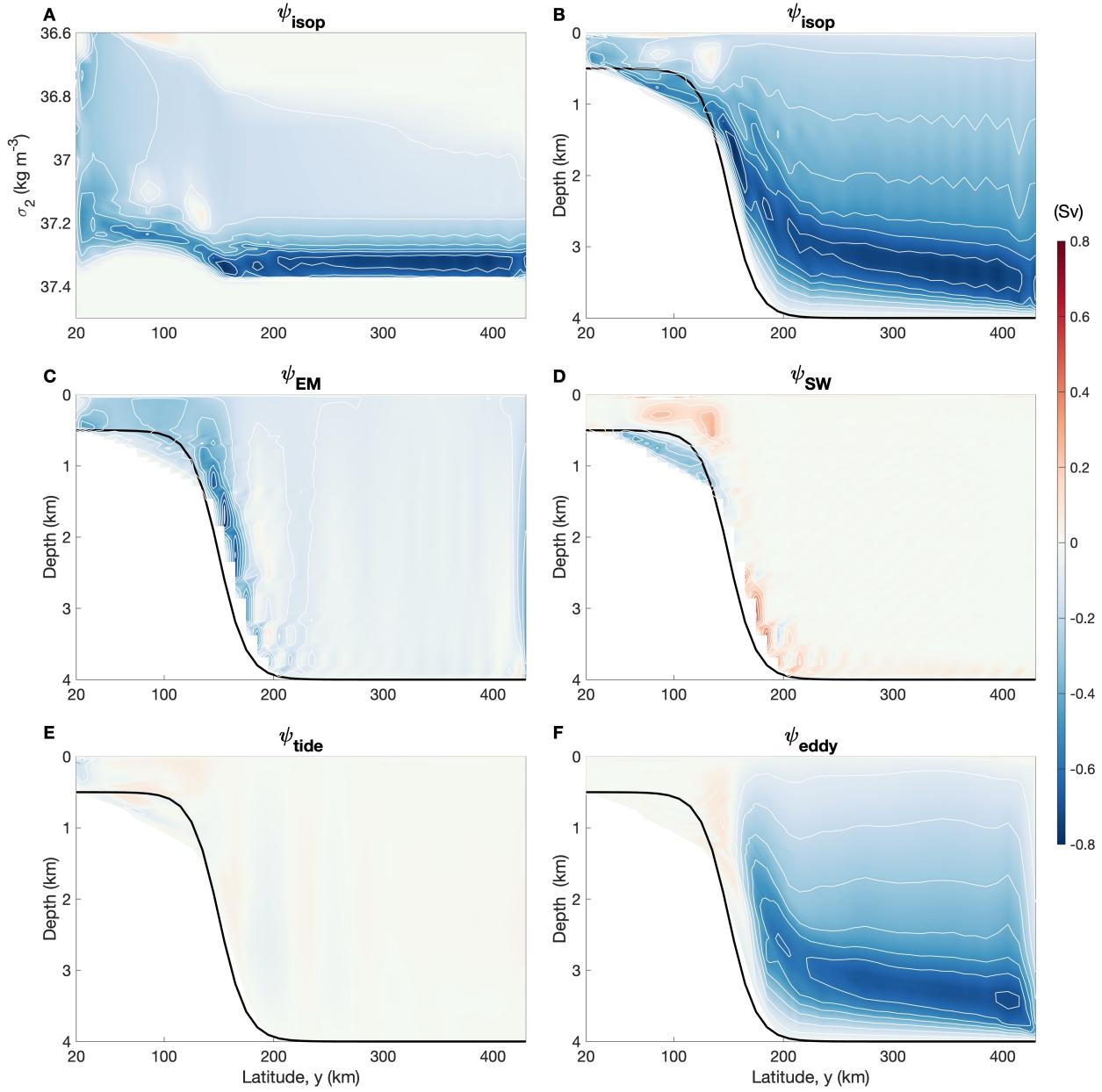


Figure 3.24: Temporal decomposition of overturning streamfunction for the dense-shelf case. As Fig. 3.13, but for simulations with 10-km horizontal resolution.

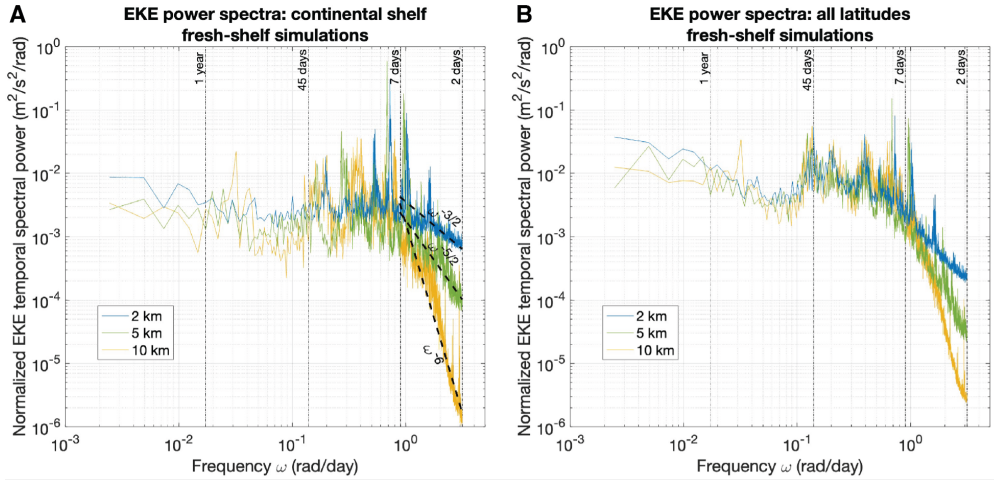


Figure 3.25: EKE power spectra for fresh-shelf simulations with different horizontal resolutions, normalized by the length of the timeseries. (A) EKE spectrum over the continental shelves (latitude $y=20\text{-}125\text{ km}$ and depth $z=0\text{-}500\text{ m}$). (B) Surface 500 m EKE spectrum for all latitudes (latitude $y=20\text{-}430\text{ km}$ excluding the 20km sponge layers at the southern and northern boundaries, and depth $z=0\text{-}500\text{ m}$).

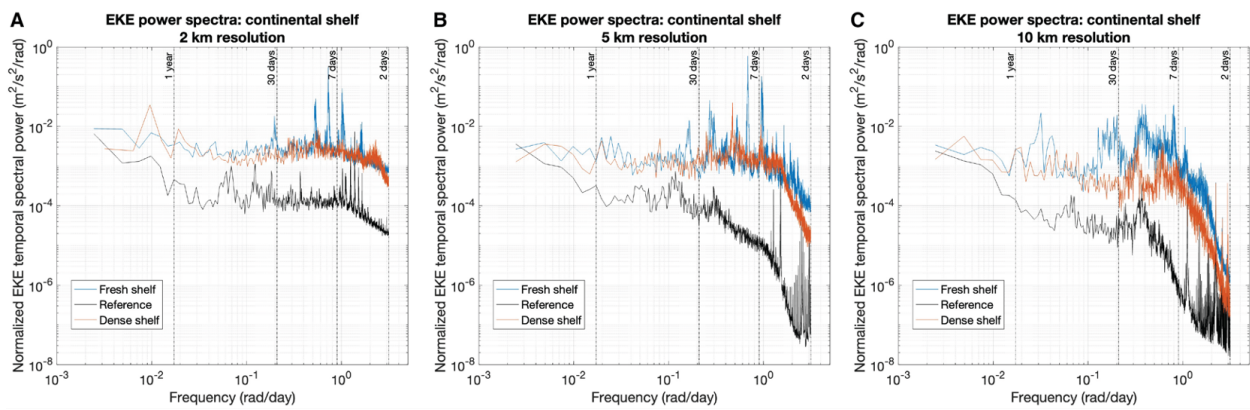


Figure 3.26: EKE power spectra over the continental shelves (latitude $y=20\text{-}125\text{ km}$, depth $z=0\text{-}500\text{ m}$), normalized by the length of the timeseries. (A) Fresh-shelf, reference, and dense-shelf simulations in the 2-km model. (B) 5-km model. (C) 10-km model.

CHAPTER 4

Antarctic slope undercurrent and onshore heat transport driven by meltwater upwelling

This chapter contains the manuscript by Y. Si, A. L. Stewart, A. Silvano, and A. Naveira Garabato, to be submitted.

Abstract

Elevated ice shelf melt rates in West Antarctica have been attributed to transport of warm Circumpolar Deep Water (CDW) onto the continental shelf via bathymetric troughs. These inflows are supplied by an eastward, subsurface slope current that opposes the westward momentum input from local winds and tides, referred to as the Antarctic slope undercurrent. Despite its importance to basal melt, the mechanism via which the undercurrent forms, and thus what controls the shoreward heat transport, remains unclear. In this study, the dynamics of the undercurrent is investigated using a high-resolution process model with coupled ocean, sea ice, and ice shelf components. Over a wide range of parameters, the sensitivities of the undercurrent strength, shoreward heat transport, and ice shelf melt rates to winds, tides, diapycnal mixing, and geometry are explored. It is shown that the bathymetric steering of the undercurrent toward the ice shelf is driven by upwelling of meltwater across density surfaces within the ice shelf cavity. Increased basal melt therefore strengthens the undercurrent and enhances onshore CDW transport, which indicates a previously unrecognized positive feedback that may accelerate future melt of ice shelves, potentially further destabilizing the West Antarctic Ice Sheet.

4.1 Introduction

The volume loss of the West Antarctic ice shelves is accelerating, with the most rapid ice-shelf thinning and iceberg calving detected in the Amundsen Sea (Paolo et al., 2015; Liu et al., 2015; Rignot et al., 2013; Pritchard et al., 2012). The warm Circumpolar Deep Water (CDW), a water mass up to 4°C above local freezing temperature (Jacobs et al., 2011), drives strong basal melt and retreat of the grounding line when it intrudes beneath the ice shelves, which reduces the ability of ice shelves to buttress the flow of the ice sheet into the ocean (Gudmundsson et al., 2019), leading to sea level rise (DeConto et al., 2021). Since much of the grounded ice lies below sea level, the West Antarctic Ice Sheet is particularly vulnerable to warm water intrusion and may completely collapse in the future (Joughin et al., 2021; Joughin and Alley, 2011). To accurately predict the future of the West Antarctic Ice Sheet and global sea-level rise, it is essential to understand the mechanisms of heat delivery and the feedback between ocean circulation and ice shelf melt.

Near the Antarctic margins, wind stress and tides, the primary forces of the ice-ocean system, inject westward momentum into the slope current: The westward local wind stress drives surface ocean currents to the west (Walker et al., 2013; Hazel and Stewart, 2019); tidal oscillation advects positive vorticity southward to the continental shelf due to vortex squeezing, and negative vorticity northward to the deep ocean due to vortex stretching, generating a westward residual circulation along the continental slope (Robinson, 1981). Counterintuitively, both observations and numerical models have confirmed the existence of eastward undercurrents along the continental shelf break of West Antarctica (e.g., Silvano et al., 2022; Kimura et al., 2017; Walker et al., 2013; Azaneu et al., 2023). Previous studies have suggested that the melt rates of the Amundsen Sea ice shelves co-vary with the strength of the undercurrent because when encountering submarine troughs, the undercurrent transports CDW directly toward ice shelf cavities (Silvano et al., 2022; Jourdain et al., 2017). In spite of its importance in driving basal melt, it remains unclear what drives the eastward undercurrent at the ocean subsurface. Therefore, a mechanistic understanding of how different forcings such as winds and tides regulate undercurrent strength and heat transport is still lacking.

Previous studies indicated that winds, tides, meltwater, and topography may influence the

variability of the West Antarctic slope undercurrent and ice shelf melt. Winds over the continental shelf and slope have been suggested to control the fluctuations in undercurrent flow (Dotto et al., 2020; Kimura et al., 2017) and ocean heat delivery onto the West Antarctic continental shelves (Dotto et al., 2019). Silvano et al. (2022) showed that, on decadal time scales, the undercurrent variability and ice shelf melt are affected by the variability in the tropical Pacific through atmospheric teleconnection. In addition, the ice-shelf melt response to perturbed winds is strongly influenced by melt-induced circulation (Donat-Magnin et al., 2017). Tides also play a role in modulating the ice shelf melt rates by increasing dynamical ice/ocean exchange (Jourdain et al., 2019; Robertson, 2013). Jourdain et al. (2017) found a linear relationship between volume transport into the cavity and ice shelf melt rate in an Amundsen Sea regional model, suggesting that meltwater may drive CDW towards the ice shelf. Though the formation dynamics of undercurrents in other parts of the ocean have been reported in previous literature (e.g., Chen et al., 2021; Li and Gan, 2020), they can not be directly applied to West Antarctica due to the lack of ice-ocean interactions and the remarkable difference in hydrographic conditions, topographic geometry, and wind forcing. Thus, the mechanism underlying the formation of the West Antarctic slope undercurrent is still ambiguous.

In this study, the dynamics of the West Antarctic slope undercurrent is investigated using a high-resolution process model with coupled ocean, sea ice, and ice shelf. We show that there is a positive feedback between the undercurrent and ice shelf melt: Stronger meltwater upwelling leads to stronger slope undercurrent and enhanced onshore heat transport in a warming climate, accelerating future melt of ice shelves. We reveal the mechanism of undercurrent formation and provide a mechanistic explanation of this positive feedback by analyzing the vorticity budget within the CDW layer. The theory is further verified by a suite of sensitivity experiments with varying winds, tides, diapycnal mixing, and geometry.

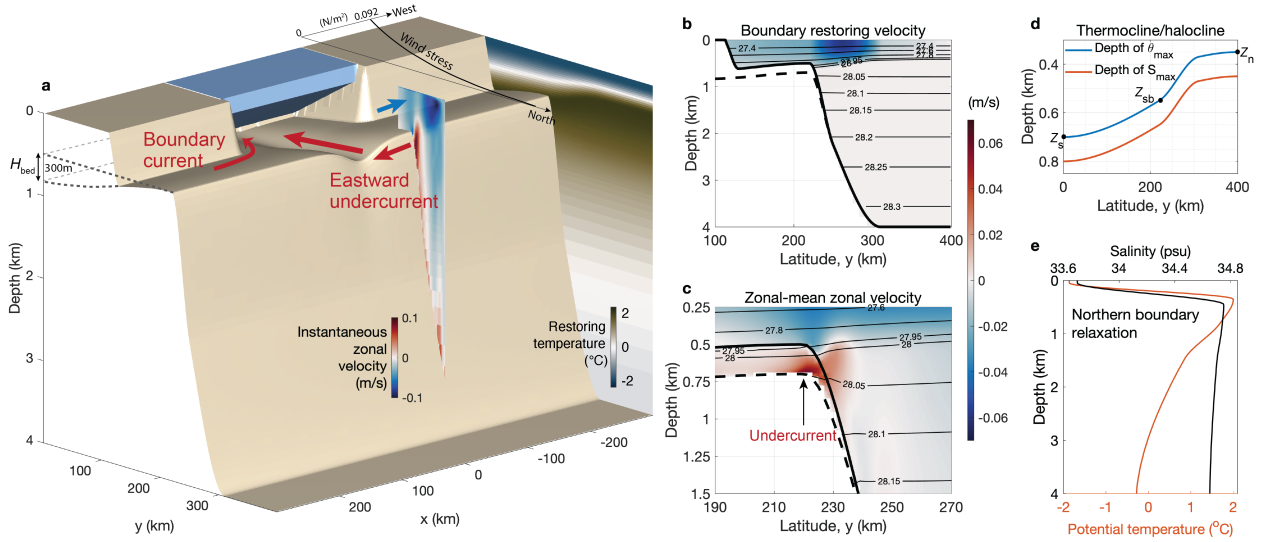


Figure 4.1: Model configuration. **a**, Model bathymetry, ice shelf, wind stress amplitude, restoring temperature at the zonal boundaries, and a snapshot of zonal velocity over the continental slope. **b**, Zonal velocity (color) and neutral density (thin black contours) prescribed at the two sponge layers of the eastern and western boundaries. The boundary-layer zonal velocity is set by vertically integrating the thermal-wind relation from the seafloor to level z , assuming zero velocity at the seafloor. The shallowest and deepest bathymetric contours are indicated by the thick solid and dashed lines, respectively. **c**, Zonal-mean zonal velocity overlaid by neutral density contours in the reference simulation. The 20-km zonal sponge layers at the zonal boundaries have been excluded from the calculation of the zonal mean. **d**, Depth of the thermocline and halocline (defined as the depth of the maximum potential temperature and salinity, respectively) restored at the zonal boundaries, which is also prescribed as an initial condition across the domain. For a stable stratification, the salinity maximum needs to be deeper than the temperature maximum. The thermocline depth at the northern boundary (Z_n) is fixed to 350 m for all simulations. The thermocline depth at the southern boundary (Z_s) and at the shelf break (Z_{sb}) are varied in some simulations (Table 4.1). **e**, Northern boundary restoring temperature and salinity.

4.2 Simulating West Antarctic slope undercurrent and ice shelf melt

Figure 4.1 illustrates the model configuration. The model with coupled ocean, sea ice, and ice shelf components has been configured into a 600 km (zonal) \times 400 km (meridional) \times 4000 m (vertical) domain, with the ice-shelf front and coastline at the latitudes of 100 km and 120 km, respectively. The model bathymetry is set based on the ocean bathymetry in the Amundsen Sea, West Antarctica (Schaffer and Timmermann, 2016), where the slope undercurrent is observed. The continental shelf has a depth of 500 m at the shelf break, deepening toward the southern boundary

with a 300 m change in bedrock elevation ($H_{\text{bed}} = 300$ m, Fig. 4.1a). There is a submarine trough that connects the shelf break to the ice-shelf cavity, with a depth of 300 m and a width of 30 km. The model is forced by time-invariant surface air conditions that are representative of the annual mean state of the Amundsen Sea, with steady northwestward winds weakening linearly offshore (Fig. 4.1a; Methods). We restore ocean temperature, salinity, velocity, and sea ice properties including ice thickness, concentration, and ice velocity at the zonal boundaries and northern boundary within a sponge layer with a width of 20 km (Methods). Note that boundary zonal velocities are directed westward (Fig. 4.1b), i.e., the formation of the eastward undercurrent is not in any way imposed by the boundary conditions. Further details on model configuration, including boundary conditions, surface air conditions, model resolution, viscosity, diffusivity, tides, etc., are provided in Methods.

As listed in Table 4.1, we conducted perturbation experiments with varied winds, tides, vertical diffusivity, bedrock elevation of the continental shelf (H_{bed}), and width of the trough (W_{tr}). We additionally ran simulations with different boundary conditions (a deeper thermocline at all boundaries) or different shelf geometry (no trough over the shelf). We covary thermocline depth, winds, and shelf geometry in some simulations. We choose to vary these parameters because **(i)** winds and tides are the primary mechanical forcings of the ice-ocean system in the Antarctic Slope Current (e.g., [Thompson et al., 2018](#)); **(ii)** observations and numerical models have shown that the basal melt rate is correlated with the thickness of CDW over the shelf (e.g., [Dotto et al., 2019](#); [Jenkins et al., 2016](#)), which is set by the difference between the thermocline depth and bedrock elevation; **(iii)** submarine troughs affect the speed of the undercurrent ([Walker et al., 2013](#)) and shelf/slope exchange ([Hampson and Pringle, 2022](#)); **(iv)** vertical mixing modulates isopycnal geometry, possibly affecting the strength of the undercurrent. To explicitly investigate how meltwater affects the shelf/slope circulation and on-shelf heat transport, we designed four simulations with a pseudo-ice shelf, in which the ice-shelf thermodynamics were turned off and meltwater fluxes were prescribed at the tilted interface between the ice shelf and the ocean (Methods).

The reference simulation captures the salient features of the circulation system, heat transport, and melt rate in the Amundsen Sea. The sea surface height increases toward the continental shelf (Fig. 4.2a,d) due to wind-induced Ekman transport and the imposed inflow boundary conditions

Short name	h_{i0}	(U_{a0}, V_{a0})	A_{tide}	W_{tr}	H_{bed}	H_{tr}	Z_{sb}	Z_s	κ^{3D}	Ice shelf	ω_{melt}
	(m)	(m/s)	(m/s)	(km)	(m)	(m)	(m)	(m)	(m ² /s)		(m/s)
Reference	1.0	(-5, 5)	0	30	300	200	550	700	—	Real	—
Wind_2	1.0	(-2, 2)	0	30	300	200	550	700	—	Real	—
Wind_8	1.0	(-8, 8)	0	30	300	200	550	700	—	Real	—
Hbed_0	1.0	(-5, 5)	0	30	0	200	550	700	—	Real	—
Hbed_150	1.0	(-5, 5)	0	30	150	200	550	700	—	Real	—
Hbed_450	1.0	(-5, 5)	0	30	450	200	550	700	—	Real	—
Wtr_15	1.0	(-5, 5)	0	15	300	200	550	700	—	Real	—
Tide_0.025	1.0	(-5, 5)	0.025	30	300	200	550	700	—	Real	—
Tide_0.05	1.0	(-5, 5)	0.05	30	300	200	550	700	—	Real	—
Kmax_1e-4	1.0	(-5, 5)	0	30	300	200	550	700	0.0001	Real	—
Kmax_1e-3	1.0	(-5, 5)	0	30	300	200	550	700	0.001	Real	—
Kmax_3e-3	1.0	(-5, 5)	0	30	300	200	550	700	0.003	Real	—
DeepThermo	1.0	(-5, 5)	0	30	300	200	750	1000	—	Real	—
DeepWind_2	1.0	(-2, 2)	0	30	300	200	750	1000	—	Real	—
DeepWind_8	1.0	(-8, 8)	0	30	300	200	750	1000	—	Real	—
DeepHbed_0	1.0	(-5, 5)	0	30	0	200	750	1000	—	Real	—
Htr_0	1.0	(-5, 5)	0	30	300	0	550	700	—	Real	—
Htr_0Hbed_0	1.0	(-5, 5)	0	30	0	0	550	700	—	Real	—
Htr_0Deep	1.0	(-5, 5)	0	30	300	0	750	1000	—	Real	—
Htr_0Hbed_0Deep	1.0	(-5, 5)	0	30	0	0	750	1000	—	Real	—
Melt_0	1.0	(-5, 5)	0	30	300	200	550	700	—	Pseudo 0	—
Melt_8	1.0	(-5, 5)	0	30	300	200	550	700	—	Pseudo 8/Nt	—
Melt_16	1.0	(-5, 5)	0	30	300	200	550	700	—	Pseudo 16/Nt	—
Melt_24	1.0	(-5, 5)	0	30	300	200	550	700	—	Pseudo 24/Nt	—

Table 4.1: **List of experiments.** The reference simulation and perturbed parameters are marked in boldface. h_{i0} is the initial ice thickness across the domain, and the restoring ice thickness at the eastern, western, and northern boundaries. U_{a0} and V_{a0} are the zonal and meridional wind extrema at the southern boundary, respectively. The magnitude of the wind speed decreases linearly offshore. A_{tide} is the prescribed tidal current amplitude at the northern boundary. W_{tr} is the half-width of the trough. H_{bed} is the change in bedrock elevation from the shelf break to the southern boundary. H_{tr} is the depth of the trough over the continental shelf. The thermocline depth at the northern boundary, shelf break, and southern boundary are Z_n ($Z_n = 350$ m in all simulations), Z_{sb} , and Z_s , respectively, with larger values corresponding to a deeper thermocline (Fig. 4.1d). κ^{3D} is the maximum value of the 3D vertical diffusivity. ω_{melt} is the equivalent basal melt rate prescribed at the titled surface the pseudo ice shelf (0, 8, 16, and 24 m/yr, respectively). Nt = 3.0672×10^7 is the number of seconds per year.

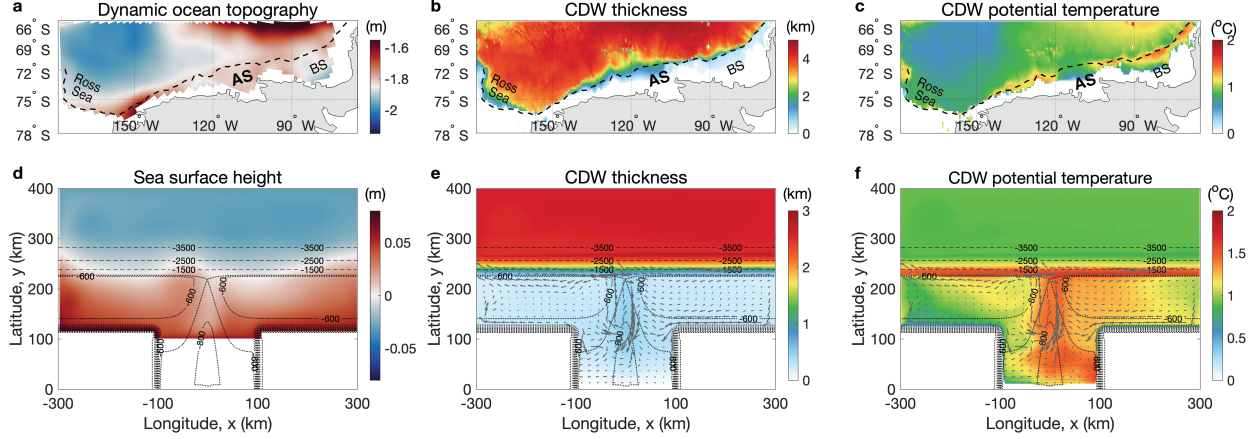


Figure 4.2: Comparison of the reference simulation with observations. **a**, Mean dynamic ocean topography of the Ross Sea, Amundsen Sea (AS), and Bellingshausen Sea (BS) averaged from 2011 to 2013. Data taken from Armitage et al. (2018). **b,c**, Climatological (1991 – 2020) mean CDW thickness and mean CDW potential temperature from the World Ocean Atlas 2023 (Locarnini et al., 2023). **d**, Sea surface height anomaly, **e**, CDW thickness, and **f**, depth-averaged CDW potential temperature in the reference simulation, overlaid by gray arrows of CDW volume flux over the shelf and upper slope ($y \leq 250$ km). The bathymetric contours are denoted by the thin dashed lines with an interval of 1000 m, and thin dotted lines with an interval of 100 m.

with a westward geostrophic flow. The CDW (defined as potential temperature warmer than 0°C hereafter) thickness is about 250 m over the continental shelf and 550 m in the trough, increasing to about 2.6 km in the deep ocean (Fig. 4.2b,e). Consistent with Jacobs et al. (2011), the CDW potential temperature reaches 1.5°C over the shelf and slope, nearly 3.5°C above the freezing temperature, decreasing to less than 1°C in the deep ocean. The circulation in the CDW layer is cyclonic in the trough, consisting of a narrow, eastward slope undercurrent upstream (west) of the trough, a strong southward CDW inflow, and a northward return flow (Fig. 4.3a). Fig. 4.4 shows the cross-sections of potential temperature, salinity, and zonal velocity in the reference simulation, which agrees well with the observation of Amundsen Sea slope undercurrent by Walker et al. (2013): The undercurrent is stronger upstream of the trough and significantly weakened downstream of the trough, suggesting a net onshore flow within the trough. Both in nature and in the simulations, the eastward undercurrent is present despite the strong mechanical forcing due to winds and tides that favors westward flow. In addition, the undercurrent transports sufficient heat through the trough to the ice shelf to cause a realistic amount of basal melt (16.0 m/yr) in the reference simulation,

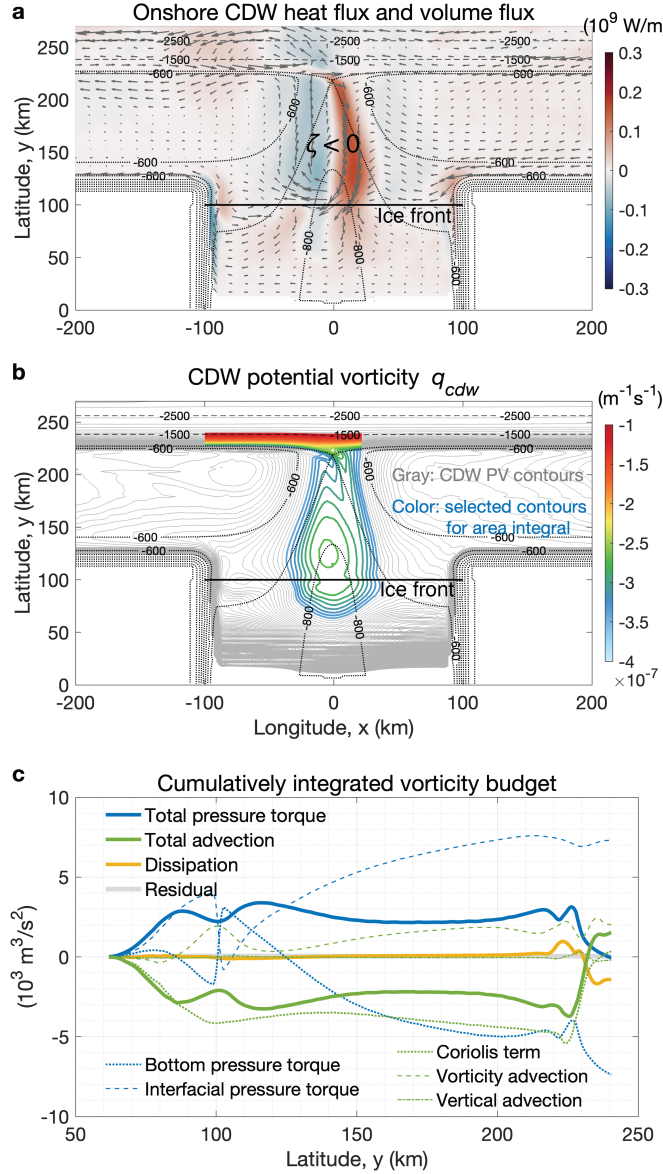


Figure 4.3: Area-integrated vorticity budget of the cyclonic circulation in the CDW layer. **a,** Onshore CDW heat flux (color) and CDW volume flux (arrows) in the reference simulation, with red corresponding to shoreward (southward) heat flux. There is a cyclonic flow (relative vorticity $\zeta < 0$) comprising the slope undercurrent and the CDW circulation in the trough. The black solid line denotes the location of the ice shelf front at $y = 100 \text{ km}$. The bathymetric contours are denoted by the thin dashed lines with an interval of 1000 m, and thin dotted lines with an interval of 100 m. **b,** Potential vorticity (PV) of the CDW layer denoted by the gray contours with an interval of $10^{-8} \text{ m}^{-1}\text{s}^{-1}$. The colored PV contours denote the selected region, with the maximum and minimum PV values of $-1.0 \times 10^{-7} \text{ m}^{-1}\text{s}^{-1}$ and $-3.5 \times 10^{-7} \text{ m}^{-1}\text{s}^{-1}$, respectively. Over the shelf break and upper slope ($225 \text{ km} \leq y \leq 240 \text{ km}$), the selected region is cut off at $x = -100 \text{ km}$ and $x = 40 \text{ km}$, respectively. **c,** The vorticity budget of the CDW layer cumulatively integrated from south to north within the selected region shown in panel **b**, as a function of latitude.

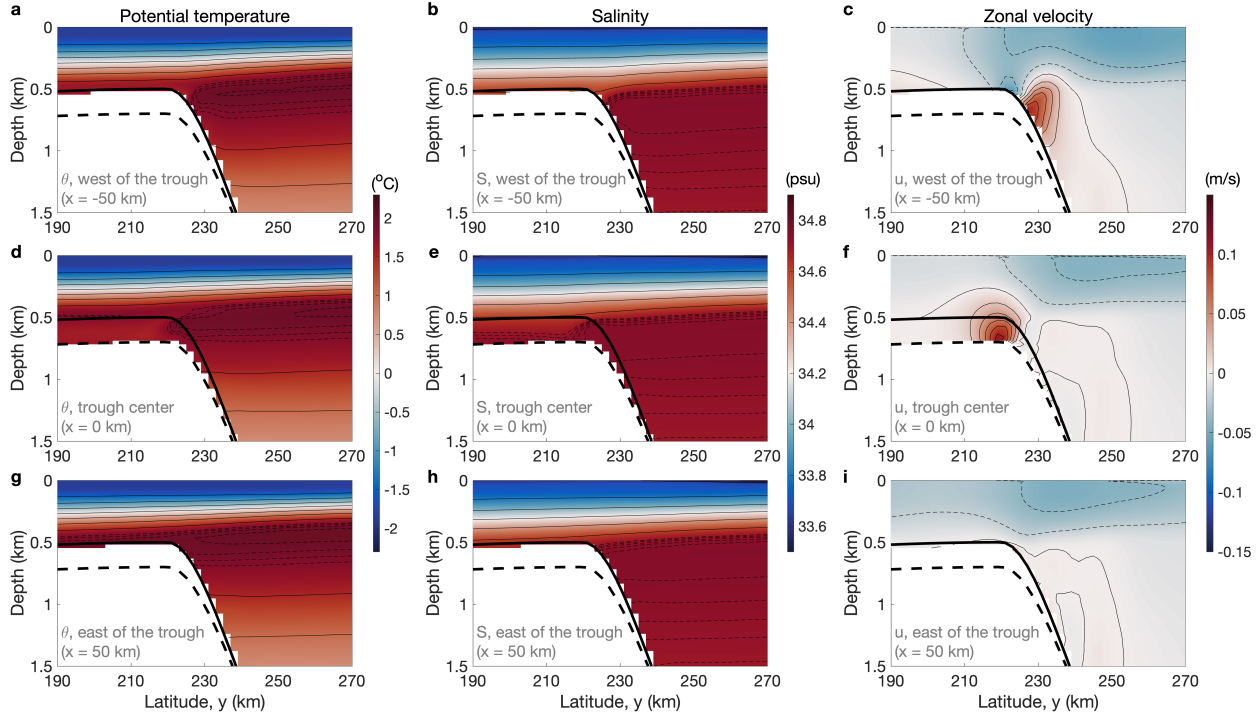


Figure 4.4: Cross-sections of potential temperature, salinity, and zonal velocity. **a-c**, West of the trough at $x = -50$ km. **d-f**, Trough center at $x = 0$ km. **g-i**, East of the trough at $x = 50$ km. The shallowest and deepest bathymetric contours are indicated by the thick solid and dashed lines, respectively.

which is comparable with the major ice shelves in the Amundsen Sea (Pine Island 16.2 ± 1 m/yr and Thwaites 17.7 ± 1 m/yr; [Rignot et al., 2013](#)).

4.3 Buoyancy-driven slope undercurrent and onshore CDW heat transport

The perturbation simulations indicate a correlation between the undercurrent transport (Eq. 4.16) and ice shelf melt (Fig. 4.5e and Fig. 4.6c). The undercurrent is relatively strongly modulated by processes that change the isopycnal geometry, such as tides, buoyancy forcing, and diapycnal mixing. Across all the varied parameters, the change in bedrock elevation of the continental shelf (H_{bed}) exerts the strongest control on the undercurrent and ice-shelf melt rate. Larger H_{bed} corresponds to a thicker CDW layer over the shelf and a larger heat content. Through pumping warm water onto the shelf, tides of the typical amplitude observed in the Amundsen Sea (0.025 m/s in the deep

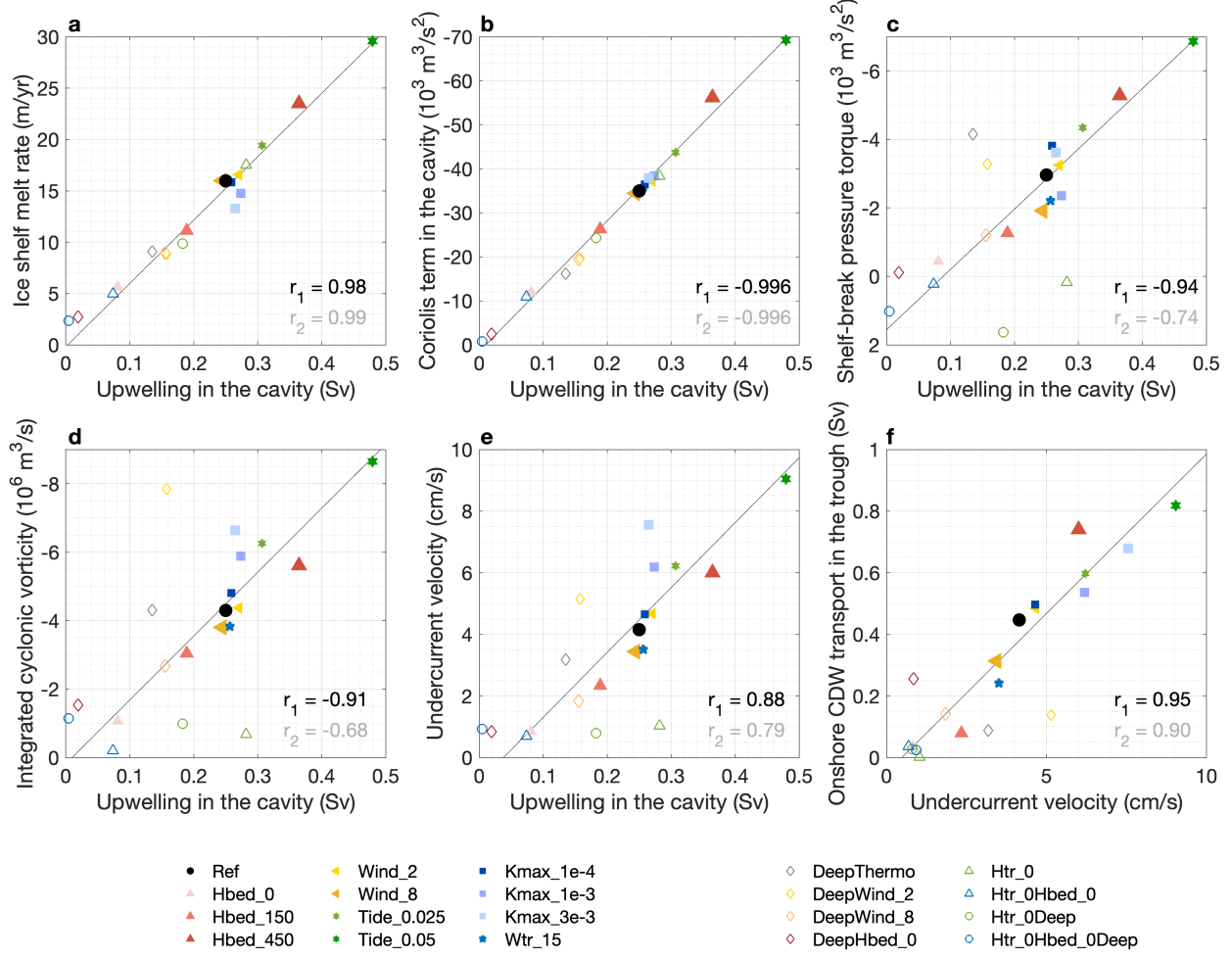


Figure 4.5: Perturbation experiments. Correlation between the diapycnal upwelling across the 0°C isotherm in the ice-shelf cavity with **a**, ice shelf melt rate, **b**, Coriolis term in the CDW vorticity budget integrated within the cavity, **c**, total pressure torque of the CDW layer integrated over the shelf break west of the trough (210 km $\leq y \leq$ 235 km, $-120 \text{ km} \leq x \leq 0 \text{ km}$, the green box in Fig. 4.9i), **d**, cyclonic vorticity integrated over the shelf break west of the trough, and **e**, transport-weighted undercurrent velocity west of the trough (Eq. 4.17). **f**, Correlation between transport-weighted undercurrent velocity and shoreward CDW transport within the trough ($1 \text{ Sv} = 10^6 \text{ m/s}$, Eq. 4.19). The names of the experiments in the figure are consistent with Table 4.1. In each panel, r_1 is the correlation coefficient for simulations with fixed topographic geometry and boundary isopycnal geometry, denoted by the filled markers; r_2 is the correlation coefficient for all simulations, including simulations with varied topographic geometry and boundary isopycnal geometry, denoted by the hollow markers; the thin black line is the linear fit for the filled markers.

ocean; see Methods) increase ice-shelf melt by 3.5 m/yr (22%), consistent with previous estimates (e.g., Robertson, 2013). Details on the melt rate sensitivity are discussed in the Methods.

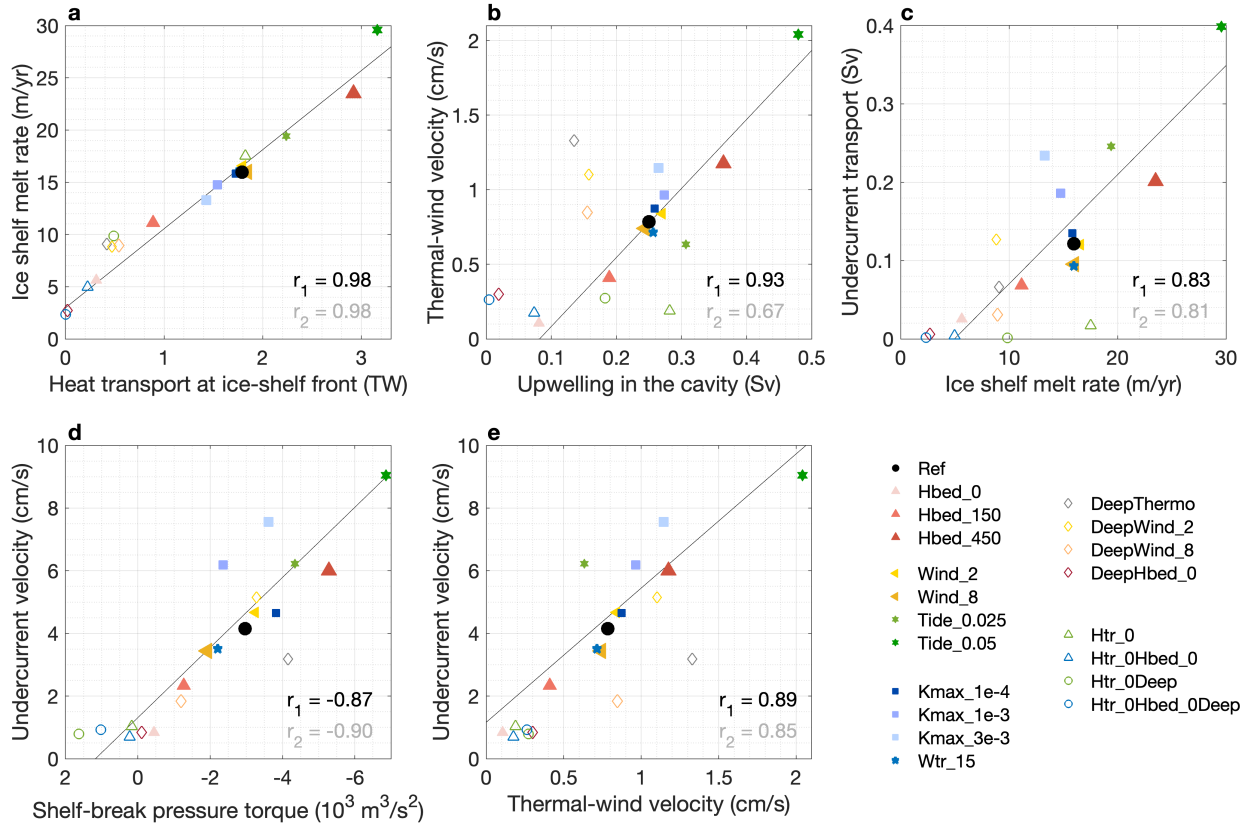


Figure 4.6: Perturbation experiments. **a**, Correlation between the cumulative heat transport at the ice-shelf front ($y = 100$ km) with ice shelf melt rate. **b**, Correlation between the diapycnal upwelling across the 0°C isotherm in the ice-shelf cavity with the thermal-wind velocity, which is a quantification of the cross-slope buoyancy gradient (Eq. 4.18b). **c**, Correlation between ice shelf melt rate and zonal-mean undercurrent transport west of the trough ($1 \text{ Sv} = 10^6 \text{ m/s}$; Eq. 4.16). **e,f**, Correlation between the transport-weighted undercurrent velocity (Eq. 4.17) with the pressure torque of the CDW layer integrated over the shelf break west of the trough ($210 \text{ km} \leq y \leq 235 \text{ km}$, $-120 \text{ km} \leq x \leq 0 \text{ km}$, the green box in Fig. 4.8i) and thermal-wind velocity (Eq. 4.18b), respectively. The names of the experiments in the figure are consistent with Table 4.1. In each panel, r_1 is the correlation coefficient for simulations with fixed topographic geometry and boundary isopycnal geometry, denoted by the filled markers; r_2 is the correlation coefficient for all simulations, including simulations with varied topographic geometry and boundary isopycnal geometry, denoted by the hollow markers; the thin black line is the linear fit for the filled markers.

Since winds and tides exert forces that oppose the undercurrent, the correlation between undercurrent and ice-shelf melt raises the hypothesis that the undercurrent is driven by sub-ice shelf buoyancy fluxes. To evaluate this hypothesis and provide insight into how basal melt influences shelf/slope circulation and shoreward heat transport, we designed four controlled exper-

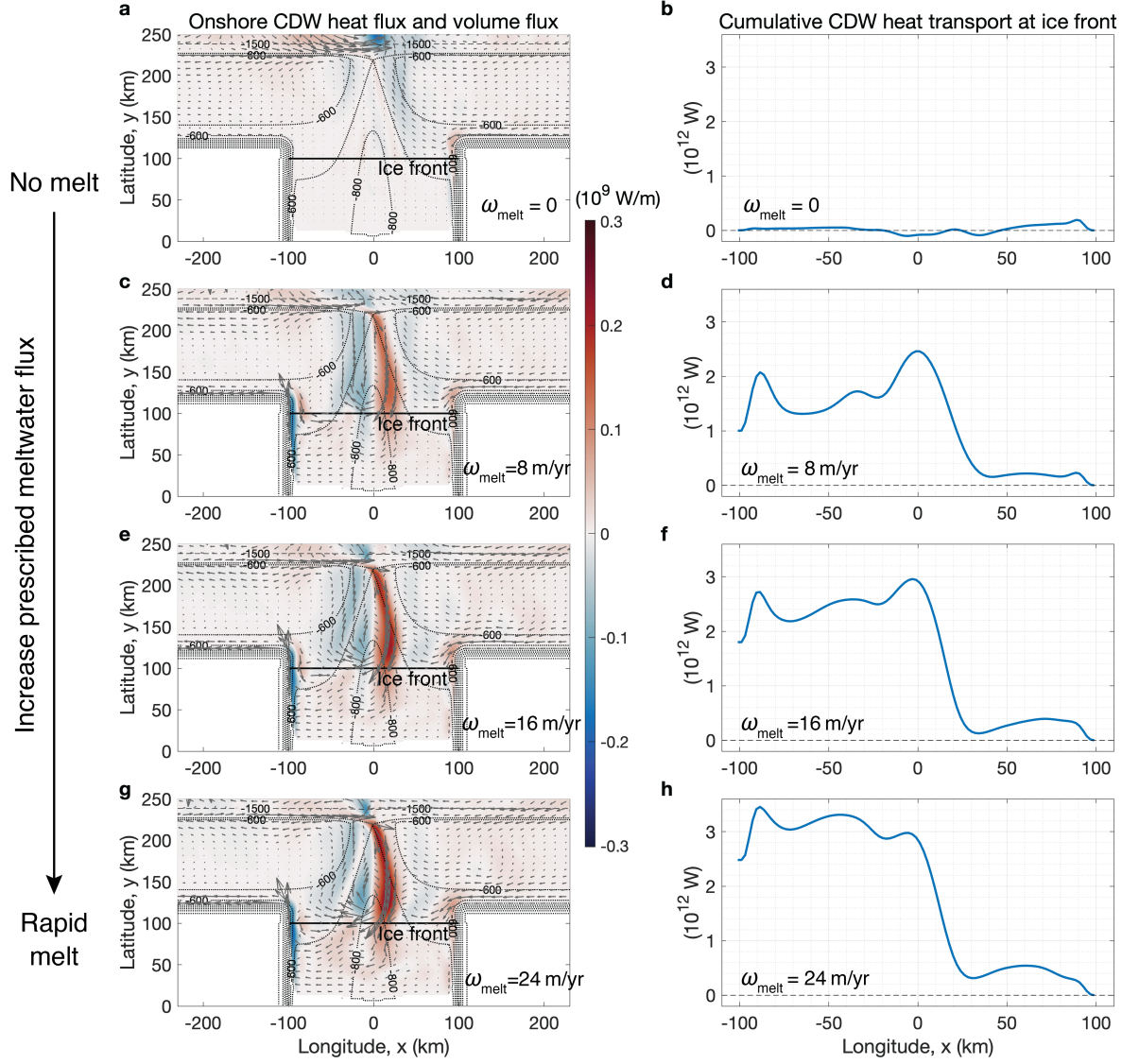


Figure 4.7: Onshore CDW heat transport increases with a larger prescribed meltwater flux. Left column: Vertically integrated heat flux (color) and volume flux (arrows) in the CDW layer, with red corresponding to shoreward (southward) heat flux. The black solid line denotes the location of the ice shelf front at $y = 100$ km. The bathymetric contours are denoted by the thin dashed lines with an interval of 1000 m, and thin dotted lines with an interval of 100 m. Right column: Cumulative CDW heat transport at the ice shelf front as a function of longitude. The CDW heat flux is first integrated vertically and then integrated zonally along the ice shelf front, from $x = 100$ km to $x = -100$ km. **a-b**, Pseudo-ice shelf with no melt. **c-g**, The equivalent basal melt rates prescribed at the titled surface of the pseudo-ice shelf (ω_{melt}) are 8, 16, and 24 m/yr, respectively. Configurations of the pseudo-ice shelf simulations are presented in the section “Pseudo-ice shelf” in the Methods and in Table 4.1.

iments with a “pseudo-ice shelf”. In these experiments, we turn off ice shelf thermodynamics and prescribe heat and salt fluxes at the tilted interface between the pseudo-ice shelf and the ocean (see Methods) to create equivalent melt rates of $\omega_{\text{melt}} = 0, 8, 16, 24 \text{ m/yr}$. Figure 4.7 shows that increased meltwater flux drives stronger shoreward CDW transport in the trough ($-50 \text{ km} \leq x \leq 50 \text{ km}, 100 \text{ km} \leq y \leq 225 \text{ km}$), increasing from 0.015 Sv (no melt, Fig. 4.7a, $1 \text{ Sv} = 10^6 \text{ m}^3/\text{s}$) to 0.64 Sv (strong melt, Fig. 4.7g). We calculate the cumulative CDW heat transport integrated westward along the ice shelf front, as a function of latitude. When the ice shelf is not melting, the cumulative CDW heat transport is zero at the ice front (Fig. 4.7a, b); with stronger prescribed meltwater flux, the total CDW heat transport toward the ice shelf increases remarkably (Fig. 4.7c-g). Note that driving CDW shoreward is not a guaranteed outcome in these experiments: The system could in principle adjust to a state in which surface waters are lightened/cooled in the cavity, or in which CDW is drawn in along the coast from the zonal domain boundaries.

In addition, the eastward transport of the slope undercurrent doubles with a strong prescribed melt rate ($\omega_{\text{melt}} = 24 \text{ m/yr}$) compared with no melt ($\omega_{\text{melt}} = 0 \text{ m/yr}$). A weak undercurrent appears in the simulation with no melt (Fig. 4.7a), provided that there is an offshore buoyancy gradient and a trough over the continental slope, the mechanism of which will be discussed later. Note that this does not conflict with the hypothesis that the undercurrent is buoyancy-driven because, in the real ocean, the offshore buoyancy gradient is established by meltwater from local ice shelves as well as remote sources. In agreement with [Thompson et al. \(2020\)](#), our results emphasize the potential control of remote buoyancy forcing (e.g., meltwater advection from upstream ice shelves) on shoreward heat transport in West Antarctica.

In the rest of this section, we investigate the formation mechanism of the buoyancy-driven slope undercurrent. Since the slope undercurrent and shoreward CDW transport in the trough form a cyclonic circulation (Fig. 4.3a), the question of what drives the undercurrent can be narrowed down to the following: (i) Which process injects cyclonic vorticity into the system? (ii) How is the cyclonic vorticity transported to the shelf break? This motivates us to analyze the vorticity budget of the CDW layer.

By calculating the curl of the depth-integrated CDW momentum equation in a steady state (see

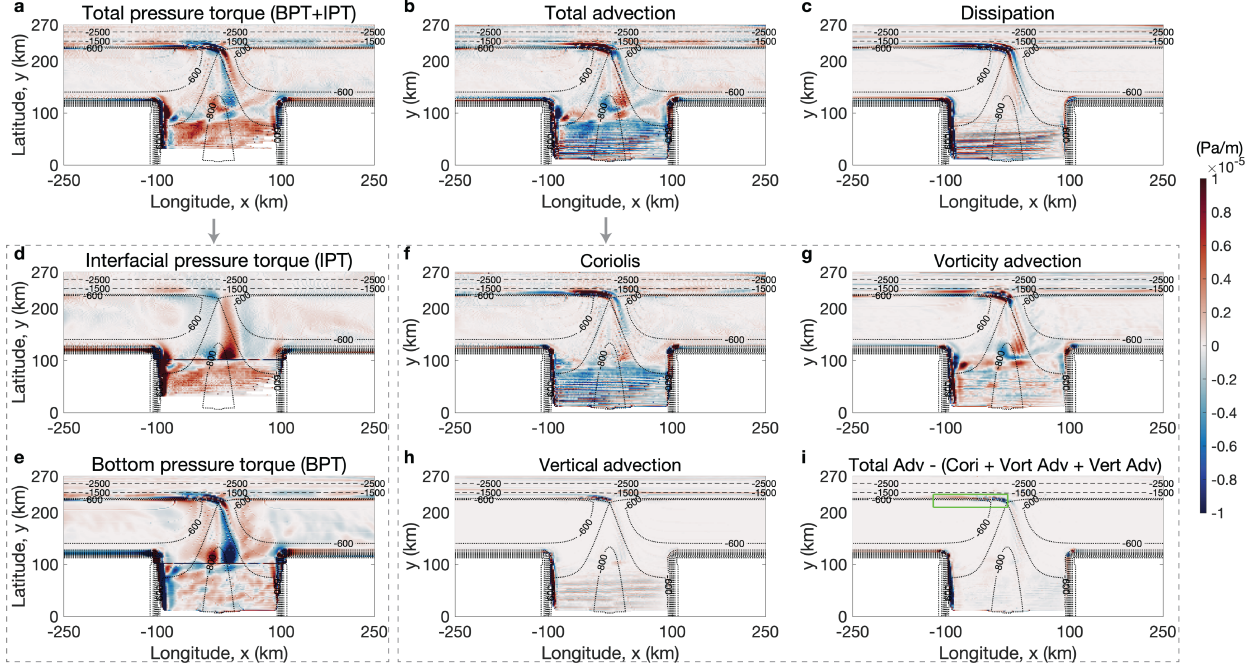


Figure 4.8: Vorticity budget of the CDW layer. The total advection (**b**) balances total pressure torque (**a**) and dissipation (**c**). The total pressure torque comprises the interfacial pressure torque (**d**) and bottom pressure torque (**e**). The total advection comprises the Coriolis term (**f**), vorticity advection (**g**), vertical advection (**h**), and residual term (**i**). The bathymetric contours are denoted by the thin dashed lines with an interval of 1000 m, and thin dotted lines with an interval of 100 m. The green box in panel **i** indicates the selected region to calculate the shelf-break-integrated relative vorticity and pressure torque of the CDW layer, presented in Fig. 4.5c, d and Fig. 4.6c, respectively.

Methods), it is shown that meltwater upwelling in the ice-shelf cavity injects cyclonic vorticity into the CDW layer. Fig. 4.8 shows the vorticity budget of the CDW layer, with blue corresponding to the contribution of each term to cyclonic vorticity ($\zeta < 0$) and red corresponding to anticyclonic vorticity ($\zeta > 0$). For the leading order terms, the total advection is balanced by total pressure torque; the dissipation is non-negligible only over the shelf break. As CDW melts the ice shelf, the meltwater transforms CDW into a lighter, fresher water mass, which corresponds to diapycnal velocity out of the CDW layer. In the ice-shelf cavity, the Coriolis term, which is associated with diapycnal upwelling, contributes to the cyclonic vorticity in the CDW layer (Fig. 4.8f, Eq. 4.15). The total pressure torque of the CDW layer is comprised of bottom pressure torque (BPT) exerted by the titled topography to the flow, and the interfacial pressure torque (IPT) exerted by the titled isotherm between the CDW

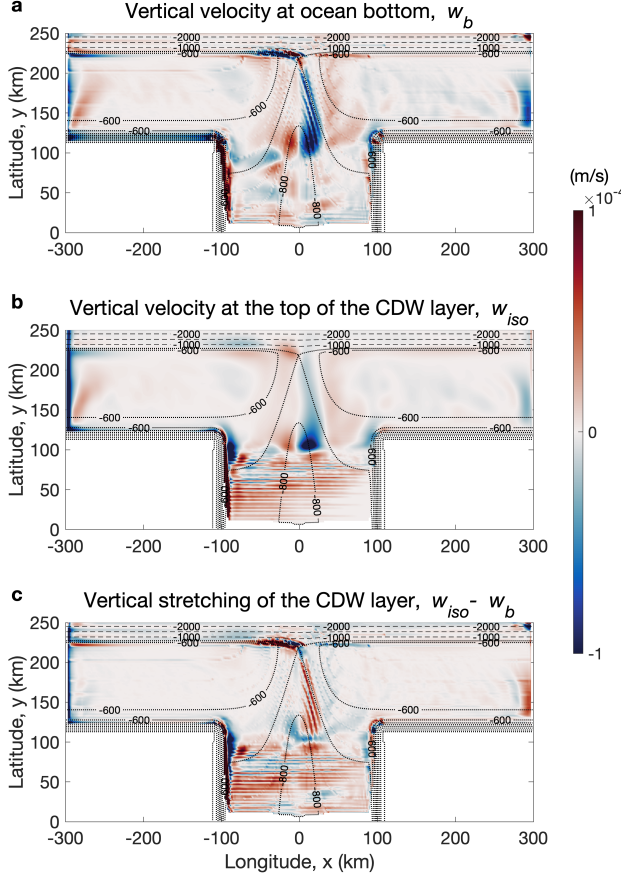


Figure 4.9: Vertical velocities and vertical stretching for the reference simulation. **a**, Vertical velocity at the ocean bottom (ω_{bot}). **b**, Vertical velocity at the upper bound of the CDW layer (ω_{up}). **c**, Vertical stretching of the CDW layer ($\omega_{\text{up}} - \omega_{\text{bot}}$).

layer and the surface layer. Within the trough, as CDW flows from the shelf break to the ice front, the downward bottom velocity associated with the deepening of the topography leads to negative bottom pressure torque (Figs. 4.8e, 4.9a, Eq. 4.12a), which is partially canceled by the interfacial pressure torque due to the downward velocity at the top of the CDW layer (Figs. 4.8d, 4.9b, Eq. 4.12b). Vertical stretching of the CDW layer in the east part of the trough is associated with the negative total pressure torque (Figs. 4.8a, 4.9c, Eq. 4.13). Other terms such as vorticity advection, vertical advection, and kinetic energy gradient are less important.

Based on Stokes' theorem, the area integral of vorticity over an enclosed surface is equal to the line integral of circulation around the boundary of the surface. To explain what drives the cyclonic circulation of the undercurrent, we calculate the area integral of the vorticity budget. We

use potential vorticity (PV) contours to select a region (Fig. 4.3b), because a flow that is close to adiabatic and frictionless approximately follows the PV contours. The PV of the CDW layer is defined as

$$q_{\text{cdw}} \equiv \frac{f + \partial_x v_{\text{cdw}} - \partial_y u_{\text{cdw}}}{h_{\text{cdw}}}, \quad (4.1)$$

where f is the Coriolis parameter, u_{cdw} and v_{cdw} are the depth-averaged velocity of the CDW layer, and h_{cdw} is the CDW thickness. Figure 4.3c shows the cumulatively integrated vorticity budget from south to north within the selected region, as a function of latitude. Same as Fig. 4.8f, Fig. 4.3c shows that the Coriolis term associated with meltwater upwelling in the ice-shelf cavity injects cyclonic (negative) vorticity into the system. In addition, the area-integrated total pressure torque is zero (the value at $y = 240$ km in Fig. 4.3c), suggesting that the pressure torque is neither a source nor a sink of the CDW vorticity; instead, it acts to horizontally transport the cyclonic vorticity from the ice-shelf cavity to the shelf break ([Stewart et al., 2021](#); Eq. 4.14 in Methods).

Using a suite of perturbation experiments, we solidify the theory that as CDW melts the ice shelf, diapycnal upwelling of meltwater generates cyclonic vorticity, which is transported from the ice-shelf cavity to the shelf break by the vorticity flux associated with the total pressure torque (named as “pressure-torque vorticity flux” hereafter, Eq. 4.14), leading to steering of the undercurrent toward the ice shelf. It is verified that higher ice-shelf melt rates lead to stronger diapycnal upwelling in the cavity (Fig. 4.5a) and enhanced cyclonic vorticity input to the CDW layer by the Coriolis term (Fig. 4.5b). For simulations with fixed topographic geometry and boundary isopycnal (the filled markers with correlation coefficient r_1 in each panel), upwelling in the cavity is highly correlated with the total pressure torque and cyclonic vorticity integrated over the shelf break upstream of the trough (defined by the green box in Fig. 4.9) (Fig. 4.5c,d). As a result, stronger ice shelf melt enhances eastward transport of the slope undercurrent (Fig. 4.5e), which drives stronger shoreward CDW transport within the trough (Fig. 4.5f) and thus larger magnitude of heat reaching the ice-shelf front (Fig. 4.6a). For simulations with no trough, the undercurrent transport (almost zero) is not correlated with ice-shelf melt (green and blue hollow markers in Fig. 4.5e), which further vindicates that the transport of pressure-torque vorticity flux through the trough plays a key role in slope undercurrent generation. Furthermore, the simulations with a

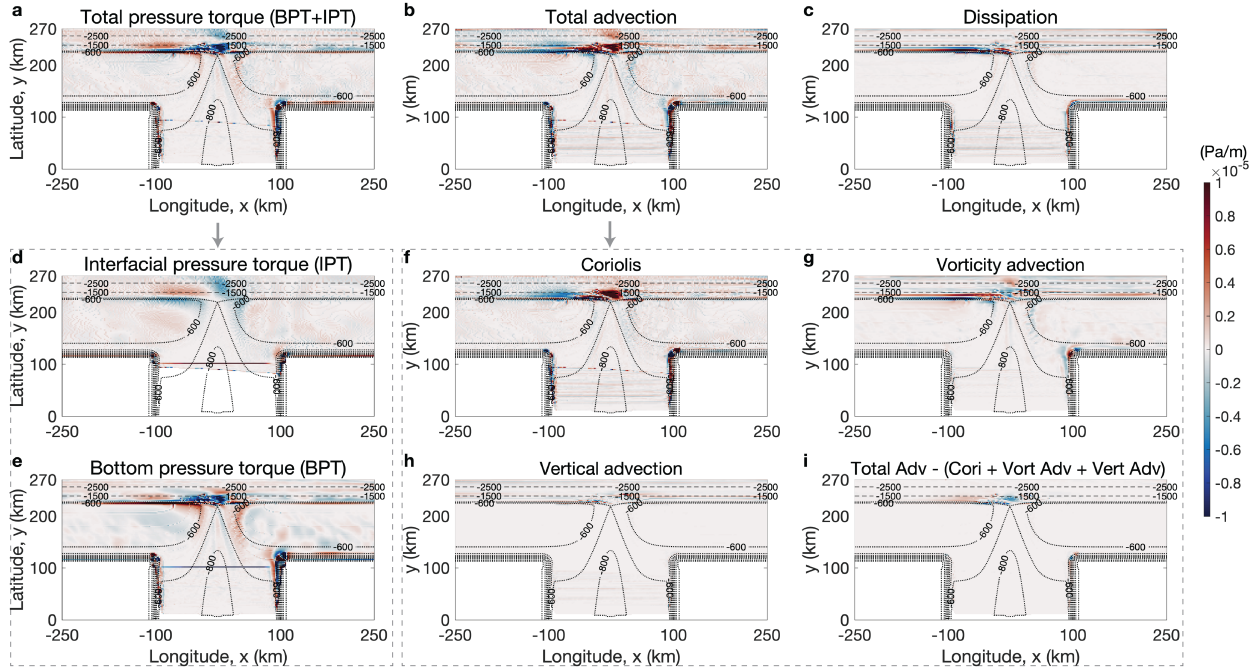


Figure 4.10: CDW vorticity budget for the pseudo ice shelf simulation with no melt. Figure labels are the same as Fig. 4.8.

deeper thermocline (i.e., a steeper slope front) prescribed at the zonal boundaries do not fit closely into the theory described above. This is potentially because the relatively strong westward flow in the upper layer arising from the steeper slope front prohibits the transfer of vorticity flux from the continental shelf to the continental slope. The undercurrent velocity in the simulation with a deeper thermocline and weaker winds (DeepWind_2) is relatively strong (Fig. 4.5e) because in this case, the westward surface current is faster than the sea ice, resulting in an eastward momentum input to the ocean from the ice-ocean stress. In the case of a pseudo-ice shelf that does not melt, the weak undercurrent is associated with a standing wave that is anticyclonic northward of the shelf break (Fig. 4.7a), which is possibly driven by the positive relative vorticity input from Coriolis advection at the mouth of the submarine trough (Fig. 4.10f).

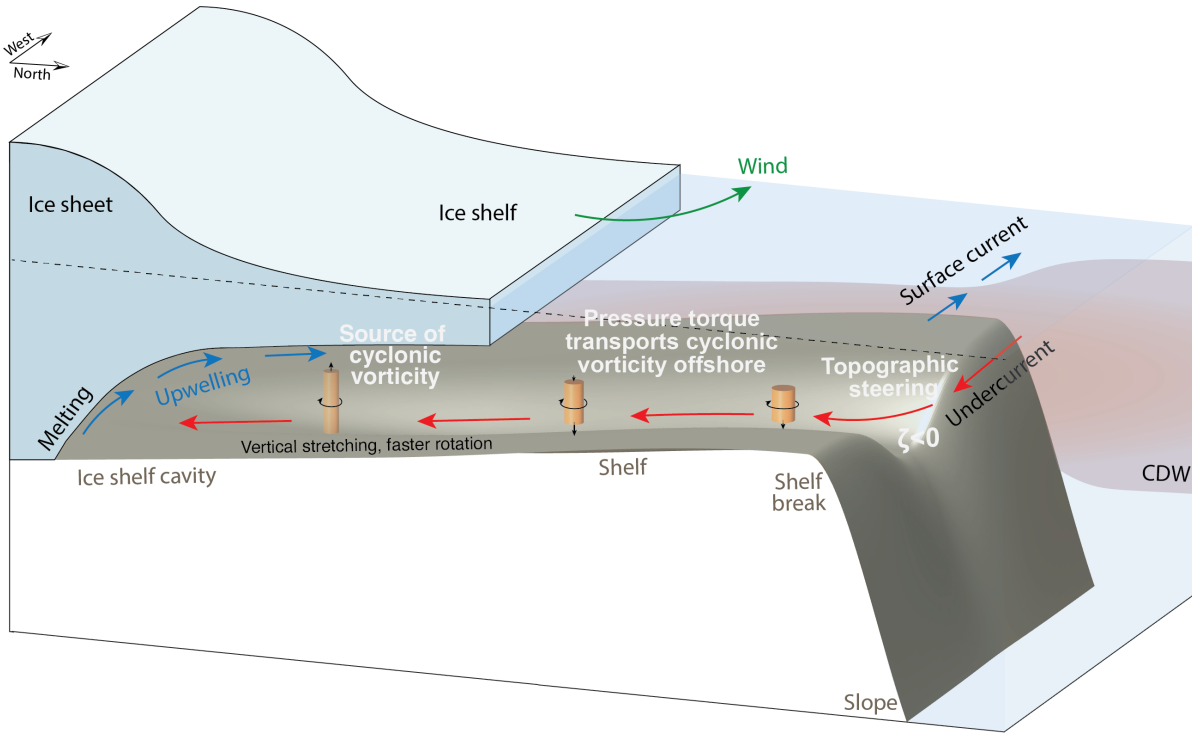


Figure 4.11: Schematic illustrating the mechanism of Antarctic Slope Undercurrent formation. The ice shelf meltwater creates an offshore buoyancy gradient with shoreward deepening of the thermocline, which is maintained by shoreward Ekman transport associated with westward coastal winds. As CDW melts the ice shelf, ice-shelf meltwater transforms the CDW to a lighter water mass and vertically stretches the CDW layer, which injects cyclonic vorticity into the CDW layer. The source of the cyclonic vorticity is then transported offshore by the pressure-torque vorticity flux (Eq. 4.14), provided that there is a trough extending onto the shelf. Over the shelf break, the cyclonic vorticity steers CDW toward the ice shelf, driving an eastward undercurrent west of the trough. Stronger basal melt leads to stronger diapycnal upwelling of meltwater, increasing the strength of the slope undercurrent and therefore enhancing onshore CDW heat transport. The vertical stretching of the CDW layer is illustrated by the orange columns, with black arrows at the top or bottom of the columns denoting the direction of the stretching and circular arrows denoting the resulting cyclonic rotation. As CDW flows towards the ice shelf, it is primarily stretched downward following the topography (Extended Fig. 4.9); within the ice shelf cavity, the CDW layer is stretched upward due to the upwelling of meltwater.

4.4 Implications for future melt of West Antarctic ice shelves

In summary, the mechanism of the Antarctic Slope Undercurrent formation is investigated using an idealized model with coupled ocean, sea ice, and ice shelf. It is found that the undercurrent forms with realistic strength provided that there is a trough allowing access to the continental shelf and ice

shelf cavity, and that there is a cross-slope buoyancy gradient. The cross-shelf buoyancy gradient is mainly contributed by ice-shelf meltwater (Bett et al., 2020), and is maintained by wind-driven shoreward Ekman transport. The controlled experiments with the pseudo-ice shelf demonstrate that the shoreward heat transport in the trough is driven by sub-ice shelf buoyancy fluxes. We establish a direct dynamical link between the undercurrent transport and ice shelf melt using the vorticity balance within the layer of intruding CDW. Our results suggest that the Antarctic Slope Undercurrent observed in West Antarctica is driven by cyclonic vorticity input from meltwater upwelling in the ice shelf cavities. Figure 4.11 illustrates the mechanism of Antarctic Slope Undercurrent formation: As CDW melts the ice shelf, diapycnal upwelling of the meltwater vertically stretches the CDW layer, injects cyclonic vorticity into the CDW layer; the cyclonic vorticity is transported from the ice shelf cavity to the shelf break by the vorticity flux associated with the total pressure torque, which drives the slope undercurrent and leads to steering of CDW toward the ice shelf. Increased basal melt drives stronger slope undercurrent and enhanced onshore CDW heat transport, which indicates a previously unrecognized positive feedback that may accelerate future melt of ice shelves, potentially further destabilizing the West Antarctic Ice Sheet.

Since remote buoyancy forcing can also affect the offshore buoyancy gradient and thus undercurrent strength, our results emphasize the potential control of remote forcing on undercurrent strength and shoreward heat transport in West Antarctica. Our idealized model does not account for various complexities such as the realistic topography with multiple troughs, the presence of multiple ice shelves, and the wide range of forcing time scales. Using an idealized ocean model, Haigh et al. (2023) highlighted the essential role of a meridional ridge east of the ice shelf in shaping the ocean circulation and driving warm CDW towards the south, but their model does not include any thermodynamic forcing from sea ice and ice shelf, and therefore lack potentially important feedback between ocean circulation and ice shelf melt. As revealed by St-Laurent et al. (2013), the interaction of the mean flow and Rossby waves with the topography plays a role in driving onshore heat transport. How complex topography, high-frequency wind variability, transient eddies, and waves affect the dynamics of the undercurrent and shoreward heat transport in West Antarctica requires further study. Future investigations and assessments of sea level rise scenarios

should focus on the positive feedback uncovered here as a potentially important player in the future evolution and stability of the West Antarctic Ice Sheet.

4.5 Methods

4.5.1 Model configuration

The model is developed based on the Massachusetts Institute of Technology General Circulation Model (MITgcm) ([Marshall et al., 1997a,b](#)). It simulates thermodynamic ice-ocean interactions at the base of a static ice shelf using friction velocity-dependent turbulent heat and salt transfer coefficients ([Holland and Jenkins, 1999](#)) and also includes the pressure and quadratic frictional stress of the ice shelf to the waters beneath. The ocean component is modeled via the hydrostatic Boussinesq equations with a polynomial approximation of the equation of state ([McDougall et al., 2003](#)). A fully dynamic-thermodynamic sea ice package is implemented in the model, with viscous-plastic sea ice rheology and seven thickness categories for sea ice thermodynamics ([Hibler, 1979, 1980; Winton, 2000; Losch et al., 2010](#)).

The baroclinic Rossby radius of deformation is about 3.9 km over the shelf and 9.8 km in the deep ocean. Therefore, a high horizontal resolution is required to resolve mesoscale eddies over the shelf, which limits the domain size. The horizontal resolution of the model is 2 km and the vertical grid spacing increases from 3.3 m near the ocean surface to 333 m toward the seafloor, with 68 vertical layers in total. The vertical grid spacing in the ice shelf cavity ranges from 25 m to 29 m. Though the vertical resolution is known to have an influence on the representation of ice shelf melt rates (e.g., [Gwyther et al., 2020](#)), increasing the number of vertical layers from 68 to 100 leads to only a 3% decrease in the melt rates in this model, therefore we use 68 vertical levels for all the simulations.

A high-order nonlinear advection scheme (7th order one-step method with monotonicity preserving limiter) is implemented for potential temperature, salinity, and sea ice scalar state variables. The surface shortwave radiation is set to zero, and a downward longwave radiation of 341 W/m^2

is implemented to approximately control the sea ice thickness during the simulation. Standard bulk formulae are used to estimate the atmosphere-sea ice-ocean fluxes of momentum, heat, and freshwater. For both the ocean and sea ice, the inner and outer relaxation time scales are 10 days and 0.5 days, respectively. The time step is approximately 170 s.

The boundary hydrography is inspired by observations (Jacobs et al., 2011; Locarnini et al., 2023) with a mixed-layer depth of approximately 50 m and a thermocline depth of approximately 300 m at the northern boundary (Fig. 4.1e). The boundary conditions at the two zonal boundaries are the same, with the thermocline and halocline deepening toward the coastline (Fig. 4.1d). The boundary halocline is 100 m deeper than the thermocline to obtain a stable stratification, similar to the structure that occurs in nature. At the northern boundary, both the zonal and meridional velocities are restored to zero except for two simulations with prescribed barotropic tides in the meridional direction (see Methods). At the zonal boundaries, the meridional velocity is prescribed by assuming zero seafloor velocity and vertically integrating the thermal-wind shear from the seafloor to depth z (Fig. 4.1b).

$$u_{\text{boundary}}(y, z) = \int_{\eta_b}^z \frac{g}{\rho_0 f} \frac{\partial \rho_{\text{boundary}}(y, z')}{\partial y} dz', \quad (4.2)$$

where η_b is the seafloor elevation, g is the gravitational acceleration, ρ_0 is the reference density, f is the Coriolis parameter, and ρ_{boundary} is the potential density calculated from the restoring temperature and salinity at the zonal boundaries.

Assuming a free-drift sea ice boundary condition, we solve Eq. 4.3 for sea ice velocities (u_i, v_i) for each latitude at the zonal boundaries. The Coriolis term on the left-hand side is balanced by the air-ice stress and ice-ocean stress on the right-hand side:

$$-\rho_i h_{i0} f v_i = \rho_a C_{ai} \sqrt{u_a^2 + v_a^2} u_a - \rho_o C_{io} \sqrt{(u_i - u_o^s)^2 + v_i^2} (u_i - u_o^s), \quad (4.3a)$$

$$\rho_i h_{i0} f u_i = \rho_a C_{ai} \sqrt{u_a^2 + v_a^2} v_a - \rho_o C_{io} \sqrt{(u_i - u_o^s)^2 + v_i^2} v_i, \quad (4.3b)$$

where $\rho_i = 920 \text{ kg/m}^3$ is the sea ice density, $\rho_a = 1.3 \text{ kg/m}^3$ is the air density, $\rho_o = 1027 \text{ kg/m}^3$ is

the reference density of the seawater, $h_{i0} = 1$ m is the boundary sea ice thickness, $C_{ai} = 2.0 \times 10^{-3}$ is the air-ice drag coefficient, $C_{io} = 5.54 \times 10^{-3}$ is the ocean-sea ice drag coefficient, (u_a, v_a) are the wind velocities as a function of latitude, and $u_0^s = u_{\text{boundary}}(y, 0)$ is the ocean surface zonal velocity at the zonal boundaries. We conducted simulations with varying meridional and zonal winds (Table 4.1), with stronger winds corresponding to increased sea ice velocity and larger ice-ocean shear. Other parameters of surface air conditions, sea ice, and drag coefficients are the same as Table 1 of [Si et al. \(2022\)](#): the surface (2-m) air temperature is -10°C ; the surface specific humidity is 5.7 g/kg ; the downward longwave radiation is 324 W/m^2 ; the downward shortwave radiation is zero; the sea ice salinity retention fraction on freezing is 0.3; the frazil to sea ice conversion rate is 0.01; the quadratic air-ocean drag coefficient is 1×10^{-3} ; the quadratic ocean bottom drag coefficient is 2×10^{-3} .

The model is implemented with the Smagorinsky viscosity with a biharmonic viscosity factor of 4 ([Smagorinsky, 1963, 1993](#); [Griffies and Hallberg, 2000](#)). The vertical eddy viscosity is set to $3 \times 10^{-4} \text{ m}^2/\text{s}$. For most simulations, a uniform vertical diffusivity of $10^{-5} \text{ m}^2/\text{s}$ is implemented. In three perturbation simulations, we allow three-dimensional (3D) specification of vertical diffusivity. The 3D diffusivity peaks at the seafloor and decreases exponentially with height above bathymetry to a minimum of $5 \times 10^{-6} \text{ m}^2/\text{s}$, with an e-folding scale of 150m. The maximum values of the 3D vertical diffusivity (κ_{\max}^{3D}) are 10^{-4} , 10^{-3} , and $3 \times 10^{-3} \text{ m}^2/\text{s}$, respectively. According to previous studies ([Scott et al., 2021](#); [Robertson, 2013](#); [Breadley et al., 2017](#); [Howard et al., 2004](#)), $\kappa_{\max}^{3D} = 3 \times 10^{-3} \text{ m}^2/\text{s}$ is much larger than observed, but κ_{\max}^{3D} in the range of 10^{-4} to $5 \times 10^{-4} \text{ m}^2/\text{s}$ is typical for West Antarctic continental shelf and slope, and $\kappa_{\max}^{3D} \sim 10^{-3} \text{ m}^2/\text{s}$ has been observed over the ridge.

The barotropic tides in the Amundsen Sea are dominant by the diurnal tidal constituent K1 with a period of around 1 day and an amplitude of around 0.02 m/s in the deep ocean ([Jourdain et al., 2019](#)). In two perturbation simulations, idealized barotropic tidal currents are prescribed at the northern boundary, with a tidal period of 24 hours. The tidal current amplitudes prescribed at the northern boundary are 0.025 and 0.05 m/s, respectively (Table 4.1). Due to mass conservation, the resulting tidal current amplitudes are approximately 0.2 and 0.4 m/s over the shelf break in the two

simulations, respectively (Loder, 1980).

Each simulation has been integrated for more than 12 model years, with a typical spin-up time of less than 7 years determined by the time series of domain-averaged kinetic energy, temperature, and salinity. The time average of the last five years is used for analysis.

4.5.2 Insensitivity of ice-shelf melt rate to wind perturbation and the presence of trough in the idealized model

The ice-shelf melt rate does not decrease with no trough (Fig. 4.5f), though in this case, the eastward undercurrent transport is only 1/7 of the reference value and there is no southward CDW transport through the trough. It turns out that the coastal boundary current east of the ice shelf also transports heat toward the ice front (Fig. 4.12a, c), especially in the case with no trough. We find that there is a compensation between heat transport through the trough and by the coastal boundary current (Fig. 4.12b, d). Due to this compensation, adding or removing a trough does not affect the melt rate. Since submarine troughs appear in the front of almost all major ice shelves, the simulations with a trough may be more relevant to nature. Moreover, as multiple ice shelves exist in the Amundsen Sea, the coastal boundary current east of one ice shelf may have been transformed into a colder and fresher flow by upstream ice shelves. Nevertheless, this finding emphasizes the potentially important role of coastal boundary currents in ice-shelf melt that needs to be understood thoroughly in the future.

The ice-shelf melt rate is insensitivity to variations in local wind speed, which might be an artifact resulting from the zonal boundary conditions: Since the thermocline depth is relaxed toward a fixed curve at the zonal boundaries (Fig. 4.1d), the thickness of the CDW layer over the shelf is largely affected by the boundary conditions rather than wind variations, which is potentially a caveat of this model. Fig. 4.12g-h indicates that with stronger surface northwestward winds, the trough heat transport decreases while the boundary current heat transport increases, leading to the same total CDW heat transport at the ice front and thus the same ice-shelf melt rates.

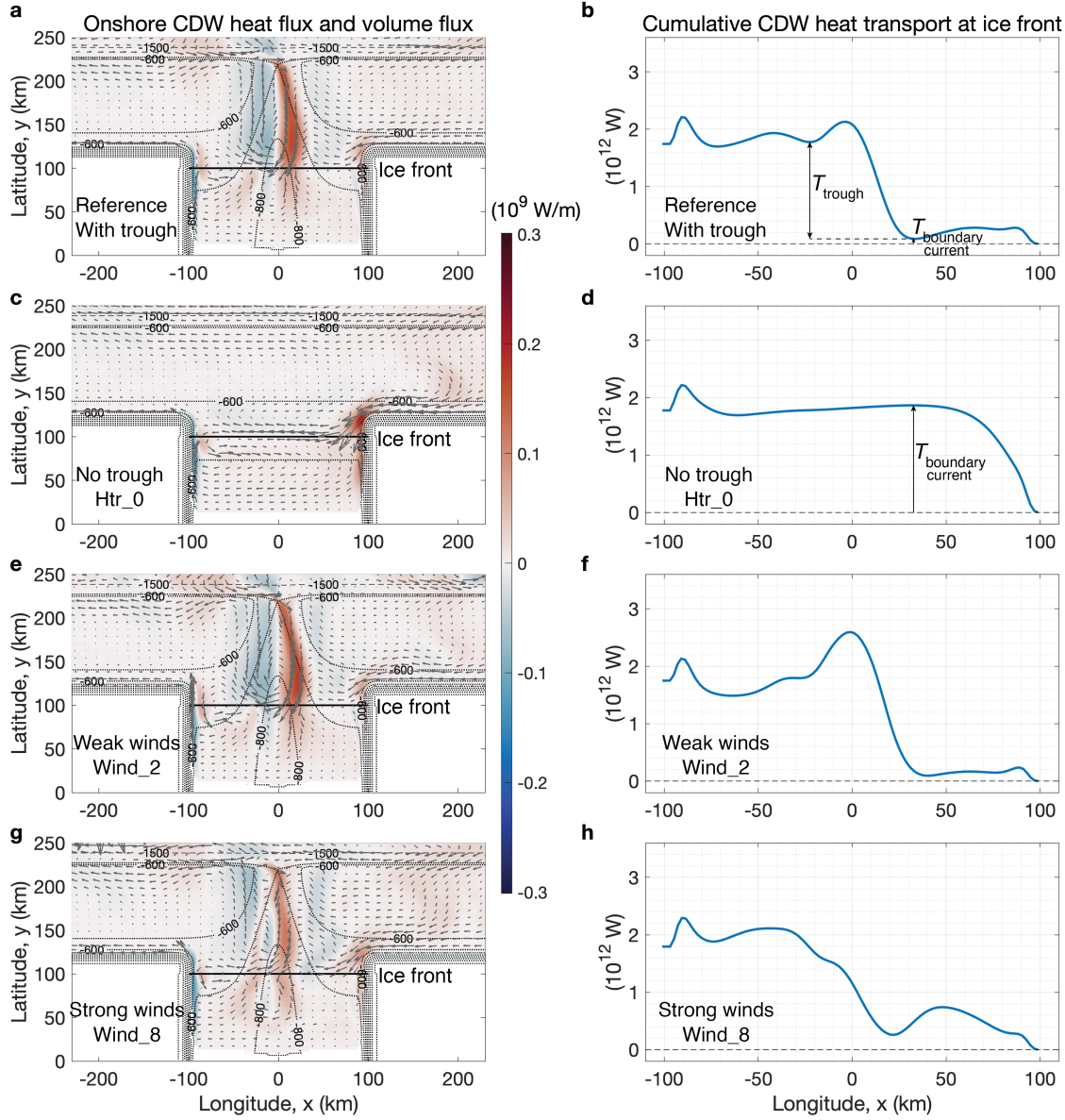


Figure 4.12: A compensation between heat transport through the trough and by the boundary current. Left column: Vertically integrated heat flux (color) and volume flux (arrows) in the CDW layer, with red corresponding to shoreward (southward) heat flux. The black solid line denotes the location of the ice shelf front at $y = 100$ km. The bathymetric contours are denoted by the thin dashed lines with an interval of 1000 m, and thin dotted lines with an interval of 100 m. Right column: Cumulative shoreward CDW heat transport at the ice shelf front as a function of longitude. The CDW heat flux is first integrated vertically and then integrated zonally along the ice shelf front, from $x = 100$ km to $x = -100$ km. **a-b**, The reference simulation. T_{trough} is the heat carried by the undercurrent through the trough (T_{trough}). $T_{\text{boundary current}}$ is the heat carried by the coastal boundary current. **c-d**, The simulation with no trough. **e-f**, The simulation with weak surface winds ($U_{a0} = -2 \text{ m/s}$, $V_{a0} = 2 \text{ m/s}$). **g-h**, The simulation with strong surface winds ($U_{a0} = -8 \text{ m/s}$, $V_{a0} = 8 \text{ m/s}$).

4.5.3 Pseudo-ice shelf

To investigate the feedback between meltwater discharge and onshore heat transport carried by the slope undercurrent, we conducted simulations with a pseudo-ice shelf to control the melt rate explicitly. We add fixed temperature and salinity fluxes (sink of heat and dilution of salt) associated with ice shelf melt to the ocean thermodynamic equations. This is implemented by restoring temperature and salinity at the ice shelf-ocean interface, described below.

At the tilted interface between the ice shelf and the ocean, the temperature and salinity tendencies are modified so that

$$\frac{d\chi}{dt} \Rightarrow \frac{d\chi}{dt} - \frac{\chi - \chi_{\text{relax}}}{\tau_\chi}, \quad (4.4)$$

where χ represents the potential temperature (T) or salinity (S) of the ocean, χ_{relax} is the relaxation value, and τ_χ is the relaxation time scale. Using an infinite time scale $\tau_\chi = \tau_{\text{inf}} = 10^{20}$ s, we relax temperature and salinity toward $\chi_{\text{relax}} = \tau_{\text{inf}} Q_{\text{melt}}^\chi$, where $Q_{\text{melt}}^\chi < 0$ represents the temperature and salinity fluxes due to ice shelf melt. Since $|\chi| \ll |\chi_{\text{relax}}|$, the tendency terms turn into

$$\frac{d\chi}{dt} \Rightarrow \frac{d\chi}{dt} - \frac{\chi - \tau_{\text{inf}} Q_{\text{melt}}^\chi}{\tau_{\text{inf}}} \Rightarrow \frac{d\chi}{dt} + Q_{\text{melt}}^\chi. \quad (4.5)$$

In the rest of this section, we estimate Q_{melt}^T and Q_{melt}^S by assuming a constant and uniform melt rate. As ice shelf melts, the latent heat of fusion decreases ocean temperature beneath the ice shelf.

$$\rho_o c_p Q_{\text{melt}}^T \Delta z = -\omega_{\text{melt}} L_f \rho_o. \quad (4.6)$$

where $c_p = 3974 \text{ J/kg}/^\circ\text{C}$ is the specific heat capacity of seawater, $\Delta z = \Delta z(x, y) \approx 25$ to 29 m is the thickness of the grid cells right beneath the ice shelf, ω_{melt} is the prescribed basal melt rate in the unit of m/s, and $L_f = 3.34 \times 10^5 \text{ J/kg}$ is the heat of fusion for ice. Therefore,

$$Q_{\text{melt}}^T(x, y) = -\frac{\omega_{\text{melt}} L_f}{c_p \Delta z(x, y)}, \quad (4.7a)$$

$$T_{\text{relax}} = \tau_{\text{inf}} Q_{\text{melt}}^T. \quad (4.7b)$$

To a good approximation, the salinity of the ice shelf is zero (Holland and Jenkins, 1999). We assume that the mass of salt in the ocean layer right beneath the ice shelf (M_{salt}) is conserved during ice shelf melt, $M_{\text{salt}} = M_0 S_{\text{ref}}$, where $M_0 = \rho_0 \Delta z \Delta A$ is the total ocean mass of that layer, ΔA is the horizontal area, and $S_{\text{ref}} = 34.3$ psu is the reference salinity in the unit of psu (practical salinity unit). After an infinitesimal time step δt , the ice shelf meltwater has diluted ocean salinity by increasing the total mass of liquid from M_0 to M'_0 ,

$$M'_0 = \rho_0 \Delta z \Delta A + \rho_{\text{melt}} \omega_{\text{melt}} \Delta A \delta t, \quad (4.8)$$

where $\rho_{\text{melt}} = 1000$ kg/m³ is the reference density of meltwater. The salinity of these grid cells becomes $S' = M_{\text{salt}} / M'_0$. Given $\delta t \rightarrow 0$,

$$Q_{\text{melt}}^S(x, y) = \frac{S' - S_{\text{ref}}}{\delta t} = -\frac{S_{\text{ref}}}{\delta t + \frac{\rho_0}{\rho_{\text{melt}}} \frac{\Delta z}{\omega_{\text{melt}}}} \approx -\frac{\omega_{\text{melt}} S_{\text{ref}} \rho_{\text{melt}}}{\rho_0 \Delta z}, \quad (4.9a)$$

$$S_{\text{relax}} = \tau_{\text{inf}} Q_{\text{melt}}^S. \quad (4.9b)$$

We conducted simulations with prescribed melt rates of 0, 8, 16, and 24 m/yr, respectively (see Table 4.1). The ice shelf thermodynamics were turned off. For the simulation with zero melt, no relaxation temperature or salinity was prescribed at the tilted interface.

4.5.4 Depth-integrated CDW vorticity budget

Over the continental shelf and upper slope ($y < 270$ km and ocean depth < 3 km), the CDW layer (defined as water warmer than 0°C) directly sits over the topography. We vertically integrate the horizontal momentum equation from the seafloor ($z = \eta_b(x, y)$) to the upper bound of the CDW

layer ($z = \eta_{\text{iso}}(x, y)$), the elevation of the isotherm between the CDW layer and the surface water):

$$\begin{aligned}
& \underbrace{\rho_0 \int_{\eta_b}^{\eta_{\text{iso}}} \frac{\partial \mathbf{u}}{\partial t} dz}_{\text{Tendency}} = - \underbrace{\int_{\eta_b}^{\eta_{\text{iso}}} \nabla_h p dz}_{\text{Pressure gradient force}} + \underbrace{\tau_b}_{\text{Bottom friction}} + \underbrace{\mathcal{V}}_{\text{Viscous diffusion}} \\
& \quad + \underbrace{\rho_0 \int_{\eta_b}^{\eta_{\text{iso}}} \left(\underbrace{-f \hat{k} \times \mathbf{u}}_{\text{Coriolis}} - \underbrace{\hat{k} \times \zeta \mathbf{u}}_{\text{Vorticity adv.}} - \underbrace{w \partial_z \mathbf{u}}_{\text{Vertical adv.}} - \underbrace{\nabla_h \mathbf{u}^2 / 2}_{\text{KE gradient}} \right) dz}_{\text{Total advection}}, \tag{4.10}
\end{aligned}$$

where $\mathbf{u} \equiv (u, v)$ is the horizontal velocity, w is the vertical velocity, $\nabla_h \equiv (\partial_x, \partial_y)$ is the horizontal gradient operator, \hat{k} is the unit vector along the z-axis, and $\zeta = \hat{k} \cdot (\nabla_h \times \mathbf{u})$ is the relative vorticity. The term $-(\mathbf{u} \cdot \nabla) \mathbf{u}$ is written as the sum of vorticity advection, vertical advection, and kinetic energy (KE) gradient. The Coriolis term is included in the total advection in order to be consistent with MITgcm's diagnostics.

To obtain a relatively smooth result of the CDW vorticity budget, we vertically interpolate the depth-integrated momentum equation (Eq. 4.10) to a much finer vertical grid with ~ 3400 layers. Then, we take the curl of the steady-state ($\partial_t \mathbf{u} \equiv 0$) CDW momentum equation and apply the Leibniz integral rule to the pressure torque.

$$\begin{aligned}
0 & \approx \underbrace{\mathbf{J}(p, \eta_{\text{iso}})}_{\text{Interfacial pres. torque}} \Big|_{z=\eta_{\text{iso}}} - \underbrace{\mathbf{J}(p, \eta_b)}_{\text{Bottom pres. torque}} \Big|_{z=\eta_b} + \underbrace{\hat{k} \cdot (\nabla_h \times (\tau_b + \mathcal{V}))}_{\text{Dissipation}} + \\
& \quad \underbrace{\hat{k} \cdot \left(\nabla_h \times \rho_0 \int_{\eta_b}^{\eta_{\text{iso}}} (-f \hat{k} \times \mathbf{u} - \hat{k} \times \zeta \mathbf{u} - w \partial_z \mathbf{u} - \nabla_h \mathbf{u}^2 / 2) dz \right)}_{\text{Total advection}}, \tag{4.11}
\end{aligned}$$

where $\mathbf{J}(A, B) = (\partial_x A \partial_y B - \partial_x B \partial_y A)$ is the Jacobian operator and the equation $\mathbf{J}(p|_{z=\eta}, \eta) = \mathbf{J}(p, \eta)|_{z=\eta}$ has been applied to the derivation above ($\eta = \eta_b$ or η_{iso}). The total pressure torque is expressed as the sum of the bottom pressure torque (BPT) and the interfacial pressure torque (IPT) between the CDW layer and the surface layer. In the open ocean where $y \geq 270$ km and ocean depth ≥ 3 km, the bottom layer with potential temperature lower than 0°C also exerts pressure torque to

the CDW layer above. This bottom layer has negligible impact on the undercurrent and therefore is excluded from the analysis throughout this manuscript.

4.5.5 Pressure torques and vertical stretching of the CDW layer

Under the assumption of geostrophic balance, the bottom pressure torque (BPT) at the seafloor and interfacial pressure torque (IPT) at the upper bound of the CDW layer are approximately

$$\text{BPT} = -\mathbf{J}(p, \eta_b) \Big|_{z=\eta_b} = -\rho_0 f (\mathbf{u}^g \cdot \nabla_h \eta_b) \Big|_{z=\eta_b} \approx -\rho_0 f w_b, \quad (4.12a)$$

$$\text{IPT} = \mathbf{J}(p, \eta_{\text{iso}}) \Big|_{z=\eta_{\text{iso}}} = \rho_0 f (\mathbf{u}^g \cdot \nabla_h \eta_{\text{iso}}) \Big|_{z=\eta_{\text{iso}}} \approx \rho_0 f (w_{\text{iso}} - \omega^{\text{dia}}), \quad (4.12b)$$

where f is the Coriolis parameter, w is the vertical velocity, $\mathbf{u}^g = (u^g, v^g)$ is the geostrophic velocity, the subscripts \bullet_b and \bullet_{iso} denote seafloor and the interface between the CDW and surface water, respectively, and ω^{dia} is the diapycnal velocity across the 0°C isotherm. Therefore, the total pressure torque is approximately

$$\text{Total pressure torque} = \text{BPT} + \text{IPT} \approx \rho_0 f \underbrace{(w_{\text{iso}} - w_b)}_{\text{Vertical stretching}} - \omega^{\text{dia}}. \quad (4.13)$$

The negative total pressure torque in the trough is generated by the vertical stretching of the CDW layer (Figs. 4.8a and 4.9c).

In addition, as suggested by [Stewart et al. \(2021\)](#), the total pressure torque can be written in the form of a horizontal transport term:

$$\begin{aligned} \text{Total pressure torque} &= \mathbf{J}(p, \eta_{\text{iso}}) \Big|_{z=\eta_{\text{iso}}} - \mathbf{J}(p, \eta_b) \Big|_{z=\eta_b} \\ &= \nabla_h \cdot \underbrace{\left((p \nabla_h^\dagger \eta_{\text{iso}}) \Big|_{z=\eta_{\text{iso}}} - (p \nabla_h^\dagger \eta_b) \Big|_{z=\eta_b} \right)}_{\text{Pressure-torque vorticity flux}} \end{aligned} \quad (4.14)$$

where $\nabla_h^\dagger = (-\partial_y, \partial_x)$ is the conjugate of ∇_h . The total pressure torque is the horizontal divergence

of the “pressure-torque vorticity flux”.

4.5.6 Coriolis term and diapycnal upwelling

The Coriolis term in the vorticity equation can be expressed as

$$\begin{aligned} \text{Coriolis} &= -\hat{k} \cdot (\nabla_h \times \rho_0 \int_{\eta_b}^{\eta_{\text{iso}}} f \hat{k} \times \mathbf{u} dz) \\ &\approx f \rho_0 (w^{\text{iso}} - w^b) - \rho_0 \int_{\eta_b}^{\eta_{\text{iso}}} \beta v dz \\ &= \rho_0 f \omega^{\text{dia}} - \rho_0 \int_{\eta_b}^{\eta_{\text{iso}}} \beta v dz, \end{aligned} \quad (4.15)$$

where ω^{dia} is the diapycnal velocity across the upper bound of the CDW layer and $\beta = \partial_y f$ is the Rossby parameter. Averaged over 5 years in the equilibrium state, the velocity of the isotherm is approximately zero. Therefore, the diapycnal velocity ω^{dia} is the difference between w^{iso} and w^b . In the ice shelf cavity, the Coriolis term approximately equals $f \rho_0 \omega^{\text{dia}}$, which is contributed by meltwater upwelling.

4.5.7 Transport-weighted undercurrent velocity and cross-slope buoyancy gradient

The undercurrent transport in Fig. 4.6c is defined as the zonal-average eastward transport over the shelf break west of the trough ($-280 \text{ km} \leq x \leq 0, 210 \text{ km} \leq y \leq 235 \text{ km}, \eta_b \leq z \leq 0$):

$$T^{\text{east}} = \frac{\iiint u dV}{L_{x0}}, \quad (4.16)$$

where $L_{x0} = 280 \text{ km}$. The undercurrent strength is additionally quantified by the transport-weighted eastward velocity over the shelf break west of the trough ($-280 \text{ km} \leq x \leq 0, 210 \text{ km} \leq y \leq 235 \text{ km}$,

$\eta_b \leq z \leq 0$, excluding the 20-km sponge layer at the western boundary):

$$\mathcal{U}^{\text{east}} = \frac{\iiint u^n \cdot u dV}{\substack{\iiint u^n dV \\ u > 0}} \quad (n = 1), \quad (4.17)$$

In the two equations above, the latitudinal and longitudinal spans of the region are selected based on the location of the undercurrent (Fig. 4.4c, f). We calculate the transport-weighted velocity ($n = 1$) instead of the traditionally defined volume-averaged velocity ($n = 0$) because, beyond the core of the undercurrent, a large portion of the slope has near zero eastward velocity (Fig. 4.4c, f, i), leading to very small volume-averaged eastward velocities for all the simulations. Since the transport-weighted and volume-averaged velocities are highly correlated ($r = 0.99$), using the transport-weighted method does not affect the interpretation of the results but yields a better visual correspondence with cross-sections of the undercurrent zonal velocity.

To quantify the cross-slope buoyancy gradient, we first calculate the geostrophic velocity by vertically integrating the thermal-wind shear over the shelf break, with the assumption of zero bottom velocity (Eq. 4.18a), and then calculate the volume average (Eq. 4.18b, referred to as “thermal-wind velocity” in the manuscript). We use the volume average instead of the transport-weighted method in Eq. 4.18b in order to estimate the bulk buoyancy gradient.

$$u_g(x, y, z) = \int_{\eta_b}^z \frac{g}{\rho_0 f} \frac{\partial \rho}{\partial y} dz'. \quad (4.18a)$$

$$\mathcal{U}_g^{\text{east}} = \frac{\iiint_{\substack{\text{shelf break} \\ u_g > 0}} u_g dV}{\iiint_{\substack{\text{shelf break} \\ u_g > 0}} dV}, \quad (4.18b)$$

Fig. 4.6 shows that stronger ice-shelf melt leads to a larger cross-slope buoyancy gradient (panel b) and drives an undercurrent that approximately follows the thermal-wind relation (panel d). Stronger undercurrent velocity is associated with stronger shelf-break pressure torque, indicating the topographic control of the undercurrent strength (Fig. 4.6c).

4.5.8 Shoreward CDW transport within the trough

The shoreward CDW transport within the trough (Fig. 4.5f) is calculated by integrating the southward velocity ($v < 0$) across $-50 \text{ km} \leq x \leq 50 \text{ km}$, $100 \text{ km} \leq y \leq 225 \text{ km}$, and $\eta_b \leq z \leq \eta_{\text{cdw}}$, and then divided by the length of the trough ($L_{\text{trough}} = 125 \text{ km}$):

$$\mathcal{T}_{\text{trough}}^{\text{south}} = \frac{\iiint_{v<0} v dV}{L_{\text{trough}}}. \quad (4.19)$$

CHAPTER 5

Conclusions and future work

In this section, we summarize Chapters 2-4 of this dissertation and discuss some open questions and plans for future research.

5.1 Summary

In Chapter 2, we investigate the momentum transfer in the ocean-sea ice system of the ASC. Using a high-resolution coupled ocean-sea ice model of the ASC, we found that sea ice plays an important role in horizontally redistributing wind-input momentum away from the continental slope by ice internal stress. Over the slope, no momentum is transferred vertically via isopycnal form stress due to topographic eddy suppression, leading to an equilibrium state in which the surface ocean velocity matches the ice velocity. In order to explicitly turn off the effect of eddy suppression, we developed a reduced-order model for the mechanical interactions between ocean and sea ice. The reduced-order model reveals that the fundamental reason for the vanishing of the ice-ocean momentum transfer at the core of the ASC and the resulting ice-ocean velocity match is the suppression of transient and standing eddies over the continental slope. This study implies that the sea ice and ocean circulations are tightly linked at the core of the ASC and should be understood together in future model studies of the ASC. In addition, it is important to resolve the eddies or otherwise represent their suppression over the continental slope.

In Chapter 3, we study heat transport across the ASF. It is found that shoreward heat transport is primarily controlled by the salinity gradient of the shelf waters: Both freshening and salinification of the shelf waters relative to the offshore waters lead to increased heat flux onto the continental

shelf. For salty shelves, the overturning consists of a dense water outflow that drives a shoreward heat flux near the seafloor; for fresh shelves, there is a shallow, eddy-driven overturning circulation that is associated with an export of fresh surface waters and a near-surface shoreward heat flux. The eddy-driven overturning associated with coastal freshening may lead to a positive feedback in a warming climate: Large volumes of meltwater increase shoreward heat transport, causing further melt of ice shelves.

In Chapter 4, we explore the formation mechanism of the West Antarctic slope undercurrent. The undercurrent emerges with realistic strength and spatial pattern given a cross-slope buoyancy gradient and a trough that allows CDW to access the continental shelf and ice shelf cavity. By analyzing the vorticity budget within the CDW layer, it is found that the slope undercurrent is driven by the cyclonic vorticity input associated with meltwater upwelling in the ice shelf cavity. The total pressure torque acts to horizontally transport the cyclonic vorticity from the ice-shelf cavity to the shelf break. Increased basal melt strengthens the undercurrent and enhances the onshore heat flux, which implies another positive feedback that may accelerate future melt of ice shelves, potentially further destabilizing the West Antarctic Ice Sheet.

5.2 Looking ahead

5.2.1 Circumpolar variability and onshore heat transport

Though previous circum-Antarctic simulations have revealed many dynamics of the Antarctic margins, they have significant caveats, e.g., they did not include ice shelves and/or did not fully resolve eddies over the shelf and slope due to the coarse resolution. It remains unclear where are the “hot spots” of ocean heat transport toward Antarctic glaciers. In addition, it is not well understood to what extent small-scale and/or high-frequency variability such as eddies, tides, and dense outflows modulate onshore heat transport in the realistic geometry of the Antarctic margins. To close these scientific gaps, we have been developing a high-resolution Southern Ocean regional model with coupled ocean, sea ice, and ice shelves. This model spans the entire Southern Ocean, with an integration period of a few decades. Both the horizontal and vertical resolutions are fine

enough to resolve small-scale processes such as mesoscale eddies, shelf waves, and dense outflows. We have successfully run the model for several 26-year cycles using $1/3^\circ$ (16 km) and $1/6^\circ$ (8 km) horizontal grid spacing, and a few years with $1/12^\circ$ (4 km) resolution. The highest horizontal resolution will be $1/24^\circ$ (2 km) in our ongoing study. The vertical grid of this model has a higher resolution near the ocean surface and in the ice shelf cavities, with 113 levels in total.

We are going to focus on the following science questions: (i) Where are the “hot spots” of exchanges of heat, mass, and properties between the continental shelf and the open ocean in different sectors of the Antarctic margins? (ii) What is the role of small-scale and/or high-frequency variability in modulating cross-slope exchanges? (iii) How do the dynamic and thermodynamic processes associated with sea ice and ice shelves affect the along-slope circulation and cross-slope exchanges? To answer Question (i), we will calculate the cumulative heat, salt, and mass transport around Antarctica, following [Morrison et al. \(2020\)](#). To address Question (ii), we will temporally decompose ocean heat transport, kinetic energy, and streamfunctions into mean and eddy components, using the tools developed by [Stewart et al. \(2018, 2019\)](#). As for Question (iii), we will diagnose the momentum balance for the ocean and sea ice following [Si et al. \(2022\)](#), and analyze the heat budget for the ocean, sea ice, and individual ice shelves in different sectors of the Antarctic margins following [Si et al. \(2023\)](#).

5.2.2 West Antarctic slope undercurrent

In Chapter 4, the idealized representation of West Antarctic shelf/slope circulation does not account for various complexities such as the realistic topography with multiple troughs, the presence of multiple ice shelves, and the wide range of forcing time scales. Therefore, we plan to evaluate the melt-driven formation mechanisms of the West Antarctic slope undercurrent using a regional model. Following the methods described in Chapter 4, we plan to analyze the vorticity budget of the CDW layer adjacent to the Amundsen Sea ice shelves.

In addition, the transient response of the Antarctic slope undercurrent to wind forcing is not well understood. In our idealized model (Chapter 4), the undercurrent is not very sensitive to winds

compared to other varied parameters such as tides, vertical diffusivity, and shelf bathymetry. In addition, the melt rate does not change with varying wind. The insensitivity of melt and undercurrent to local winds might be an artifact resulting from the zonal boundary conditions. Based on previous studies, the undercurrent and melt should respond to higher frequency fluctuations in wind forcing. How high-frequency wind variability, transient eddies, and waves affect the dynamics of the undercurrent requires further study.

5.2.3 Tidal-mean compensation

There is a compensation between the tidal component and mean component in ocean advection (Chapter 2), meridional heat transport, and overturning circulation (Chapter 3), which has been found in an idealized model ([Si et al., 2022, 2023](#)) as well as a high-resolution regional model with realistic configuration and forcings ([Stewart et al., 2018, 2019](#)). It is still unclear what sets the baroclinic structure of the tidal overturning (Fig. 3.12E), how tides drive the strong cross-shelf Eulerian-mean overturning (Fig. 3.12C), and how general this compensation is in the real ASC. This tidally-driven cross-shelf mean flow is potentially important in deriving accurate estimates of cross-shelf exchanges in observational studies. In addition, instead of being compensated by the mean flow, it is unclear whether a model with a better representation of shear-driven mixing and bottom boundary layer processes might allow for a net tidally-driven heat/volume flux across the shelf. A future investigation is needed to provide insight into the mechanism of tidal-mean compensation in the ASC.

5.2.4 Seasonality of momentum transfer in the ASC

In Chapter 2 we investigate the momentum transfer in the ice-ocean system of the ASC in typical winter conditions, excluding seasonal variations. The conclusions are applicable to the annual-mean state of the real ASC. However, sea ice thickness and ice concentration vary notably with seasons around the Antarctic margins, which significantly changes the ability of sea ice to mediate momentum transfer between the wind and the ocean. It remains to be understood how

circulation and momentum balance respond to seasonal variations of sea ice, winds, and buoyancy forcing. The theory of coupled ocean-sea ice mechanical interactions described in Chapter 2 needs to be evaluated for different seasons and regions based on observations and high-resolution regional modeling (e.g., the Southern Ocean regional model described in section 5.2.1).

BIBLIOGRAPHY

- Adusumilli, Susheel and Fricker, Helen Amanda and Siegfried, Matthew R and Padman, Laurie and Paolo, Fernando S and Ligtenberg, Stefan RM, 2018: Variable basal melt rates of antarctic peninsula ice shelves, 1994–2016. *Geophys. Res. Lett.*, **45** (9), 4086–4095, <https://doi.org/10.1002/2017GL076652>.
- Amante, C., and B. W. Eakins, 2009:ETOPO1 1 Arc-Minute Global Relief Model: Procedures, Data Sources and Analysis. NOAA Technical Memorandum NESDIS NGDC-24. *National Geophysical Data Center, NOAA*, <https://doi.org/10.7289/V5C8276M>.
- Arakawa, A., and V. R. Lamb, 1977: Computational design of the basic dynamical processes of the UCLA general circulation model. *General circulation models of the atmosphere*, **17** (Supplement C), 173–265, <https://doi.org/10.1016/B978-0-12-460817-7.50009-4>.
- Armitage, T. W. K., R. Kwok, A. F. Thompson, and G. Cunningham, 2018: Dynamic topography and sea level anomalies of the Southern Ocean: Variability and teleconnections. *J. Geophys. Res. Oceans*, **123** (1), 613–630, <https://doi.org/10.1002/2017JC013534>.
- Arnscheidt, C. W., J. Marshall, P. Dutrieux, C. D. Rye, and A. Ramadhan, 2021: On the settling depth of meltwater escaping from beneath Antarctic ice shelves. *J. Phys. Oceanogr.*, **51** (7), 2257–2270, <https://doi.org/10.1175/JPO-D-20-0286.1>.
- Azaneu, M., B. Webber, K. J. Heywood, K. M. Assmann, T. S. Dotto, and E. P. Abrahamsen, 2023: Influence of shelf break processes on the transport of warm waters onto the eastern Amundsen Sea continental shelf. *J. Geophys. Res. Oceans*, e2022JC019535, <https://doi.org/10.1029/2022JC019535>.
- Bai, Y., Y. Wang, and A. L. Stewart, 2021: Does Topographic Form Stress Impede Prograde Ocean Currents? *J. Phys. Oceanogr.*, <https://doi.org/10.1175/JPO-D-20-0189.1>.
- Barth, A., and Coauthors, 2015: Assimilation of sea surface temperature, sea ice concentration

and sea ice drift in a model of the Southern Ocean. *Ocean Modell.*, **93**, 22–39, <https://doi.org/10.1016/j.ocemod.2015.07.011>.

Bett, D. T., P. R. Holland, A. C. Naveira Garabato, A. Jenkins, P. Dutrieux, S. Kimura, and A. Fleming, 2020: The impact of the Amundsen Sea freshwater balance on ocean melting of the West Antarctic Ice Sheet. *J. Geophys. Res. Oceans*, **125** (9), e2020JC016305, <https://doi.org/10.1029/2020JC016305>.

Bintanja, R., G. J. van Oldenborgh, S. Drijfhout, B. Wouters, and C. Katsman, 2013: Important role for ocean warming and increased ice-shelf melt in Antarctic sea-ice expansion. *Nat. Geosci.*, **6** (5), 376–379, <https://doi.org/10.1038/NGEO1767>.

Blumsack, S. L., and P. J. Gierasch, 1972: Mars: The effects of topography on baroclinic instability. *J. Atmos. Sci.*, **29** (6), 1081–1089, [https://doi.org/10.1175/1520-0469\(1972\)029<1081:MTEOTO>2.0.CO;2](https://doi.org/10.1175/1520-0469(1972)029<1081:MTEOTO>2.0.CO;2).

Boccaletti, G., R. Ferrari, A. Adcroft, D. Ferreira, and J. Marshall, 2005: The vertical structure of ocean heat transport. *Geophys. Res. Lett.*, **32** (10), <https://doi.org/10.1029/2005GL022474>.

Brearley, J. A., M. P. Meredith, A. C. N. Garabato, H. J. Venables, and M. E. Inall, 2017: Controls on turbulent mixing on the West Antarctic Peninsula shelf. *Deep Sea Res. Part II*, **139**, 18–30, <https://doi.org/10.1016/j.dsr2.2017.02.011>.

Brink, K., 1991: Coastal-trapped waves and wind-driven currents over the continental shelf. *Annu. Rev. Fluid Mech.*, **23** (1), 389–412, <https://doi.org/10.1146/annurev.fl.23.010191.002133>.

Brink, K., and S. Lentz, 2010: Buoyancy arrest and bottom Ekman transport. Part II: Oscillating flow. *J. Phys. Oceanogr.*, **40** (4), 636–655, <https://doi.org/10.1175/2009JPO4267.1>.

Brink, K. H., 2010: Topographic rectification in a forced, dissipative, barotropic ocean. *J. Mar. Res.*, **68** (3-4), 337–368, <https://doi.org/10.1357/002224010794657209>.

Brink, K. H., 2011: Topographic rectification in a stratified ocean. *J. of Mar. Res.*, **69** (4-5), 483–499, <https://doi.org/10.1357/002224011799849354>.

- Brink, K. H., 2013: Instability of a tidal mixing front in the presence of realistic tides and mixing. *J. Mar. Res.*, **71** (3), 227–251, <https://doi.org/10.1357/002224013807719473>.
- Bronselaer, B., M. Winton, S. M. Griffies, W. J. Hurlin, K. B. Rodgers, O. V. Sergienko, R. J. Stouffer, and J. L. Russell, 2018: Change in future climate due to antarctic meltwater. *Nature*, **564** (7734), 53–58, <https://doi.org/10.1038/s41586-018-0712-z>.
- Bryden, H. L., D. Halpern, and R. D. Pillsbury, 1980: Importance of eddy heat flux in a heat budget for Oregon coastal waters. *J. Geophys. Res.: Oceans*, **85** (C11), 6649–6653, <https://doi.org/10.1029/JC085iC11p06649>.
- Bull, C. Y. S., A. Jenkins, N. C. Jourdain, I. Vaňková, P. R. Holland, P. Mathiot, U. Hausmann, and J.-B. Sallée, 2021: Remote control of Filchner-Ronne Ice Shelf melt rates by the Antarctic Slope Current. *J. Geophys. Res. Oceans*, **126** (2), e2020JC016550, <https://doi.org/10.1029/2020JC016550>.
- Chelton, D. B., R. A. DeSzoeke, M. G. Schlax, K. El Naggar, and N. Siwertz, 1998: Geographical variability of the first baroclinic Rossby radius of deformation. *J. Phys. Oceanogr.*, **28** (3), 433–460, [https://doi.org/10.1175/1520-0485\(1998\)028<0433:GVOTFB>2.0.CO;2](https://doi.org/10.1175/1520-0485(1998)028<0433:GVOTFB>2.0.CO;2).
- Chen, C., and R. C. Beardsley, 1995: A numerical study of stratified tidal rectification over finite-amplitude banks. Part I: Symmetric banks. *J. Phys. Oceanogr.*, **25** (9), 2090–2110, [https://doi.org/10.1175/1520-0485\(1995\)025<2090:ANSOST>2.0.CO;2](https://doi.org/10.1175/1520-0485(1995)025<2090:ANSOST>2.0.CO;2).
- Chen, R., J. C. McWilliams, and L. Renault, 2021: Momentum Governors of California Undercurrent Transport. *J. Phys. Oceanogr.*, **51** (9), 2915–2932, <https://doi.org/10.1175/JPO-D-20-0234.1>.
- Cherian, D. A., and K. H. Brink, 2018: Shelf flows forced by deep-ocean anticyclonic eddies at the shelf break. *J. Phys. Oceanogr.*, **48** (5), 1117–1138, <https://doi.org/10.1175/JPO-D-17-0237.1>.
- Danabasoglu, G., and J. C. Mc Williams, 1995: Sensitivity of the global ocean circulation to

- parameterizations of mesoscale tracer transports. *J. Clim.*, **8** (12), 2967–2987, [https://doi.org/10.1175/1520-0442\(1995\)008<2967:SOTGOC>2.0.CO;2](https://doi.org/10.1175/1520-0442(1995)008<2967:SOTGOC>2.0.CO;2).
- De Lavergne, C., J. B. Palter, E. D. Galbraith, R. Bernardello, and I. Marinov, 2014: Cessation of deep convection in the open Southern Ocean under anthropogenic climate change. *Nat. Clim. Change*, **4** (4), 278–282, <https://doi.org/10.1038/NCLIMATE2132>.
- DeConto, R. M., and Coauthors, 2021: The Paris Climate Agreement and future sea-level rise from Antarctica. *Nature*, **593** (7857), 83–89, <https://doi.org/10.1038/s41586-021-03427-0>.
- Depoorter, M. A., J. L. Bamber, J. A. Griggs, J. T. Lenaerts, S. R. Ligtenberg, M. R. van den Broeke, and G. Moholdt, 2013: Calving fluxes and basal melt rates of Antarctic ice shelves. *Nature*, **502** (7469), 89–92, <https://doi.org/10.1038/nature12567>.
- Donat-Magnin, M., N. C. Jourdain, P. Spence, J. Le Sommer, H. Gallée, and G. Durand, 2017: Ice-shelf melt response to changing winds and glacier dynamics in the Amundsen Sea sector, Antarctica. *J. Geophys. Res. Oceans*, **122** (12), 10 206–10 224, <https://doi.org/10.1002/2017JC013059>.
- Döös, K., and D. J. Webb, 1994: The Deacon cell and the other meridional cells of the Southern Ocean. *J. Phys. Oceanogr.*, **24** (2), 429–442, [https://doi.org/10.1175/1520-0485\(1994\)024<429:TDCATO>2.0.CO;2](https://doi.org/10.1175/1520-0485(1994)024<429:TDCATO>2.0.CO;2).
- Dotto, T. S., and Coauthors, 2019: Wind-driven processes controlling oceanic heat delivery to the Amundsen Sea, Antarctica. *J. Phys. Oceanogr.*, **49** (11), 2829–2849, <https://doi.org/10.1175/JPO-D-19-0064.1>.
- Dotto, T. S., and Coauthors, 2020: Control of the oceanic heat content of the Getz-Dotson Trough, Antarctica, by the Amundsen Sea Low. *J. Geophys. Res.: Oceans*, **125** (8), e2020JC016113, <https://doi.org/10.1029/2020JC016113>.
- Dutrieux, P., and Coauthors, 2014: Strong sensitivity of Pine Island ice-shelf melting to climatic variability. *Science*, **343** (6167), 174–178, <https://doi.org/10.1126/science.1244341>.

Fer, I., E. Darelius, and K. B. Daae, 2016: Observations of energetic turbulence on the Weddell Sea continental slope. *Geophys. Res. Lett.*, **43** (2), 760–766, <https://doi.org/10.1002/2015GL067349>.

Ferreira, D., and J. Marshall, 2006: Formulation and implementation of “residual-mean” ocean circulation model. *Ocean Modell.*, **13** (1), 86–107, <https://doi.org/10.1016/j.ocemod.2005.12.001>.

Flexas, M. d. M., M. P. Schodlok, L. Padman, D. Menemenlis, and A. H. Orsi, 2015: Role of tides on the formation of the Antarctic Slope Front at the Weddell-Scotia Confluence. *J. Geophys. Res. Oceans*, **120** (5), 3658–3680, <https://doi.org/10.1002/2014JC010372>.

Fogwill, C., S. Phipps, C. Turney, and N. Golledge, 2015: Sensitivity of the Southern Ocean to enhanced regional Antarctic ice sheet meltwater input. *Earth's Future*, **3** (10), 317–329, <https://doi.org/10.1002/2015EF000306>.

Garabato, A. C. N., and Coauthors, 2017: Vigorous lateral export of the meltwater outflow from beneath an Antarctic ice shelf. *Nature*, **542** (7640), 219–222, <https://doi.org/10.1038/nature20825>.

Garreau, P., and R. Maze, 1992: Tidal rectification and mass transport over a shelf break: A barotropic frictionless model. *J. Phys. Oceanogr.*, **22** (7), 719–731, [https://doi.org/10.1175/1520-0485\(1992\)022<0719:TRAMTO>2.0.CO;2](https://doi.org/10.1175/1520-0485(1992)022<0719:TRAMTO>2.0.CO;2).

Gent, P. R., and J. C. Mcwilliams, 1990: Isopycnal mixing in ocean circulation models. *J. Phys. Oceanogr.*, **20** (1), 150–155, [https://doi.org/10.1175/1520-0485\(1990\)020<0150:IMOCM>2.0.CO;2](https://doi.org/10.1175/1520-0485(1990)020<0150:IMOCM>2.0.CO;2).

Gent, P. R., J. Willebrand, T. J. McDougall, and J. C. McWilliams, 1995: Parameterizing eddy-induced tracer transports in ocean circulation models. *J. Phys. Oceanogr.*, **25** (4), 463–474, [https://doi.org/10.1175/1520-0485\(1995\)025<0463:PEITTI>2.0.CO;2](https://doi.org/10.1175/1520-0485(1995)025<0463:PEITTI>2.0.CO;2).

Gill, A. E., 1973: Circulation and bottom water production in the Weddell Sea. *Deep Sea Res. and*

Oceanographic Abstracts, Elsevier, Vol. 20, 111–140, [https://doi.org/10.1016/0011-7471\(73\)90048-X](https://doi.org/10.1016/0011-7471(73)90048-X).

Goddard, P. B., C. O. Dufour, J. Yin, S. M. Griffies, and M. Winton, 2017: CO₂-induced ocean warming of the Antarctic continental shelf in an eddying global climate model. *J. Geophys. Res. Oceans*, **122** (10), 8079–8101, <https://doi.org/10.1002/2017JC012849>.

Goldberg, D., D. Holland, and C. Schoof, 2009: Grounding line movement and ice shelf buttressing in marine ice sheets. *J. Geophys. Res. Earth Surf.*, **114** (F4), <https://doi.org/10.1029/2008JF001227>.

Golledge, N. R., E. D. Keller, N. Gomez, K. A. Naughten, J. Bernales, L. D. Trusel, and T. L. Edwards, 2019: Global environmental consequences of twenty-first-century ice-sheet melt. *Nature*, **566** (7742), 65–72, <https://doi.org/10.1038/s41586-019-0889-9>.

Graham, J. A., K. J. Heywood, C. P. Chavanne, and P. R. Holland, 2013: Seasonal variability of water masses and transport on the Antarctic continental shelf and slope in the southeastern Weddell Sea. *J. Geophys. Res.: Oceans*, **118** (4), 2201–2214, <https://doi.org/10.1002/jgrc.20174>.

Greene, C. A., A. S. Gardner, N.-J. Schlegel, and A. D. Fraser, 2022: Antarctic calving loss rivals ice-shelf thinning. *Nature*, **609** (7929), 948–953, <https://doi.org/10.1038/s41586-022-05037-w>.

Griffies, S. M., and R. W. Hallberg, 2000: Biharmonic friction with a Smagorinsky-like viscosity for use in large-scale eddy-permitting ocean models. *Mon. Weather Rev.*, **128** (8), 2935–2946, [https://doi.org/10.1175/1520-0493\(2000\)128<2935:BFWASL>2.0.CO;2](https://doi.org/10.1175/1520-0493(2000)128<2935:BFWASL>2.0.CO;2).

Gudmundsson, G., 2013: Ice-shelf buttressing and the stability of marine ice sheets. *The Cryosphere*, **7** (2), 647–655, <https://doi.org/10.5194/tc-7-647-2013>.

Gudmundsson, G. H., F. S. Paolo, S. Adusumilli, and H. A. Fricker, 2019: Instantaneous Antarctic ice sheet mass loss driven by thinning ice shelves. *Geophys. Res. Lett.*, **46** (23), 13 903–13 909, <https://doi.org/10.1029/2019GL085027>.

Gwyther, D. E., K. Kusahara, X. S. Asay-Davis, M. S. Dinniman, and B. K. Galton-Fenzi, 2020: Vertical processes and resolution impact ice shelf basal melting: A multi-model study. *Ocean Modell.*, **147**, 101 569, <https://doi.org/10.1016/j.ocemod.2020.101569>.

Haigh, M., P. R. Holland, and A. Jenkins, 2023: The influence of bathymetry over heat transport onto the Amundsen Sea continental shelf. *J. Geophys. Res. Oceans*, e2022JC019460, <https://doi.org/10.1029/2022JC019460>.

Hallberg, R., 2013: Using a resolution function to regulate parameterizations of oceanic mesoscale eddy effects. *Ocean Modell.*, **72**, 92–103, <https://doi.org/10.1016/j.ocemod.2013.08.007>.

Hampson, P. M., and J. M. Pringle, 2022: Glacial Troughs Enhance Shelf/Slope Exchange in the Barotropic Limit. *J. Geophys. Res.: Oceans*, **127** (6), e2021JC018207, <https://doi.org/10.1029/2021JC018207>.

Hattermann, T., 2018: Antarctic thermocline dynamics along a narrow shelf with easterly winds. *J. Phys. Oceanogr.*, **48** (10), 2419–2443, <https://doi.org/10.1175/JPO-D-18-0064.1>.

Hattermann, T., and G. Rohardt, 2018: Kapp Norvegia Antarctic Slope Front climatology. PANGAEA, <https://doi.org/10.1594/PANGAEA.893199>, supplement to: Hattermann, Tore (2018): Antarctic Thermocline Dynamics along a Narrow Shelf with Easterly Winds. *J. Phys. Oceanogr.*, 48(10), 2419-2443, <https://doi.org/10.1175/JPO-D-18-0064.1>.

Haumann, F. A., N. Gruber, M. Münnich, I. Frenger, and S. Kern, 2016: Sea-ice transport driving Southern Ocean salinity and its recent trends. *Nature*, **537** (7618), 89–92, <https://doi.org/10.1038/nature19101>.

Hazel, J. E., and A. L. Stewart, 2019: Are the near-Antarctic easterly winds weakening in response to enhancement of the Southern Annular Mode? *J. Climate*, **32** (6), 1895–1918, <https://doi.org/10.1175/JCLI-D-18-0402.1>.

Hellmer, H. H., F. Kauker, R. Timmermann, and T. Hattermann, 2017: The fate of the southern

- Weddell Sea continental shelf in a warming climate. *J. Clim.*, **30** (12), 4337–4350, <https://doi.org/10.1175/JCLI-D-16-0420.1>.
- Heorton, H. D. B. S., D. L. Feltham, and J. C. R. Hunt, 2014: The response of the sea ice edge to atmospheric and oceanic jet formation. *J. Phys. Oceanogr.*, **44** (9), 2292–2316, <https://doi.org/10.1175/JPO-D-13-0184.1>.
- Hetland, R. D., 2017: Suppression of baroclinic instabilities in buoyancy-driven flow over sloping bathymetry. *J. Phys. Oceanogr.*, **47** (1), 49–68, <https://doi.org/10.1175/JPO-D-15-0240.1>.
- Heywood, K. J., R. A. Locarnini, R. D. Frew, P. F. Dennis, and B. A. King, 1998: Transport and water masses of the Antarctic Slope Front system in the eastern Weddell Sea. *Ocean, Ice, and Atmosphere: Interactions at the Antarctic Continental Margin, Antarct. Res. Ser.*, **75**, 203–214, <https://doi.org/10.1029/AR075p0203>.
- Heywood, K. J., and Coauthors, 2014: Ocean processes at the Antarctic continental slope. *Philos. Trans. R. Soc. London, Ser. A*, **372** (2019), 20130 047, <https://doi.org/10.1098/rsta.2013.0047>.
- Hibler, W. D., III, 1979: A dynamic thermodynamic sea ice model. *J. Phys. Oceanogr.*, **9** (4), 815–846, [https://doi.org/10.1175/1520-0485\(1979\)009<815:ADTSIM>2.0.CO;2](https://doi.org/10.1175/1520-0485(1979)009<815:ADTSIM>2.0.CO;2).
- Hibler, W. D., III, 1980: Modeling a variable thickness sea ice cover. *Mon. Weather Rev.*, **108** (12), 1943–1973, [https://doi.org/10.1175/1520-0493\(1980\)108<1943:MAVTSI>2.0.CO;2](https://doi.org/10.1175/1520-0493(1980)108<1943:MAVTSI>2.0.CO;2).
- Holland, D. M., and A. Jenkins, 1999: Modeling thermodynamic ice–ocean interactions at the base of an ice shelf. *J. Phys. Oceanogr.*, **29** (8), 1787–1800, [https://doi.org/10.1175/1520-0485\(1999\)029<1787:MTIOIA>2.0.CO;2](https://doi.org/10.1175/1520-0485(1999)029<1787:MTIOIA>2.0.CO;2).
- Holland, P. R., 2014: The seasonality of Antarctic sea ice trends. *Geophys. Res. Lett.*, **41** (12), 4230–4237, <https://doi.org/10.1002/2014GL060172>.
- Holland, P. R., R. E. Hewitt, and M. M. Scase, 2014: Wave breaking in dense plumes. *J. Phys. Oceanogr.*, **44** (2), 790–800, <https://doi.org/10.1175/JPO-D-13-0110.1>.

Holland, P. R., and R. Kwok, 2012: Wind-driven trends in Antarctic sea-ice drift. *Nat. Geosci.*, **5** (12), 872–875, <https://doi.org/10.1038/NGEO1627>.

Howard, E., A. McC. Hogg, S. Waterman, and D. P. Marshall, 2015: The injection of zonal momentum by buoyancy forcing in a southern ocean model. *J. Phys. Oceanogr.*, **45** (1), 259–271, <https://doi.org/10.1175/JPO-D-14-0098.1>.

Howard, S., J. Hyatt, and L. Padman, 2004: Mixing in the pycnocline over the western Antarctic Peninsula shelf during Southern Ocean GLOBEC. *Deep Sea Res. Part II*, **51** (17-19), 1965–1979, <https://doi.org/10.1016/j.dsr2.2004.08.002>.

Huneke, W. G. C., A. Klocker, and B. K. Galton-Fenzi, 2019: Deep bottom mixed layer drives intrinsic variability of the Antarctic Slope Front. *J. Phys. Oceanogr.*, **49** (12), 3163–3177, <https://doi.org/10.1175/JPO-D-19-0044.1>.

Huthnance, J., 1973: Tidal current asymmetries over the Norfolk Sandbanks. *Estuarine Coastal Mar. Sci.*, **1** (1), 89–99, [https://doi.org/10.1016/0302-3524\(73\)90061-3](https://doi.org/10.1016/0302-3524(73)90061-3).

Isachsen, P. E., 2011: Baroclinic instability and eddy tracer transport across sloping bottom topography: How well does a modified Eady model do in primitive equation simulations? *Ocean Modell.*, **39** (1-2), 183–199, <https://doi.org/10.1016/j.ocemod.2010.09.007>.

Jacobs, S. S., 1991: On the nature and significance of the Antarctic Slope Front. *Mar. Chem.*, **35** (1-4), 9–24, [https://doi.org/10.1016/S0304-4203\(09\)90005-6](https://doi.org/10.1016/S0304-4203(09)90005-6).

Jacobs, S. S., 2006: Observations of change in the Southern Ocean. *Philos. Trans. R. Soc. A*, **364** (1844), 1657–1681, <https://doi.org/10.1098/rsta.2006.1794>.

Jacobs, S. S., and C. F. Giulivi, 2010: Large multidecadal salinity trends near the Pacific–Antarctic continental margin. *J. Clim.*, **23** (17), 4508–4524, <https://doi.org/10.1175/2010JCLI3284.1>.

Jacobs, S. S., A. Jenkins, C. F. Giulivi, and P. Dutrieux, 2011: Stronger ocean circulation and increased melting under Pine Island Glacier ice shelf. *Nat. Geosci.*, **4** (8), 519–523, <https://doi.org/10.1038/NGEO1188>.

Jenkins, A., P. Dutrieux, S. Jacobs, E. J. Steig, G. H. Gudmundsson, J. Smith, and K. J. Heywood, 2016: Decadal ocean forcing and Antarctic ice sheet response: Lessons from the Amundsen Sea. *Oceanography*, **29** (4), 106–117, <https://doi.org/10.5670/oceanog.2016.103>.

Joughin, I., and R. B. Alley, 2011: Stability of the West Antarctic ice sheet in a warming world. *Nat. Geosci.*, **4** (8), 506–513, <https://doi.org/10.1038/NGEO1194>.

Joughin, I., D. Shapero, P. Dutrieux, and B. Smith, 2021: Ocean-induced melt volume directly paces ice loss from Pine Island Glacier. *Sci. Adv.*, **7** (43), eabi5738, <https://doi.org/10.1126/sciadv.abi5738>.

Jourdain, N. C., P. Mathiot, N. Merino, G. Durand, J. Le Sommer, P. Spence, P. Dutrieux, and G. Madec, 2017: Ocean circulation and sea-ice thinning induced by melting ice shelves in the Amundsen Sea. *J. Geophys. Res.: Oceans*, **122** (3), 2550–2573, <https://doi.org/10.1002/2016JC012509>.

Jourdain, N. C., J.-M. Molines, J. Le Sommer, P. Mathiot, J. Chanut, C. de Lavergne, and G. Madec, 2019: Simulating or prescribing the influence of tides on the Amundsen Sea ice shelves. *Ocean Modell.*, **133**, 44–55, <https://doi.org/10.1016/j.ocemod.2018.11.001>.

Jullion, L., A. C. N. Garabato, M. P. Meredith, P. R. Holland, P. Courtois, and B. A. King, 2013: Decadal freshening of the Antarctic Bottom Water exported from the Weddell Sea. *J. Clim.*, **26** (20), 8111–8125, <https://doi.org/10.1175/JCLI-D-12-00765.1>.

Kimura, S., and Coauthors, 2017: Oceanographic controls on the variability of ice-shelf basal melting and circulation of glacial meltwater in the Amundsen Sea Embayment, Antarctica. *J. Geophys. Res.: Oceans*, **122** (12), 10 131–10 155, <https://doi.org/10.1002/2017JC012926>.

King, M. A., R. J. Bingham, P. Moore, P. L. Whitehouse, M. J. Bentley, and G. A. Milne, 2012: Lower satellite-gravimetry estimates of Antarctic sea-level contribution. *Nature*, **491** (7425), 586–589, <https://doi.org/10.1038/nature11621>.

- Koentopp, M., O. Eisen, C. Kottmeier, L. Padman, and P. Lemke, 2005: Influence of tides on sea ice in the Weddell Sea: Investigations with a high-resolution dynamic-thermodynamic sea ice model. *J. Geophys. Res. Oceans*, **110** (C2), <https://doi.org/10.1029/2004JC002405>.
- Kolmogorov, A. N., 1941: The local structure of turbulence in incompressible viscous fluid for very large Reynolds numbers. *Cr Acad. Sci. URSS*, **30**, 301–305.
- Kowalik, Z., and A. Y. Proshutinsky, 1995: Topographic enhancement of tidal motion in the western Barents Sea. *J. Geophys. Res. Oceans*, **100** (C2), 2613–2637, <https://doi.org/10.1029/94JC02838>.
- Kusahara, K., and K. I. Ohshima, 2014: Kelvin waves around Antarctica. *J. Phys. Oceanogr.*, **44** (11), 2909–2920, <https://doi.org/10.1175/JPO-D-14-0051.1>.
- Lamb, K. G., 2014: Internal wave breaking and dissipation mechanisms on the continental slope/shelf. *Annu. Rev. Fluid Mech.*, **46**, 231–254, <https://doi.org/10.1146/annurev-fluid-011212-140701>.
- Le Pailh, N., T. Hattermann, O. Boebel, T. Kanzow, C. Lüpkes, G. Rohardt, V. Strass, and S. Herbette, 2020: Coherent seasonal acceleration of the Weddell sea boundary current system driven by upstream winds. *J. Geophys. Res.: Oceans*, **125** (10), e2020JC016316, <https://doi.org/10.1029/2020JC016316>.
- Leppäranta, M., 2011: *The drift of sea ice*. Springer Science & Business Media.
- Li, J., and J. Gan, 2020: On the formation dynamics of the north equatorial undercurrent. *J. Phys. Oceanogr.*, **50** (5), 1399–1415, <https://doi.org/10.1175/JPO-D-19-0142.1>.
- Liu, Y., J. C. Moore, X. Cheng, R. M. Gladstone, J. N. Bassis, H. Liu, J. Wen, and F. Hui, 2015: Ocean-driven thinning enhances iceberg calving and retreat of Antarctic ice shelves. *Proc. Natl. Acad. Sci.*, **112** (11), 3263–3268, <https://doi.org/10.1073/pnas.1415137112>.
- Locarnini, M., and Coauthors, 2018: World Ocean Atlas 2018, Volume 1: Temperature. <https://www.ncei.noaa.gov/products/world-ocean-atlas>.

Locarnini, R. A., and Coauthors, 2023: World Ocean Atlas 2023, Volume 1: Temperature. <https://www.ncei.noaa.gov/access/world-ocean-atlas-2023/>.

Lockwood, J. W., C. O. Dufour, S. M. Griffies, and M. Winton, 2021: On the role of the Antarctic Slope Front on the occurrence of the Weddell Sea polynya under climate change. *J. Climate*, **34** (7), 2529–2548, <https://doi.org/10.1175/JCLI-D-20-0069.1>.

Loder, J. W., 1980: Topographic rectification of tidal currents on the sides of Georges Bank. *J. Phys. Oceanogr.*, **10** (9), 1399–1416, [https://doi.org/10.1175/1520-0485\(1980\)010<1399:TROTCO>2.0.CO;2](https://doi.org/10.1175/1520-0485(1980)010<1399:TROTCO>2.0.CO;2).

Losch, M., A. Fuchs, J.-F. Lemieux, and A. Vanselow, 2014: A parallel Jacobian-free Newton–Krylov solver for a coupled sea ice–ocean model. *J. Comput. Phys.*, **257**, 901–911, <https://doi.org/10.1016/j.jcp.2013.09.026>.

Losch, M., D. Menemenlis, J.-M. Campin, P. Heimbach, and C. Hill, 2010: On the formulation of sea-ice models. Part 1: Effects of different solver implementations and parameterizations. *Ocean Modell.*, **33** (1), 129–144, <https://doi.org/10.1016/j.ocemod.2009.12.008>.

Lüpkes, C., and V. M. Grynk, 2015: A stability-dependent parametrization of transfer coefficients for momentum and heat over polar sea ice to be used in climate models. *J. Geophys. Res.: Atmos.*, **120** (2), 552–581, <https://doi.org/10.1002/2014JD022418>.

Lüpkes, C., V. M. Grynk, J. Hartmann, and E. L. Andreas, 2012: A parametrization, based on sea ice morphology, of the neutral atmospheric drag coefficients for weather prediction and climate models. *J. Geophys. Res.: Atmos.*, **117** (D13), <https://doi.org/10.1029/2012JD017630>.

Marshall, J., A. Adcroft, C. Hill, L. Perelman, and C. Heisey, 1997a: A finite-volume, incompressible Navier Stokes model for studies of the ocean on parallel computers. *J. Geophys. Res.*, **102**, 5753–5766, <https://doi.org/10.1029/96JC02775>.

Marshall, J., C. Hill, L. Perelman, and A. Adcroft, 1997b: Hydrostatic, quasi-hydrostatic, and

- nonhydrostatic ocean modeling. *J. Geophys. Res.*, **102**, 5733–5752, <https://doi.org/10.1029/96JC02776>.
- Marshall, J., and K. Speer, 2012: Closure of the meridional overturning circulation through Southern Ocean upwelling. *Nat. Geosci.*, **5** (3), 171–180, <https://doi.org/10.1038/ngeo1391>.
- Masich, J., T. K. Chereskin, and M. R. Mazloff, 2015: Topographic form stress in the Southern Ocean state estimate. *J. Geophys. Res. Oceans*, **120** (12), 7919–7933, <https://doi.org/10.1002/2015JC011143>.
- Masich, J., M. R. Mazloff, and T. K. Chereskin, 2018: Interfacial form stress in the southern ocean state estimate. *J. Geophys. Res. Oceans*, **123** (5), 3368–3385, <https://doi.org/10.1029/2018JC013844>.
- Mathiot, P., H. Goosse, T. Fichefet, B. Barnier, and H. Gallée, 2011: Modelling the seasonal variability of the Antarctic Slope Current. *Ocean Sci.*, **7** (4), 455–470, <https://doi.org/10.5194/os-7-455-2011>.
- McDougall, T. J., D. R. Jackett, D. G. Wright, and R. Feistel, 2003: Accurate and computationally efficient algorithms for potential temperature and density of seawater. *J. Atmos. Oceanic Technol.*, **20** (5), 730–741, [https://doi.org/10.1175/1520-0426\(2003\)20<730:AACEAF>2.0.CO;2](https://doi.org/10.1175/1520-0426(2003)20<730:AACEAF>2.0.CO;2).
- McWilliams, J. C., 2008: The nature and consequences of oceanic eddies. *Ocean modeling in an eddying regime*, **177**, 5–15, <http://www.ccpo.odu.edu/~klinck/Reprints/PDF/mcwilliamsOMER2008.pdf>.
- Meniel, L., A. Timmermann, O. E. Timm, and A. Mouchet, 2010: Climate and biogeochemical response to a rapid melting of the West Antarctic Ice Sheet during interglacials and implications for future climate. *Paleoceanography*, **25** (4), <https://doi.org/10.1029/2009PA001892>.
- Moorman, R., A. K. Morrison, and A. McC. Hogg, 2020: Thermal Responses to Antarctic Ice Shelf Melt in an Eddy-Rich Global Ocean–Sea Ice Model. *J. Climate*, **33** (15), 6599–6620, <https://doi.org/10.1175/JCLI-D-19-0846.1>.

Morrison, A., A. M. Hogg, M. H. England, and P. Spence, 2020: Warm Circumpolar Deep Water transport toward Antarctica driven by local dense water export in canyons. *Science advances*, **6** (18), eaav2516, <https://doi.org/10.1126/sciadv.aav2516>.

Muench, R., L. Padman, A. Gordon, and A. Orsi, 2009: A dense water outflow from the Ross Sea, Antarctica: Mixing and the contribution of tides. *J. Mar. Syst.*, **77** (4), 369–387, <https://doi.org/10.1016/j.jmarsys.2008.11.003>.

Munk, W. H., and E. Palmén, 1951: Note on the dynamics of the antarctic circumpolar current 1. *Tellus*, **3** (1), 53–55, <https://doi.org/10.1111/j.2153-3490.1951.tb00776.x>.

Mysak, L. A., 1980: Topographically trapped waves. *Annu. Rev. Fluid Mech.*, **12** (1), 45–76, <https://doi.org/10.1146/annurev.fl.12.010180.000401>.

Nakayama, Y., K. I. Ohshima, Y. Matsumura, Y. Fukamachi, and H. Hasumi, 2014a: A Numerical Investigation of Formation and Variability of Antarctic Bottom Water off Cape Darnley, East Antarctica. *J. Phys. Oceanogr.*, **44** (11), 2921–2937, <https://doi.org/10.1175/JPO-D-14-0069.1>.

Nakayama, Y., R. Timmermann, C. B. Rodehacke, M. Schröder, and H. H. Hellmer, 2014b: Modeling the spreading of glacial meltwater from the Amundsen and Bellingshausen Seas. *Geophys. Res. Lett.*, **41** (22), 7942–7949, <https://doi.org/10.1002/2014GL061600>.

Nakayama, Y., R. Timmermann, M. Schröder, and H. H. Hellmer, 2014c: On the difficulty of modeling Circumpolar Deep Water intrusions onto the Amundsen Sea continental shelf. *Ocean Modelling*, **84**, 26–34, <http://dx.doi.org/10.1016/j.ocemod.2014.09.007>.

Nakayama, Y., and Coauthors, 2019: Pathways of ocean heat towards Pine Island and Thwaites grounding lines. *Sci. Rep.*, **9** (1), 16 649, <https://doi.org/10.1038/s41598-019-53190-6>.

Nakayama, Y., and Coauthors, 2021: Antarctic Slope Current modulates ocean heat intrusions towards Totten Glacier. *Geophysical Research Letters*, e2021GL094149, <https://doi.org/10.1029/2021GL094149>.

Naughten, K. A., K. J. Meissner, B. K. Galton-Fenzi, M. H. England, R. Timmermann, and H. H. Hellmer, 2018: Future projections of Antarctic ice shelf melting based on CMIP5 scenarios. *J. Climate*, **31** (13), 5243–5261, <https://doi.org/10.1175/JCLI-D-17-0854.1>.

Naveira Garabato, A. C., and Coauthors, 2019: Phased response of the subpolar Southern Ocean to changes in circumpolar winds. *Geophys. Res. Lett.*, **46** (11), 6024–6033, <https://doi.org/10.1029/2019GL082850>.

Nicholls, K. W., S. Østerhus, K. Makinson, T. Gammelsrød, and E. Fahrbach, 2009: Ice-ocean processes over the continental shelf of the southern Weddell Sea, Antarctica: A review. *Rev. Geophys.*, **47** (3), <https://doi.org/10.1029/2007RG000250>.

NOAA National Geophysical Data Center, 2009: ETOPO1 1 Arc-Minute Global Relief Model. *NOAA National Centers for Environmental Information*, <https://doi.org/10.7289/V5C8276M>.

Nøst, O. A., M. Biuw, V. Tverberg, C. Lydersen, T. Hattermann, Q. Zhou, L. H. Smedsrød, and K. M. Kovacs, 2011: Eddy overturning of the Antarctic Slope Front controls glacial melting in the Eastern Weddell Sea. *J. Geophys. Res.*, **116**, C11 014, <https://doi.org/10.1029/2011JC006965>.

Núñez-Riboni, I., and E. Fahrbach, 2009: Seasonal variability of the Antarctic Coastal Current and its driving mechanisms in the Weddell Sea. *Deep Sea Res. Part I*, **56** (11), 1927–1941, <https://doi.org/10.1016/j.dsr.2009.06.005>.

Nurser, A. G., and M.-M. Lee, 2004: Isopycnal averaging at constant height. Part II: Relating to the residual streamfunction in Eulerian space. *J. Phys. Oceanogr.*, **34** (12), 2740–2755, <https://doi.org/10.1175/JPO2650.1>.

Padman, L., S. Y. Erofeeva, and H. A. Fricker, 2008: Improving Antarctic tide models by assimilation of ICESat laser altimetry over ice shelves. *Geophys. Res. Lett.*, **35** (22), <https://doi.org/10.1029/2008GL035592>.

Padman, L., H. A. Fricker, R. Coleman, S. Howard, and L. Erofeva, 2002: A new tide model

for the Antarctic ice shelves and seas. *Ann. Glaciol.*, **34**, 247–254, <https://doi.org/10.3189/172756402781817752>.

Padman, L., S. L. Howard, A. H. Orsi, and R. D. Muench, 2009: Tides of the northwestern Ross Sea and their impact on dense outflows of Antarctic Bottom Water. *Deep Sea Res. Part II*, **56** (13), 818–834, <https://doi.org/10.1016/j.dsr2.2008.10.026>.

Paolo, F. S., H. A. Fricker, and L. Padman, 2015: Volume loss from Antarctic ice shelves is accelerating. *Science*, **348** (6232), 327–331, <https://doi.org/10.1126/science.aaa0940>.

Pattyn, F., and M. Morlighem, 2020: The uncertain future of the Antarctic Ice Sheet. *Science*, **367** (6484), 1331–1335, <https://doi.org/10.1126/science.aaz5487>.

Powers, J. G., K. W. Manning, D. H. Bromwich, J. J. Cassano, and A. M. Cayette, 2012: A decade of Antarctic science support through AMPS. *Bull. Am. Meteorol. Soc.*, **93** (11), 1699–1712, <https://doi.org/10.1175/BAMS-D-11-00186.1>.

Powers, J. G., A. J. Monaghan, A. M. Cayette, D. H. Bromwich, Y.-H. Kuo, and K. W. Manning, 2003: Real-Time Mesoscale Modeling Over Antarctica: The Antarctic Mesoscale Prediction System* The Antarctic Mesoscale Prediction System. *Bull. Am. Meteorol. Soc.*, **84** (11), 1533–1546, <https://doi.org/10.1175/BAMS-84-11-1533>.

Pritchard, H., S. R. Ligtenberg, H. A. Fricker, D. G. Vaughan, M. R. van den Broeke, and L. Padman, 2012: Antarctic ice-sheet loss driven by basal melting of ice shelves. *Nature*, **484** (7395), 502–505, <https://doi.org/10.1038/nature10968>.

Rackow, T., C. Wesche, R. Timmermann, H. H. Hellmer, S. Juricke, and T. Jung, 2017: A simulation of small to giant Antarctic iceberg evolution: Differential impact on climatology estimates. *J. Geophys. Res. Oceans*, **122** (4), 3170–3190, <http://dx.doi.org/10.1002/2016JC012513>.

Redi, M. H., 1982: Oceanic isopycnal mixing by coordinate rotation. *Journal of Physical Oceanography*, **12** (10), 1154–1158, [https://doi.org/10.1175/1520-0485\(1982\)012<1154:OIMBCR>2.0.CO;2](https://doi.org/10.1175/1520-0485(1982)012<1154:OIMBCR>2.0.CO;2).

Rignot, E., S. Jacobs, J. Mouginot, and B. Scheuchl, 2013: Ice-shelf melting around Antarctica. *Science*, **341** (6143), 266–270, <https://doi.org/10.1126/science.1235798>.

Robertson, R., 2013: Tidally induced increases in melting of Amundsen Sea ice shelves. *J. Geophys. Res.: Oceans*, **118** (6), 3138–3145, <https://doi.org/10.1002/jgrc.20236>.

Robinson, I., 1981: Tidal vorticity and residual circulation. *Deep Sea Res. Part A*, **28** (3), 195–212, [https://doi.org/10.1016/0198-0149\(81\)90062-5](https://doi.org/10.1016/0198-0149(81)90062-5).

Rosenberg, M., and R. Gorton, 2019: BROKE West Survey, Marine Science Cruise AU0603 - Oceanographic Field Measurements and Analysis, Ver. 2. <https://doi.org/10.26179/5ceb6d79c35a4>.

Sadai, S., A. Condron, R. DeConto, and D. Pollard, 2020: Future climate response to Antarctic Ice Sheet melt caused by anthropogenic warming. *Sci. Adv.*, **6** (39), eaaz1169, <https://doi.org/10.1126/sciadv.aaz1169>.

Schaffer, J., and R. Timmermann, 2016: Greenland and Antarctic ice sheet topography, cavity geometry, and global bathymetry (RTopo-2), links to NetCDF files. *Supplement to: Schaffer et al. (2016): A global, high-resolution data set of ice sheet topography, cavity geometry, and ocean bathymetry. Earth System Science Data*, **8**(2), 543–557, <https://doi.org/10.5194/essd-8-543-2016>, <https://doi.org/10.1594/PANGAEA.856844>.

Schloesser, F., T. Friedrich, A. Timmermann, R. M. DeConto, and D. Pollard, 2019: Antarctic iceberg impacts on future Southern Hemisphere climate. *Nature Climate Change*, **9** (9), 672–677, <https://doi.org/10.1038/s41558-019-0546-1>.

Schmidtko, S., K. J. Heywood, A. F. Thompson, and S. Aoki, 2014: Multidecadal warming of Antarctic waters. *Science*, **346** (6214), 1227–1231, <https://doi.org/10.1126/science.1256117>.

Scott, R. M., J. A. Brearley, A. C. Naveira Garabato, H. J. Venables, and M. P. Meredith, 2021: Rates and mechanisms of turbulent mixing in a coastal embayment of the West Antarctic Peninsula. *J. Geophys. Res.: Oceans*, **126** (5), e2020JC016861, <https://doi.org/10.1029/2020JC016861>.

Si, Y., A. Stewart, and I. Eisenman, 2022: Coupled ocean/sea ice dynamics of the antarctic slope current driven by topographic eddy suppression and sea ice momentum redistribution. *J. Phys. Oceanogr.*, <https://doi.org/10.1175/JPO-D-21-0142.1>.

Si, Y., A. L. Stewart, and I. Eisenman, 2023: Heat transport across the Antarctic Slope Front controlled by cross-slope salinity gradients. *Sci. Adv.*, **9** (18), eadd7049, <https://doi.org/10.1126/sciadv.add7049>.

Silvano, A., S. R. Rintoul, B. Peña-Molino, W. R. Hobbs, E. van Wijk, S. Aoki, T. Tamura, and G. D. Williams, 2018: Freshening by glacial meltwater enhances melting of ice shelves and reduces formation of Antarctic Bottom Water. *Sci. Adv.*, **4** (4), eaap9467, <https://doi.org/10.1126/sciadv.aap9467>.

Silvano, A., and Coauthors, 2022: Baroclinic Ocean Response to Climate Forcing Regulates Decadal Variability of Ice-Shelf Melting in the Amundsen Sea. *Geophys. Res. Lett.*, **49** (24), e2022GL100646, <https://doi.org/10.1029/2022GL100646>.

Smagorinsky, J., 1963: General circulation experiments with the primitive equations: I. The basic experiment. *Mon. Weather Rev.*, **91** (3), 99–164, [https://doi.org/10.1175/1520-0493\(1963\)091<0099:GCEWTP>2.3.CO;2](https://doi.org/10.1175/1520-0493(1963)091<0099:GCEWTP>2.3.CO;2).

Smagorinsky, J., 1993: Some historical remarks on the use of nonlinear viscosities. *Evolution of Physical Oceanography*, B. Galperin, and S. Orszag, Eds., Cambridge University Press, 3–36.

Spall, M. A., and J. F. Price, 1998: Mesoscale variability in Denmark Strait: The PV outflow hypothesis. *J. Phys. Oceanogr.*, **28** (8), 1598–1623, [https://doi.org/10.1175/1520-0485\(1998\)028<1598:MVIDST>2.0.CO;2](https://doi.org/10.1175/1520-0485(1998)028<1598:MVIDST>2.0.CO;2).

Spence, P., S. M. Griffies, M. H. England, A. M. Hogg, O. A. Saenko, and N. C. Jourdain, 2014: Rapid subsurface warming and circulation changes of Antarctic coastal waters by poleward shifting winds. *Geophysical Research Letters*, **41** (13), 4601–4610, <https://doi.org/10.1002/2014GL060613>.

- Spence, P., R. M. Holmes, A. M. Hogg, S. M. Griffies, K. D. Stewart, and M. H. England, 2017: Localized rapid warming of West Antarctic subsurface waters by remote winds. *Nature Climate Change*, **7** (8), 595–603, <https://doi.org/10.1038/NCLIMATE3335>.
- St-Laurent, P., J. M. Klinck, and M. S. Dinniman, 2013: On the role of coastal troughs in the circulation of warm circumpolar deep water on Antarctic shelves. *J. Phys. Oceanogr.*, **43** (1), 51–64, <https://doi.org/10.1175/JPO-D-11-0237.1>.
- Stern, A., L.-P. Nadeau, and D. Holland, 2015: Instability and mixing of zonal jets along an idealized continental shelf break. *J. Phys. Oceanogr.*, **45** (9), 2315–2338, <https://doi.org/10.1175/JPO-D-14-0213.1>.
- Stern, A. A., A. Adcroft, and O. Sergienko, 2016: The effects of Antarctic iceberg calving-size distribution in a global climate model. *J. Geophys. Res. Oceans*, **121** (8), 5773–5788, <https://doi.org/10.1002/2016JC011835>.
- Stewart, A. L., 2021: Mesoscale, tidal, and seasonal/interannual drivers of the weddell sea overturning circulation. *J. Phys. Oceanogr.*, **51** (12), 3695–3722, <https://doi.org/10.1175/JPO-D-20-0320.1>.
- Stewart, A. L., and A. M. Hogg, 2017: Reshaping the Antarctic circumpolar current via Antarctic bottom water export. *J. Phys. Oceanogr.*, **47** (10), 2577–2601, <https://doi.org/10.1175/JPO-D-17-0007.1>.
- Stewart, A. L., A. Klocker, and D. Menemenlis, 2018: Circum-Antarctic shoreward heat transport derived from an eddy-and tide-resolving simulation. *Geophys. Res. Lett.*, **45** (2), 834–845, <https://doi.org/10.1002/2017GL075677>.
- Stewart, A. L., A. Klocker, and D. Menemenlis, 2019: Acceleration and overturning of the Antarctic Slope Current by winds, eddies, and tides. *J. Phys. Oceanogr.*, **49** (8), 2043–2074, <https://doi.org/10.1175/JPO-D-18-0221.1>.

Stewart, A. L., J. C. McWilliams, and A. Solodoch, 2021: On the role of bottom pressure torques in wind-driven gyres. *J. Phys. Oceanogr.*, **51** (5), 1441–1464, <https://doi.org/10.1175/JPO-D-20-0147.1>.

Stewart, A. L., and A. F. Thompson, 2013: Connecting Antarctic cross-slope exchange with Southern Ocean overturning. *J. Phys. Oceanogr.*, **43** (7), 1453–1471, <https://doi.org/10.1175/JPO-D-12-0205.1>.

Stewart, A. L., and A. F. Thompson, 2015: Eddy-mediated transport of warm Circumpolar Deep Water across the Antarctic Shelf Break. *Geophys. Res. Lett.*, **42**, 432–440, <https://doi.org/10.1002/2014GL062281>.

Stewart, A. L., and A. F. Thompson, 2016: Eddy generation and jet formation via dense water outflows across the Antarctic continental slope. *J. Phys. Oceanogr.*, **46** (12), 3729–3750, <https://doi.org/10.1175/JPO-D-16-0145.1>.

Swart, N. C., S. T. Gille, J. C. Fyfe, and N. P. Gillett, 2018: Recent Southern Ocean warming and freshening driven by greenhouse gas emissions and ozone depletion. *Nat. Geosci.*, **11** (11), 836–841, <https://doi.org/10.1038/s41561-018-0226-1>.

Swingedouw, D., T. Fichefet, P. Huybrechts, H. Goosse, E. Driesschaert, and M.-F. Loutre, 2008: Antarctic ice-sheet melting provides negative feedbacks on future climate warming. *Geophys. Res. Lett.*, **35** (17), <https://doi.org/10.1029/2008GL034410>.

Thompson, A. F., K. J. Heywood, S. Schmidtko, and A. L. Stewart, 2014: Eddy transport as a key component of the Antarctic overturning circulation. *Nat. Geosci.*, **7** (12), 879–884, <https://doi.org/10.1038/ngeo2289>.

Thompson, A. F., K. G. Speer, and L. M. Schulze Chretien, 2020: Genesis of the Antarctic Slope Current in West Antarctica. *Geophys. Res. Lett.*, **47** (16), e2020GL087802, <https://doi.org/10.1029/2020GL087802>.

- Thompson, A. F., A. L. Stewart, P. Spence, and K. J. Heywood, 2018: The Antarctic Slope Current in a changing climate. *Rev. Geophys.*, **56** (4), 741–770, <https://doi.org/10.1029/2018RG000624>.
- Towns, J., and Coauthors, 2014: XSEDE: Accelerating scientific discovery. *Computing in Science & Engineering*, **16** (5), 62–74, doi:10.1109/MCSE.2014.80.
- Tréguier, A.-M., and J. C. McWilliams, 1990: Topographic influences on wind-driven, stratified flow in a β -plane channel: An idealized model for the Antarctic Circumpolar Current. *J. Phys. Oceanogr.*, **20** (3), 321–343, [https://doi.org/10.1175/1520-0485\(1990\)020<0321:TIOWDS>2.0.CO;2](https://doi.org/10.1175/1520-0485(1990)020<0321:TIOWDS>2.0.CO;2).
- Tschudi, M., C. Fowler, J. Maslanik, J. S. Stewart, and W. N. Meier, 2016: Polar Pathfinder daily 25 km EASE-Grid Sea Ice motion vectors, version 3. *National Snow and Ice Data Center Distributed Active Archive Center, accessed February*, <https://doi.org/10.5067/O57VAIT2AYYY>.
- Vallis, G. K., 2017: *Atmospheric and oceanic fluid dynamics*. Cambridge University Press, 136 pp., <https://doi.org/10.1017/9781107588417>.
- Vancoppenolle, M., S. Bouillon, T. Fichefet, H. Goosse, O. Lecomte, M. Morales Maqueda, and G. Madec, 2012: The Louvain-la-Neuve sea ice model. *Notes du pole de modélisation, Institut Pierre-Simon Laplace (IPSL), Paris, France*, (31), <https://www.researchgate.net/publication/265061445>.
- Walker, D. P., A. Jenkins, K. M. Assmann, D. R. Shoosmith, and M. A. Brandon, 2013: Oceanographic observations at the shelf break of the Amundsen Sea, Antarctica. *J. Geophys. Res.: Oceans*, **118** (6), 2906–2918, <https://doi.org/10.1002/jgrc.20212>.
- Wang, Q., S. Danilov, and J. Schröter, 2009: Bottom water formation in the southern Weddell Sea and the influence of submarine ridges: Idealized numerical simulations. *Ocean Modell.*, **28** (1), 50–59, <https://doi.org/10.1016/j.ocemod.2008.08.003>.
- Wang, Y., and A. L. Stewart, 2018: Eddy dynamics over continental slopes under retrograde winds:

- Insights from a model inter-comparison. *Ocean Modell.*, **121**, 1–18, <https://doi.org/10.1016/j.ocemod.2017.11.006>.
- Wang, Y., and A. L. Stewart, 2020: Scalings for eddy buoyancy transfer across continental slopes under retrograde winds. *Ocean Modell.*, **147**, 101 579.
- Wei, H., and Y. Wang, 2021: Full-depth scalings for isopycnal eddy mixing across continental slopes under upwelling-favorable winds. *J. Adv. Model. Earth Syst.*, e2021MS002498, <https://doi.org/10.1029/2021MS002498>.
- Wei, H., Y. Wang, A. L. Stewart, and J. Mak, 2022: Scalings for eddy buoyancy fluxes across prograde shelf/slope fronts. *J. Adv. Model. Earth Syst.*, **14** (12), e2022MS003 229, <https://doi.org/10.1029/2022MS003229>.
- Whitney, F., W. Crawford, and P. Harrison, 2005: Physical processes that enhance nutrient transport and primary productivity in the coastal and open ocean of the subarctic NE Pacific. *Deep Sea Res. Part II*, **52** (5-6), 681–706, <https://doi.org/10.1016/j.dsr2.2004.12.023>.
- Whitworth, T., and A. H. Orsi, 2006: Antarctic Bottom Water production and export by tides in the Ross Sea. *Geophys. Res. Lett.*, **33** (12), <https://doi.org/10.1029/2006GL026357>.
- Whitworth, T., III, A. H. Orsi, S.-J. Kim, W. D. Nowlin Jr, and R. A. Locarnini, 1998: Water masses and mixing near the Antarctic Slope Front. *Ocean, ice, and atmosphere: interactions at the Antarctic continental margin*, **75**, 1–27, <https://doi.org/10.1029/AR075p0001>.
- Winton, M., 2000: A reformulated three-layer sea ice model. *J. Atmos. Oceanic Technol.*, **17** (4), 525–531, [https://doi.org/10.1175/1520-0426\(2000\)017<0525:ARTLSI>2.0.CO;2](https://doi.org/10.1175/1520-0426(2000)017<0525:ARTLSI>2.0.CO;2).
- Worby, A. P., C. A. Geiger, M. J. Paget, M. L. Van Woert, S. F. Ackley, and T. L. DeLiberty, 2008: Thickness distribution of Antarctic sea ice. *J. Geophys. Res. Oceans*, **113** (C5), <https://doi.org/10.1029/2007JC004254>.

Zhang, J., and D. A. Rothrock, 2003: Modeling global sea ice with a thickness and enthalpy distribution model in generalized curvilinear coordinates. *Mon. Weather Rev.*, **131** (5), 845–861, [https://doi.org/10.1175/1520-0493\(2003\)131<0845:MGSIWA>2.0.CO;2](https://doi.org/10.1175/1520-0493(2003)131<0845:MGSIWA>2.0.CO;2).

Zhou, Q., T. Hattermann, O. Nøst, M. Biuw, K. Kovacs, and C. Lydersen, 2014: Wind-driven spreading of fresh surface water beneath ice shelves in the Eastern Weddell Sea. *J. Geophys. Res.: Oceans*, **119** (6), 3818–3833, <http://dx.doi.org/10.1002/2013JC009556>.

Zwally, H. J., J. C. Comiso, C. L. Parkinson, D. J. Cavalieri, and P. Gloersen, 2002: Variability of Antarctic sea ice 1979–1998. *J. Geophys. Res. Oceans*, **107** (C5), 9–1, <https://doi.org/10.1029/2000JC000733>.

Zweng, M., and Coauthors, 2019: World Ocean Atlas 2018, Volume 2: Salinity. <https://www.ncei.noaa.gov/products/world-ocean-atlas>.